A Study of the Interactions of 200 A GeV ^{16}O and ^{32}S Ions in Nuclear Emulsion

Simon Kin-chung Yuen
University College London

Submitted to the University of London
for the degree of
Doctor of Philosophy
June 1992

Abstract

The general features of the hadronic inelastic interactions of 200 A GeV ^{16}O and ^{32}S ions with emulsion nuclei have been compared and contrasted. The fragmentation of ^{16}O and ^{32}S ions into projectile fragments of $Z \geq 2$ has been investigated. The multiplicity distribution of slow, target associated particles and fast, shower particles and the correlations among various multiplicity parameters have been studied for varying degrees of projectile fragmentation. The results are consistent with a geometrical model. Rapidity analysis of a particular class of events, which exhibit complete projectile break-up without overt sign of low-energy target fragmentation, has been carried out.

A systematic study of the electromagnetic dissociation(EMD) of ^{16}O and ^{32}S projectiles into exclusive channels of charged fragments at an incident energy of 200 A GeV has been carried out. The photoproduction cross-sections on ^{16}O and ^{32}S were determined by estimating the energy released in each interaction and assuming a model for the intensity and energy spectrum of the virtual photons. While there was good agreement for both ^{16}O and ^{32}S results for (γ, p) processes when compared with real photons data, especially in the giant dipole region, the rates for the (γ, α) processes were found to be an order of magnitude larger than expected. However, events, which have all the features ascribed to electromagnetic breakup plus a low-energy recoil proton, have been identified in interactions of ^{16}O. An eikonal distorted-wave impulse approximation(DWIA) estimate of the target A-dependence of strong interaction diffractive dissociation, based on the hydrogen data, suggests that most of the (C α) final states might in fact be of hadronic origin.

The mean free paths of fragments(Z=2-7) from the interaction of ^{16}O at 200 A GeV at different distances from their production point have been investigated and were found to be the same, independent of their multiplicity, target size, production generation and production mechanism.

Acknowledgements

During the preparation of this thesis, I have been assisted and encouraged by many people to whom I am deeply indebted.

First of all, I would like to thank the Nuclear Emulsion Group at University College London for providing the facilities necessary for the writing of this thesis and especially my supervisor, Professor D. H. Davis for leading the group and also for his valuable comments, discussions, guidance and encouragement during my years at University College. I would also like to thank Dr. D. N. Tovee and Professor C. Wilkin for their helpful advice on various occasions throughout this work.

I would like to express my gratitude to Mrs. J. Gardner and Miss Z. House for the scanning and measurements of data at University College and to all other laboratories, Dublin, Rome, Salerno and Turin in the collaboration for their contributions to this work.

Thanks are due to my fellow postgraduates, Dr. J. R. Dodd, Dr. D. Shaw, P. L. Makkar, A. Khan and S. F. Salih for numerous useful discussions and for their moral support and comradeship.

Away from physics, I am particularly indebted to G. Yung, J. Chan and K. Lau for many enlightening discussions. My special thanks are due to those friends whose kindness and support enabled me to survive the struggle.

Finally I would like to express my most sincere thanks to my parents and sisters for their love and encouragement. No amount of written words can do justice to the thanks I owe them.

Contents

List of Figures

List of Tables

Chapter 1

Introduction

Physicists have long searched for a new state of nuclear matter obtained at high density and temperature when the repulsive core of the nuclear force could be overcome. In the framework of quantum chromodynamics, this state should be a plasma of quarks and gluons, within which colour charge should freely propagate. Theoretical estimates for the density and temperature at which such a state can be achieved range from a few times to an order of magnitude larger than the normal nuclear density, which is 0.15 GeV/fm^3 at low temperature, or of temperatures above 200 MeV, at low quark chemical potential. The successful acceleration of 200 A GeV ^{16}O and ^{32}S ions at CERN provides strong hopes of reaching these conditions and opening a totally new area in the field of heavy ion studies.

The enthusiasm in the pursuit of creating highly compressed nuclear matter encompasses demands from various fields. Since the discovery of nuclei in 1911, nuclear physics has primarily centred on studies of nuclei under conditions in which the nuclear density is close to its equilibrium value and the excitation energy is relatively low. However experiments with high-energy heavy ions offer an opportunity to study the nuclear equation of state, the fundamental relationship specifying how the pressure depends upon density and internal energy. Theoretical speculations suggest that the nuclear equation of state is extremely complicated, and increase in density may cause nuclear matter to undergo one or more phase transitions. Compression that amounts to doubling the nuclear density from its normal value could lead to pion condensation[1], a state containing a large number of bound pions. Compression to several times normal nuclear density could result

in a density isomer, or a quasistable state existing at other than normal nuclear density. Still further compression could produce quark-gluon plasma in which quarks and gluons that are believed to comprise nucleons become deconfined.

In addition, studies of quark-gluon plasma may bear astrophysical implications since the very high pressure at the core of a neutron star could lead to its formation. This would affect the dynamics of the star and in particular its cooling rate. Furthermore it will contribute to the understanding of the early stages of the Universe. The temperature varies as $t^{1/2}$ as one approaches the Big Bang. Eventually a temperature, at which the quark-gluon plasma is formed, may be obtained. This occurred at about 10^{-5} sec after the Big Bang when the temperature of the Universe was 200 MeV.

Although the goal for the study of ultra-relativistic heavy ion interactions is to discover the quark-gluon plasma, the much more immediate objective is to investigate how favourable the experimental conditions are for a phase transition from hadronic matter to quark-gluon matter. In order to understand the background, on which the various proposed signals of quark-gluon plasma formation can be searched for, questions related to the *normal* reaction mechanisms have to be addressed. Therefore, the primary aim of the present work is to establish the characteristics to be expected of normal heavy ion-emulsion nucleus collisions by studying sizeable and unbiased samples of the hadronic inelastic interactions of 200 A GeV ^{16}O and ^{32}S ions with emulsion nuclei. In addition, at ultra-relativistic energies, ion beams are electromagnetic as well as hadronic probes. Indeed it is expected that the cross-section for projectile electromagnetic dissociation(EMD) increases with energy as well as with the charge of both projectile and target nuclei, representing a considerable fraction of the total projectile fragmentation cross-section in ultra-relativistic heavy-ion collisions. Finally, in view of the contradictory results obtained about the anomalous behaviour of projectile fragments in the past, it would be worthwhile to study the mean free paths of projectile fragments at ultra-relativistic energies in nuclear emulsion.

Chapter 2 reviews the theoretical arguments which motivate the search for the quark-gluon plasma. A description of electromagnetic dissociation in terms of the equivalent photon or Weizsäcker-Williams method is presented, and the mean free

path of a particle traversing a medium is defined. In addition the experimental status of high-energy nucleus-nucleus collisions, of electromagnetic dissociation of nuclei, and of anomalous behaviour of projectile fragments are surveyed.

Chapter 3 is devoted to a discussion of nuclear research emulsion as a target as well as a detector. The emphasis is on scanning procedure and its optimisation to search for various categories of events. Furthermore the measurement of relative angles between secondary fragments and the determination of their charge and range are described in detail.

The general characteristics of hadronic inelastic interactions of 200 A GeV ^{16}O and ^{32}S ions in nuclear emulsion are the subject of Chapter 4. The multiplicities of shower particles and the extent of target fragmentation are studied for varying degrees of disruption of the projectile nuclei. Comparison of these results with data from p- and α-emulsion interactions at nearly the same energy per nucleon provides information about the mechanism of particle production as well as projectile and target fragmentations in heavy ion collisions. The chapter concludes with a detailed study of the rapidity distributions of those events having the topology of complete projectile break-up without any overt sign of target fragmentation.

The experimental investigation of the EMD of 200 A GeV ^{16}O and ^{32}S ions in nuclear emulsion forms the basis of Chapter 5. Exclusive channels involving charge fragments are studied as a function of the energy released. By assuming a virtual photon spectrum given by the prescription of Weizsäcker-Williams and corresponding to the nuclear elements in the emulsion, the experimental cross-sections for various channels are compared with the results obtained from real photon events, where available.

Chapter 6 compares the mean free paths in nuclear emulsion of the projectile fragments with $2 \leq Z \leq 7$ to those predicted by theoretical models. Furthermore, an investigation of the dependence of the mean free paths of these fragments on the distance from the interaction vertex is carried out. The discussion is focused on whether fluctuations, if any, of mean free paths may be interpreted on statistical grounds.

Conclusions are presented in Chapter 7.

Chapter 2

Review on High Energy Heavy Ion Collisions

2.1 Hadronic Inelastic Heavy Ion Interactions

High energy interactions between nuclei are classically divided into *peripheral*, *quasi-central* and *central* interactions. Peripheral interactions usually occur when the impact parameter b nearly equals the sum of projectile and target nuclei radii. These reactions are associated with low momentum and/or energy transfer, consequently they have a small number of generated particles and emitted target fragments. The characteristics of the emitted fragments are determined by the intrinsic Fermi momentum distribution of nucleons within the fragmenting nuclei. The projectile fragments usually fly in a narrow forward cone with momentum per nucleon equal to that of a projectile nucleon, while the target fragments are nearly isotropically distributed in the laboratory frame. In this class of events there will be target and projectile *spectators*, in addition to nucleons which participate in the initial energy and momentum transfer. These latter nucleons are called *participants*. The spectator nuclei are supposed to disintegrate through a fragmentation or an evaporation process. The rapidity distribution of peripheral interactions mainly consists of projectile and target fragmentation regions which are separable at relativistic energies as shown in Fig. 2.1(a).

In quasi-central collisions, projectile and target nuclei are close to each other while in central collisions they are even closer. The difference in the two types

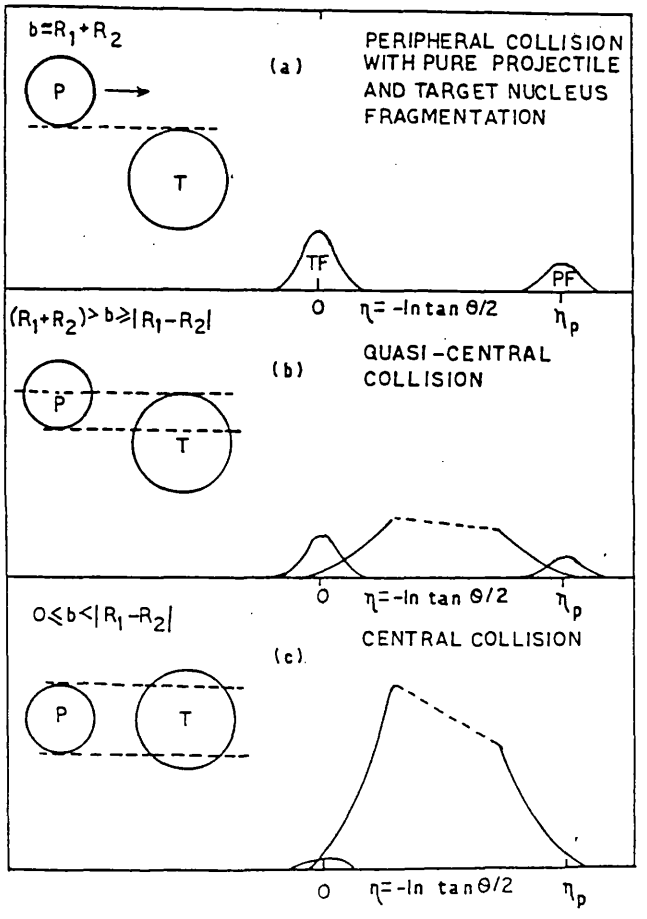

Figure 2.1: *A schematic outline of pseudorapidity distributions in heavy ion interactions at high energy.*

could be understood on the basis of the number of participant nucleons in the interaction. In both cases, the whole kinematically allowed rapidity space is available for produced particles, the difference being in the degree of population of the central region. The interaction is central when the impact parameter is less than the absolute value of the difference between the interacting nuclei radii, i.e. $b > |R_P - R_T|$, where R_P and R_T are the projectile and target nuclei radii, respectively. These events are characterized by large multiplicities of the generated particles and the emitted target fragments. The emission of particles is symmetric with respect to the direction of the incident beam. In central collisions where $R_P < R_T$, all projectile nucleons are participants and not projectile spectators. When a nucleon is no longer a spectator but participates in the interaction, it is scattered into rapidity space between the projectile and target fragmentation regions. When $R_P < R_T$, the rapidity space, available for the particles, is almost limited to the interval between the projectile and target fragmentation regions as shown in Fig. 2.1(c).

Fig. 2.2 shows the microphotograph of a typical example of a central interaction between a 200 A GeV ^{16}O projectile nucleus and a heavy(Ag,Br) emulsion nucleus.

2.1.1 Historical background

The study of high energy nucleus-nucleus collisions began with the discovery of the heavy ion component in primary cosmic rays by Freier *et al.*[2,3] in 1948, long before the high energy heavy ion beams became available at laboratory accelerators. These studies were aimed at determining the fragmentation cross-sections and mean free paths of nuclei as these data are required for estimating the elemental composition of cosmic rays at the source and for studying their interstellar propagation mechanism. Most of the fundamentals of experimental and theoretical approaches were established by Bradt and Peters[4,5,6,7], Kaplon *et al.*[8] and Eisenberg[9]. Although these studies provided a preview of the physics of the interactions between relativistic nuclei, systematic and extensive studies of nucleus-nucleus interactions at high energies could not be pursed due to the low flux and wide energy range of the cosmic ray nuclei. Furthermore, the simpler

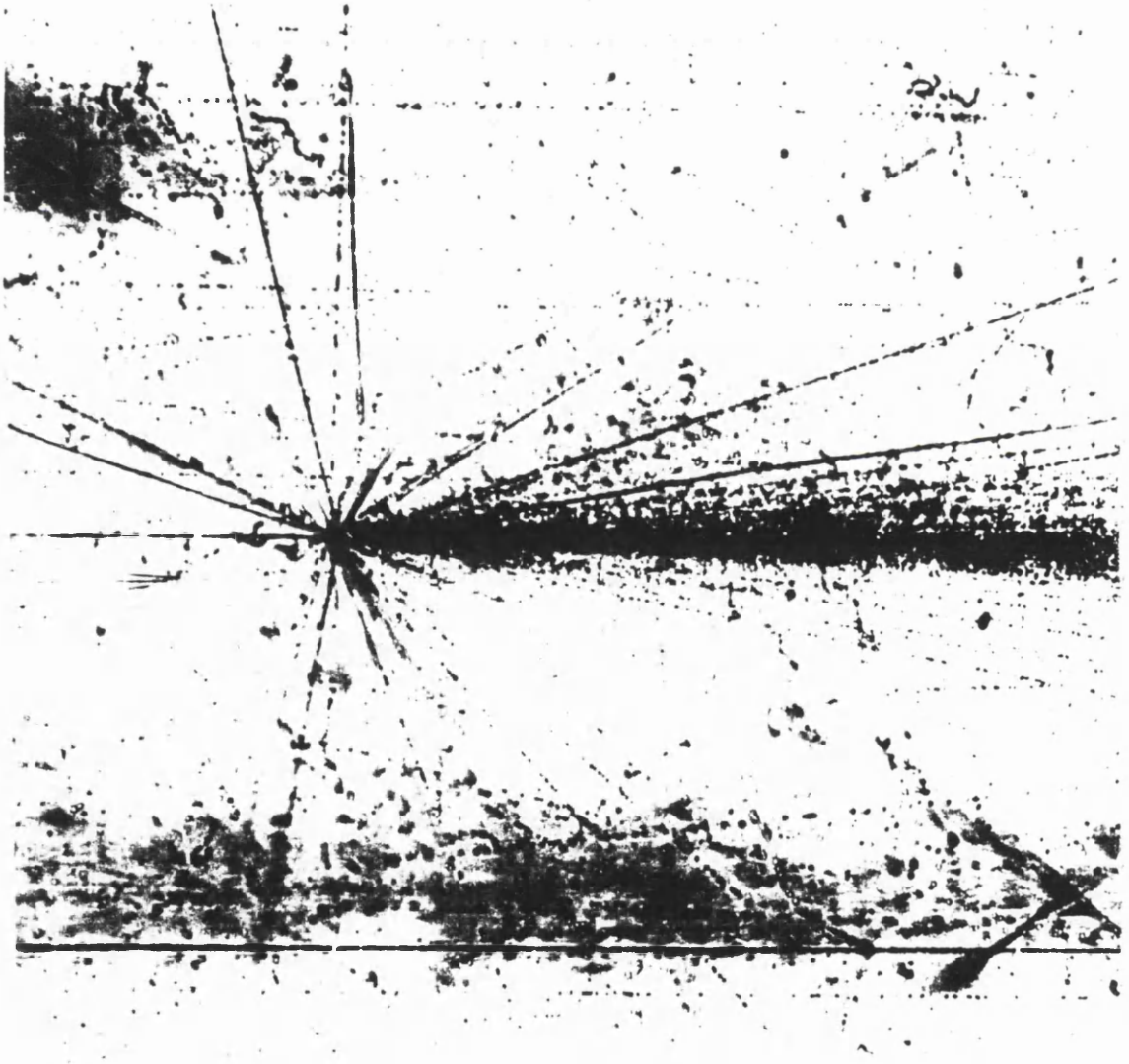

Figure 2.2: *Microphotograph of a central interaction between a 200 A GeV* ^{16}O *projectile nucleus and a heavy(Ag,Br) emulsion nucleus.*

nucleon-nucleon interaction was not well understood at that time and nucleus-nucleus collisions were(and still are) regarded as very complicated.

In the early seventies, when heavy ion accelerators like Bevalac at Berkeley with energies up to 2.6 A GeV and JINR Synchrophasotron at Dubna with energies up to 4.5 A GeV became available, interest in the study of nucleus-nucleus collisions was revived. In less than a year, the kinetic energies of accelerated beams in the laboratory increased by more than two orders of magnitude. This has turned the physics of heavy ions into the relativistic regime. Experimental techniques and theoretical concepts from high energy physics are used with the additional complication that multi-nucleon systems having large dynamic ranges in particle multiplicities, charges, mass, excitation energies and possibly nuclear temperatures and densities are the objects under investigation. Thus heavy-ion physics encompasses the demands from the fields of nuclear physics, cosmic rays and high energy physics.

The early experiments at Bevalac on projectile fragmentation studied fragmentation cross-sections that are vital for the understanding of cosmic ray sources and propagation of heavy nuclei in the interstellar medium. Other experiments on target fragmentation have focused on light fragment production from heavy targets, primarily in the target and near target regions of rapidity, but with brief excursions into those of midrapidity. These experiments[10,11,12,13,14,15,16,17,18] gave evidence that the hypothesis of limiting fragmentation[19,20], developed to describe the single-particle inclusive spectra from high energy elementary particle interactions, is applicable to relativistic heavy ion interactions. The isotopic production cross-sections and spectral distributions of spectator fragment nuclei were found to be independent of energy for beam energies 1-2 A GeV.

Related to the hypothesis of limiting fragmentation is the factorization hypothesis for cross-sections which states that the cross-section for the production of F at high energy may be expressed as a product $\sigma_{BT}^{F} = \sigma_{B}^{F}\gamma_{T}$ where the cross-section σ_{B}^{F} depends only on the beam and fragment and γ_{T}, the target factor, depends only on the target. As part of an experiment pertaining to the electromagnetic dissociation of relativistic ^{18}O(see sec. 2.2), Olson *et al.*[21] demonstrated that factorization of the isotopic cross-sections for nuclear processes is valid to better than 5 %.

Experiments studying the reaction characteristics of the midrapidity region did not provide any evidence for new states of nuclear matter as theoretical speculation might suggest. A multitude of theoretical and/or phenomenological models(e.g. fireball/firesteak model[22,23,24,25,26], clean-knockout model[27]), widely differing in their initial assumptions, have fitted these data, especially the innumerable single-particle inclusive spectra, equally well. These models represent the extrema in their assumptions as to the basic mechanisms in relativistic heavy ion collisions, ranging from the formation of a fully equilibrated thermodynamic system[23,25] to the single nucleon-nucleon scattering[27]. Neither have the investigations of particle multiplicities and of strange particle production revealed any new, unexpected features of the interactions.

The search for exotic phenomena has also led to the observation of isotopes far from stability. Symons *et al.*[28] and Westfall *et al.*[29] have accelerated Ar and Ca beams and discovered 16 new isotopes in projectile fragments. However these interactions are still in the realm of peripheral interactions and fall short of the compression needed for the production of quark matter.

All these results appeared to convey the message that there was a definite need for a new generation of relativistic heavy ion experiments conducted at considerably higher energies than had been available up to that time. A positive response to this message was the acceleration of ultra-relativistic beams which created a new frontier of particle and nuclear physics. At Brookhaven, oxygen and silicon ions were accelerated up to 15 A GeV, but the programme will be extended all the way to incident gold ions in the near future. At CERN, oxygen ions and sulphur ions, of incident energies 200 A GeV, were shot at a variety of nuclear targets. The present experiment was carried out at CERN in 1986 and 1987 as part of the efforts to investigate the mechanism of high energy nucleus-nucleus interaction.

2.1.2 Quark-gluon plasma

The Standard Model predicts that at high enough energy density nuclear matter undergoes a phase transition into a deconfined plasma of quarks and gluons in which chiral symmetry is restored[30,31]. The study of such a transition is important since the Universe probably underwent such a transition in the opposite

direction when in the very early stages after the Big Bang the energy density fell below a few GeV/fm^3. At that moment the deconfined quark-gluon plasma started to hadronize. The chemical potential of the different quark flavours at the transition stage and the hadronization mechanism probably played a significant role in determining the ratio of matter to antimatter as well as the fraction of baryons and mesons in the resulting hadronic state. Since from the quark-antiquark combinatorics at the moment of confinement it is expected that far more mesons than baryons would be produced, and since a fraction of the meson energy eventually ends up in the form of neutrinos, the actual path that was followed during hadronization is relevant to the missing mass problem and to questions of whether the Universe is open or closed.

According to the Standard Model, hadrons consist of quarks and gluons. Quarks are pointlike($r < 10^{-3}$ fm) particles with spin=1/2 and have fractional electric charges($\pm$ 2/3 e or $\pm$ 1/3 e) as well as a weak charge(couple to $W^{\pm}$ and Z). Furthermore quarks come in six different flavours, namely, up(u), down(d), strange(s), charm(c), bottom(b) and top(t). On the other hand, gluons do not couple to electroweak fields but carry about 50 % of the hadron momentum. Gluons are the fields of the strong interaction which couple to the *colour charge* of quarks and are therefore responsible for their strong interaction.

The older *naive* quark models and the modern theory of Quantum Chromodynamics(QCD) describe a wide range of different phenomena; some of them fairly quantitatively(the *hard* interactions, i.e., those involving large momentum transfers and thus probing the point-like nature of the constituents, e.g., deep-inelastic lepton interactions, e^+e^- annihilation into hadrons, high p_T hadron production in pp interactions); others more qualitatively(the spectrum of known resonances and particles, and *soft* interactions of hadrons, i.e. those with small momentum transfers, e.g. the normal hadron-hadron interactions).

However, up to this day, no isolated quarks or gluons have been observed. It is believed that quarks are constituents of a conceptually new kind which are confined in hadrons and cannot exist as isolated particles. In the language of QCD, quarks come in three colours and are confined because only colour singlets can exist in nature. Colour singlets can be formed by combining three quarks with different

colours, or a quark and an antiquark with the corresponding anti-colour, or by a superposition of these combinations. All known hadrons(stable or resonances) are thought to be constructed either from three valence quarks[$(q_1 q_2 q_3)$ = baryons], or a valence quark and a valence anti-quark[$(q_1 \overline{q}_2)$ = mesons], plus some amount of sea quarks[$\sum_i (q_i \overline{q}_i)$] and some gluons.

So far no hadrons have been observed which can be unambiguously assigned to theoretically possible, *exotic* colour-singlet combinations of more than three valence quarks or of only gluons. If single isolated quarks cannot be observed because of confinement, it is not only natural but also compulsive to search for more complex states

In the past years, questions have been raised about the necessity of a quark model to understand the structure of nuclei. New incentives were provided when the European Muon Collaboration(EMC) at CERN discovered that the structure functions of nuclei are not simple superpositions of structure functions of nucleons(the *EMC effect*). Since this result was obtained at high Q^2(invariant squared momentum transfer), it reflects presumably more than the trivial fact that nuclei are not superpositions of free nucleons, but are complicated structures of bound nucleons. It revived speculations that nuclei may contain confinement volumes or *bags* with six, nine or more quarks. The occurrence of such large bags within nuclei has also been hypothesized to explain other odd phenomena. However the EMC effect and these phenomena cannot be considered as a proof that large bags exist within nuclei in their ground state. Therefore, the basic question of whether more than three valence quarks can be bound in a single confinement volume remains unanswered.

A theoretical response to this question came from lattice QCD(LQCD) at finite temperature. LQCD predicts that at an energy density about 10 times the one of nuclei in their ground state($\sim$ 2 GeV/fm^3), nuclear matter composed of almost separate nucleons will fuse into a quark-gluon plasma(QGP) - quarks will be deconfined, before they are essentially confined in their host nucleons. After the deconfinement phase transition , they will move freely in a larger confinement volume.

It is believed that the experimental proof of such a phase transition is almost as important a test for QCD as finding the W or Z particles was for the theory of electroweak interactions. According to theoretical estimates, the necessary temperature and pressure or baryon density can indeed be reached in nucleus-nucleus collisions at ultra-relativistic energies. This explains the excitement and remarkable activation of interest for nucleus-nucleus collisions in the past few years.

The conditions for a deconfinement phase transition from nuclear to quark-gluon matter are assumed to be: sufficiently high-energy density(of the order of 2 GeV/fm^3) in a sufficiently large volume(of the order of 1 to 100 fm^3) and thermodynamic equilibrium. Various signals for detecting the deconfinement phase transition have been proposed. They include increased yield of strange particles[32,33], change of the spectrum of dileptons or of direct photons[34], decreased yield of charmed particles[35], non-statistical fluctuations of particle densities as a function of rapidity in individual events etc.

2.2 Electromagnetic Dissociation in Heavy Ion Interaction

2.2.1 Historical background

In addition to effects due to strong interaction, dissociation of heavy ions may also result from the electromagnetic interaction between projectile and target nuclei at impact parameters larger than the range of the nuclear force. This process is thought to take place when a relativistic heavy ion passes near a high Z target nucleus at impact parameter which may significantly exceed the sum of projectile and target radii, i.e. $b > R_P + R_T$. A virtual photon from the Coulomb field of the target nucleus is absorbed by the projectile resulting in the excitation of a giant resonance($10 < E < 40$ MeV), or the quasi-deuteron effect($40 < E < 140$ MeV), or nucleon resonance($E > 140$ MeV), depending on the energy of the photon. A similar process can occur to the target nuclei.

The cross-section for projectile electromagnetic dissociation(EMD) is expected to increase with energy and charge of both projectile and target nuclei roughly as

ln E, Z_P and Z_T^2, respectively. In the case of ^{32}S-Pb interactions at 200 A GeV, it is larger than the corresponding hadronic cross-section.

EMD of relativistic heavy ions was predicted by Butler and Pearson[36] and later observed in the collisions of cosmic-ray relativistic heavy ions in nuclear emulsion[37,38] The first EMD experiment using heavy ion beams was performed by Heckman and Lindstrom[39] looking at excitations in ^{12}C and ^{16}O projectiles at energies of 1.05 and 2.1 A GeV on a variety of targets(^{12}C, ^{27}Al, ^{64}Cu, ^{108}Ag, and ^{208}Pb), while Westfall[40] also found evidence for projectile EMD from a single-particle inclusive experiment with projectile ^{56}Fe. Measured EMD cross-sections for nucleon emission ranged from 0 to 50 mb. Olson *et al.*[21] later measured excitation of ^{18}O projectiles at 1.7 A GeV on ^{48}Ti, ^{208}Pb, and ^{238}U with cross-sections up to 140 mb. Studies of ^{197}Au and ^{59}Co target excitation[41,42,43,44] were later reported with cross-sections all the way up to 1970 mb for ^{139}La projectiles at 1.26 A GeV. Lighter projectiles were also used[41,42,43,44,45] with smaller cross-sections. All these studies have been for projectile energies less than or equal to 2.1 A GeV. The measurements were made at Berkeley Bevalac. However some very interesting measurements have also been made at the Brookhaven AGS using ^{28}Si projectiles at 14.5 A GeV[46] and at the CERN SPS using ^{16}O and ^{32}S projectiles at 60 and 200 A GeV[47,48,49,50,51,52].

2.2.2 Weizsäcker-Williams Method

The simplest way to describe the reaction mechanism in the relativistic electromagnetic interaction is provided by the equivalent photon method, which is originally due to Fermi[53] and later on developed by Weizsäcker[54] and Williams[55]. In the literature it is also commonly referred to as the Weizsäcker and Williams method. A more detailed description of the method can be found in the textbook of Jackson[56] on classical electrodynamics.

In the model of Weizsäcker and Williams, the electromagnetic field of a point-charge target T is seen by a passing point-charge projectile P as a flux of photons as shown in Fig. 2.3. The photon energy spectrum is computed classically as the

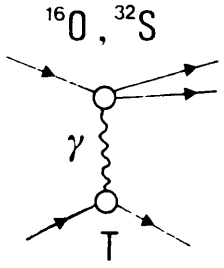

Figure 2.3: *Diagram of projectile electromagnetic dissociation(EMD).*

Fourier transform of the time-varying electromagnetic field[56]:

$$\frac{dI}{d\omega} = \frac{2Z_T^2e^2}{\pi c\beta^2}\{xK_0(x)K_1(x) - \frac{1}{2}\beta^2x^2[K_1^2(x) - K_0^2(x)]\}\ , \qquad (2.2.1)$$

where K_i are modified Bessel functions of order i, and $x = \omega b/\beta\gamma c$. Here b is the impact parameter, γ the Lorentz factor, and β the velocity of the incident charge in units of c. Putting the photon energy $E_\gamma = \hbar\omega$, the maximum energy of the spectrum is

$$E_{max} \approx \frac{\hbar\gamma c}{b_{min}}\ , \qquad (2.2.2)$$

where b_{min}, the minimum impact parameter, is in practice the sum of the radii of the colliding nuclei. Under our conditions, E_{max} ranges from 5 to 10 GeV, depending on the sizes of the projectile and target nuclei.

For $E_\gamma \ll E_{max}$(in practice, for E <0.2E_{max}) and $\beta \approx$1, eq. 2.2.1 appropriately summed over the possible impact parameters can be approximated by

$$N(E_\gamma) = \frac{2Z_T^2e^2}{\pi\hbar cE_\gamma}(ln(1.123\hbar\gamma c/E_\gamma b_{min}) - \frac{1}{2})\ . \qquad (2.2.3)$$

A quantum mechanical approach to the virtual photon method using the plane wave Born approximation[57] yields virtual photon spectra distinguished by multipolarities. The E1 and M1 spectrum are almost identical with the classically derived one when $\beta \rightarrow 1$, whereas the E2 spectrum differs considerably in the low-energy region[58].

The total charge changing cross-section σ_{EMD} for EMD can be written in a form decomposed by multipolarities:

$$\sigma_{EMD} = \sum_j \int (N_{Ej}(E_\gamma)\sigma_\gamma^{Ej}(E_\gamma) + (N_{Mj}(E_\gamma)\sigma_\gamma^{Mj}(E_\gamma) dE_\gamma \ , \tag{2.2.4}$$

where the subscripts E and M specify electric and magnetic transition, respectively, and j is the angular momentum quantum number. $\sigma_\gamma^{Ej}(\sigma_\gamma^{Mj})$ is the charge changing photonuclear cross-section due to electric(magnetic) transition and is measured experimentally with real photons. For high values of the Lorentz factor $\gamma \gg 1$ as given in our experiment the field lines made by the target nucleus within the projectile nucleus appear more uniform and less radial and resemble the plane electromagnetic wave fields. Therefore all multipolarities are contained with nearly the same weight in the virtual photon spectrum: $N_{E1} \approx N_{M1} \approx N_{E2} ... \equiv N$ and σ_{EMD} can be written as:

$$\sigma_{EMD} = \int N(E_\gamma) \sum_j (\sigma_\gamma^{Ej}(E_\gamma) + \sigma_\gamma^{Mj}(E_\gamma)) dE_\gamma \tag{2.2.5}$$

$$= \int N(E_\gamma)\sigma_\gamma(E_\gamma) dE_\gamma \ . \tag{2.2.6}$$

But for photon energies $E_\gamma \leq 30$ MeV, N_{E2} is significantly greater than N_{E1}. In this region a weighted photon spectrum corresponding to the relative strength of the giant dipole and quadrupole resonances should be used. The relative strength can roughly be estimated using sum rules as shown in ref.[59]. For E_γ >30 MeV weighting is without any effect.

Nuclear emulsion is an heterogeneous target but, owing to the Z_T^2 dependence in eq. 2.2.3, the heaviest constituents(Ag and Br) contribute more than 95% of the total intensity of photons. Fig. 2.4 shows the low-energy part of the photon spectrum for a 200 A GeV ^{16}O projectile for the various constituents of the nuclear emulsion. The corresponding spectra for ^{32}S projectiles almost overlap the oxygen ones.

The response of the projectile nucleus to the flux of photons is governed by its photonuclear cross-section, which to first approximation, is proportional to Z_P. Depending on the energy of the incident quanta, the most effective absorption mechanisms are the giant dipole resonance for 10< E <40 MeV, the quasi-deuteron effect for higher energies, and pion production above the corresponding energy

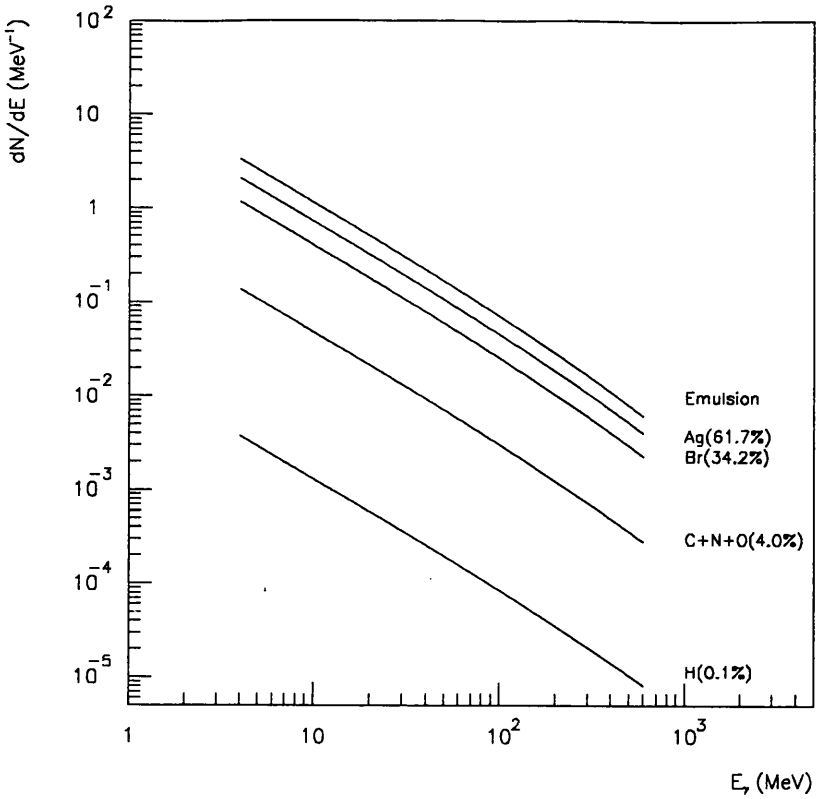

Figure 2.4: *The energy spectrum of virtual photons for 200 A GeV ^{16}O projectiles in nuclear emulsion.*

threshold($\approx$140 MeV). Absorption through the giant resonance usually results in the emission of a single nucleon, leaving the residual nucleus in its ground state or in some exited level. The kinetic energy of the fragments in the c.m. system is small, of the order of the binding energy of the ejected nucleons. The quasi-deuteron effect[60] becomes important as the energy increases, because the Fermi momentum of a single nucleon inside the nucleus is too small to satisfy the conservation of energy and momentum, and therefore an interaction with a cluster of nucleons is required. This effect would lead to the emission of more than one nucleon, and the total kinetic energy of the outgoing fragments is correspondingly larger than in the previous case. Above the threshold for pion production, the excitation of baryon resonances can contribute, and pions are emitted in addition to nuclear fragments. This process dominates at high energy.

Extensive studies on γ-nuclei cross-sections, especially those at the lowest energies, were often based on experiments each aiming to detect a single or a few channels, usually in an inclusive manner. In high energy projectile electromagnetic dissociation, the fragments are confined within a small forward cone with

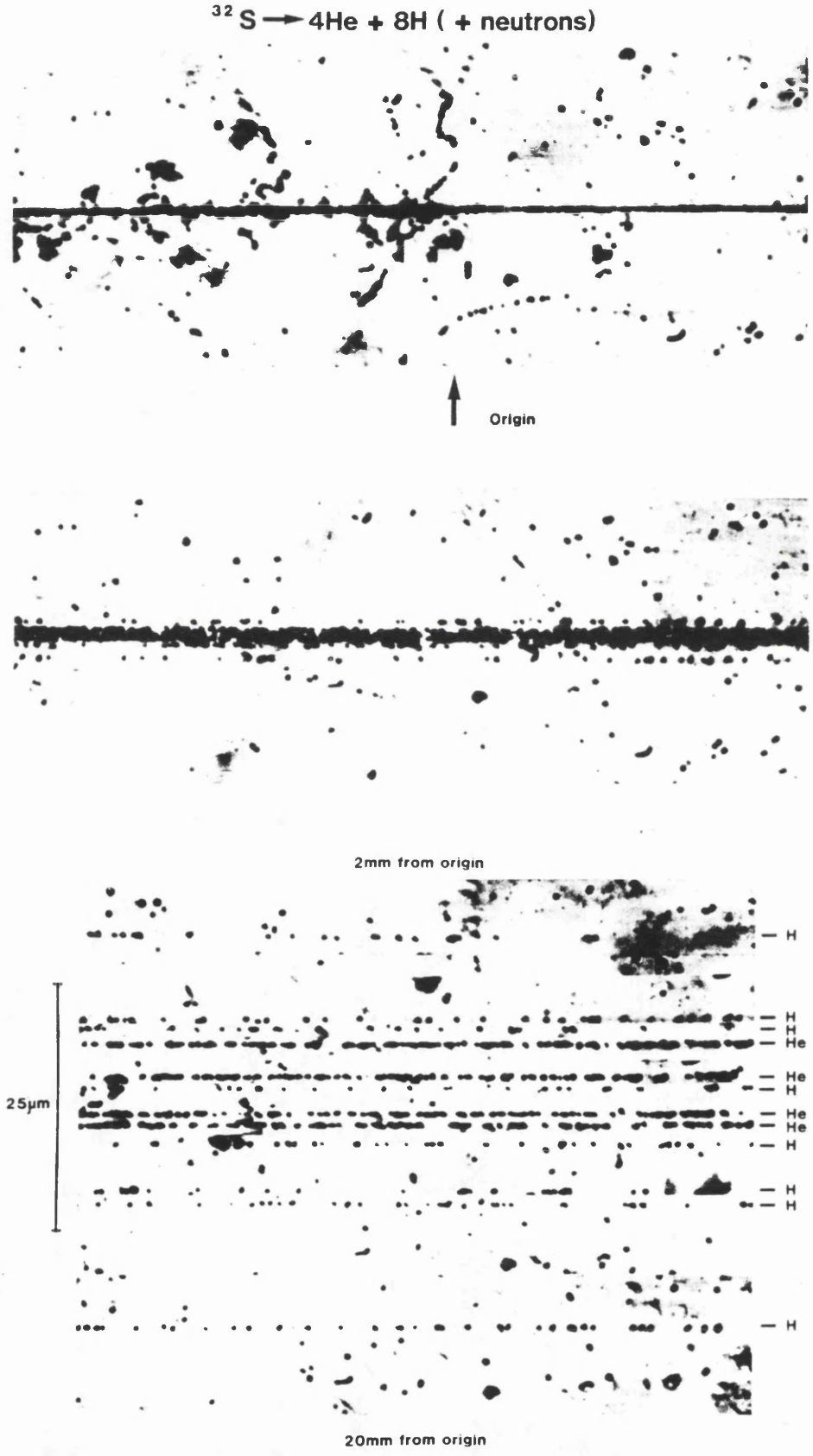

Figure 2.5: *Microphotograph of a complex projectile EMD(200 A GeV ^{32}S).*

momentum per nucleon almost equal to that of the beam. No sign of excitation of the target nucleus is expected. All the possible configurations involving charged projectile fragments can be easily detected in nuclear research emulsions with a high efficiency. In addition, measurement of relative angles among the fragments allows a reasonable estimate of the total kinetic energy released in each interaction. Fig. 2.5 shows the microphotograph of a complex example of projectile electromagnetic dissociation.

A flux of photons similar to that experienced by the projectile is also seen by the target as coming from the projectile. As a result, the target nucleus emits low-energy fragments isotropically, and the projectile continues undisturbed. Fig. 2.6 shows the microphotograph of a probable example of such a process. However, due to the complex composition of nuclear emulsions and the low efficiency in the detection of such events, the electromagnetic dissociation of target nuclei will not be considered here.

2.3 Anomalons

2.3.1 Historical background

In 1954, six years after the discovery of the heavy-ion component in cosmic rays, projectile fragments from relativistic heavy ion collisions were reported, apparently, having anomalously short interaction mean free paths[61]. These fragments of short mean free paths are called *anomalons*. Subsequent cosmic ray experiments appeared to confirm this result[62,63,64,65,66].

The first detailed and systematic study of anomalons was carried out by Judek [65] in emulsions exposed to cosmic rays. On the basis of mean free path measurements of relativistic cosmic ray primary and secondary nuclei, Judek concluded that a few percent of the secondary nuclei with charges $1 \leq Z \leq 4$ had anomalous mean free paths of the order of 3 cm and that the stars produced by the anomalous nuclei had the characteristics of ordinary nuclear collisions as observed in nuclear emulsion. However more systematic studies led to mixed conclusions. Freier and

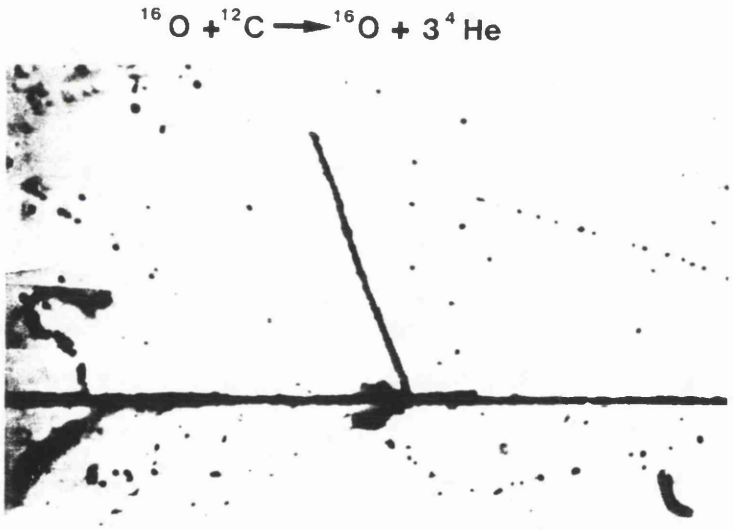

Figure 2.6: *Microphotograph of a possible target EMD(200 A GeV ^{16}O).*

Waddington[68] were unable to confirm the existence of anomalons whereas Barber *et al.*[69] confirmed the anomalous behaviour of projectile fragments in cosmic ray data.

It was not until beams of accelerated nuclei became available that the technical and statistical limitations of the cosmic ray experiments could effectively be eliminated and the problem systematically pursued. In 1972 Judek[67] exposed an emulsion stack to 1.8 A GeV ^{16}O beam and confirmed her earlier result on anomalons. Later Friedländer *et al.*[70,71] carried out a systematic study of projectile fragments with $3 \leq Z \leq 26$ from ^{16}O and ^{56}Fe collisions in nuclear emulsion at ~ 2 A GeV and suggested that 6 % of the projectile fragments were anomalons with an interaction mean free path of 2.5 cm. Jain and Das[72] and Aggarwal *et al.*[73] also confirmed the anomalous behaviour of projectile fragments in emulsion with $3 \leq Z \leq 26$ emitted from heavy ion beams of ^{40}Ar and ^{56}Fe at an energy of $\sim$2 A GeV. Furthermore a CR-39 plastic etched detector study by Tincknell *et al.*[74] using ^{40}Ar of 1.85 A GeV from Berkeley reported positively on the existence of anomalons in the range $9 \leq Z \leq 17$, while a similar study by Heinrich *et al.*[75] reported negatively. The result of a search for anomalous fragments in 1.8 A GeV ^{40}Ar interactions in nuclear emulsion[76] was consistent with the nonexistence of anomalons, whereas Aggarwal *et al.*[77] reported positively the existence of anomalons produced by 1.52 A GeV ^{84}Kr collisions in nuclear emulsion. Searches using Cherenkov detectors for anomalons of $13 \leq Z \leq 17$ produced in lucite by 1.82 A GeV ^{40}Ar and 1.88 A GeV ^{56}Fe were negative[78,79]. There is some suggestion that the anomalon effect is more marked for projectile fragments in the range $29 \leq Z \leq 36$ than those in $15 \leq Z \leq 28$[80].

There is also disagreement as to whether or not anomalons of low Z occur. Jain *et al.*[81,82] found the interaction mean free paths of α particles, emitted from beams of ^{40}Ar, ^{56}Fe and ^{84}Kr of energy $1 \leq E \leq 2$ A GeV, to be independent of distances from their production points. Similar studies[83,84] also could not find anomalons of Z=2, 3, or 4 but other emulsion[85,86] as well as bubble chamber[87] experiments reported the existence of anomalons for fragments of Z=2. Another bubble chamber experiment[88] found evidence for anomalons of Z=6 while Khan[89] did not observe any Z=2 anomalons but found evidence for anomalons of $3 \leq Z \leq 6$. However, recent experiments[90,91,92] did not observe

any anomalous behaviour in the mean free paths of Z=2 fragments emitted from the collisions of ^{16}O and ^{32}S at 60 and 200 A GeV in nuclear emulsions.

Among the experiments reporting positively on the phenomenon there is general agreement that the enhancement in interaction cross-section of the fragments disappears some 1 to 2 cm from their point of origin. Two models have been discussed to interpret this enhanced cross-section. Friedländer *et al.*[70,71] assumed the production of anomalons in an abundance of a few percent relative to ordinary fragments and of mean free path considerably shorter than for a regular nucleus of the same Z. Alternatively, another model assumed by Barber *et al.*[69] suggests the production of anomalons in a relative abundance of some tens of percent with a mean free path shorter than expected by a factor of less than 2 in which case the anomalous property would be lost by some electrically-neutral process after a few times 10^{-11} sec. In either case the anomalous interaction probability would have to persist for at least a few times 10^{-11} sec for the phenomenon to have been detected.

Extensive statistical analysis[71] appears to establish the effect at the level of several standard deviations, although it has been suggested[93] that it is an artifact of statistical bias in the mean free path estimate.

There have been a number of theoretical attempts to explain the existence of anomalons. Some of these suggestions are conventional, making use of the well established ideas in nuclear and particle physics, while others are highly exotic. A wide range of speculations has been proposed: quasi-molecular structure in nuclei[94]; unconventional nuclear structure[95], multi-quark compound resonances[96], hidden colour excitations[97], diquark deuteron[98], broken quantum chromodynamics[99,100,101], unconfined quarks[102], hadronic monopole[103], unconfined gluon fields[104], low density quark blobs[105], pineuts[106], vacuum perturbation outside pion-condensed nuclei[107].

2.3.2 Definition of mean free path

Consider the passage of a homogeneous beam of particles through a target medium of constant density of ρ target nuclei per unit volume. Let σ be the total cross-

section for interactions. The probability of interaction per unit length is given by $\gamma = \rho\sigma$. If the medium is heterogenous, with ρ_i and σ_i being the number density and the interaction cross-section for the ith component, then

$$\gamma = \sum_i \rho_i \sigma_i \ . \tag{2.3.1}$$

One would expect that γ is a function of the distance x along the projectile path since the σ_i's depend on the projectile energy.

Let $n(x)$ be the fraction of projectiles that have not interacted after travelling a distance x from the their starting points in the medium. $n(x)$ decreases with increasing x according to the differential equation

$$\frac{dn(x)}{dx} = -\gamma(x)n(x) \tag{2.3.2}$$

The solution to this equation is

$$n(x) = e^{-\int_0^x \gamma(x')dx'}. \tag{2.3.3}$$

For relativistic nuclei, σ_i, and thus γ_i, depend mainly on geometrical considerations and are fairly energy independent. Assuming γ being independent of x, the solution becomes

$$n(x) = e^{-\gamma x} \ . \tag{2.3.4}$$

If we replace the track lengths by time intervals, this is just the law of radioactive decay. The probability density $f(x)$ for an interaction distance x is given by

$$f(x) = \gamma e^{-x/\lambda} \ . \tag{2.3.5}$$

The mean free path is thus defined as

$$\lambda = \int_0^\infty x\gamma e^{-\gamma x} dx = \frac{1}{\gamma} \ . \tag{2.3.6}$$

The geometrical dependence of the cross-section, in its simplest approximation, is expressed in the Bradt-Peters form[6],

$$\sigma_{12} = \pi r_0^2 (A_1^{1/3} + A_2^{1/3} - \delta)^2 \ , \tag{2.3.7}$$

where r_0 and δ are constants and A_1 and A_2 are the baryon numbers of target and projectile nuclei. Furthermore, it has been suggested that the mean free paths of relativistic projectile nuclei follow an approximate power law of the form[70,71,72]:

$$\lambda(Z) = \Lambda Z^{-b} \ . \tag{2.3.8}$$

where Z is the charge of the nuclei and Λ and b are parameters determined experimentally.

Chapter 3

Experimental Techniques

3.1 Introduction

The detection of radiation by exposure of photographic plates dates back to the discovery of X-rays by Bequerel in 1896. Nuclear research emulsion today still remains an important detector for experiments requiring the best possible spatial resolution.

Due to their continuous sensitivity, to their exceptional spatial resolution in three dimensions($\approx$ 1 μm) and to their 4π solid angle coverage, emulsions have been used in pioneering work that can guide far more refined experiments. Besides being both a target as well as a detector, emulsion is a composite material and is ideal for study of interactions with different nuclei. It is not only capable of counting particles but also giving information concerning their charge, their mass, their energy, their angular distribution, and their modes of collision and decay. Unexpected features, not specifically included as a trigger in another experiment, are recorded in emulsion anyway and can be studied at any time. In addition, in the past two decades, new methods of exposure and of analysis of nuclear emulsions were developed, primarily with the aim of exploiting their characteristics in the search for short-lived particles carrying heavy flavours(charm, beauty...). With the development of high resolution tracking, computer-aided scanning has enhanced the analysing power of this technique.

Emulsions consist of myriads of small crystals of silver halide, mostly bromide but with a small admixture of iodide, embedded in gelatine[37]. A layer of the emulsion, typically 600 μm thick, covers a plate, a number of which may be piled together to form a stack. Sometimes the emulsion is loaded with metal wires, foil or powdered layers to give a well-defined target.

When light falls on the emulsion or ionizing particles pass through it, some of the halide grains are modified in such a way that on immersing the plate in a reducing bath, called the *developer*, they are turned into grains of silver. The latter, being made up of finely divided crystalline aggregates, appear black. The modifications in the grains due to the action of radiations are invisible, and the effect is described as the formation of a *latent image.* Thus, a series of grains is formed along the trajectory of the particle which is termed as a *track.* A minimum ionizing particle produces $\sim$ 270 developed grains per millimetre of track length.

When a particle with charge $Z_P e$ and mass M_P traverses a medium of atomic number Z_T and mass number A_T, it excites and ionizes the atoms of the medium through Coulomb interactions. This results in a loss of energy of the incident particle. The rate of energy loss dE per unit length dx traversed is given approximately by the relation[110]:

$$-\frac{dE}{dx} = \frac{4\pi N Z_T Z_P^2 e^4}{m_e v^2 A_T}[ln\frac{2m_e v^2}{I(1-\beta^2)} - \beta^2] \ , \qquad (3.1.1)$$

where v is the velocity of the incident particle, N is the number of atoms per cm^3 of the stopping material, I is the mean ionisation potential of all the electrons in the medium, m_e is the electron mass and $\beta=\frac{v}{c}$. It is clear from eq. 3.1.1 that the energy loss does not depend on the mass of the particle. Instead the energy loss is a function of velocity and charge. Since the logarithmic term varies only slightly with v, the energy loss is proportional to $\frac{Z_P^2}{v^2}$ and $\frac{Z_T}{A_T}$.

3.2 Experimental Details

3.2.1 Irradiation of the stacks

Emulsion pellicles of 600 μm thickness were prepared at CERN from Fuji ET 7B gel just prior to exposure. This procedure was carried out in an atmosphere of 70

% relative humidity and the resulting emulsions were found to have a density of $(3.60 \pm 0.01) \times 10^3$ kg m^{-3}, which is some 6 % lower than the so-called 'standard' one[108], measured at 58 % R.H. Under the assumption that the disparity in the density is due solely to an increase in water content of the present emulsion, the elemental abundances have been calculated for the major constituents and these are compared to those of standard emulsion in Table 3.1.

Table 3.1: *Composition of emulsions*

Element	Standard (10^{20} atoms/cm^3)	Fuji (10^{20} atoms/cm^3)
H	322	350
C	138	127
N	32	29
O	95	114
Br	101	93
Ag	101	93

Having been poured, dried and peeled from their glass backing, the emulsions were guillotined to produce pellicles of the desired dimensions, 160mm$\times$50mm$\times$600μm. These were then assembled into stacks of which two, each of 62 pellicles, were exposed to the 200 A GeV ^{16}O beam in the West Area at CERN in December 1986 and four, each of 60 pellicles, were exposed to the 200 A GeV ^{32}S beam in November 1987. In all exposures, the beam was parallel to the longer side and horizontal with respect to the pellicle surface.

3.2.2 Scanning

In order to reduce the bias against detecting small stars, the search for interactions was carried out using a line-scanning technique. In this investigation, tracks of beam particles were located 10 mm from the entrance edge of the emulsion stack and those within the central 80 % of the pellicle thickness were followed for a

distance of 30 mm or until an interaction point was reached. Total path lengths of 349 m and 214 m were scanned for the oxygen and sulphur samples, respectively.

However, in order to increase the statistics of our samples, additional scanning was made for ^{16}O-emulsion interactions, in some plates for all classes of interactions and in others for only those satisfying the EMD classification. As a result a further 510 m of 200 A GeV ^{16}O track have been added to those obtained from the original 349 m.

Hadronic interaction

When an interaction was reached, the following features of the interaction were recorded: the number of black tracks N_b(if of protons, of kinetic energy <30 MeV) and the number of grey tracks N_g(corresponding to protons in the energy range 30-300 MeV) in the forward and backward hemispheres, the presence of doubly and multiply charged fragments of the projectile nucleus proceeding from the interaction essentially undeviated from the original beam direction, and the approximate number of near-minimum ionizing(shower) particles N_s. Once a hadronic interaction was found, the incoming track was also carefully examined at higher magnification to ensure that it was indeed a beam track and not tightly bunched fragments of an undetected EMD.

Events which exhibit no shower particles and one low-energy 'proton', with the projectile ion emerging essentially undeviated, have been noted. These events have been ascribed to elastic collision on free protons in the emulsion or to the electromagnetic dissociation of the target nuclei. However, the scanning efficiency for such events is too low for meaningful estimates of the corresponding cross-sections to be made and they have thus not been considered further.

EMD

Some EMD events, in particular those where a single proton emitted at a very small angle to the beam, are not discernable at the interaction vertex but only become apparent further downstream. Therefore, apparently non-interacting beam

particles were followed for an additional 10-20 mm solely to detect such interactions occurring within the fiducial region.

The electromagnetic interaction between the projectile and the medium it traverses results in the ejection of very low-energy electrons called δ rays and electron pairs, and increases rapidly with projectile charge. The majority of these can be recognized by eye and discarded, but tracks of electrons of medium or high-energy(the tail of the distribution) can be identified in emulsion only when followed for a sufficient length. This would have increased the scanning time considerably. Thus, all events exhibiting solely one or two wide angle(>5mrad to the beam particle) minimum ionizing particles were rejected. This criterion eliminates almost all the high-energy knock-on electrons and most of the pairs, but no EMD candidates, in the selected range of photon energies. Consequently, nuclear interactions which present such topologies have also been removed from the sample.

For all the projectile EMD candidates, an accurate scan was performed upstream and downstream from the probable interaction point(uncertain to ± 1 mm or more in the most difficult cases) to check for the presence of previously undetected signs of a small hadronic interaction. At this stage, all interactions showing no target nuclear excitation(black or grey prongs) and with all tracks emitted within 5 mrad to the beam were considered as candidates for projectile EMD.

The charges as well as the angles of outgoing fragments relative to the heaviest one were determined for each EMD candidate in order to categorize them into various break-up channels and to estimate the total c.m. kinetic energy released in the interaction.

Diffractive dissociation

A search was carried out among the sample scanned for hadronic interactions to find events which may be ascribed to hadronic diffractive dissociation of ^{16}O on hydrogen. They have a topology characteristic of an EMD of ^{16}O to either (C He) or (N H) plus a track of a low-energy single-charged particle at the interaction vertex. The direction of such a track with respect to the primary beam was measured, as well as its range where possible(sec. 3.2.4).

Projectile fragments

In a subsample of the oxygen events the tracks of forward-going projectile fragments of charge greater than one, assuming that they retain the original 200 A GeV beam momentum, were subjected to the following analysis. The charge of the fragment was determined from grain density(helium) and δ-ray density(heavier ions) measurements, with the charge resolution achieved from δ-ray measurements, made over a distance of about 2 mm(see sec. 3.2.4). The track was then followed for a distance of 60 mm or until an interaction point was reached, the following being extended for a further 10-20 mm beyond the fiducial region for the reasons already stated. The same features of secondary interactions were recorded as for primary ones and once again forward-going projectile fragments had their charges ascertained and were followed a further 60 mm or until they interacted. This procedure was repeated until any remaining forward fragments had gone 60 mm or they had left the pellicles. The establishment of the fragment charges in this way also enable the primary oxygen interactions to be examined in greater detail. As for the sulphur sample, the charges of the forward-going projectile fragments were determined by counting δ-gaps(see sec. 3.2.4). However, features of secondary or tertiary interactions were not recorded for the sulphur sample.

Those secondary(or tertiary etc.) interactions that occur within 2 millimetres from the primary vertex have been discarded when determining the mean free paths of projectile fragmentss of various charges. Consequently, their track lengths were not included in the total followed track length of the corresponding projectile fragmentss. There are two reasons for this cut. Firstly, in order to measure the charge of the fragment, a minimum of 2 millimetres is necessary for δ-ray counting. Secondly, it is difficult to resolve individual tracks emitted close($<$1 mrad) to the beam direction in the vicinity of the primary vertex.

3.2.3 Angular Measurements

Angles between outgoing fragments are determined by measuring the plane(α) and dip(δ) angles. The plane angle is defined as the angle to the direction of particle motion in the x-y plane(right-handed x, y, z coordinate frame) measured

counterclockwise with respect to the x-axis. It is also known as the azimuth angle or the projection angle. The dip angle, δ, for a track is the angle between the track in unprocessed emulsion and its own projection on the x-y plane, taken positive when the direction of the particle motion is upward and in the direction of increasing z coordinate. The space angle θ between two tracks having plane angles (α_1, δ_1) and (α_2, δ_2) is calculated from the measurements as follows:

$$cos\theta = cos\delta_1 cos\delta_2 [cos(\alpha_2 - \alpha_1) + tan\delta_1 tan\delta_2] \ . \qquad (3.2.1)$$

In the investigation of projectile EMD, the angles of outgoing fragments were measured relative to the heaviest one. Relative distances between tracks at increasing distances, typically in the range from 10 to 40 mm, from the interaction vertex were measured. Plane and dip angles were computed by fitting the trajectories to straight lines through the measured coordinates. Consequently eq. 3.2.1 becomes

$$cos\theta = cos\delta cos\alpha \ , \qquad (3.2.2)$$

where α, δ and θ are angles of the track measured relative to the heaviest fragment. Assuming an error of ~ 0.5 μm in the coordinates, the space angles are accurate to within 0.05 mrad, including the error due to multiple scattering, except in a few cases where one of the outgoing fragments interacted after a short distance.

Local distortions may result from the method of development and subsequent sticking of the emulsion pellicles on glass and can affect the determination of the track angles, particularly those of steeply inclined tracks. The coordinates of the points measured on the distorted 'proton' track, in those events ascribed to the hadronic diffractive dissociation of the ^{16}O ion, were corrected following an extension of the method of Apostolakis and Major[109], and the emission angles redetermined. Assuming that the pellicle suffered from a regular 'C-shaped' distortion, the horizontal displacement, Δ, of a point at height z_0 in a processed emulsion of thickness d is given by

$$\Delta = \overline{K_1}(\frac{z_0}{d}) + \overline{K_2}(\frac{z_0}{d})^2 \ . \qquad (3.2.3)$$

The term $\overline{K_1}(z_0/d)$ represents a linear displacement which is zero at the glass-emulsion surface interface and has the value $\overline{K_1}$ at the air-emulsion surface. The second term, $\overline{K_2}(z_0/d)^2$, represents the $\overline{K_2}$, or curvature distortion. It has been

assumed that the direction of the track near the air surface is the same as the original one and thus that the first order distortion vector is exactly twice the second order one, i.e. $\overline{K_1} = -2\overline{K_2}$. The coordinates of a number of points along the proton track were measured and for each track an independent least square method applied gave the parameters of the distortion vectors, and hence the corrected coordinates.

Such distortions do not affect the measurements of the small opening angle between the particles from the break up of the projectile.

3.2.4 Track parameters and their measurements

Charge

Charge measurements were performed on projectile EMD candidates and on a sample of hadronic inelastic interactions by determining the relative density of δ-rays along the beam track and each of the outgoing fragments. It was possible to recognize by eye the charge of fragments with Z=1 and 2, and therefore systematic measurements were performed only on fragments with $Z > 2$. A sample of fragments with Z=2 was also measured, and in all cases the previous judgement was confirmed.

The linear density of δ-rays for a particle with $\beta \approx 1$ is:

$$\frac{dn}{dx} = aZ^2 \ , \tag{3.2.4}$$

with $a \approx 1/\text{mm}$ in nuclear emulsion[108]. The exact value of a depends on the operative definition of a δ-ray, in practice on the accepted minimum range - and thus energy - of the ejected electrons. In this technique a δ-ray is defined to be one that projects radially a minimum of $\sim$1.5 μm from the centre of the track[108].

The counting of δ-rays can determine the charge of tracks up to $Z \approx 10$, but for higher values of the charge the δ-ray density becomes too large and it is no longer possible to disentangle single, scattered electron tracks. Therefore for fragments with $Z > 8$, charge was determined by measuring P_0, the ratio of the number

of times no δ-rays were observed in a cell length t to the total number of cells examined[71]:

$$P_0 = e^{-aZ^2t} \quad , \tag{3.2.5}$$

where the value of a is the same as in eq. 3.2.4 if the same convention is used. The error in the charge measurement can be shown to be

$$\delta Z = \frac{1}{2}k(aL)^{-1/2} \quad , \tag{3.2.6}$$

where L is the total length considered. The value of k is 1 with the first method(this is the minimum statistical error), whereas it depends on P_0 in the second, being $k \leq 1.3$ for $P_0 \geq 0.4$.

Fig. 3.1 and 3.2 display the typical charge spectra obtained by counting δ-ray densities and δ-rays gaps, respectively, on primary and secondary tracks. Both spectra show a dispersion on individual charges in agreement with that expected from the measured length L, usually 2-5 mm. It is seen that the accuracy is good enough to detect, unambiguously, differences of one unit of charge around Z=8 and two such units around Z=16.

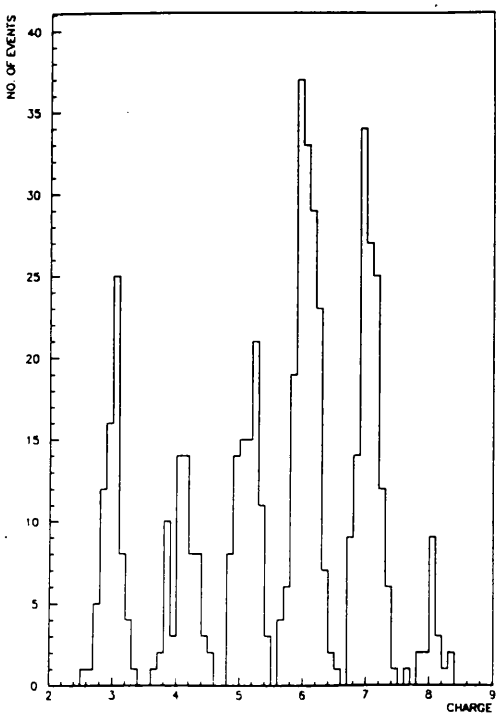

Figure 3.1: *Charge spectrum, from δ-ray density, of a sample of secondary projectile fragments from 200 A GeV ^{16}O-emulsion interactions.*

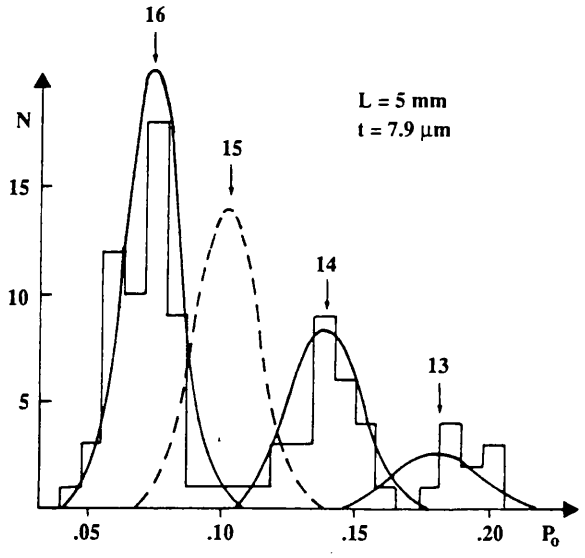

Figure 3.2: *Charge spectrum, from δ-ray gaps, of a sample of primaries and of fragments from projectile EMDs(200 A GeV ^{32}S on emulsion). Solid line: expected shape, normalized to Z=14. Dashed line: Z=15, not measured in this sample.*

Range

The average distance traversed by a charged particle in a medium before its kinetic energy reduces to zero is called the range of the particle. If the distance is measured from an arbitrary point to the stopping point along the track, it is called the residual range. It gives a measure of the kinetic energy of the particle at that point.

If a particle has initial kinetic energy E_0 and loses energy at a space rate, $-\frac{dE}{dx}$, per unit path when penetrating a medium, the distance it will traverse before coming to rest is:

$$R_0 = \int_0^{E_0} \frac{dE}{-dE/dx} \ . \tag{3.2.7}$$

Of course $-\frac{dE}{dx}$ is a statistical variable and therefore eq. 3.2.7 is only an approximation to the mean range. Individual ranges will disperse around the mean value R.

In our investigation, the range of a particle is the length of its path in emulsion before the emulsion has been processed. The range is calculated by breaking up

the track into into n essentially straight segments and evaluating the sum

$$R = \sum_{i=1}^{n}[(x_i - x_{i-1})^2 + (y_i - y_{i-1})^2 + S_z^2(z_i - z_{i-1})^2]^{1/2} \qquad (3.2.8)$$

where (x_0,y_0,z_0), $(x_1,y_1,z_1)...(x_n,y_n,z_n)$ are the coordinates of the points on the track connected by the segments, and S_z is the shrinkage factor in the z direction.

In some cases, the range could not be measured as the proton left the emulsion stack before coming to rest. However, in each case it was judged, from an examination of its ionization and scattering, to be close to rest. Consequently only a small underestimate of the proton's momentum is incurred by using the observed track length.

Chapter 4

Hadronic Inelastic Reactions of 200 A GeV ^{16}O and ^{32}S Ions with Nuclear Emulsion Nuclei

4.1 Introduction

The acceleration in 1986 and 1987 of ^{16}O and ^{32}S beams to 200 A GeV at the CERN SPS opened a new frontier of particle and nuclear physics, namely the study of high-energy density systems with hundreds of quarks and gluons created in the central collisions of nuclei with heavy targets. Experiments were set up to find a new state of matter, the quark-gluon plasma. It is believed that a phase transition leading to deconfinement should occur given sufficiently high-energy and/or baryon density achievable by compression or heating of cold matter[30].

However, in order to detect this *abnormal* nuclear phenomenon, we first have to understand the normal nuclear collision mechanism at ultra-relativistic energy. Hence a study of sizeable and unbiased samples of the hadronic inelastic interactions of 200 A GeV ^{16}O and ^{32}S ions with emulsion nuclei has been carried out.

In this chapter the general characteristics of the hadronic inelastic reactions of 200 A GeV ^{16}O and ^{32}S ions with emulsion nuclei are compared and contrasted. Using a minimum-bias sample of 3938 ^{16}O-emulsion interactions and of 2319 ^{32}S-emulsion interactions, the multiplicity distributions of shower, grey, black and

heavily ionizing particles and correlations among various multiplicity parameters have been studied. The rapidity distributions of those events which exhibit complete projectile breakup without any overt sign of low-energy target fragmentation have also been determined. The results may be interpreted within a simple geometrical model.

4.2 Mean Free Paths

The mean free paths for primary ^{16}O and ^{32}S ions at energies 1.4 to 200 A GeV in nuclear emulsion are summarized in Table 4.1. The analysis and discussion of the mean free paths of secondary(+ tertiary ...) projectile fragments will be presented in chapter 6. The hadronic inelastic mean free path λ_{had} for 200 A GeV ^{16}O ions determined here, 120 $\pm$ 1 mm is in accord with values found by other workers at the same energy, *viz.* 116 $\pm$ 3 mm[112], 120 $\pm$ 3 mm[114] and 115 $\pm$ 6 mm[113] in spite of the fact that emulsions with slightly different compositions were used in the other experiments which should decrease their path lengths by about 3 %. It is also noted that the mean free paths of ^{16}O ion in nuclear emulsion at energies beyond 2 A GeV exhibit energy independence, within statistical errors.

On the other hand the hadronic inelastic mean free path for 200 A GeV ^{32}S ions, 92 $\pm$ 2 mm is much shorter than the other reported value of 110 $\pm$ 3 mm[51,92]. The difference in the composition of the emulsions should produce the opposite effect. Any systematic errors due to scanning efficiency would tend to increase the mean free path.

However, it is reassuring that the variation in our result from ^{16}O to ^{32}S is in agreement with our optical model calculation. Simplified Glauber calculations[115,116] have been made of the hadronic inelastic cross-sections of various 200 A GeV projectile nuclei present in nuclear emulsion. Neglecting the effects of nuclear correlations and excitation, the amplitudes correspond to the eikonal solution to the folding model approximation to the nuclear optical potential. Standard values are assumed for the proton and neutron radii of nuclei. The measured values, 39.0 and 6.9 mb[117], of the nucleon-nucleon total and total elastic cross-section, respectively, are used. Hence there are no free parameters in the predictions of the

Table 4.1: *Global data on the hadronic inelastic interactions of primary ^{16}O, ^{32}S and secondary(+ tertiary, ...) projectile fragments in nuclear emulsion.*

Projectile	Energy (A GeV)	L (m)	N_{had}	λ_{had} (mm)	Refs.
He	200	91.1	398	228 ± 11	this exp.
Li	200	6.3	37	171 ± 28	this exp.
Be	200	6.1	41	149 ± 23	this exp.
B	200	8.4	64	131 ± 16	this exp.
C	200	18.1	125	145 ± 13	this exp.
N	200	20.3	161	126 ± 10	this exp.
O	2.0	-	-	137 ± 11	[111]
O	2.0	-	-	126 ± 5	[111]
O	2.1	141.74	1092	130 ± 5	[111]
O	14.6	-	385	121 ± 2	[112]
O	60	-	372	119 ± 4	[112]
O	60	16.37	131	125 ± 11	[49]
O	60	63.53	497	128 ± 6	[113]
O	200	-	503	116 ± 3	[112]
O	200	39.30	342	115 ± 6	[113]
O	200	-	1855	120 ± 3	[114]
O	200	860.57	7144	120 ± 1	this exp.
S	200	127.38	1157	110 ± 3	[51,92]
S	200	214.46	2319	92 ± 2	this exp.

Table 4.2: *Glauber calculations of σ_{had} of various 200 A GeV projectile nuclei upon target emulsion nuclei.*

Projectile Nucleus	σ_{had} (mb) Target Nucleus						λ_{had} (mm)	λ_{had} (mm) Renormalised
	H	C	N	O	Br	Ag		
^{1}H	32	253	278	318	1004	1266	319[a]	355[a]
^{3}He	87	505	542	604	1520	1847	203	226
^{4}He	100	533	568	634	1562	1891	195	217
^{6}Li	168	775	822	901	2006	2384	144	161
^{9}Be	220	874	922	1008	2159	2552	130	149
^{11}B	241	896	942	1030	2187	2584	127	142
^{12}C	253	919	965	1055	2224	2624	124	138
^{14}N	278	965	1012	1104	2297	2706	119	132
^{16}O	318	1055	1104	1201	2442	2861	110	123
^{32}S	523	1448	1508	1623	3058	3517	83	92

[a] Computed for standard emulsion.

mean free paths quoted in Table 4.2. When compared with values in Table 4.2, the observed mean free paths due to hadronic inelastic interactions (λ_{had}) appear to be about 10% longer than predicted. This disagreement might suggest that a group of inelastic interactions, which involve little excitation of the target and/or projectile nuclei, have not been detected. Furthermore, the loss due to scanning efficiency would lead to longer mean free paths. Assuming that the fraction of this class of inelastic interactions is independent of the projectile nuclei, the predicted mean free paths are normalized to the observed mean free paths of 200 GeV protons in emulsion, namely 355 $\pm$ 8 mm [118]. The normalized mean free paths for ^{16}O and ^{32}S, 123 and 92 mm respectively, agree very well with the observed values. Similarly, the normalized mean free paths predicted for lighter projectile fragments agree within errors with those observed in Table 4.1.

Sato *et al.*[119] studied the interaction cross-sections of high energy nucleus in emulsion with the Glauber model and a Hartree-Fock type variational calculation for the nuclear structure. They found that the hadronic inelastic mean free path of a projectile in emulsion can be expressed by

$$\lambda_{had} = (AR_p^2 + BR_p + C)^{-1}$$
$$with \quad A = \pi \sum n_i, \quad B = 2\pi \sum n_i R_i, \quad C = \pi \sum n_i R_i^2. \tag{4.2.1}$$

n_i is the composition of the nuclear component i in the emulsion. R_i and R_p are the interaction radii of the ith component nuclei and of the projectile, respectively. Although Sato *et al.* calculated the interaction radii in the case of scattering at incident energy 1.88 A GeV, the interaction radius is considered to be an energy independent characteristic nuclear radius in nucleus-nucleus scattering due to the energy independence of the interaction cross-sections of nuclei at high energies.

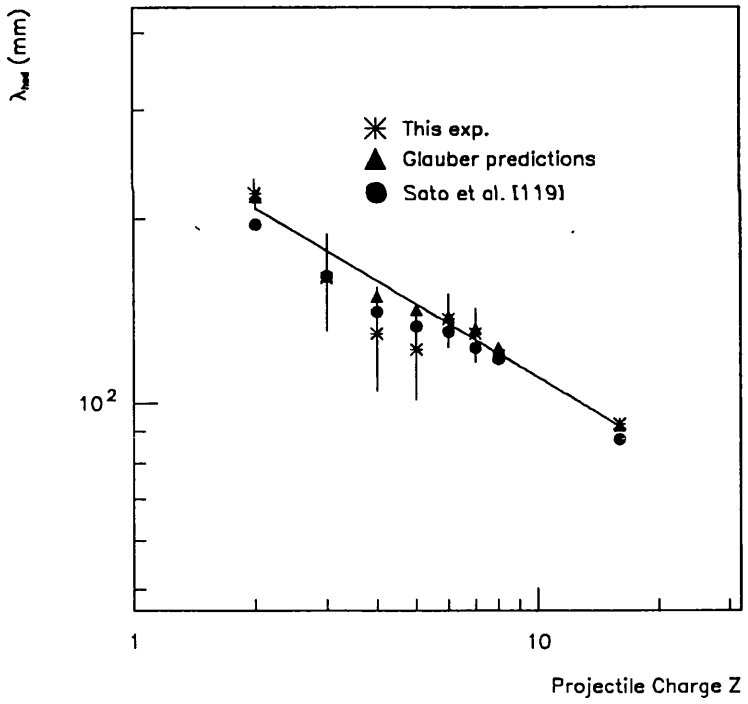

Figure 4.1: *The experimental hadronic inelastic mean free paths obtained with the ^{16}O and ^{32}S beams at 200 A GeV and the theoretical values calculated. The fit to the experimental data gives λ_{had}=272.7 $Z^{-0.393}$ mm.*

In Fig. 4.1, we compare our calculated hadronic inelastic mean free paths and those by Sato *et al.* with the experimental values obtained with the ^{16}O and ^{32}S beam. There is good agreement between the theoretical and experimental values, and they all exhibit a Z-dependence. Sato *et al.*'s parameterization would suggest

that the hadronic inelastic mean free paths of the projectiles have a Z dependence of the form $\lambda_{had} \propto Z^{-0.37}$ since $R_p \propto Z^{0.41}$ and the rest of the equation also has a weak Z dependence. On the other hand our simplified Glauber calculation also predicts that $\lambda_{had} \propto Z^{-0.39}$. A fit to the experimental data gives a relation of the form $\lambda_{had} = \Lambda Z^{-b}$[70] where $\Lambda = 272.7 \pm 15.7$ mm and $b = 0.393 \pm 0.025$. Furthermore, our observed values are roughly in agreement with those reported by other workers [70,72,69,73,84] at 1-2 A GeV displayed in Table 4.3.

Table 4.3: *Experimental values of the parameters* Λ *and* b.

Energy(A GeV)	Λ (mm)	b	Data Type	Reference
2	304 ± 16	0.44 ± 0.02	primary beams and theoretical prediction	[70]
2	324 ± 17	0.42 ± 0.024	projectile fragments	[72]
> 0.4	251 ± 17	0.34 ± 0.03	cosmic rays	[69]
1	340 ± 18	0.42 ± 0.024	projectile fragments	[73]
1.8	241 ± 12	0.34 ± 0.03	primary beams and projectile fragments	[84]
200	273 ± 16	0.39 ± 0.03	primary beams and projectile fragments	this exp.

However, one must realize that the Z-dependence of the hadronic inelastic mean free path is inaccurate because the mean free paths are also expected to have an isotopic dependence. The theoretical values shown in Fig. 4.1 are those of even-even nuclei with the exception of ^{9}Be. For a fixed value of Z, the projectile fragments do not have a homogeneous composition. In addition to nuclei within the valley of stability, there may also be long-lived neutron-rich isotopes of which the relative abundances are unknown. Hence, the experimentally observed mean free paths correspond to the average mean free paths of admixtures of isotopes.

4.3 Fragmentation Studies

4.3.1 General features

The gross topological features observed for the inelastic nuclear interactions of ^{16}O and ^{32}S ions are shown in Table 4.4. The forward fragments with charge $Z \geq 2$ are those making small angles($\leq$ 1 mrad) with respect to the beam direction and likely to be noninteracting clusters within the incident projectile nuclei. Events grouped under 'none' are those that involve the emission of minimum ionizing shower tracks only, and therefore can be associated with complete disintegration of the projectile. These events are the most central or near-central interactions.

The 3938 ^{16}O-emulsion hadronic interactions in Table 4.4 are an unbiased subsample of the overall sample(7144 hadronic interactions). Two separate scanning for oxygen-emulsion interactions was carried out, but the second one was focused on the search for projectile EMD and the interaction features of some of the hadronic events were not recorded. Thus they are only used in the calculation of the hadronic mean free paths in sec. 4.2 but not the following analysis.

The relative abundances of different classes of events for ^{16}O projectiles at 60[49] and 200 A GeV are approximately the same. The relative abundance of central events for ^{16}O at the two energies are exactly the same, but there are small variations in specific peripheral reaction channels. On the other hand, the fraction of central events, those having no forward projectile fragments with $Z > 1$, for ^{32}S at 200 A GeV(16.3%) is much less than ^{16}O at 200 A and 60 A GeV(30.5%). Thus, in ultra-relativistic heavy ion interactions, the relative rate of a particular channel of projectile fragmentation depends strongly on the projectile mass(A) but not on the energy.

In Table 4.4, N_h is the average number of emitted target fragments, where N_h=N_b+N_g, and their average values are given for each category. The overall forward-backward asymmetry observed for black prongs is +0.075$\pm$0.008 for the oxygen and +0.099$\pm$0.010 for the sulphur sample. This is consistent with the isotropic evaporation from a slowly forward-moving spallation product. The corresponding values for the grey tracks, which are mainly knock-on target protons,

Table 4.4: *Topological features observed for inelastic interactions of ^{16}O and ^{32}S ions with emulsion nuclei at 60 and 200 A GeV.*

Beam	Energy (GeV/A)	Nuclear interactions	Forward fragments										Refs.
			None	1α	2α	3α	4α	5α	6α	$1\ Z \geq 3$ no α	$1\ Z \geq 3$ + α's	2,3 $Z \geq 3$	
^{16}O	60	131	40	27	14	5	1	—	—	35	9	—	
			30.5%	20.6%	10.7%	3.8%	0.8%	—	—	26.7%	6.9%	—	[6]
		$\langle N_h \rangle$=9.5±0.8	17.8	9.5	7.6	5.3	1.0	—	—	2.8	5.5	—	
^{16}O	200	3938	1201	690	458	207	9	—	—	1147	222	4	present
			30.5%	17.5%	11.6%	5.3%	0.2%	—	—	29.1%	5.6%	0.1%	work
		$\langle N_h \rangle$=7.5±0.1	13.5	8.1	5.1	3.3	2.4	—	—	3.7	2.8	3.0	
		$\langle N_s \rangle$=41.6±1.1	87.1	44.4	25.2	13.4	5.0	—	—	13.5	11.4	15.5	
^{32}S	200	2319	379	240	157	108	54	22	6	796	530	27	present
			16.3%	10.4%	6.8%	4.7%	2.3%	0.9%	0.3%	34.3%	22.9%	1.2%	work
		$\langle N_h \rangle$=7.4±0.2	14.9	12.1	9.1	7.3	6.2	6.6	2.5	4.0	4.9	5.3	
		$\langle N_s \rangle$=56.3±2.1	155.9	102.3	72.5	51.7	28.7	37.9	14.7	16.6	25.3	27.1	

are very positive, 0.361±0.008 and 0.403±0.011, respectively for ^{16}O and ^{32}S. Furthermore both N_h and N_s increase monotonically with increasing extent of projectile fragmentation. The correlation between the the degree of fragmentation of the target and of the projectile will be discussed in sec. 4.3.3.

Very similar values for 200 A GeV ^{16}O ion fragmentation to those presented in Table 4.4 were found by Adamovich *et al.*[120], namely no forward fragments 29.0 ± 1.2%, $Z > 2$(presumably including those accompanied by helium emission) 36.0 ± 1.3 %, one alpha 17.0 ± 1.0%, two alpha 12.1 ± 0.8%, three alpha 5.6 ± 0.7%, and 4 alpha 0.3 ± 0.2%.

Sengupta *et al.*[113] also studied the relative abundance of ^{16}O and ^{32}S ions into various fragmentation channels at 60 and 200 A GeV. They categorized their

Table 4.5: *Percentile abundances of ^{16}O and ^{32}S fragmentation in terms of multiple alpha events.*

Event type	60 A GeV ^{16}O		200 A GeV ^{16}O		200 A GeV ^{32}S	
	ref. [49]	ref. [113]	this exp.	ref. [113]	this exp.	ref. [113]
central	30.5±4.8	30.4±2.5	30.5±0.9	31.6±3.0	16.3±0.8	20.8±1.4
peripheral	69.5±7.3	69.6±3.7	69.5±1.3	68.4±4.5	83.7±1.9	79.2±2.8
0 alpha	26.7±4.5	32.4±2.6	29.1±0.9	31.6±3.0	34.9±1.2	31.1±1.8
1 alpha		20.3±2.0	22.6±0.8	21.6±2.5	24.8±1.0	26.9±1.6
2 alpha		10.3±1.4	12.2±0.6	9.4±1.7	13.8±0.8	12.9±1.1
3 alpha		6.6±1.2	5.3±0.4	5.6±1.3	6.3±0.5	5.6±0.7
4 alpha			0.2±0.1		2.5±0.3	1.6±0.4
5 alpha					0.9±0.2	0.8±0.3
6 alpha					0.3±0.1	0.3±0.2

events in terms of the number of projectile helium fragments(with or without other

fragments of charge $Z \geq 3$). A comparison with our data is presented in Table 4.5. Our relative abundances of different kinds of hadronic events for ^{16}O at 60 and 200 A GeV compare well with the values reported by Sengupta *et al.*[113]. However, the relative abundance of central events for ^{32}S at 200 A GeV in our data is much less than that reported in ref.[113]. It has been noted in sec. 4.2 that the hadronic inelastic mean free path for ^{32}S at 200 A GeV observed by Sengupta *et al.*(110±3 mm) is much greater than our observed value(92±2 mm). The discrepancy seems to lie in the class of peripheral events where we have recorded 25% more such events than Sengupta *et al.* This difference is too large to be explained by variation in emulsion conditions. Since peripheral events of ^{32}S can easily be missed, the discrepancy may suggest that their scanning efficiency for such events in the ^{32}S sample is low.

4.3.2 Target fragmentation

Multiplicity distribution of N_h, N_g and N_b

The normalized multiplicity distributions of the heavily ionizing target fragments N_h are shown in fig 4.2 for hadronic inelastic interactions of ^{16}O and ^{32}S and helium forward-going projectile fragments in our sample together with those from proton emulsion interactions at 200 to 400 GeV[118]. Table 4.6 compares the percentages of each distribution in various intervals of N_h. Events with $N_h > 8$ are definitely interactions upon Ag or Br nuclei, but target identification for events with $N_h \leq 8$ is more difficult and requires measurement of the ranges of the target fragments[121]. Nonetheless, the Glauber calculations in sec. 4.2 provide estimates of the relative proportions of interactions upon hydrogen, the light(C, N, O) and heavy(Ag, Br) emulsion nuclei. The ratios change markedly with the projectile mass, and the heavier the projectile the more important the interactions on the lighter targets. Some typical values are shown in Table 4.7.

Comparing the N_h distributions, it is noted that there is a small increase in the fraction of interactions with $N_h = 0$ from proton- to sulphur-emulsion interactions, even though the increase is not as large as that predicted from Table 4.7. Furthermore in the case of a proton beam, only 13 % of the interactions with $N_h \leq 1$ are

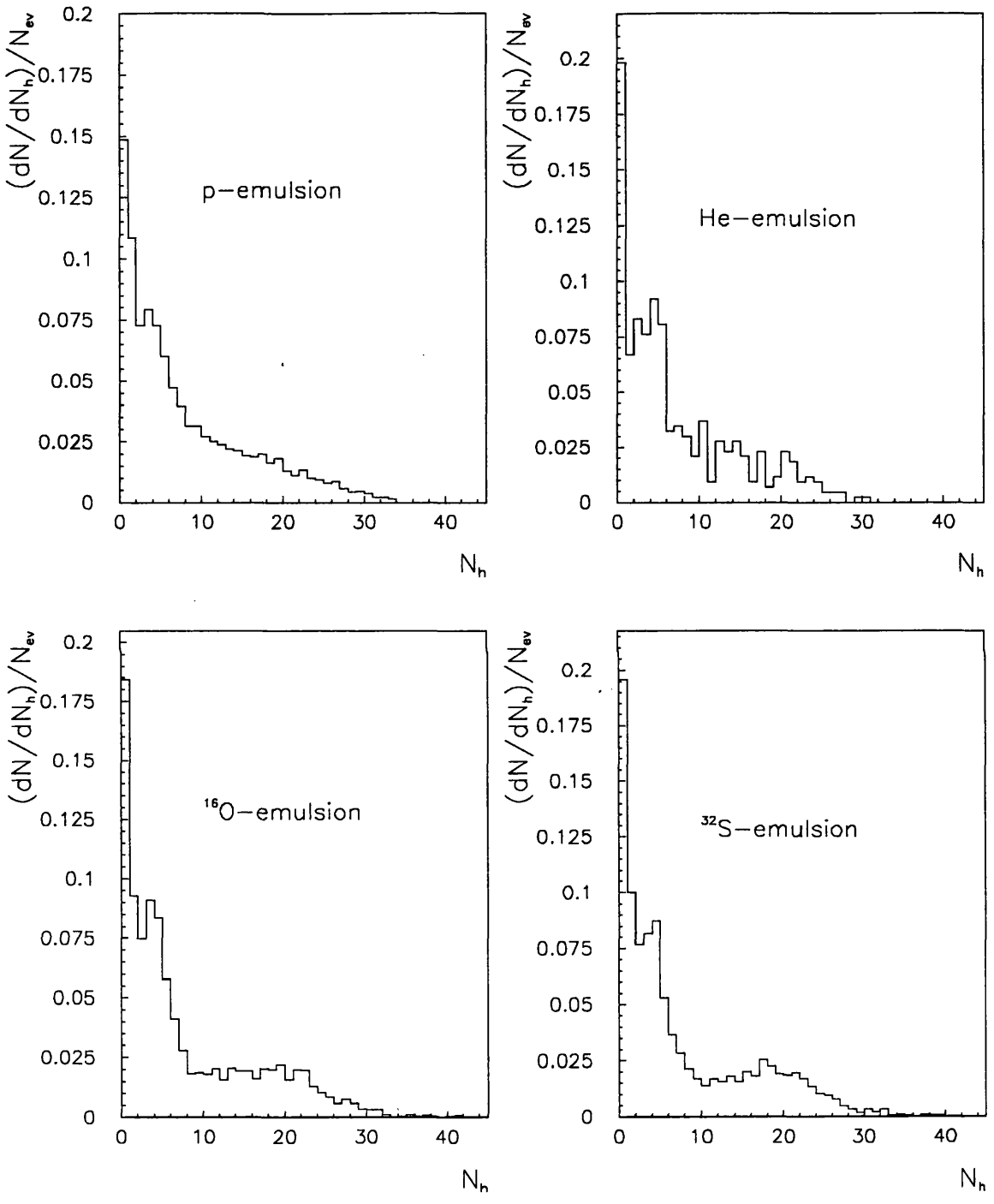

Figure 4.2: *Normalized multiplicity distributions of N_h from interactions of ^{16}O and ^{32}S ions and He projectile fragments, together with those from proton-emulsion interactions at 200-400 GeV[118].*

Table 4.6: *Percentage distribution between various intervals of N_h for H[118](200-400 GeV), He, ^{16}O, and ^{32}S projectiles.*

Projectile	N_h 0	1	2-4	5-8	9-15	≥ 16
^{1}H $\langle N_h \rangle = 7.63 \pm 0.08$	14.7±0.4	10.8±0.3	22.3±0.5	18.0±0.4	16.8±0.4	17.4±0.4
He $\langle N_h \rangle = 6.75 \pm 0.34$	19.8±2.1	6.7±1.2	25.1±2.4	17.7±2.0	16.6±2.0	14.1±1.8
^{16}O $\langle N_h \rangle = 7.56 \pm 0.15$	18.4±0.8	9.3±0.6	24.9±0.9	14.5±0.7	13.1±0.7	19.8±0.8
^{32}S $\langle N_h \rangle = 7.42 \pm 0.17$	19.6±0.9	10.0±0.7	24.5±1.0	13.9±0.8	11.6±0.7	20.3±0.9

due to interactions on a hydrogen target; whereas this fraction rises to 51% for ^{32}S projectiles. In addition, there is a significant decrease of the fraction with $5 \leq N_h \leq 15$. This feature gives rise to a shallow minimum in the distribution for $N_h \approx 10$ in the ^{32}S sample and to a plateau in the ^{16}O sample; it is completely absent in those for both He and proton-emulsion interactions. Finally in the proton sample, interactions with $N_h > 8$ represent about 47% of the interactions on Ag or Br nuclei whereas this fraction increases to 63% for ^{32}S projectiles.

This behaviour is also evident in the multiplicity distribution of the grey prongs, which are mostly knock-on protons in the energy range 30-300 MeV, as shown in Fig. 4.3. The fraction of interactions in the region $0 \leq N_g \leq 1$ does not vary significantly with different projectiles, but there is a consistent decrease in the region $2 \leq N_g \leq 4$ as the mass of the projectile increases. The contribution of interactions with $N_g > 8$ also rises with increasing projectile mass. Furthermore, the average multiplicity of grey multiplicities per event $\langle N_g \rangle$ increases slowly when going from proton-(2.70±0.17) to sulphur-emulsion interactions(3.12±0.08).

In Fig. 4.4, the normalized multiplicity distributions of the black prongs, which are singly and multiply charged evaporation particles from the target, exhibit sim-

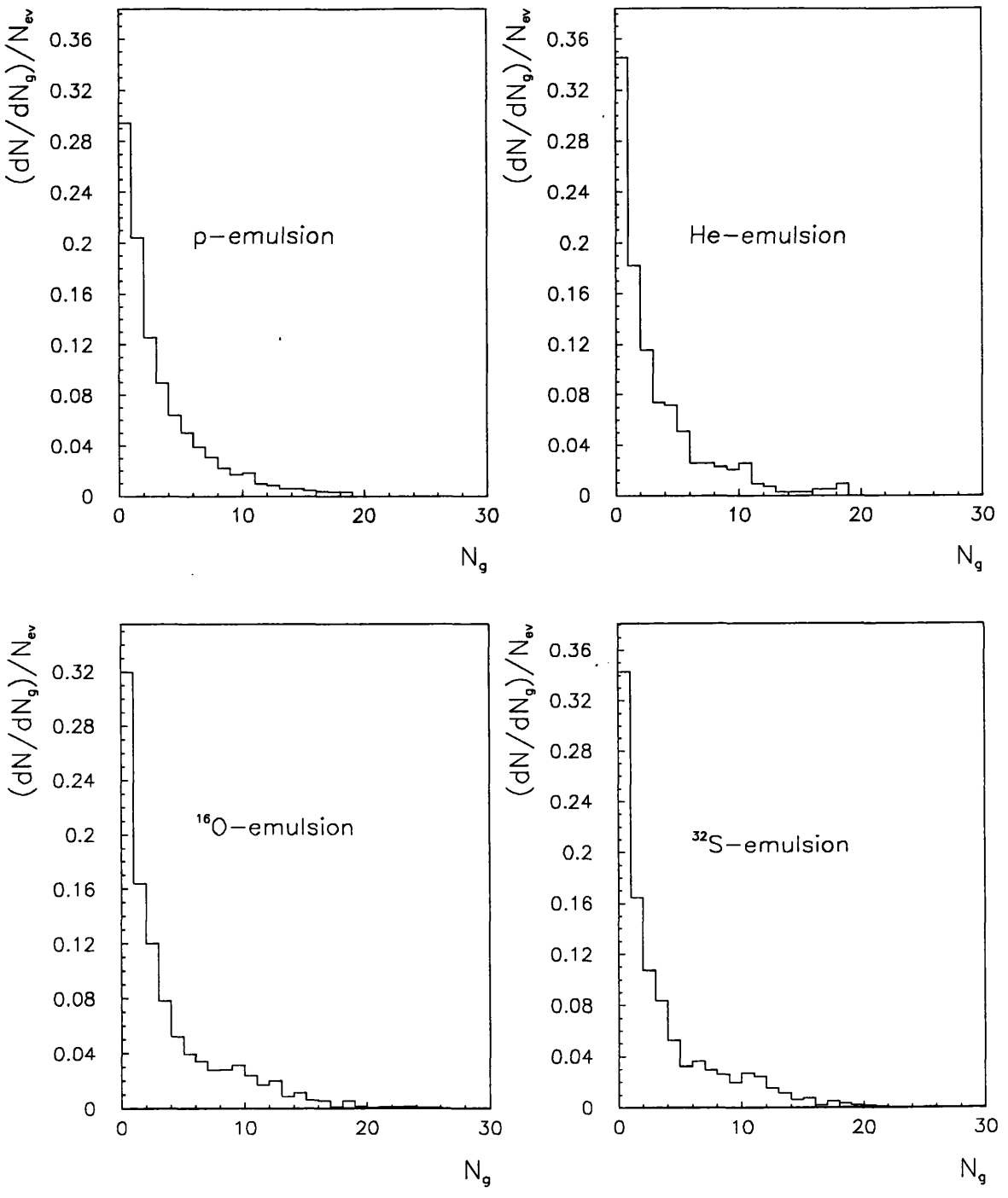

Figure 4.3: *Normalized multiplicity distributions of N_g from interactions of ^{16}O and ^{32}S ions and He projectile fragments, together with those from proton-emulsion interactions at 200-400 GeV[118].*

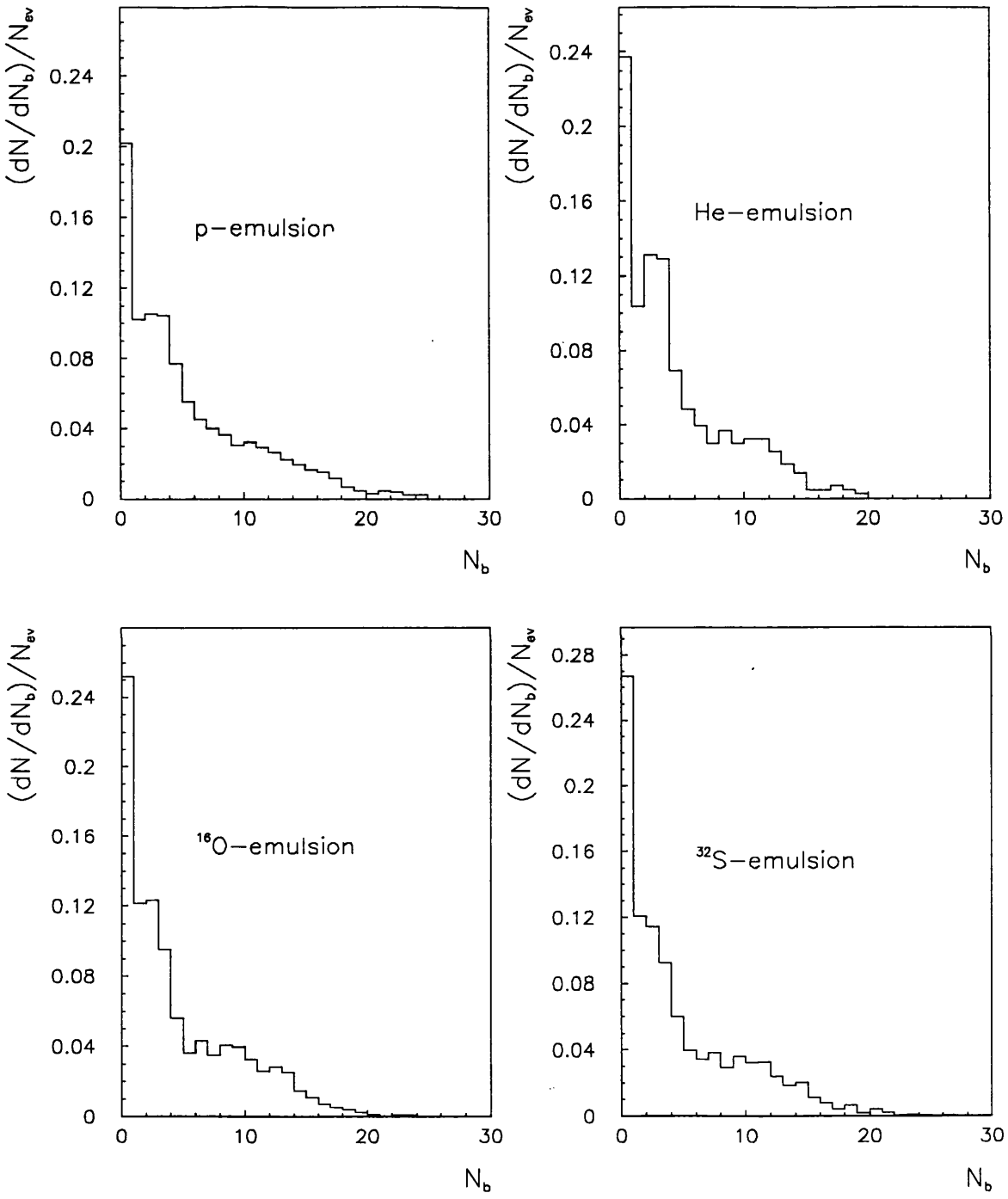

Figure 4.4: *Normalized multiplicity distributions of N_b from interactions of ^{16}O and ^{32}S ions and He projectile fragments, together with those from proton-emulsion interactions at 200-400 GeV[118].*

Table 4.7: *Relative proportions of interactions upon light and heavy emulsion nuclei according to the Glauber model.*

Projectile nucleus	Target nucleus H (%)	C, N, O (%)	Ag, Br (%)
^{1}H	3.3	23.6	73.1
^{4}He	6.9	30.5	62.6
^{6}Li	8.5	32.5	59.0
^{9}Be	10.0	32.9	57.1
^{12}C	11.0	32.9	56.1
^{16}O	12.3	33.4	54.4
^{32}S	15.2	34.2	50.6

ilar shapes when ranging from proton- to sulphur-emulsion interactions, although the contribution of interactions with small N_b rises with increasing projectile mass. However on average the multiplicity distributions of black prongs exhibit projectile independence, and the average number of black prongs per event remains constant within statistical limits when ranging from helium- to sulphur-emulsion interactions: 4.05±0.21 for He, 4.25±0.08 for ^{16}O and 4.30±0.10 for ^{32}S.

Previous work[118,122,123,124] on high-energy hadron-nucleus interactions in emulsion has shown that the numbers of target associated particles(N_h, N_g or N_b) emitted in an interaction are related to the number of hadron-nucleon collisions ν inside the target nucleus. When the recoiling nucleons pass through the nuclear matter, a number of secondary collisions would occur and each of them would either escape outside the nucleus or stop inside the nucleus and share its energy with the rest of the nucleus, thereby raising the temperature which governs the evaporation process.

If this idea is extended to nucleus-nucleus interactions, the dependence of the multiplicity distributions of target fragments on projectile may be understood in terms of the geometry of the collisions. For a given impact parameter, the increase in projectile size would increase the number of participant projectile and target

nucleons and consequently the cascading process is more pronounced. This increase is insignificant in collisions upon light emulsion nuclei(C, N, O) since their sizes are comparable to or even smaller than those of the projectiles. However, for the heavy emulsion nuclei(Ag, Br) the interaction volume would increase significantly as the number of incident projectile nucleons impinging on the target nucleus increases. Thus, it is not surprising that the fraction of interactions on (Ag,Br) with $N_g > 5$ (or $N_h > 8$) rises with increasing projectile mass. As a result, the interactions with light nuclei(C, N, O) and with heavy nuclei(Ag, Br) become well separated whereby most of the $N_h \leq 8$ events are due to interactions on light nuclei and the $N_h > 8$ events represent the majority of the interactions on heavy emulsion nuclei. Ref.[125] and [126] observed a similar projectile dependence of the grey particle production, while the multiplicity distribution of the grey prongs is found to be independent of projectile energy at incident energies beyond $\sim$ 1 A GeV [125,126,127,128].

On the other hand, the multiplicity distributions of black prongs are relatively undisturbed by the variation of projectile. This projectile independence of the black prong production is also reported in other experiments[125,128,126]. Adamovich *et al.*[128]'s suggestion that N_b relates only to the non-overlapping part of the target nucleus fails to explain why a proton induced interaction leaves a remaining target spectator of the same size as in the ^{16}O or ^{32}S case. Several models currently used also fail to reproduce the multiplicity distribution of the black prong producing particles[126,129].

The particles producing black prongs are spectator fragments in the target nucleus, and are emitted a long time($\approx 10^{-17}$s) after the passage of the incident projectile in the evaporation process of the target nucleus. Despite the rise in the number of intranuclear collisions and consequently the increase in the energy deposition within the interaction volume, the number of the evaporated target fragments seems to be unaffected by the increase in projectile mass. It is also noted that while the forward-backward asymmetry of grey particles remains constant within statistical limits, the forward-backward asymmetry of black particles increases considerably when ranging from helium to sulphur induced interactions(see Table 4.8).

Table 4.8: *The forward-backward asymmetry($\frac{F-B}{F+B}$) of black and grey particles in He-, ^{16}O- and ^{32}S-emulsion interactions.*

Projectile	Forward-backward Asymmetry	
	Black prongs	Grey prongs
He	0.041±0.024	0.378±0.027
^{16}O	0.075±0.008	0.361±0.008
^{32}S	0.099±0.010	0.403±0.011

This seems to indicate that the energy spectrum of the emitted protons from target nuclei gets harder with increasing projectile mass. It might also suggest that the forward velocity of the excited remanent nucleus increases as projectile mass increases. However, one must bear in mind that the charges of the target fragments are not measured and that neutral target fragments are not detected. Consequently the black particle multiplicity distributions in Fig. 4.4 do not truly represent the charge distribution nor the particle number distribution of the evaporation process. Whether the evaporation process is independent of the incident projectile cannot be determined until reliable data on charge and mass distributions of the black track producing particles are available.

The integral frequency distributions of heavy tracks N_h are shown in Fig. 4.5 which are almost independent of the mass of the projectile. The tails of the distributions extend with increasing projectile mass. The curves have two different slopes with breaks approximately corresponding to the light(C, N, O) and heavy(Ag, Br) nuclei of the emulsion target. Fig. 4.6 compares the integral frequency N_b and N_g distributions of different projectiles. Both distributions of black and grey particles appear to be fairly independent of the projectile mass.

Average number of target fragments

As the projectile mass increases, the probability of collision with heavy target nuclei diminishes, and the fraction of interactions on light nuclei becomes more

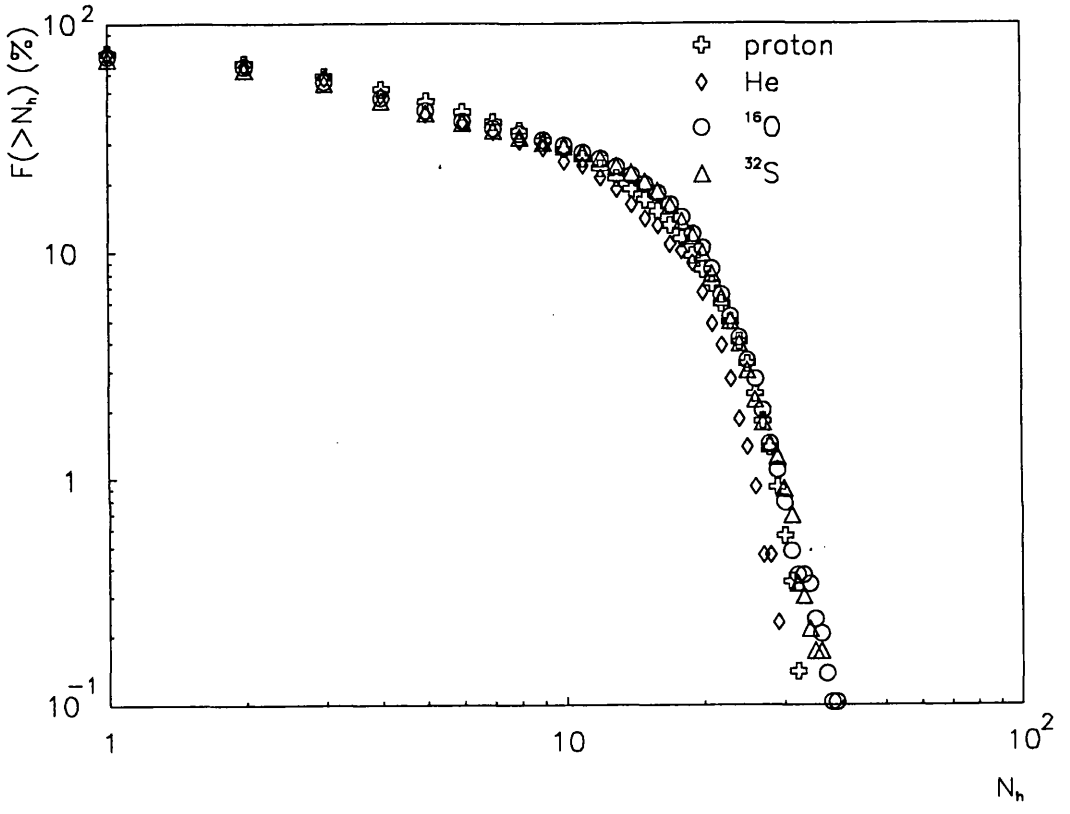

Figure 4.5: *The integral frequency distributions of N_h from interactions of ^{16}O and ^{32}S ions and He projectile fragments, together with those from proton-emulsion interactions at 200-400 GeV[118].*

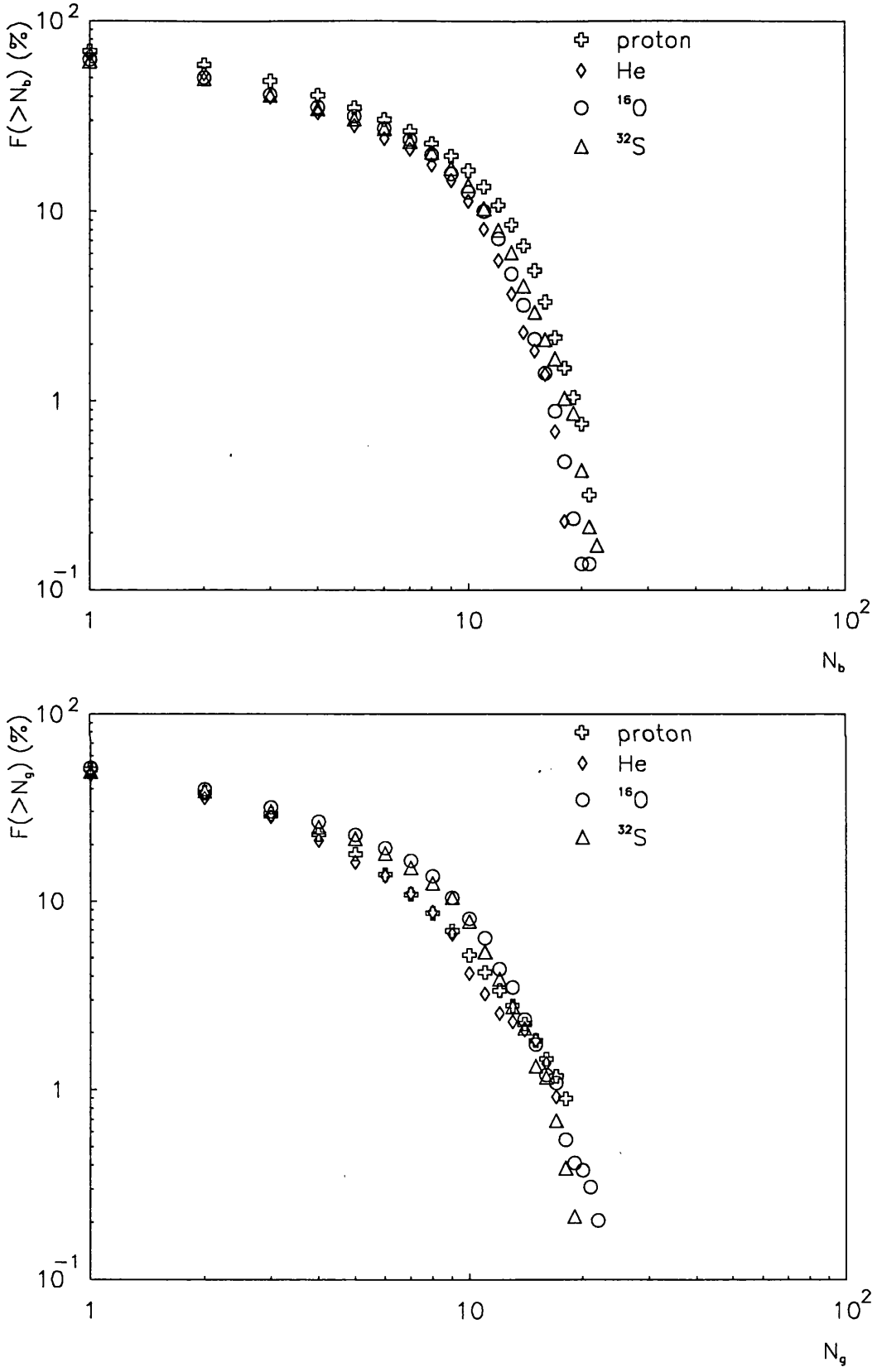

Figure 4.6: *The integral frequency distributions of (a)N_b and (b)N_g from interactions of ^{16}O and ^{32}S ions and He fragments, together with those from proton interactions[118].*

significant(see Table 4.7). Therefore, although the fraction of interactions on heavy target producing N_h values less than eight decreases with increasing projectile mass, this loss is compensated by the increased probability of collisions with lighter targets which will produce $N_h \leq 8$. As a result of this delicate compensation, the average number of heavy prongs $\langle N_h \rangle$ is constant, within small errors (except for He) when ranging from proton- to sulphur-emulsion interactions (see Table 4.6).

Very similar $\langle N_h \rangle$ values were found by Jain *et al.*[126]: 7.22±0.34, 7.42±0.36, 7.07±0.44, and 7.1±0.32 for 200 A GeV ^{32}S, 200 A GeV ^{16}O, 60 A GeV ^{16}O and projectile fragment He induced interactions, respectively. However, it is noted that in ref.[130] the average multiplicity of target associated particles N_h for 12 A GeV He interactions in emulsion was found to be noticeably higher, namely 9.48±0.37. Furthermore, Adamovich *et al.*[125] observed considerably higher multiplicity N_h values than we did in nucleus-emulsion interactions, namely 10.0±0.4 for 14.6 A GeV ^{16}O, 10.2±0.5 for 60 A GeV ^{16}O, 8.4±0.5 for 200 A GeV ^{16}O, 10.0±0.5 for 14.6 A GeV ^{28}Si, and 8.6±0.5 for 200 A GeV ^{32}S interactions. It is noted that their $\langle N_b \rangle$ values are comparable to our data. The discrepancy lies with the number of grey prongs and may be partly due to the difficulty of discrimination between them and those shower particles close to the target fragmentation region.

Angular distribution of grey particles

A study has been made of the angular distributions with respect to the primary beam direction of grey tracks, those with ionization densities J_i between 1.5 and 6.0 times minimum, J_0. While these tracks are mainly due to knock-on protons(deuterons ...) there is undoubtedly some contamination due to slow pions, especially among those with the smaller ionization values. Nevertheless, the data, shown separately for ^{16}O and ^{32}S interactions in Fig. 4.7(a) and 4.7(b) respectively, are all seen to fit curves of the form $a \exp(b \cos\theta)$. The forward peaking is more pronounced for the ^{32}S($b = 1.20 \pm 0.08$) than for the ^{16}O sample($b = 1.00 \pm 0.04$). Angular distributions of this form and with similar asymmetries were found in proton[123,131], α[130,126], ^{16}O[127,125,126], and ^{28}Si[125] interactions in emulsion. These works have shown that the angular distributions of grey tracks are almost independent of energy, projectile mass and centrality of the

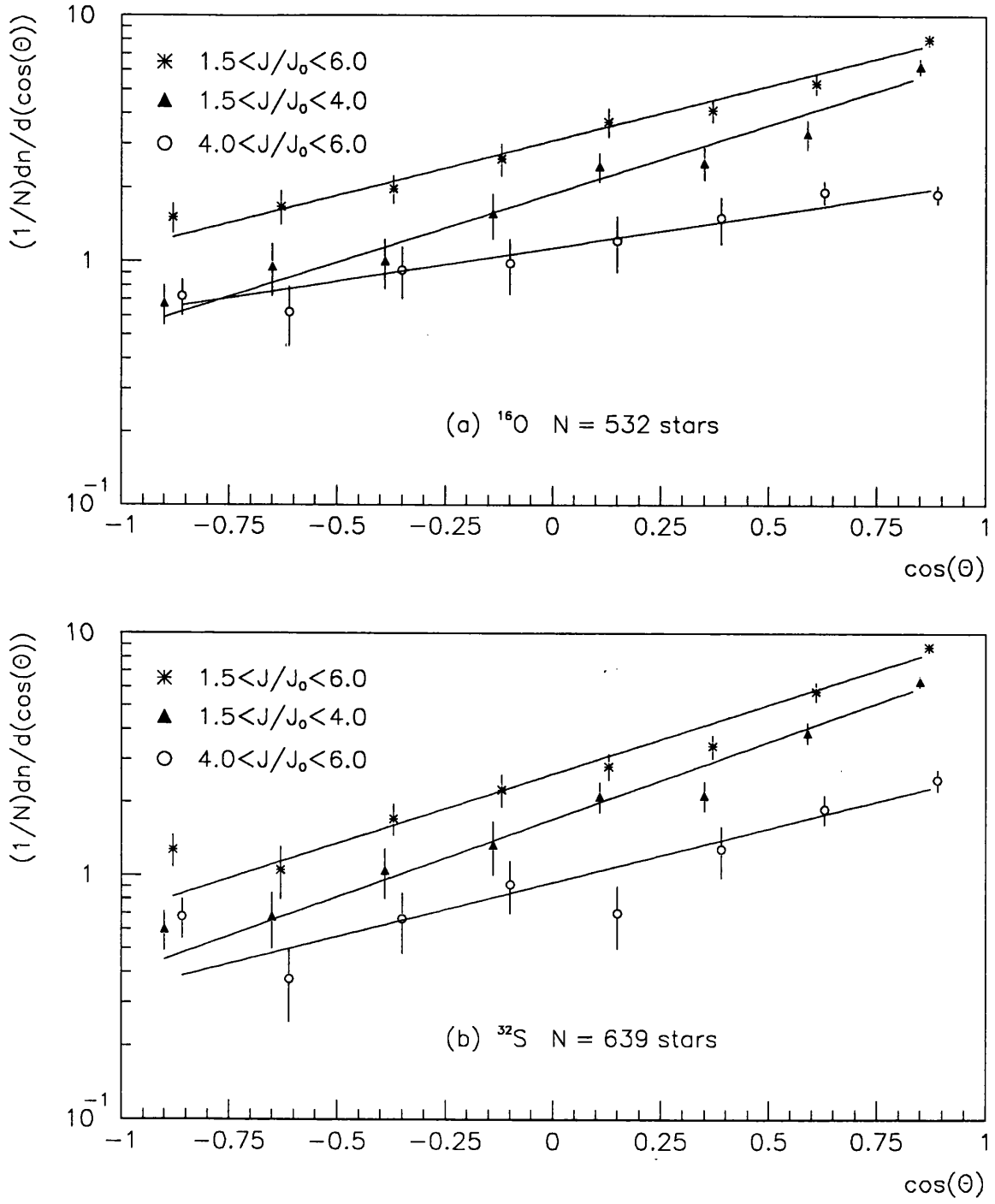

Figure 4.7: *Angular distributions of grey tracks having ionization densities between 1.5 and 6.0 times minimum, (a) from ^{16}O interactions, (b) from ^{32}S interactions. The fitted curves are of the form $ae^{bcos\theta}$.*

interaction[127,125], but several models[127,126] currently used fail to reproduce the observed shape and predicted a much more forward peaked distribution than the experimental one.

Black and grey particles correlations

The dependence of the average number of black particles $\langle N_b \rangle$ on N_g has the same behaviour for helium-. oxygen- and sulphur-emulsion interactions as shown in Fig. 4.8(a). The dependence of $\langle N_b \rangle$ increases linearly with N_g up to ~ 8, and for $N_g \geq 8$ a saturation of the $\langle N_b \rangle$-N_g correlation is reached. This behaviour is also observed by Stenlund *et al.*[118,122,123,124] in 200-400 GeV proton- and π-emulsion interactions and by Jain *et al.*[126] in 200 A GeV He-, ^{16}O- and ^{32}S-emulsion interactions.

The linear behaviour of $\langle N_b(N_g) \rangle$ at small N_g suggests the low degree of cascading in target nucleus and that the emission of each grey particle on the average makes the same contribution to the excitation energy. The agreement amongst various projectiles in $\langle N_b(N_g) \rangle$ is nontrivial since the small N_g values in ^{16}O- and ^{32}S-(Ag,Br) interactions correspond to large impact parameters when the two nuclei collide peripherally and the grey particles are protons knocked out from the surface of the target nucleus. The same number of grey particles in the helium-induced interactions, on the other hand, corresponds to smaller impact parameters, i.e., to more intensive cascading and higher excitations of the target nucleus. Unfortunately, the interactions with the light and heavy components of the emulsion are not separated in this experiment, but previous studies of proton- and ^{56}Fe-emulsion interactions at 1.8 A GeV[132] showed that p+(Ag,Br) interactions indeed exhibited a stronger dependence in the $\langle N_b(N_g) \rangle$ correlation than ^{56}Fe-(Ag,Br) interactions.

In higher N_g values, i.e., in the region attainable only in collisions with (Ag,Br) nuclei, the mean multiplicity $\langle N_b \rangle$ is independent of the number of grey particles in a star. There are two possibilities that may account for this $\langle N_b(N_g) \rangle$ behaviour. The first one is that there are only a finite number of protons in the target nuclei, and if a target nucleus loses a large number of protons during the fast reaction

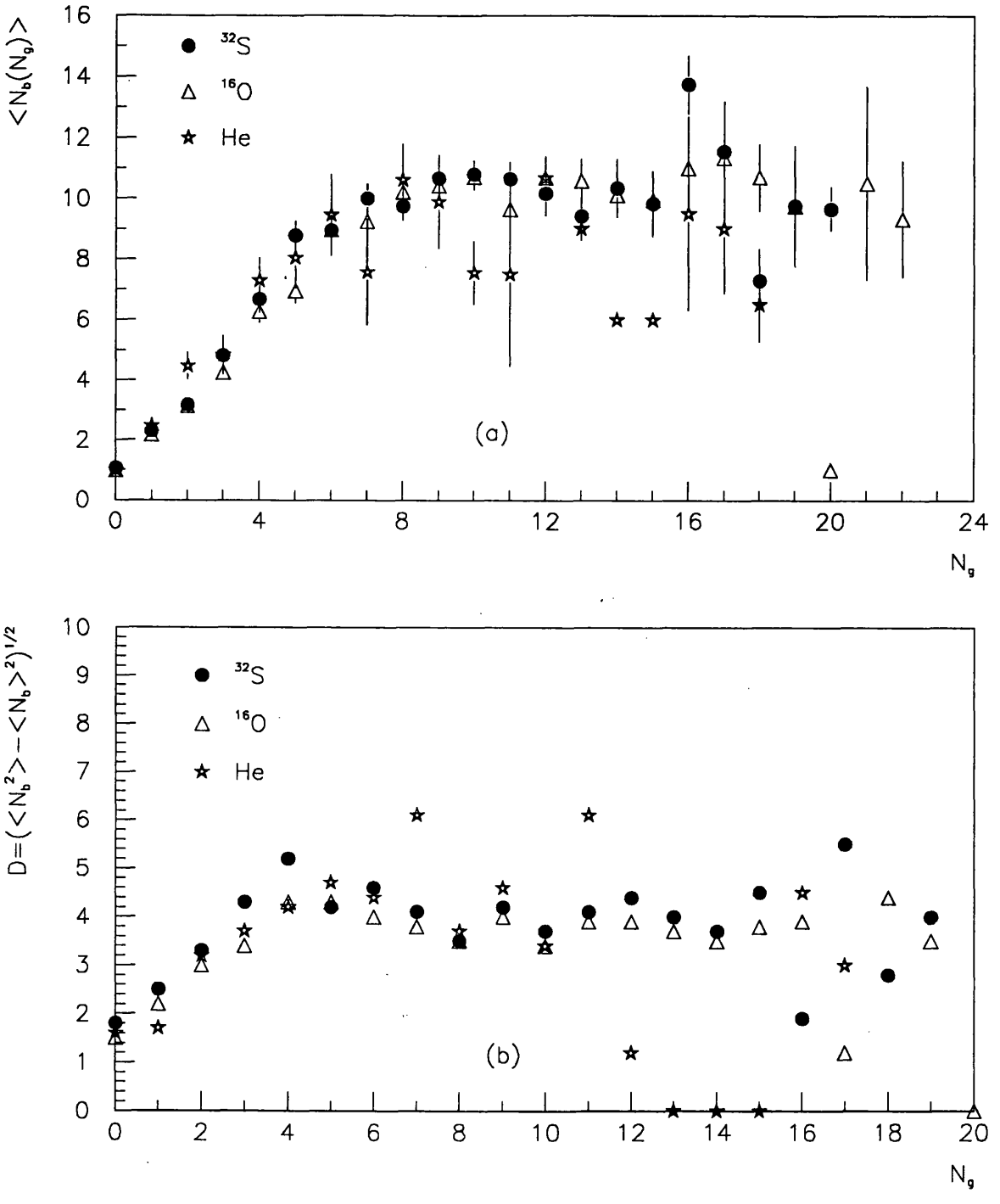

Figure 4.8: *(a)The mean number of black tracks and (b)its dispersion as a function of grey tracks from interactions of ^{16}O and ^{32}S ions and He projectile fragments at 200 GeV per nucleon.*

stage, a limited number of nucleons is left in the target nucleus residue during the second or slow stage. The second possibility is that the high excitation energies of the residue target nuclei may give rise to an explosion-like secondary particle emission, thereby resulting in their acquiring an energy exceeding the energy boundary of the black tracks. In addition, heavier fragments may be emitted than during evaporation process where lighter fragments are boiled off, thereby decreasing the number of black particles.

In Fig. 4.8(b) the corresponding dispersion $D(N_g)$, where

$$D(N_g) = \sqrt{\langle N_b^2(N_g)\rangle - \langle N_b(N_g)\rangle^2} \ , \qquad (4.3.1)$$

is displayed. The dispersion rises from 2 to about 4 and then a saturation is reached. This behaviour is approximately the same for all three projectiles despite the fact that our experimental data of He-induced interactions have poor statistics for values of $N_g > 10$.

Fig. 4.9(a) again plots the correlation between between N_g and N_b, but this time $\langle N_g(N_b)\ \rangle$ is shown. The similarities amongst the He-, ^{16}O and ^{32}S-induced interactions are obvious; in all cases $\langle N_g\rangle$ increases slowly and linearly until N_b=4, then a more rapid rise is observed up to $\sim$ 10 before reaching a plateau. The rapid increase of $\langle N_g\rangle$ between N_b=4 and 10 corresponds to the change in target nuclei from (C,N,O) to (Ag,Br). Furthermore for $N_b > 4$, $\langle N_g\rangle$ increases with increasing projectile mass when comparing the data of He-induced interactions with those of ^{16}O-induced interactions. This observation supports the assumption in sec. 4.3.2 that grey particles are related to the number of intranuclear collisions and rises with the number of incident projectile nucleons, especially in collisions with heavy emulsion nuclei(Ag, Br). However, within statistical errors the $\langle N_g\rangle$-N_b correlation does not vary when going from ^{16}O- to ^{32}S-emulsion interactions. In our analysis so far, the multiplicity of grey particles seems to increase significantly when going from He- to ^{16}O-induced interactions, but little variations are found when the projectile changes from ^{16}O to ^{32}S. Fig. 4.9(b) shows the corresponding dispersion $D(N_b)$. Unlike $D(N_g)$, $D(N_b)$ varies with the projectile. In the region N_b> 7, $D(N_b)$ are more or less the same for all three projectiles, while beyond N_b= 7 the $D(N_b)$ of He-induced interactions are generally much smaller than that of ^{16}O- and ^{32}S-induced interactions.

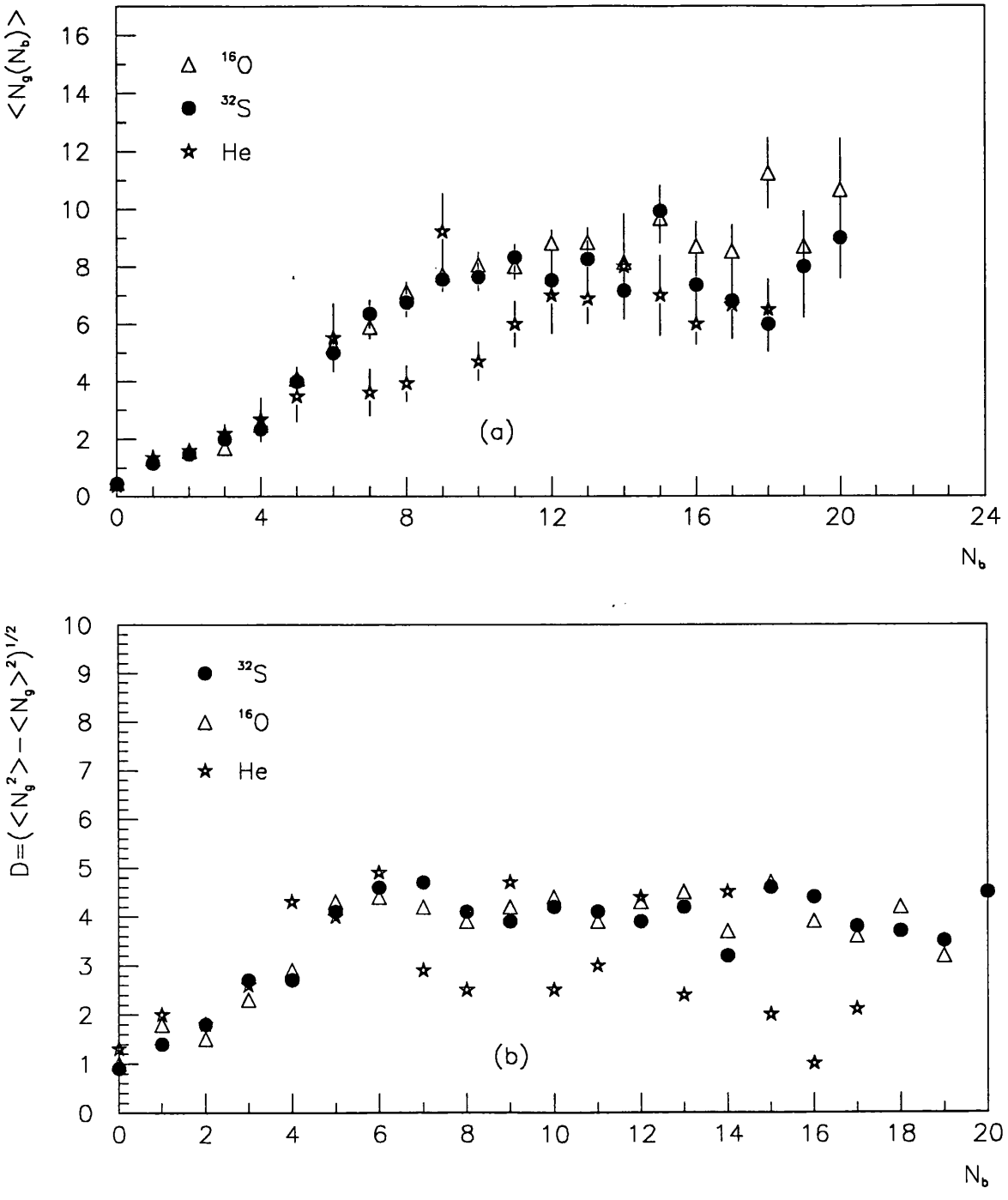

Figure 4.9: *(a)The mean number of grey tracks and (b)its dispersion as a function of black tracks from interactions of ^{16}O and ^{32}S ions and He projectile fragments at 200 GeV per nucleon.*

4.3.3 Production of shower particles

For the minimum-bias samples, the average shower-particle multiplicities for He-, ^{16}O- and ^{32}S-emulsion interactions are 17.35±0.58, 41.57±1.07 and 56.3±2.1, respectively. These values are relatively low compared to the results of other experiments at the same energy. Jain *et al.*[126] reported $\langle N_s \rangle$ = 23.59±1.2 for He, 57.30±3.1 for ^{16}O and 79.20±4.1 for ^{32}S, and on the other hand Adamovich *et al.*[125] also obtained similar values: 56.5±2.7 for ^{16}O and 79.9±4.1 for ^{32}S. However the ratio of the mean multiplicities of shower-particles for the He, ^{16}O and ^{32}S projectiles is approximately the same for all three experiments: 0.42:1:1.4. It may be that the shower-particle multiplicities for the three projectiles have been systematically underestimated in our experiment. Nonetheless, the character of the dependence of mean shower multiplicities on projectile mass remain valid.

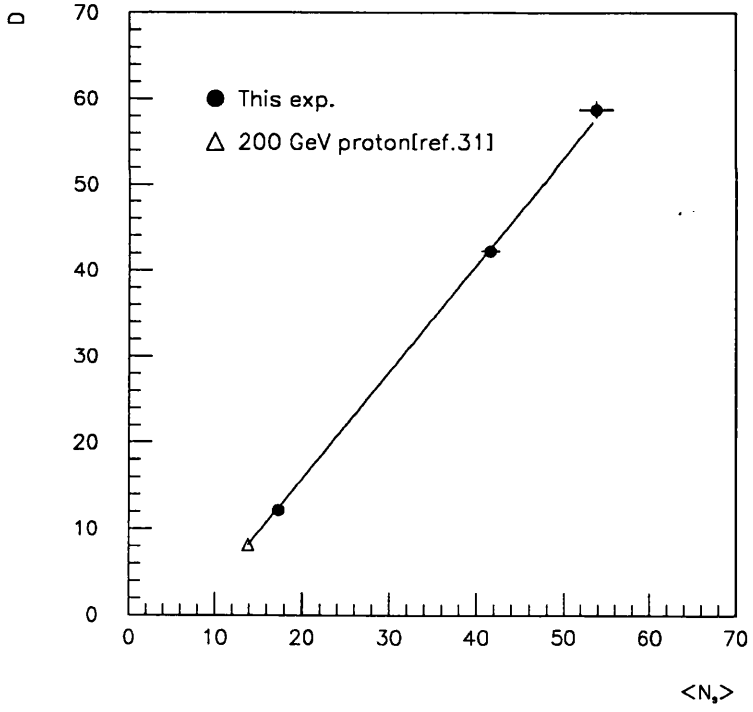

Figure 4.10: *Dispersion(D) versus mean shower particle multiplicities. The straight line is a least square fit to the data. The 200 GeV proton data are taken from ref.[133].*

The dispersion $D = \sqrt{\langle N_s^2 \rangle - \langle N_s \rangle^2}$ of the multiplicity distributions corresponding to all the projectiles is given by the relation $D = a + b\langle N_s \rangle$, where a=-9.07±0.08 and b=1.24±0.01, and is shown in Fig. 4.10. The 200 GeV proton

data is taken from ref.[133]. This linear dependence of the dispersions of multiplicity distributions on the average multiplicities is consistent with the prediction by Adamovich *et al.*[138] based on simple statistical considerations.

The multiplicity distributions of the shower-particles produced in the minimum bias events of He, ^{16}O and ^{32}S beams are shown in Fig. 4.11(a)-(c), respectively. It is noted that the maxima of the distributions all lie at the low values of multiplicities and decreases characteristically with increasing projectile mass, whereas the tails of the distributions extend with increasing projectile mass. The usual comparison of the multiplicity distributions with the Koba-Neilson-Olesen type of scaling law[134] seems irrelevant since the present distributions reflect the distributions of the participating nucleons from the interacting nuclei, rather than the multiplicity distribution from a single nucleon-nucleon collision. The fluctuation in the number of participant nucleons at fixed impact parameter is large, and the effects from binary collisions may be swamped. Furthermore violation of KNO scaling has been reported by the UA5 collaboration in the inelastic data of $p - \overline{p}$ interaction at 540 GeV centre-of-momentum energy[135]. Nevertheless, it has been reported that the shower-particles' multiplicity distributions of He, ^{16}O and ^{32}S beams, expressed in the normalized form $N_s/\langle N_s \rangle$, exhibited universal scaling irrespective of the projectile mass and energy at relativistic incident energies[112,136,137]. This scaling has been interpreted as a consequence of the nuclear geometry. Fig. 4.11(d) shows the plot of $\langle N_s \rangle \times P(N_s)$ as a function of $N_s/\langle N_s \rangle$ for ^{32}S($\bullet$), ^{16}O($\triangle$) and He projectile fragments($\star$). As can be seen, the normalized distributions for the three projectiles do not fall on the same universal curve.

Correlations of N_s with target and projectile fragmentations

In sec. 4.3.2 we have discussed the correlation between N_g and the mean number of intranuclear collisions. It is expected that N_s and N_g are also correlated. Fig. 4.12(a) plots the dependence of $\langle N_s \rangle$ on N_g for all three projectiles. The data corresponding to each beam show an approximate linear relation between $\langle N_s \rangle$ and N_g and support the assumption that the there is a positive correlation between the number of target fragments and the mean number of intranuclear collisions.

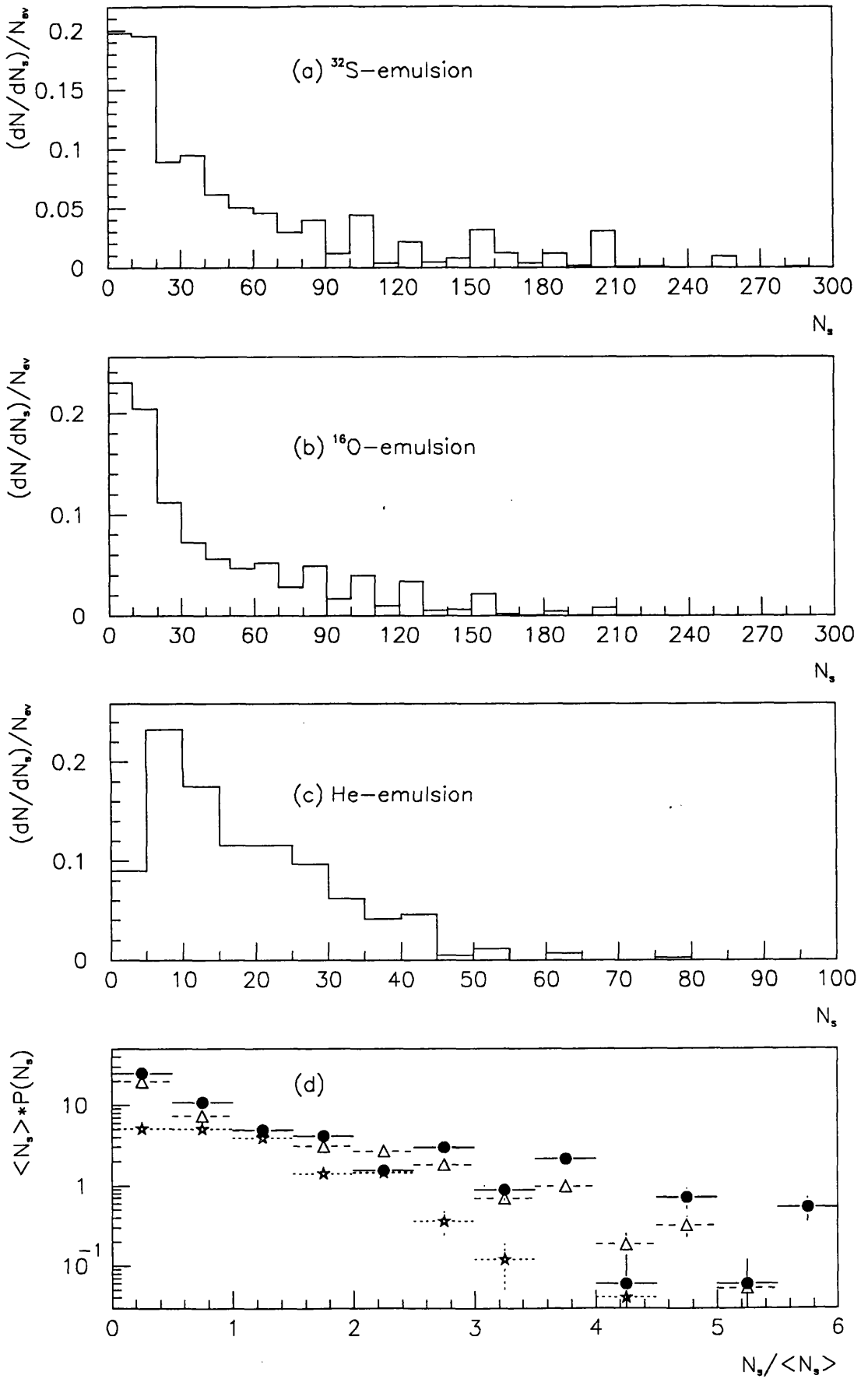

Figure 4.11: *Normalized N_s distributions for 200 A GeV (a)^{32}S, (b)$^{16}O$and (c)He; and (d)scaled N_s distributions for ^{32}S, ^{16}O and He(see text for symbols).*

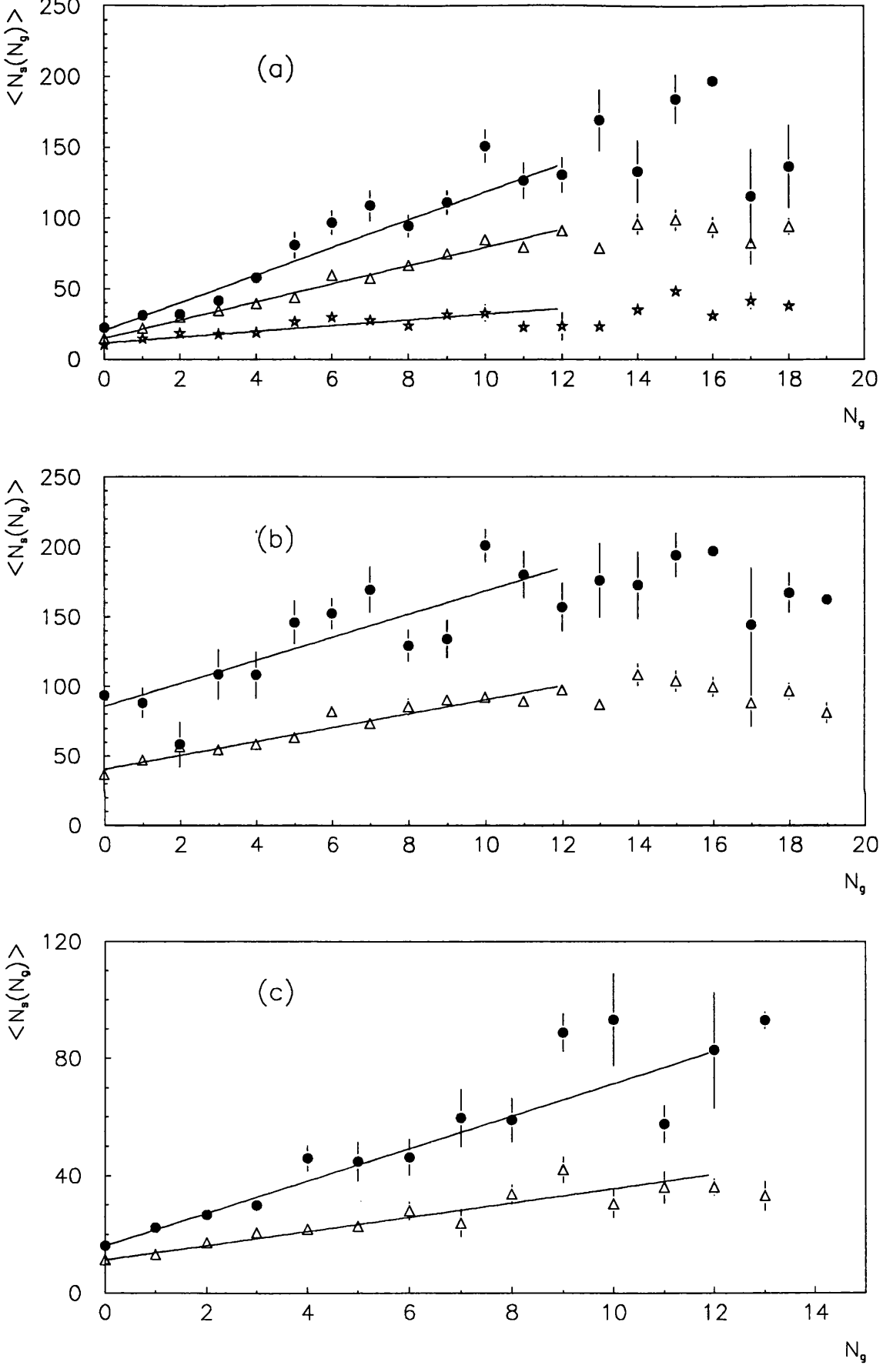

Figure 4.12: *The correlation between average N_s and N_g for (a)the minimum-bias samples, (b)central interactions and (c) peripheral interactions. The symbols used here are as in Fig. 4.11.*

The correlation between $\langle N_s \rangle$ and N_g is given by $\langle N_s \rangle = a_i + b_i N_g$ where the fitted values of the coefficients a_i and b_i are given for all three projectiles in Table 4.9.

Table 4.9: *The coefficients a_i and b_i in $\langle N_s \rangle = a_i + b_i N_g$.*

Projectile	Event Type	a_i	b_i	χ^2/DOF
^{32}S	all	20.49±0.90	9.77±0.33	3.24
	central	85.71±4.73	8.28±0.58	3.00
	peripheral	16.13±0.65	5.52±0.26	2.61
^{16}O	all	14.96±0.27	6.41±0.16	1.23
	central	40.42±1.27	5.01±0.25	1.52
	peripheral	11.33±0.17	2.43±0.08	1.33
He	all	11.60±0.49	2.04±0.17	3.57

It is noted that the mean multiplicity of shower-particles in the He-emulsion interactions is only weakly dependent on the degree of target fragmentation, while the correlation functions $\langle N_s(N_g) \rangle$ in the ^{16}O- and ^{32}S-emulsion interactions exhibit a much stronger trend to increase. This dependence of $\langle N_s(N_g) \rangle$ on projectile mass is due to the geometry of the collisions. Figs. 4.12(b) and (c) show the dependence of $\langle N_s \rangle$ on N_g for central or near-central interactions in which the whole projectile is completely disrupted, i.e. no projectile fragments with $Z \geq 2$ remain, and peripheral interactions having one or more fragments with $Z \geq 2$. Again $\langle N_s \rangle$ increases linearly with N_g for both categories of interactions, but the more central the interactions the stronger the correlation between $\langle N_s \rangle$ and N_g. The coefficients of the fitted straight lines for these figures are also given in Table 4.9.

Fig. 4.13 plots $\langle N_s \rangle / D$ as a function of N_g corresponding to ^{16}O and ^{32}S. The distributions are expressed by the relation $\langle N_s \rangle / D = c_1 + d_1 N_g$, where

projectile	c_1	d_1	χ^2/(DOF)
^{16}O	1.04±0.03	0.10±0.01	2.82
^{32}S	0.84±0.03	0.12±0.01	1.92

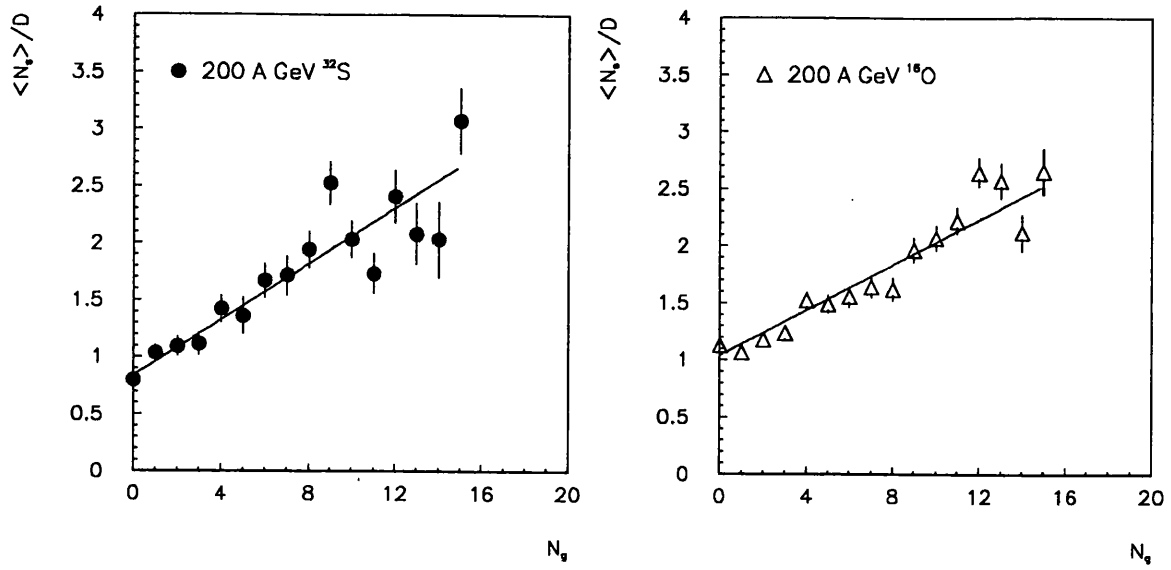

Figure 4.13: $\langle N_s \rangle / D$ *as a function of* N_g. *The solid lines are least-squares fits to the data corresponding to each projectile.*

Both fitted lines have very similar coefficients, and the distributions are almost independent of the projectile mass. Furthermore, both distributions exhibit that $\langle N_s \rangle / D$ becomes much larger than 1 as N_g increases. The dispersions of the multiplicity distributions become smaller than $\langle N_s \rangle$ due to the limited range of impact parameters as the interactions get more and more central. At high degree of overlapping between the target and projectile nuclei, this leads to much smaller dispersions than that observed for the whole minimum-bias sample. In other words, the fluctuations in the number of participant nucleons decrease with decreasing impact parameter.

The correlations amongst the degrees of disruption of the projectile ion, of the target and of the average number of shower-particles $\langle N_s \rangle$ are clearly shown in Table 4.4(sec. 4.3.1). Fig. 4.14 shows the N_h distributions for ^{16}O and ^{32}S-emulsion interactions categorised according to the kind of surviving forward projectile fragments. The central or near-central interactions exhibit the highest degree of target fragmentation($\langle N_h \rangle$=13.5±0.3 for ^{16}O and 14.9±0.5 for ^{32}S) and also the highest average number of shower-particles($\langle N_s \rangle$=87.1±2.0 for ^{16}O and 155.9±5.7 for ^{32}S). On the other hand, increasingly more peripheral interactions show heavier or

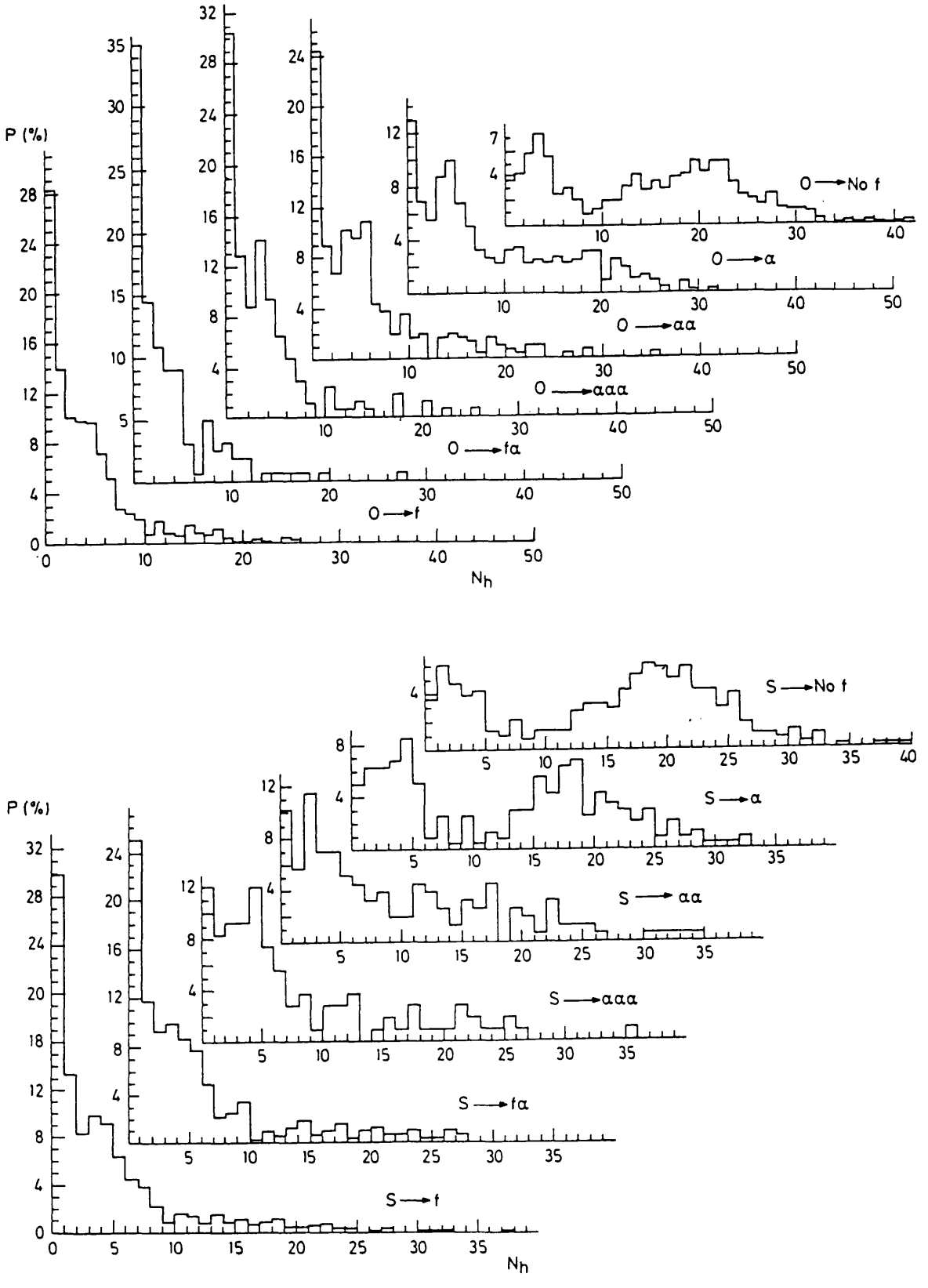

Figure 4.14: *Distributions of N_h for ^{16}O and ^{32}S ion-emulsion interactions selected according to the types of surviving fragments.*

more numerous fragments of the projectile proceeding almost undisturbed along the beam direction; in these cases both $\langle N_h \rangle$ and $\langle N_s \rangle$ decrease.

For the ^{16}O sample, where the charges of the forward-going projectile fragments have been determined, it has been possible to examine more closely the correlations of $\langle N_h \rangle$ and $\langle N_s \rangle$ with the degree of disruption of the incident ^{16}O ion. These numbers are given in Table 4.10 as a function of $\sum Z_i$, the sum of the charges of the projectile fragments of charge two or more issuing from an interaction. Since only a subsample of events was used in this work, the numbers in this table are not directly comparable with those given in Table 4.4.

From Table 4.10, it is evident that for those events with $\sum Z_i \leq 6$ both $\langle N_h \rangle$ and $\langle N_s \rangle$ are fairly constant within statistical errors for each category of the same $\sum Z_i$. This trend suggests that in these events both pion production and evaporation energy depend primarily on $\sum Z_i$, and not on the detailed nature of the projectile fragmentation. However, for the more peripheral events(i.e. events with $\sum Z_i \geq 7$), the average multiplicity of target fragments fluctuates with the details of the projectile break-up, while $\langle N_s \rangle$ depends only on $\sum Z_i$. This behaviour further supports our earlier observation that the fluctuations in the number of participant nucleons increase with decreasing centrality of the interactions. In addition, the monotonic increases of both $\langle N_h \rangle$ and $\langle N_s \rangle$ with decreasing $\sum Z_i$ emphasize that these features are intimately linked with the centrality of the primary interaction, i.e. with the effective numbers of nucleon-nucleon collisions taking place. A similar correlation of $\langle N_h \rangle$ with $\sum Z_i$ was observed by Adamovich *et al.*[120].

4.3.4 Projectile fragmentation

Total projectile fragmentation events

It is noted in Fig. 4.14 that the N_h distributions for the most central events for ^{16}O and ^{32}S interactions are similar, both being double-peaked with a pronounced minimum for N_h values around 8. Interactions, therefore, on light and heavy nuclei appear well separated. The relative rate of this kind of interaction decreases in going from ^{16}O interactions, 30.5% of all events, to 16.3% for ^{32}S. Furthermore,

Table 4.10: *Average values of N_h, N_b, N_g and N_s as a function of $\sum Z_i$ for incident ^{16}O ions.*

$\sum Z_i$		No. of interactions	$\langle N_h \rangle$	$\langle N_b \rangle$	$\langle N_g \rangle$	$\langle N_s \rangle$
8	O	17	1.77±0.46	1.53±0.38	0.24±0.10	4.65±1.06
	Cα	33	1.94±0.45	1.18±0.25	0.76±0.25	5.42±0.92
	Beαα	5	1.00±0.69	0.80±0.72	0.20±0.18	7.80±1.04
	αααα	7	3.00±0.81	2.00±0.57	1.00±0.49	4.86±1.45
	Total	62	1.94±0.30	1.34±0.19	0.60±0.15	5.34±0.61
7	N	281	3.08±0.22	2.08±0.16	0.99±0.09	9.35±0.41
	Bα	32	2.25±0.68	1.41±0.47	0.84±0.28	8.97±1.04
	Liαα	10	1.40±0.57	0.90±0.52	0.50±0.21	9.20±1.43
	Total	323	2.93±0.21	1.98±0.15	0.96±0.08	9.31±0.37
6	C	273	3.63±0.26	2.30±0.18	1.33±0.11	13.19±0.55
	Beα	43	2.67±0.48	1.88±0.34	0.79±0.18	14.63±1.83
	ααα	150	3.43±0.13	2.04±0.22	1.39±0.18	13.19±0.79
	Total	466	3.48±0.20	2.18±0.13	1.30±0.09	13.32±0.44
5	B	94	3.83±0.46	2.46±0.32	1.37±0.19	16.51±1.12
	Liα	43	3.95±0.67	2.35±0.44	1.61±0.27	15.33±1.46
	Total	137	3.87±0.38	2.42±0.26	1.45±0.15	16.14±0.89
4	Be	57	5.00±0.78	3.14±0.50	1.86±0.34	24.51±3.35
	αα	291	5.00±0.34	3.09±0.22	1.91±0.15	23.45±0.87
	Total	348	5.00±0.31	3.10±0.20	1.90±0.14	23.62±0.91
3	Li	39	6.31±1.03	4.10±0.65	2.21±0.20	26.44±3.09
2	α	460	7.96±0.34	4.63±0.20	3.33±0.16	40.15±1.20
0	-	792	13.11±0.31	6.81±0.17	6.29±0.17	75.22±1.41

quantitatively, it is observed that 26% and 37% of ^{16}O interactions on light(C,N,O) and heavy(Ag,Br) nuclei respectively result in total projectile fragmentation, while the corresponding values for ^{32}S are 11% and 23%. The considerable reduction in the comparative rates for such events from ^{16}O to ^{32}S is not unexpected. From geometrical considerations it can be seen that the probability for central and near-central interactions decreases with the increase in size of the projectile. Moreover, it is much more difficult to disrupt the heavier ^{32}S ion completely. In so far as one may give a pure geometrical interpretation to the total cross-sections, these ratios can be fairly reproduced if it is assumed that no projectile fragment with $Z \geq 2$ can proceed undisturbed after the collision if the largest dimension within the part of the projectile outside the overlap region with the target is smaller than the diameter of an alpha particle. Thus a degree of overlap of projectile and target slightly less than, or slightly more than, the diameter of the ^{16}O and ^{32}S projectiles respectively is sufficient to result in their total fragmentation.

Central or near-central ion interactions with heavy nuclei will always involve a high number of nucleons. Hence a high average number $\langle N_h \rangle$ is expected with a small probability of low N_h values. The same is not true for the collisions with the light constituents of the emulsion, so that in this case one expects to find a distribution of N_h in the whole allowed range, $0 \leq N_h \leq 8$. Indeed fits of double Gaussian to the twin-peaked N_h distributions give for ^{16}O ions $\langle N_h \rangle_{C,N,O}$ = 3.1±0.2(σ=2.8±0.2), $\langle N_h \rangle_{Ag,Br}$ = 19.0±0.4(σ=6.3±0.6) and for ^{32}S $\langle N_h \rangle_{C,N,O}$ = 1.6±0.5(σ=3.2±0.8), $\langle N_h \rangle_{Ag,Br}$ = 19.5±0.3(σ=5.4±0.3) respectively. In addition, the overall mean numbers of shower particles $\langle N_s \rangle$ are noticeably different when separated into the predominantly light ($N_h \leq 8$) and definitely heavy target ($N_h > 8$) samples, being 59 and 109 respectively for ^{16}O and 91 and 183 for ^{32}S interactions. This would indicate that there are on average about twice as many nucleon-nucleon collisions in the heavy as in the light target samples, as one would expect.

When comparing the N_h distributions of central interactions for the oxygen and sulphur samples, it is noted that the fraction of interactions with N_h >8 increases from 65.6 % to 72.0 %. The double Gaussian fits to the two distributions also indicate that $\langle N_h \rangle_{C,N,O}$ decreases while $\langle N_h \rangle_{Ag,Br}$ rises when going from oxygen to sulphur projectiles. Furthermore, the average numbers of both black and grey

tracks for central interactions increases with increasing projectile mass, namely, from 7.19±0.20 to 7.62±0.27 and 6.64±0.17 to 7.32±0.26 for N_b and N_g respectively. This behaviour suggests that as the projectile mass increases, the heavy constituents of emulsion are more effective in disrupting the projectile nuclei completely despite the drop in the probability of this class of interaction.

Fig. 4.15 shows the normalized N_b and N_g distributions corresponding to events with complete projectile fragmentation for ^{16}O and ^{32}S ion-emulsion interactions. The most striking feature is that, like the N_h distributions, the N_b distributions for both ^{16}O and ^{32}S exhibit a similar double-peaked behaviour, whereas the N_g distributions are broadly-ranged without any pronounced minimum. This behaviour indicates that in central ^{16}O- and ^{32}S-(Ag,Br) interactions, the number of recoil nucleons escaped through the nuclear matter fluctuates considerably due to multiple collisions within the target nucleus. The probability for a nucleon to escape decreases with increasing size of the nucleus and therefore the effect is much more prominent in central or near-central collisions on (Ag,Br) in which almost the entire projectile nucleus overlaps with the target nuclear matter. However, those nucleons stopped inside the nucleus share its energy with the rest of the nucleus, thereby raising temperature which governs the later evaporation process. Although the number of grey tracks emitted in central interactions upon (Ag,Br) may fall into a very broad range of values, the energy deposited in the residual nucleus via absorption of recoil nucleons is manifest in the form of emission of a large number of black tracks. Hence the N_b distributions corresponding to interactions on light and heavy emulsion nuclei become better-separated than their N_g distributions.

Complete projectile fragmentation events with $N_h = 0$ In the sample of events which have complete projectile fragmentation, about 4% of them exhibit no overt sign of low-energy target fragmentation, i.e., $N_h = 0$. For about 70% of these events in the ^{16}O sample, the number of shower particles is small, typically about 20, and each event is characterized by having several particles proceeding essentially in the beam direction. These are most probably non-interacting singly charged projectile fragments. This feature, together with the low multiplicity observed, suggests that these events are due to interactions of ^{16}O with free protons

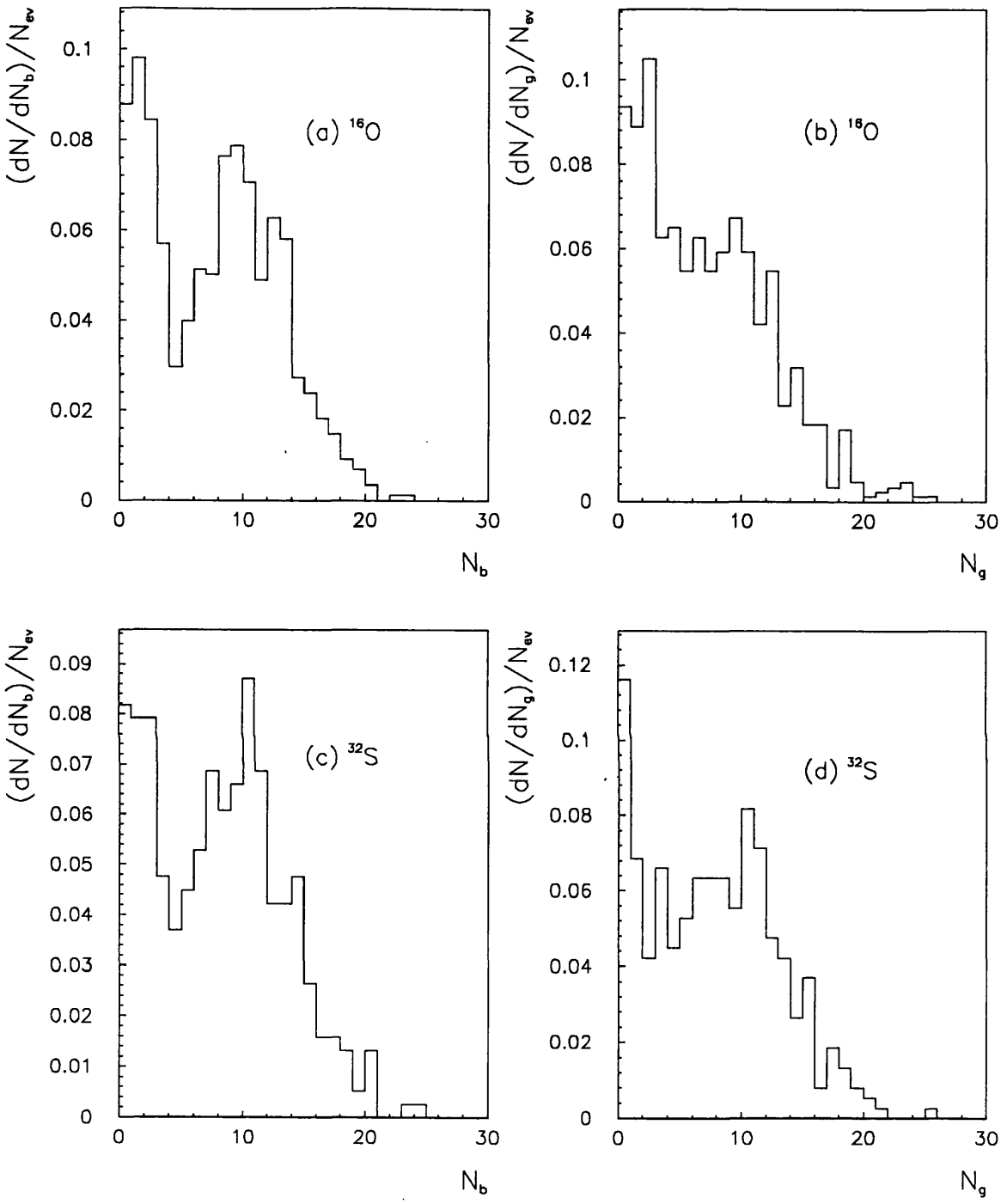

Figure 4.15: *Normalized distributions of N_b and N_g for ^{16}O and ^{32}S ion-emulsion interactions which exhibit complete projectile fragmentation.*

in the emulsion, in which the struck proton is given sufficient energy to record a track of minimum ionization. From Table 4.7, it is estimated that 7% of the ^{16}O-proton interactions give rise to complete fragmentation of the ^{16}O nucleus.

Only one of the events in the ^{32}S sample shows similar features, low multiplicity coupled with many spectator protons from the projectile, resulting in an efficiency of the order of 0.5% for protons to fragment the ^{32}S projectile completely. The rest of the sulphur interactions and the remaining oxygen ones all exhibit much high multiplicities, i.e., in the range of 60-180, much higher than can be expected from an interaction with a single proton. Therefore, they are likely to be central interactions on the light constituents(C,N,O) of the emulsion in which all of the target protons are struck sufficiently hard to receive relativistic velocities.

These assumptions are supported by the rapidity distributions of these events. The emission angles, θ, of the secondary particles from these events were measured, as were those from a few central ones known to have occurred on heavy emulsion nuclei by reason of there being many low-energy target fragments.

Often in ultra-relativistic ion-nucleus experiments, the detector geometry and events of interest are such that only particles with transverse momentum $p_T \approx p\theta \gg m$ are accepted. Thus the geometrical variable pseudorapidity η = -ln [tan(θ/2)] is a good approximation to the kinematical variable rapidity, y, despite the lack of acknowledge of the mass, m, and momentum, p, of the particle. For the events considered here, where the particles at small angles to the beam direction are largely spectator fragments from the projectile, these conditions are not fulfilled. For these events, the ratio p/m is expected to be that of the beam, i.e., 213, so that a better approximation to rapidity is given by $\tilde{y}$, where

$$y \approx \tilde{y} = \eta - \frac{1}{2}ln(1 + m^2/p^2\theta^2) + \frac{1}{2}ln(1 + m^2/p^2), \qquad (4.3.2)$$

providing sin$\theta \approx \theta$ and $m^2 \ll p^2$. The rapidity of an undeviated beam particle is 6.06. To accommodate the effects of measurement errors($\sim$ 1 mrad in space angle), particles with emission angles $\leq$ 4 mrad have been treated as spectator fragments for this purpose. The pions that fall within this narrow interval are expected to have a similarly high p/m ratio and therefore do not bias the rapidity plot significantly. Outside this angular cone, adopting an average value of 300 MeV/c for $p\theta$, $y \approx \tilde{y} \approx \eta$ - 0.11.

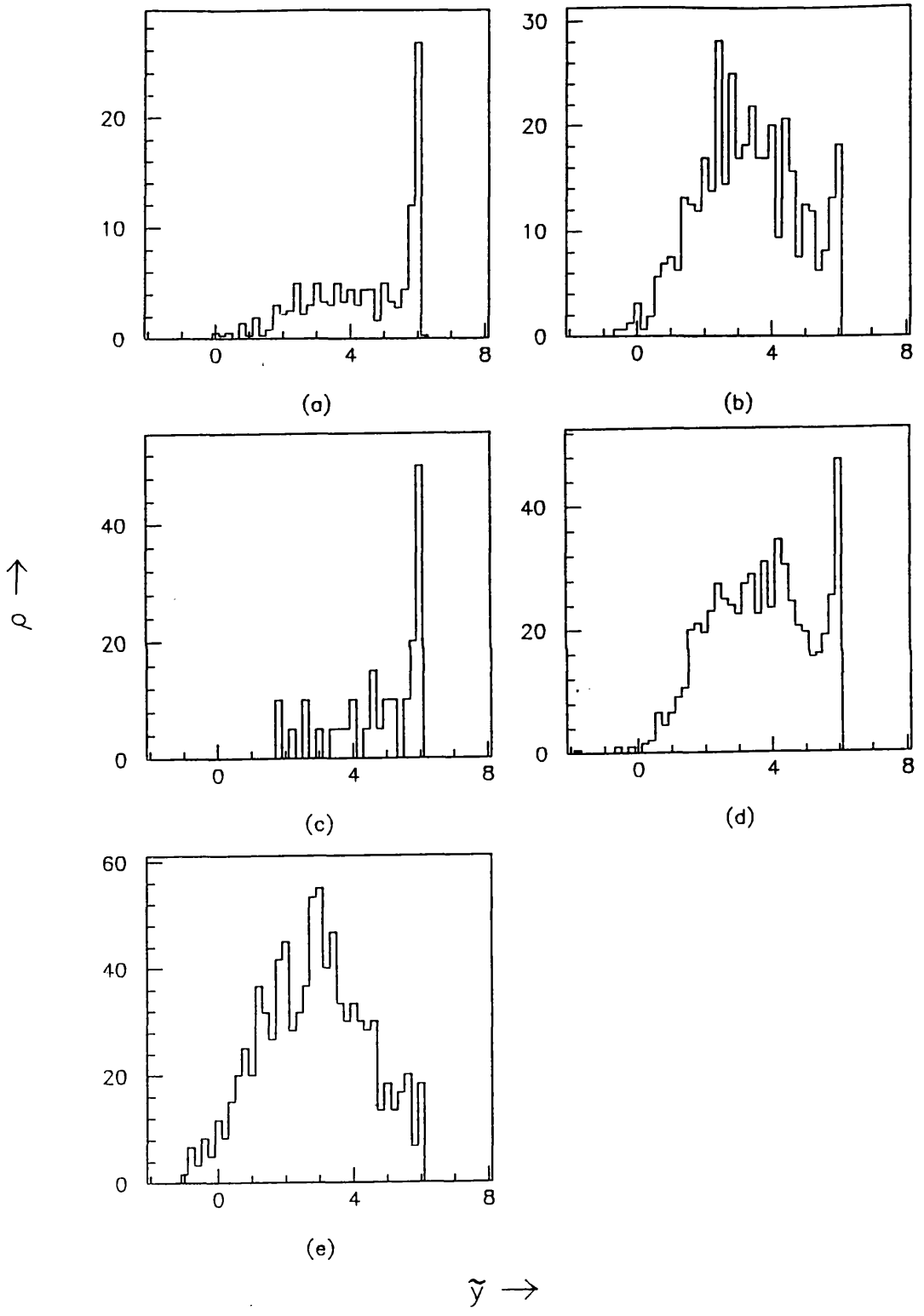

Figure 4.16: *Approximate rapidity-density distributions($\rho = N_{ev}^{-1}\, dN/dy$) (a) ^{16}O-H; (b) ^{16}O-(C,N,O); (c) ^{32}S-H; (d) ^{32}S-(C,N,O); and (e) ^{16}O-(Ag,Br) central interactions.*

Fig. 4.16(a) to (e) shows the approximate rapidity density distributions, $\tilde{y}$, summed for different categories of events. It is noted that there is a large accumulation of particles with high $\tilde{y}$ values–the projectile spectator particles–for the oxygen and sulphur interactions on free protons. On the other hand there is no large accumulation for those events ascribed to ^{16}O-(C,N,O) and no evidence for such spectators in ^{16}O-(Ag,Br) interactions, as expected. The absence of high $\tilde{y}$ particles in central ^{16}O-(Ag,Br) interactions demonstrates that the peaks in the hydrogen samples are not an artefact of the procedure used to obtain the approximate rapidity distributions $\tilde{y}$. The incomplete overlap of sulphur projectiles with the (C,N,O) target nuclei is observed in the form of a peak at high $\tilde{y}$ in Fig. 4.16(d). On subtracting the background due to pions at high $\tilde{y}$, deduced from the fraction of such particles in the central ^{16}O-(Ag,Br) events of Fig. 4.16(e), it is estimated that there are about 7, 4, 12, and 11 non-interacting protons for the ^{16}O-H, ^{16}O-(C,N,O), ^{32}S-H, and ^{32}S-(C,N,O) samples respectively.

Table 4.11 compares the average values of the rapidity distributions for each class of interaction and those expected by assuming an effective number of participant nucleons as in ref.[139] for interactions on (Ag,Br) and all nucleons as participants in collisions on (C,N,O). It is evident that our data are in agreement

Table 4.11: *Expected and observed average rapidity values*

Projectile nucleus		Target nucleus		
		H	C,N,O	Ag,Br
^{16}O	expected	4.4	3.0-3.2	2.5
	observed	4.4	3.3	2.8
^{32}S	expected	4.8	3.4-3.5	2.6
	observed	4.7	3.6	-

with the expected values.

Events with single alpha emission

The distribution of N_h for those interactions in which only one helium isotope projectile fragment remains shows for ^{32}S ion collisions a similar double-peaked behaviour to that observed for complete projectile fragmentation with $\langle N_h \rangle_{C,N,O}$ = 2.8±0.4(σ = 2.2±0.3) and $\langle N_h \rangle_{Ag,Br}$ = 18.9±0.5(σ = 4.7±0.6). There is a ratio 1.4 : 1 between the interactions on heavy(Ag,Br) and light(C,N,O) nuclei and this is approximately the same ratio as for all interactions as predicted in Table 4.7. On the other hand, the N_h distribution for this class of events for oxygen interactions does not exhibit the double-peaked feature. However any reasonable continuation of the distribution for $N_h > 8$, arising solely from interactions on heavy nuclei, to $N_h \leq 8$ indicates that the ratio of interactions on heavy and light nuclei is also similar to that for the whole sample. $\langle N_s \rangle$ again is well correlated with N_h, being 31 and 68 for oxygen and 68 and 121 for sulphur interactions for samples with $N_h \leq 8$ and $N_h > 8$ respectively.

The normalized N_b and N_g distributions for this class of events for oxygen and sulphur interactions are shown in Fig. 4.17. Again the N_b distributions display the double-peaked feature while the N_g distributions do not. A much larger fraction of the distributions for the sulphur sample can be ascribed to interactions on heavy nuclei of the emulsion than that of the oxygen sample, as expected.

For more peripheral interactions, those in which two or more He isotopes and/or a heavier fragment continue undisturbed, it is more difficult to separate interactions on heavy and light nuclei as shown in Fig. 4.14.

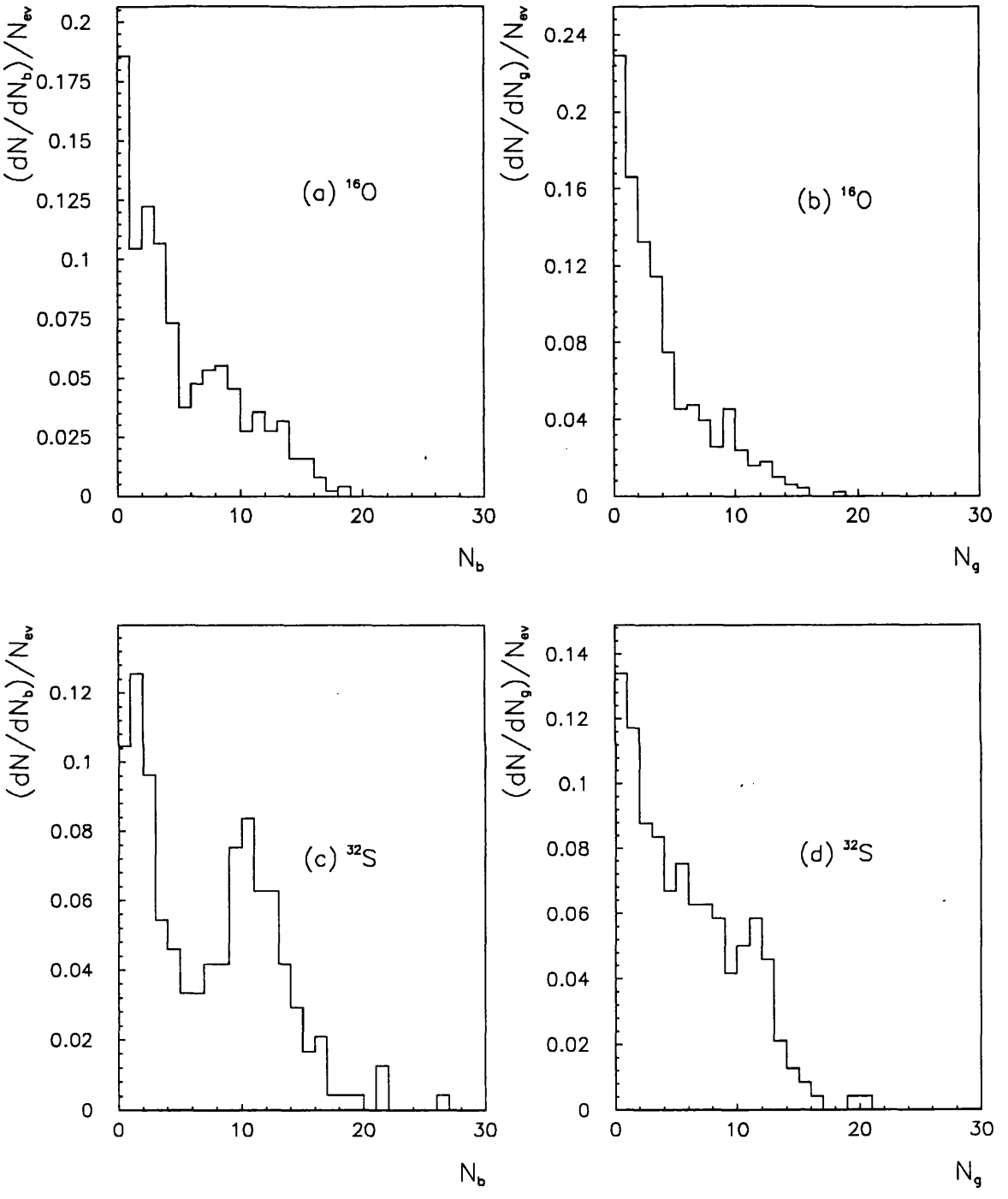

Figure 4.17: *Normalized distributions of N_b and N_g for ^{16}O and ^{32}S ion-emulsion interactions in which only one alpha projectile fragment remains.*

Chapter 5

Electromagnetic Dissociation of ^{16}O and ^{32}S at 200 A GeV

In this chapter, we present the results of a systematic study of the EMD of ^{16}O and ^{32}S projectiles into exclusive channels of charged fragments at an incident energy of 200 A GeV in nuclear emulsion. The photoproduction cross sections on ^{16}O and ^{32}S are determined by estimating the energy released in each interaction and assuming a model for the intensity and energy spectrum of the virtual photons. Furthermore we compare our results with those of the same reactions with real photons.

5.1 Experimental Results

In this section we will present the raw data and the analysis performed to remove spurious events and to correct for biases and losses.

5.1.1 Event classification

Clearly, an unbiased operative definition of projectile EMD does not exist. Peripheral nuclear interactions with neither target excitation nor pion production would have the same topology as projectile EMD. Furthermore, photo-interaction with

the emission of a pair of pions are indistinguishable from similar nuclear events. Nonetheless, we will label an interaction as a projectile EMD if:

1. the incident nucleus dissociates into at least two charged fragments;
2. there is no sign of target excitation;
3. the sum of the measured charges of all outgoing fragments is equal to that of the incident nucleus;
4. all tracks are emitted within 5 mrad to the beam.

The contamination due to nuclear interaction is very small within a sample defined in this manner. However, this sample will exclude those projectile EMDs with the emission of only one or more neutrons as well as those due to high-energy γ-rays with pion production. Although the quick fall-off of the photon spectrum with increasing energy depresses the relative rate of this last process of EMDs, this fact will be taken into account when we discuss the results.

5.1.2 Raw data

In order to increase the statistics on EMD events, two separate scans were performed. In the first scan, a total of 3290 interactions of ^{16}O nuclei was picked up by following 349.41 m of the primary track length. Out of these 3290 events, 2925 events were due to hadronic inelastic interactions and 365 ^{16}O EMD events were observed. We followed a total path length of 214.46 m of ^{32}S nuclei, during which 2319 events were observed. Among them, 515 events were ^{32}S EMDs. The second scan was performed only for ^{16}O-Em interactions, and a total path length of 511.16 m was followed. 563 ^{16}O EMDs, out of 4781 events, were found. These data are shown in Table 5.1. The ^{16}O data will be combined for analysis purpose.

Our mean free path for ^{16}O EMD at 200 GeV in nuclear research emulsion is 927$\pm$30 mm which shows considerable decrease when compared with that of the ^{16}O beam at 60 A GeV[49,51]. Not only does the mean free path for EMD

Table 5.1: *Global data on the EMD of primary ^{16}O and ^{32}S projectiles in nuclear emulsion.*

Nucleus	Scan	Energy (A GeV)	Refs.	L (m)	N_{EMD}	λ_{EMD} (mm)
^{16}O		60	[49]	16.37	9	1819 ± 606
^{16}O		60	[51]	63.53	31	2049 ± 368
^{16}O	1	200	this exp.	349.41	365	957 ± 50
^{16}O	2	200	this exp.	511.16	563	908 ± 38
^{16}O	1+2	200	this exp.	860.57	928	927 ± 30
^{32}S		200	[51]	127.38	197	647 ± 46
^{32}S		200	this exp.	214.46	515	416 ± 18

in emulsion decrease with increasing projectile energy, it also decreases markedly with increasing Z of the projectile, as expected. The mean free path for ^{32}S EMD in our raw data sample is 416±18 mm. In spite of the higher water content of our emulsion which should increase our path lengths, we observed a much shorter mean free path for raw ^{32}S EMD data than the value 647±46 mm found by G. Singh *et al.*[51] at the same energy. This may be partly due to the fact that G. Singh *et al.* used the criterion that all projectile EMD fragments have to be within a cone defined by $\theta \simeq 1$ mrad, whereas we required all the fragments to be emitted within 5 mrad.

Table 5.2 shows the numbers and relative rates of the visible channels of ^{16}O and ^{32}S EMD, classified according to their topologies, for different ranges of kinetic energy released in the interactions(see sec. 5.1.3). In our oxygen sample of 928 EMD events, 4 were not measurable due to early secondary interactions. Furthermore the 476 events in Table 5.2 represent a unbiased subsample of the 515 sulphur EMD events.

It is noted that the emission of a single hydrogen isotope(in most cases probably

Table 5.2: *Numbers and relative rates of different modes of breakup from 200 A GeV ^{16}O and ^{32}S EMD.*

$^{16}O \rightarrow$	Energy(MeV)			Fraction	$^{32}S \rightarrow$	Energy(MeV)			Fraction
	0-150	>150	(>500)	(%)		0-150	>150	(>500)	(%)
Np	503	12	(3)	55.7±2.5	Pp	251	5	-	53.8±3.4
C2p	109	17	(4)	13.6±1.2	Si2p	104	8	-	23.5±2.2
Cα	85	-	-	9.2±1.0	Siα	27	-	-	5.7±1.1
Bαp	29	2	-		Alαp	15	3	-	
B3p	5	8	(3)	4.8±0.7	Al3p	10	4	(2)	6.7±1.2
Be ...	52	27	(11)	8.5±1.0	Mg ...	9	9	(3)	3.8±0.9
Li ...	12	13	(2)	2.7±0.5	Na ... Ne ... F ...	5	10	(5)	3.2±0.8
4α	9	-	-						
3α2p	13	9	(2)		O ...				
2α4p	4	11	(3)	5.4±0.8	...	7	9	(6)	3.4±0.8
α6p	-	4	(3)		α ...				
Total	821	103	(31)		Total	428	48	(16)	

Note: two He isotopes with separation angle $\Delta\theta < 0.1$ mrad are considered as a ^{8}Be nucleus.

a proton) accounts for more than half of the EMD events in both samples. This is different from what G. Singh *et al.* observed. In their sample, the process $^{32}S \rightarrow$ Pp only has a rate of 36.5 %. On the other hand, Table 5.2 shows that the emission of two hydrogen isotopes occurs more frequently in ^{32}S than in ^{16}O EMD, whereas the situation is reversed when considering the emission of a single He isotope. In addition, the proportion of higher energy events increases with the increasing multiplicity of final state charged fragments. This is particularly noticeable in channels where only hydrogen and helium isotopes are left.

5.1.3 Estimate of the energy

Nuclear research emulsions are sensitive to charged particles only, therefore neutrons and γ-rays are in general not detected. There are cases in which electron pairs with small opening angles and high-energy interactions induced by neutral particles are observed in the vicinity of a primary non-interacting track. These events may be due to the emission of neutrons and γ-rays by the incident nucleus. However, the uncertainty of the production points of these particles prevents a meaningful use of these events. This means that projectile EMDs with the emission of neutrons alone are not detected, and those where one or more neutrons are emitted with other charged fragments are misidentified . In addition, only the charges but not the masses are determined.

In this experiment, neither the energy nor the momentum of a high-energy particle can be determined, but an estimate of the total centre of mass kinetic energy E released in the interaction was made by assigning to each fragment a mass according to its charge and a momentum per nucleon equal to that of the incident beam, i.e., 200 GeV/c. The following rules were used:

1. when only one or two minimum-ionizing particles are observed, they are assumed to be protons and neutron emission is not considered. Thus only channels ^{16}O $\rightarrow$ ^{15}Np or ^{16}O $\rightarrow$ ^{14}Cpp, and ^{32}S $\rightarrow$ ^{31}Pp or ^{32}S $\rightarrow$ ^{30}Sipp are considered;

2. in all other cases it is assumed that that A=2Z(including Z=1). The only exception is the channel O $\rightarrow$ BHeH, taken to be ^{11}Bαp(see sec. 5.2.4).

In order to estimate E, the measured angles θ_i are transformed into angles θ_i' with respect to the direction of the centre of mass of the charged fragments. The components of momentum transverse to that direction is given by $p_{T_i} = p_i\theta_i'$ and then assuming isotropy,

$$E = \sum E_i = \frac{3}{2}\sum \frac{p_{T_i}^2}{2m_i} \quad . \tag{5.1.1}$$

Rule(ii) is equivalent to stating that the average number and energy of the undetected neutrons are equal to those of the detected protons, but it does not

imply that all protons and neutrons are emitted as deuterons. The bias introduced by rule(i) and the hypothesis of isotropy will be considered in sec. 5.2.

Fig. 5.1 and 5.2 show the energy spectra computed in this manner for single or groups of channels. In this analysis, two α particles with relative emission angle $\Delta\theta < 0.1$ mrad were considered as ^{8}Be ground state.

5.1.4 Spurious events

The sources of spurious events are mainly knock-on electrons, electron pairs, and peripheral nuclear events.

Knock-on electrons

When a relativistic particle of charge Z_P and mass M_P traverses through matter, its electromagnetic field interacts with the atomic electrons. If sufficient kinetic energy is transferred to the electron, the electron may be seen projecting from the trajectory of the incident projectile.

The differential cross-section for transfer of energy in the interval dE to a stationary unbound electron is given by[110,108]:

$$(\frac{d\sigma}{dE})dE = \frac{2\pi Z_P^2 r_0^2 m_e c^2}{\beta^2}(1 - \frac{\beta^2 E}{E_{max}})\frac{dE}{E^2}cm^2 \qquad (5.1.2)$$

where β is the projectile velocity in units of c, m_e is the electron mass, and $r_0 = e^2/(m_e c^2)$. Other terms that take into account particle structure, sign of the charge and the physical state of the medium traversed are neglected in this approximation. The energy E of such knock-on electrons has a maximum value E_{max} given by:

$$E_{max} = \frac{2m_e c^2 \beta^2 \gamma^2}{1 + 2(\frac{m_e}{M_P})\gamma + (\frac{m_e}{M_P})^2} \approx 2m_e c^2 \beta^2 \gamma^2 \qquad (5.1.3)$$

where $\gamma = (1 - \beta^2)^{-1/2}$. In our conditions, E_{max} is about 40 GeV. The angle of ejection, θ, of an electron of energy E MeV is given by

$$tan\theta = \frac{1}{\sqrt{E}} \ . \qquad (5.1.4)$$

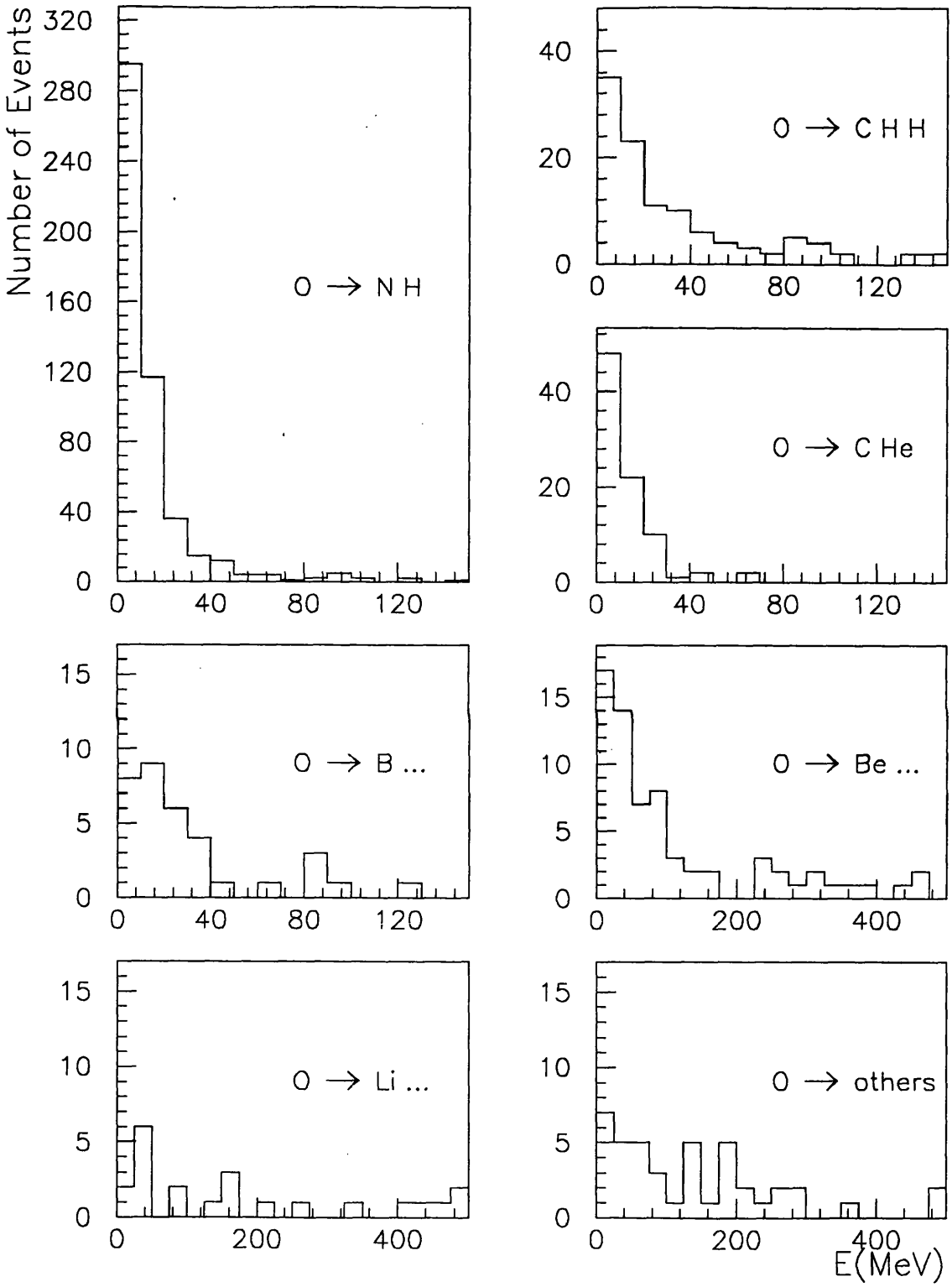

Figure 5.1: *Energy spectra for different channels observed in the raw sample of 200 A GeV ^{16}O EMDs.*

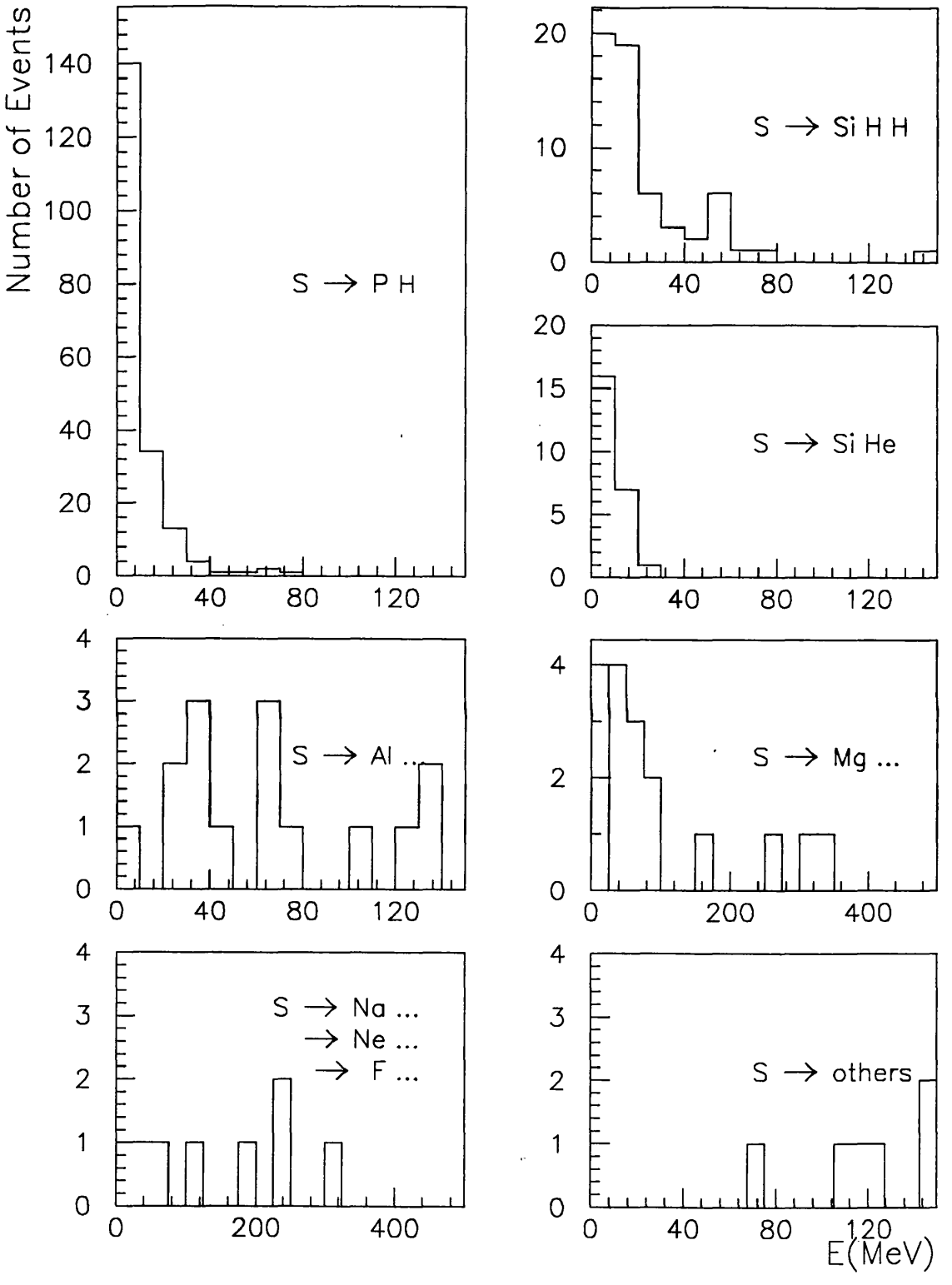

Figure 5.2: *Energy spectra for different channels observed in the raw sample of 200 A GeV ^{32}S EMDs.*

Thus the angular distribution is very wide, and the cross-section in the very forward direction vanishes.

In order to check for a possible contamination of electrons, a sample of 200 A GeV ^{32}S tracks had been carefully scanned, and the number of knock-on electrons per centimetre of track, making an angle of θ <100 mrad with the beam, was found to be 1.5. Therefore, the requirement that all EMD fragments' angles < 5 mrad would eliminate most of the knock-on electrons at the scanning stage. Any other knock-on electrons which have angles less than 5 mrad but exhibit multiple scattering are also removed either at the scanning stage or after the angular measurement. No genuine projectile EMDs should be removed by this procedure since both multiple scattering and visible bremsstrahlung are exceedingly small for high-energy nuclear fragments.

The heavier fragment of all remaining candidates after these cuts in the O $\rightarrow$ NH mode were observed to have charge Z=7, and we thus conclude there was no contamination in the sample. The same procedure has been applied to the ^{32}S sample. However, charge measurements of the heavier fragments from the sulphur sample are less accurate and more time consuming, and therefore only a fraction of the candidates in the S $\rightarrow$ SH channel has been measured.

Pair production

In pair production, an electron is raised across the gap between the filled negative-energy electron states and the states of positive energy. The process takes place in the Coulomb field of a charged particle in order to balance the energy and momentum of the incoming photon. In the case of heavy ions, electron pairs may be created in the Coulomb field of both the projectile and target nuclei.

Most of the pairs are low-energy in the frame of reference of the respective nucleus due to the shape of the photon energy spectrum. However, those created in the field of the projectile will appear to be energetic ones in the laboratory frame. Since the pairs in the projectile frame move approximately transverse to the beam direction, they will be observed in the laboratory frame moving close

to the forward direction[58]. At angles $\theta < 100$ mrad to the beam direction, we observed about 0.1 electron pairs per centimetre of the 200 A GeV ^{32}S ion track. Most of these would have been removed from the sample at the scanning stage by the criterion $\theta < 5$ mrad. Electron pairs with sufficiently small angle to the beam, if not already recognized as such, are efficiently rejected by the charge measurement requiring the sum of the fragment charges to be equal to that of the projectile.

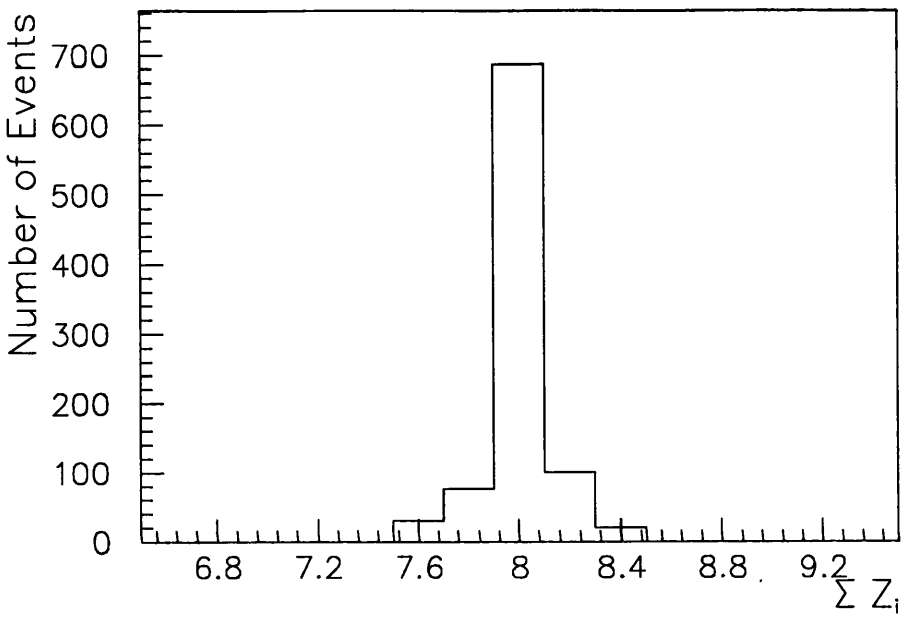

Figure 5.3: *Distribution of $\sum_i Z_i$ for sample of ^{16}O EMD candidates.*

Fig. 5.3 shows the distribution of the quantity $\sum_i Z_i$ for ^{16}O EMD candidates, where the sum is extended to the outgoing fragments. For $Z \geq 3$, Z_i is the measured charge, while for hydrogen and helium isotopes Z_i is assumed to be exactly 1 and 2, respectively. The symmetry of the distribution around the beam charge shows that indeed no contamination from single electrons is present in the sample.

Peripheral nuclear events

Peripheral nuclear events in some cases exhibit topologies similar to EMDs. Confusion may arise in grazing collisions involving peripheral nucleons of both interacting nuclei. The projectile nucleus may receive a small excitation and disintegrate

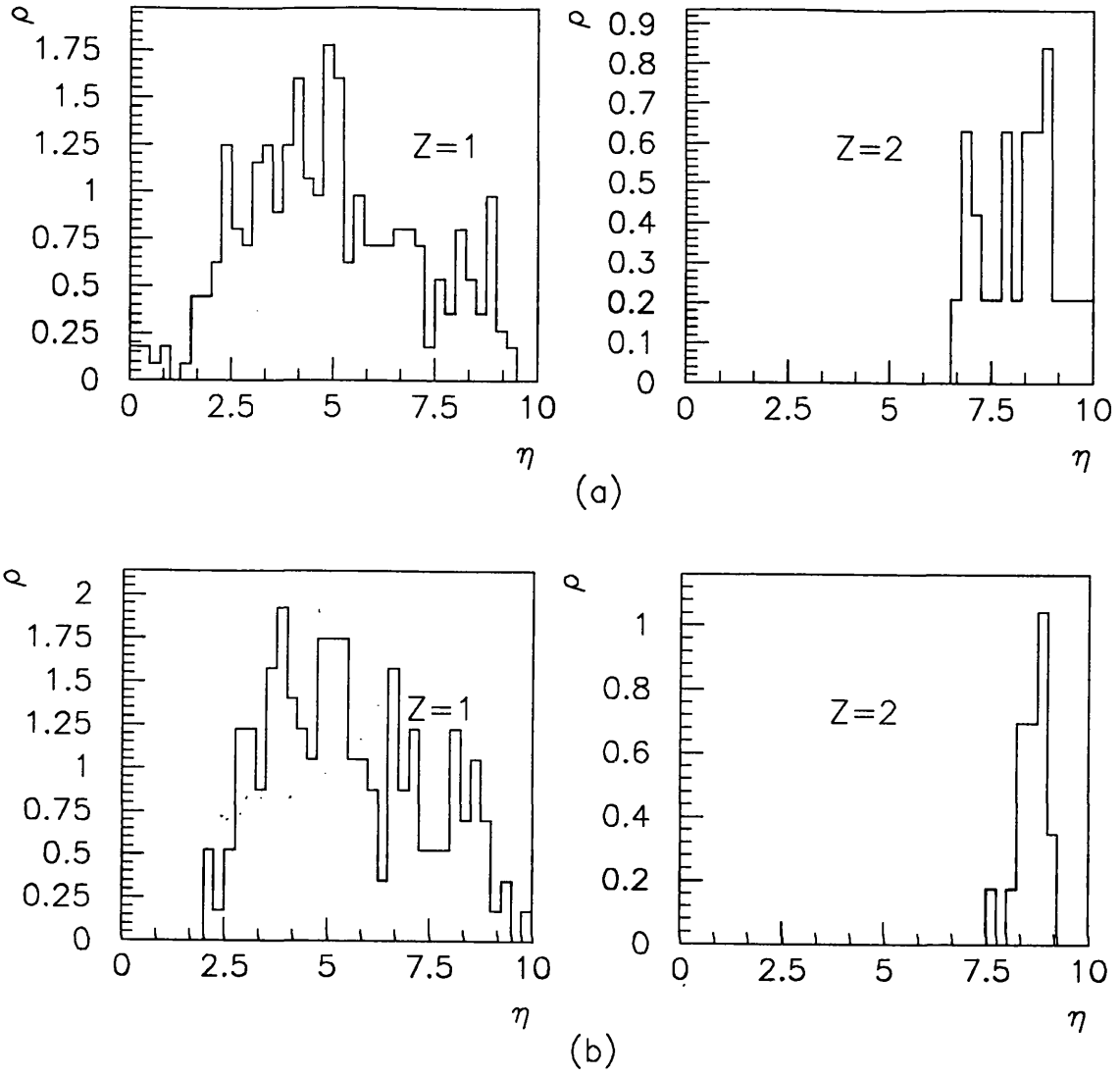

Figure 5.4: *Normalized pseudorapidity distribution($\rho = N_{ev}^{-1} dN/d\eta$) of shower and Z=2 particles in the subsamples of (a) $^{16}O(6 \leq N_s \leq 10)$ and (b) $^{32}S(6 \leq N_s \leq 12)$ peripheral nuclear interactions.*

in exactly the same way as an EMD candidate, depending on whether minimum ionizing tracks or target evaporation prongs are produced. Therefore, each EMD candidate has been carefully scanned upstream and downstream of the probable interaction point in order to check for the presence of previously undetected minimum ionization prongs at wide angles or evaporation fragments from the target.

In order to determine the number of peripheral nuclear collisions simulating an EMD event, we considered interactions where a small number of minimum ionizing particles were observed($6 \leq N_s \leq 10$ for ^{16}O and $6 \leq N_s \leq 12$ for ^{32}S). Fig. 5.4 shows the pseudorapidity(η) distribution of the shower and Z=2 particles of a sample of these events. The heaviest fragments with $Z \geq 3$ are not included because all

angles are measured relative to them, and they are thus assumed to have θ=0 or maximum pseudorapidity. The contribution of the spectator fragments with Z=2 at high pseudorapidities ($\eta \geq 6.5$) is evident. The small peak due to spectator protons($\eta \geq 7.0$) is preceded by a larger and broader distribution of produced pions.

The samples of ^{16}O and ^{32}S peripheral events were each divided into two categories: those interactions with target evaporation($N_h \geq 1$) and without(N_h=0). It is found that the ratio between events with N_h=0 and $N_h \geq 1$ is almost constant as a function of N_s^+, where N_s^+ is the number of minimum ionization tracks outside a cone of 5 mrad to the beam. This means that we can estimate the number of spurious events(N_h=0 and N_s^+=0) by taking the number of events with evaporation prongs $N_h \geq 1$ but N_s^+=0 and scaling it to represent the contribution of the total sample. The scale factor is the fraction of events with N_h=0 among those with N_s=6-10 for ^{16}O and 6-12 for ^{32}S. The details of the calculation are shown in Table 5.3. The estimated numbers of spurious events are 16 $\pm$ 6 in the first

Table 5.3: *Estimate of numbers of peripheral nuclear interactions exhibiting topologies of EMD's.*

Sample	^{16}O(1st scanning)		^{32}S	
	Total	Analysed	Total	Analysed
Nuclear Interactions	2925	920	2319	609
N_h >0,θ < 5 mrad		7		6
N_h >0,N_s=6-10*	297		245	
N_h=0,N_s=6-10*	210		211	
Nuclear interactions stimulating EMD's	7x(2925/920)(210/297)=16$\pm$6		6x(2319/609)(211/245)=20$\pm$8	

*N_s=6-12 for the sulphur sample.

scanning sample of ^{16}O and 20 $\pm$ 8 in the ^{32}S sample. However the second scanning

of the ^{16}O sample was focused on the search for EMDs, and details of the nuclear interactions were not recorded. The corresponding number of spurious events can be evaluated by scaling the number of spurious events in the first scanning to the second scanning sample, i.e., 16x(4218/2925)=23±9. Therefore, the estimated number of spurious events in the combined ^{16}O sample is 39±14.

It has been shown in sec. 4.3.3 that there is a strong correlation between the number of target participants(N_h) and the number of minimum ionization particles produced(N_s)[116,120]. However, at small N_h and N_s, this correlation is expected to be weak. As a result, we estimated the distribution of fraction of spurious events simulating EMDs as a function of energy and topology from subsamples of events with $N_h > 0$ and $N_s \leq 6$ outside θ=5 mrad, considering the tracks within θ=5 mrad as if they were the only projectile fragments. In Table 5.4, the energy was calculated in the same way as for genuine EMDs. It was not possible to

Table 5.4: *Fractions of events simulating projectile EMDs($N_h > 0$ and $N_s \leq 6$ outside θ=5 mrad)*

Break-up mode	^{16}O Energy(MeV)				Fraction	^{32}S Energy(MeV)				Fraction
	Total	0-150	>150	(>500)	(%)	Total	0-150	>150	(>500)	(%)
f	16	not measurable				9	not measurable			
fH	15	9	6	(1)	24	9	5	4	(1)	28
fHH	17	7	10	(7)	27	8	3	5	(4)	25
fHe	2	2	-	-	3	1	1	-	-	3
fHeH	3	2	1	(1)	5	-	-	-	-	-
f3H	6	2	4	(3)	10	6	3	3	(2)	19
others	19	11	8	(4)	31	8	1	7	(5)	25
Total	78					41				

compute the kinetic energy of the particular case where only a single fragment was observed. The analogous EMDs cannot be detected because they would only involve the emission of neutrons. In these background events, the emission of a

single H isotope, unlike the genuine EMDs, is no longer the dominant mode of break-up. It is clear that the fraction of such spurious events with higher energies is considerably larger, and there is also a rise in this fraction amongst complex channels.

Table 5.5 shows how the spurious events due to peripheral nuclear interactions

Table 5.5: *Estimated numbers of spurious events due to peripheral nuclear interactions in the EMD sample*

Break-up mode	^{16}O Energy(MeV)			^{32}S Energy(MeV)		
	0-150	>150	(>500)	0-150	>150	(>500)
fH	5.7	3.8	(0.6)	2.8	2.3	(0.6)
fHH	4.4	6.3	(4.4)	1.7	2.8	(2.2)
fHe	1.3	-	-	0.5	-	-
fHeH	1.3	0.6	(0.6)	-	-	-
f3H	1.3	2.5	(1.9)	1.7	1.7	(1.1)
others	6.9	5.0	(2.5)	0.6	4.0	(2.9)
Total	20.9	18.2	(10.0)	7.3	10.7	(6.8)

are shared among categories of different energies and break-up modes. For the category of E=0-150 MeV, the average contamination is small(2 to 3 %), while the fraction of background events increases to $\approx$ 20 % and $\approx$ 50 % for $E >$ 150 MeV and $E >$ 500 MeV respectively. In addition, one of the differences between this background sample and the one from genuine EMDs is that the proportion of higher energy events does not necessarily increase with increasing multiplicity in the final state. Unlike the true EMD sample, the fractions of events with the emission of two hydrogen isotopes as well as that with the emission of one He isotope are roughly the same for both ^{16}O and ^{32}S.

Loss of Events

A projectile EMD may be lost or misidentified if it is shortly followed by a nuclear interaction or by an secondary EMD that occurs before all the outgoing fragments are resolved. The number of lost or misidentified events depends on the particular channel considered and the angular distribution of the outgoing fragments. It is unlikely that a charge measurement can clarify the situation since the presence of other close tracks and the short path make it difficult for an accurate measurement to be made. Instead we have assumed that a projectile EMD would not have been detected if the secondary interaction occurred when the relative distance of the outgoing tracks, perpendicular to the beam direction, lies within an ellipse of semi-axes Δy=0.5 μm in the plane parallel to the emulsion surface and Δz= 1.5 μm in the perpendicular plane, for the oxygen sample. Due to the higher density of δ-rays, these quantities were increased to 1.0 and 3.0 μm, respectively, for the sulphur sample. The contribution of the losses has been estimated from the angular distribution of the outgoing fragments in the various channels by estimating the total *unseen* path length and by dividing it by the combined mean free path λ^* of the fragments involved where

$$\frac{1}{\lambda^*} = \sum_i \frac{1}{\lambda_i} \ . \tag{5.1.5}$$

Nuclear interaction and projectile EMD mean free paths of various fragments have been taken or interpolated from those shown in Fig. 4.1, Table 4.1 and 5.1. Most of the lost events are those with very small opening angles or small E and therefore the events involving only two fragments in the final state. This effect is relatively smaller for more complex EMDs where it often causes a misidentification rather than a loss.

The results of these calculations, both loss and misidentification, are included in the correction of the final sample. Table 5.6 shows the raw and corrected data for the oxygen and sulphur samples in the lower energy range $E < 150$ MeV. The contribution of losses and gains in the oxygen sample are similar, and therefore the overall effect is small. However, in the sulphur sample, the number of lost events is much more than those gained from EMD misidentification and peripheral nuclear interactions simulating EMDs. The net rate of loss is about 4 %.

Table 5.6: *Raw and corrected data for projectile EMD's with E < 150 MeV*

Channel	Raw data	Lost nuclear event	Lost EMD misid.	Gained EMD misid.	Gained nuclear periph.	Total corrected data
$^{16}O \rightarrow$						
Np	503	11.9	1.0	4.3	5.7	505.9
C2p	109	1.8	3.2	0.7	4.4	108.9
Cα	85	3.8	0.5	0.2	1.3	87.8
Bαp	29	0.9	1.3	0.2	1.3	29.7
B3p	5	0.3	0.3	0.3	1.3	4.0
Others	90	3.1	1.6	1.6	6.9	86.2
Total	821	29.7		28.2		822.5
$^{32}S \rightarrow$						
Pp	251	13.7	1.9	5.9	2.8	257.9+24*
Si2p	104	4.9	6.0	1.5	1.7	111.7
Siα	27	2.8	0.4	0.1	0.5	29.6
Alαp	15	0.7	1.4	0.3	-	16.8
Al3p	10	0.7	0.8	1.1	1.7	8.7
Others	21	1.5	1.0	1.6	0.6	21.3
Total	428	35.8		17.8		446.0+24

*Scanning losses

In addition to the loss of events due to early secondary interactions, another source of lost events is scanning losses. Fig. 5.5 shows plots of the relative separation angles $\Delta\alpha$ and $\Delta\delta$ for the channels $^{16}O \rightarrow$ NH and $^{32}S \rightarrow$ PH. Both of these channels involve the emission of a single minimum ionization track and a heavy fragment differing by one unit of charge from the beam. These are the events expected to be most seriously affected by scanning losses. In the oxygen sample, different sectors of the plot are found to be equally populated within statistical errors, while in the sulphur sample a (9 ± 3) % loss of events, corresponding to 24 ± 8 events, is found to occur in planes steeply inclined to the plane of the emulsions. This loss is a sign of non-uniform scanning efficiency and is expected in the sulphur sample because phosphorus tracks have a much higher δ-density than nitrogen tracks(in the ratio 4.6:1). This makes it difficult to observe a minimum-ionizing track when it is almost superimposed on the ion track. Furthermore the

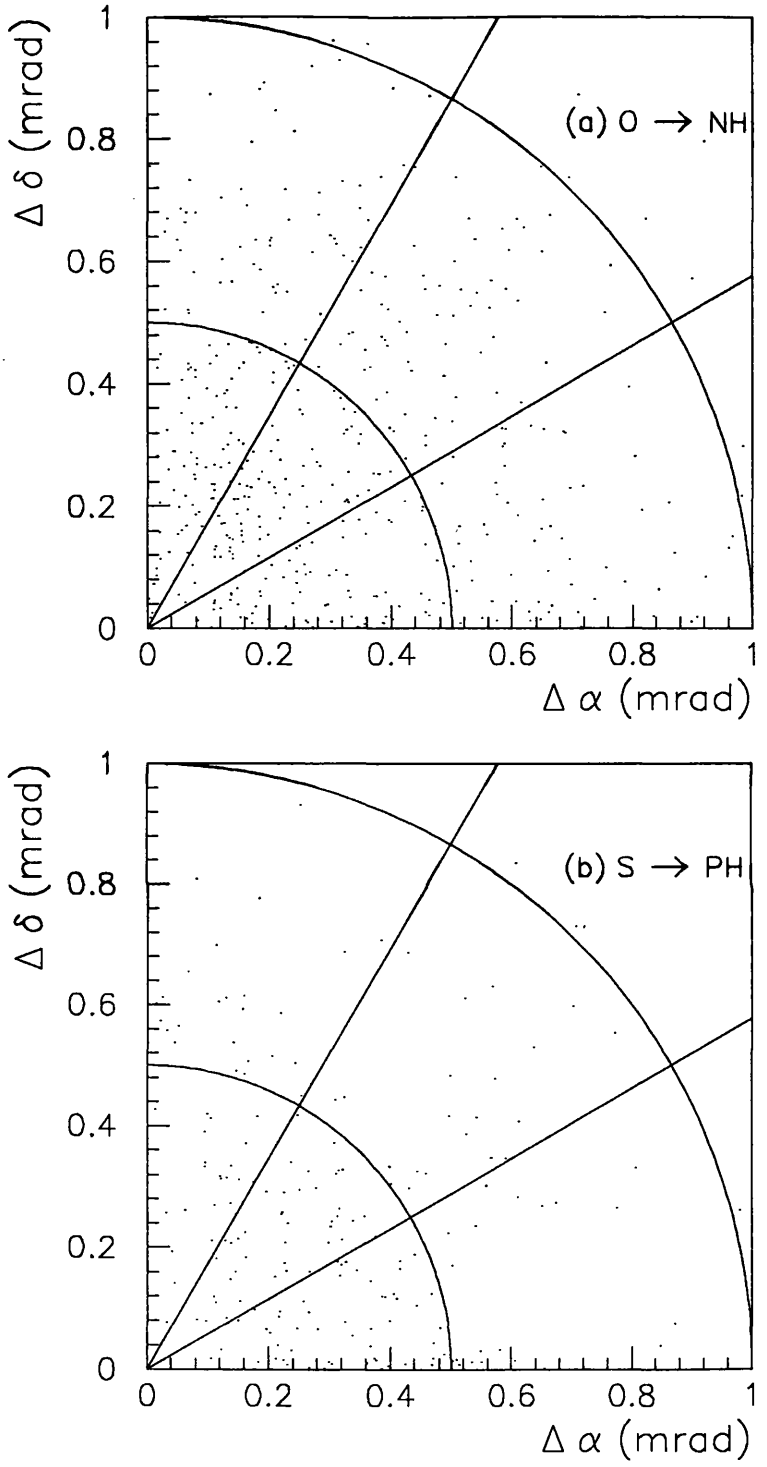

Figure 5.5: *Plots of the vertical($\Delta\delta$) versus the horizontal($\Delta\alpha$) component of the relative separation angles between the $Z=1$ track and the heavier fragment in the channels (a)$O \rightarrow NH$ and (b) $S \rightarrow PH$, both at 200 A GeV.*

relative change in δ-ray density from sulphur to phosphorus is much harder to recognize than from oxygen to nitrogen.

Events in other EMD break-up modes, involving a higher number of outgoing fragments(e.g. O $\rightarrow$ CHH, S $\rightarrow$ MgHeHH, etc.), or those with a much larger change in δ-ray density from the primary beam to the heaviest fragment(e.g. O $\rightarrow$ CHe or S $\rightarrow$ SiHe) can be detected much more easily. Plots similar to those in Fig. 5.5 for other channels show that the corresponding scanning efficiencies are close to 100 %.

5.2 Analysis of Single Channels

5.2.1 General features

Comparing the two sets of data, oxygen and sulphur, shown in Table 5.2 and 5.6 and Fig. 5.1 and 5.2, one will note their similarities as well as their differences. In both samples, the emission of a hydrogen isotope is the dominant process, occurring at a rate just over 50 % and exhibiting similar energy spectra. On the other hand, the energy spectra for the emission of a single helium isotope are similar in both samples, but the production rate for the sulphur sample is considerably higher than that of the oxygen sample. Moreover, the production rates and energy spectra of the channel with the emission of two hydrogen isotopes are different in the two samples. The energy spectra of the complex channels are much harder in the sulphur sample than in the oxygen one.

The differences between the samples can be understood in terms of the different nature of the projectiles and the different Coulomb barriers. The binding energy of oxygen is 128 MeV, and there are 21 possible channels of dissociation of which 16 have been observed. On the other hand, sulphur has a binding energy of 272 MeV and can disintegrate into more than 200 channels. Only 28 channels have been observed. Table 5.7 displays the separation energies of various combinations of fragments from oxygen and sulphur, as deduced from atomic mass excesses[140]. These energies are the minimum threshold energies for the photodisintegration of

Table 5.7: *Separation energies(B) for the various channels of dissociation. Heaviest fragment with $Z \geq 3$ is not shown.*

Projectile fragments		B(MeV)	
		^{16}O	^{32}S
	n	15.6	15.0
	nn	28.9	28.1
	p	12.1	8.9
	pn	23.0	21.2
	pp	22.3	16.1
	ppn	30.5	26.8
	^{3}He	22.8	19.1
	α	7.2	6.9
	αn	25.9	24.1
	αp	23.1	18.5
	αpn	34.6	31.6
	3p3n	62.9	59.9
	α2p2n	42.8	45.2
	4p4n	71.1	73.5
	2αpn	39.0	38.6
	α3p3n	67.3	69.3
^{16}O$\rightarrow$	4α	14.4	
	3α2p2n	42.7	
	2α4p4n	71.0	
^{32}S$\rightarrow$	^{22}Na^{6}Li2p2n		70.8
	^{20}Ne2α2p2n		54.5

^{16}O or ^{32}S into the corresponding fragments. The separation energy increases with the multiplicity and complexity of the fragments with exceptions like $^{16}O \rightarrow 4\alpha$. In the sulphur sample, the complex channels, requiring higher energy thresholds, are more suppressed than in the oxygen one because of the fall-off of the photon spectrum at high energies.

Some of the assumptions that we have made so far are clearly not valid in all circumstances. For example, in the channels involving the emission of a single minimum-ionizing particle assumed to be a proton, (sec. 5.1.3)some contributions from the emission of one or more neutrons along with the proton could be present. Beside not being able to detect neutral particles, this experiment is also not capable of distinguishing different isotopic species. Thus, some of the minimum-ionizing particles assumed to be protons could also be deuterons or even tritons.

5.2.2 Channels involving one nucleon

Assuming that the EMD process has been correctly identified and that the fragments proceed in the forward direction with the energies per nucleon possessed by the original projectile nucleus, the measured angles relate directly to the transverse momenta p_T(sec. 5.1.3) of the fragments following dissociation. The p_T distribution of the protons from the ^{15}Np sample is shown in Fig. 5.6. It has been illustrated in sec. 5.1.3 how the kinetic energy above the threshold is estimated from p_T(eq. 5.1.1). Assuming the nitrogen remains in its ground state, the sum of this kinetic energy and the threshold energy for emission of one proton (Table 5.7) gives the resonance energy. From Figs. 5.1 and 5.6 it is noted that the great majority of the ^{15}Np events may be ascribed to absorption in the giant resonance region (21< E <27 MeV)[141]. The reaction $^{16}O(\gamma,p)^{15}N^*$ occurs mainly to the ^{15}N ground state and 6.32 MeV excited state[142]. One would expect protons in the rest frame of the oxygen nucleus centred around momentum values $p^* = 150$ and 105 MeV/c respectively, and for isotropic emission[49]

$$\langle p_T \rangle = \frac{1}{4}\pi p^* \quad . \tag{5.2.1}$$

Using eq. 5.2.1, the $\langle p_T \rangle$ for the two states are 118 and 82 MeV/c respectively. The observed $\langle p_T \rangle$ in Fig. 5.6 is 102 MeV/c and therefore agrees with the above prediction.

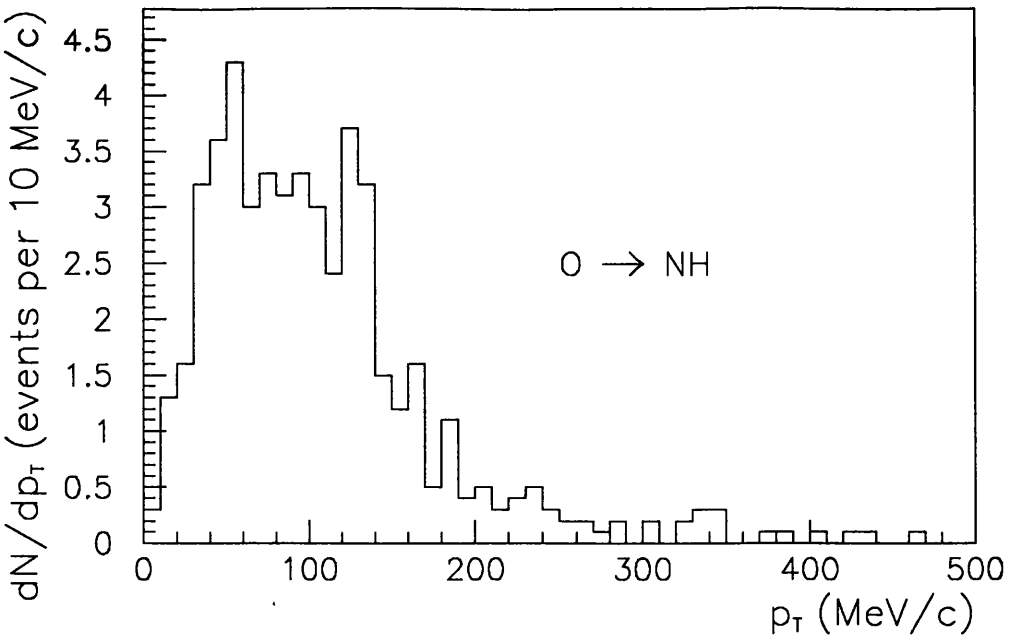

Figure 5.6: *Transverse momentum(p_T) distributions of the protons from the ^{15}NH sample, derived from the separation angles.*

The same analysis can be performed with the channel $^{32}S \rightarrow {}^{31}Pp$. Wyckoff *et al.* found that the giant dipole resonance for ^{32}S occurs in the range $18 < E < 23$ MeV. Fig. 5.7 shows the transverse momentum p_T distributions of protons in the breakup mode Pp. From Fig.s 5.2 and 5.7, we conclude that the majority of the events in this channel may be attributed to the absorption in the region of giant dipole resonance.

5.2.3 Channels involving two nucleons

It is observed in Fig. 5.1 and 5.2 the energy spectra of the channels involving the emission of two hydrogen isotopes are considerably harder and more wide-spread than the channels where a single proton is emitted. There may exist a relation between the energies and the angle of the two protons. In Fig. 5.8 we plot the azimuthal angle φ, computed in the centre of momentum of the exited nucleus, as a function of the estimated kinetic energy above the threshold for $^{16}O \rightarrow$ CHH or $^{32}S \rightarrow$ SiHH, for the oxygen and sulphur sample respectively. It is noted that no correlation exists in the present data within statistical error in any energy range.

In addition, the energies of the emitted protons are uncorrelated. It appears

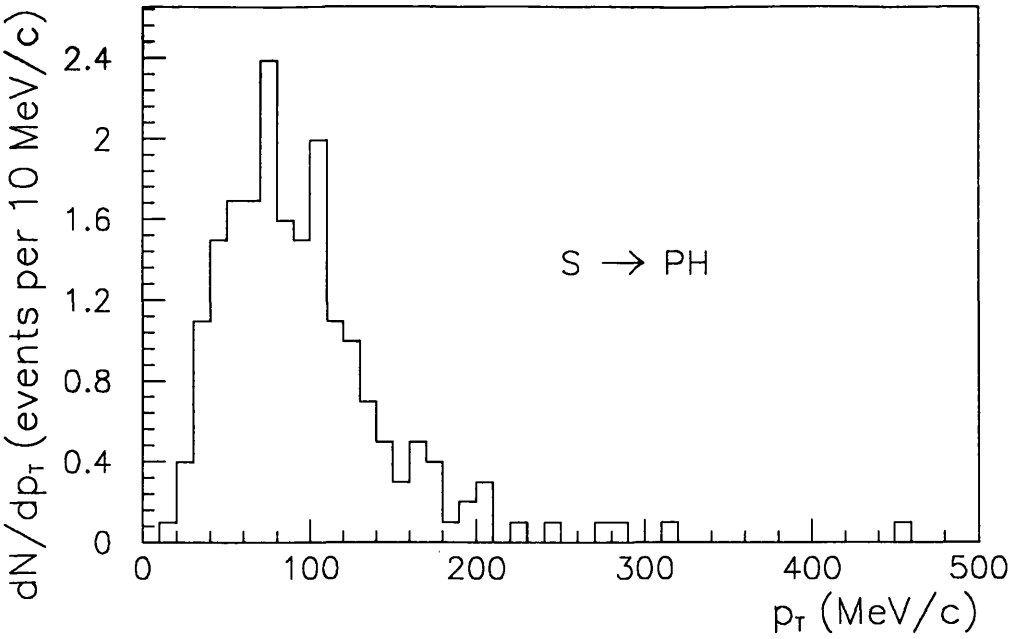

Figure 5.7: *Transverse momentum(p_T) distributions of the protons from a sub-sample of the ^{31}PH channel, derived from the separation angles.*

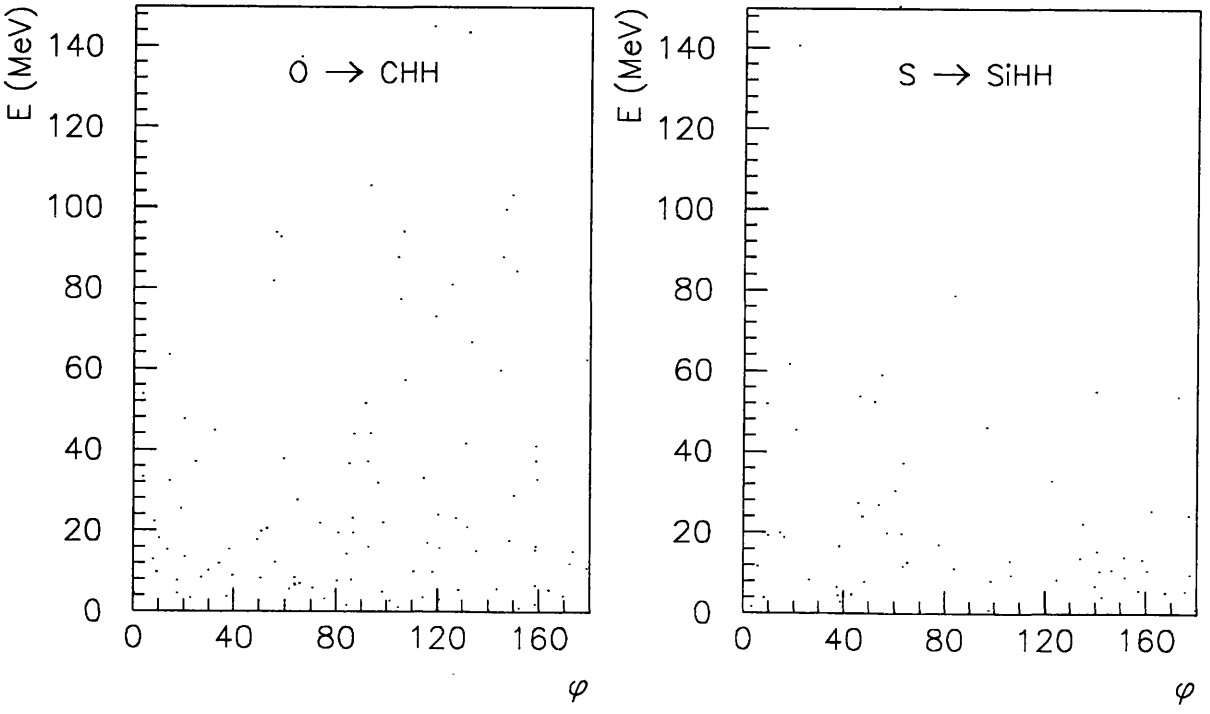

Figure 5.8: *Azimuthal angle φ between the two hydrogen isotopes as a function of the excitation energy above threshold for (a) $^{16}O \rightarrow$ CHH and(b) $^{32}S \rightarrow$ SiHH*

that one of the protons, especially in the subsamples of events with $E > 35$ MeV, is particularly energetic, and the other one behaves as if it were emitted in the channels with a single proton(Fig. 5.9). If we take each individual CHH or SiHH

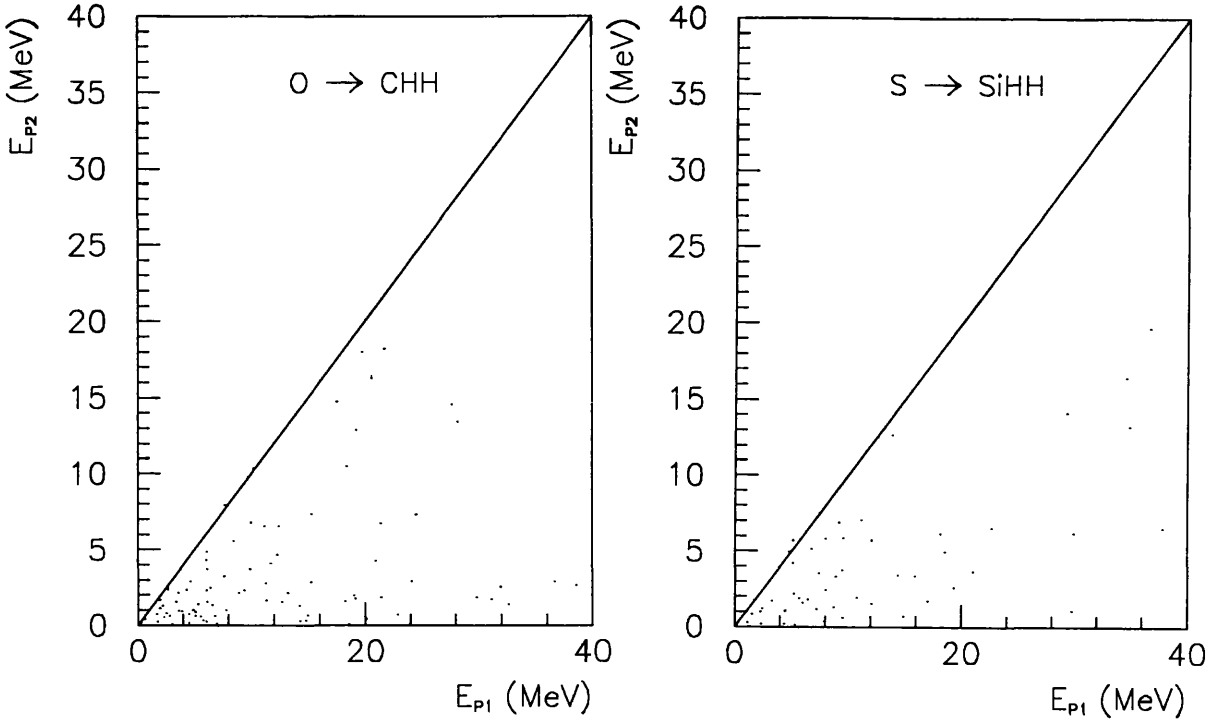

Figure 5.9: *Scatter plot of the energies of the two protons emitted in the channel (a)$^{16}O\rightarrow$ CHH and (b)$^{32}S\rightarrow$ SiHH. E_{p1} is the energy of the 'harder' proton, while E_{p2} is the energy of the 'softer' proton.*

event and treat it like a NH or PH pair, each time neglecting one proton, the energy spectra computed in this way(each event is counted as a half event) are very similar to the corresponding NH and PH spectra, as shown in Fig. 5.10 and 5.11.

In Fig. 5.12 distributions of the azimuthal angles, computed in the centre of momentum of the excited nucleus, between the protons and the carbon fragment are shown. The sign of the angles is arbitrary. It is observed that the more energetic proton, as shown in Fig. 5.12(a), is emitted essentially at 180° with respect to the carbon fragment, whereas the other outgoing proton is emitted almost isotropically. This is what one would expect of a two-stage process in which a nucleus absorbs a photon and emits a nucleon with high-energy and the recoil is taken up by the nucleus. The recoiled nucleus is left in an excited state which later deexcites with the emission of another nucleon. Since the velocity

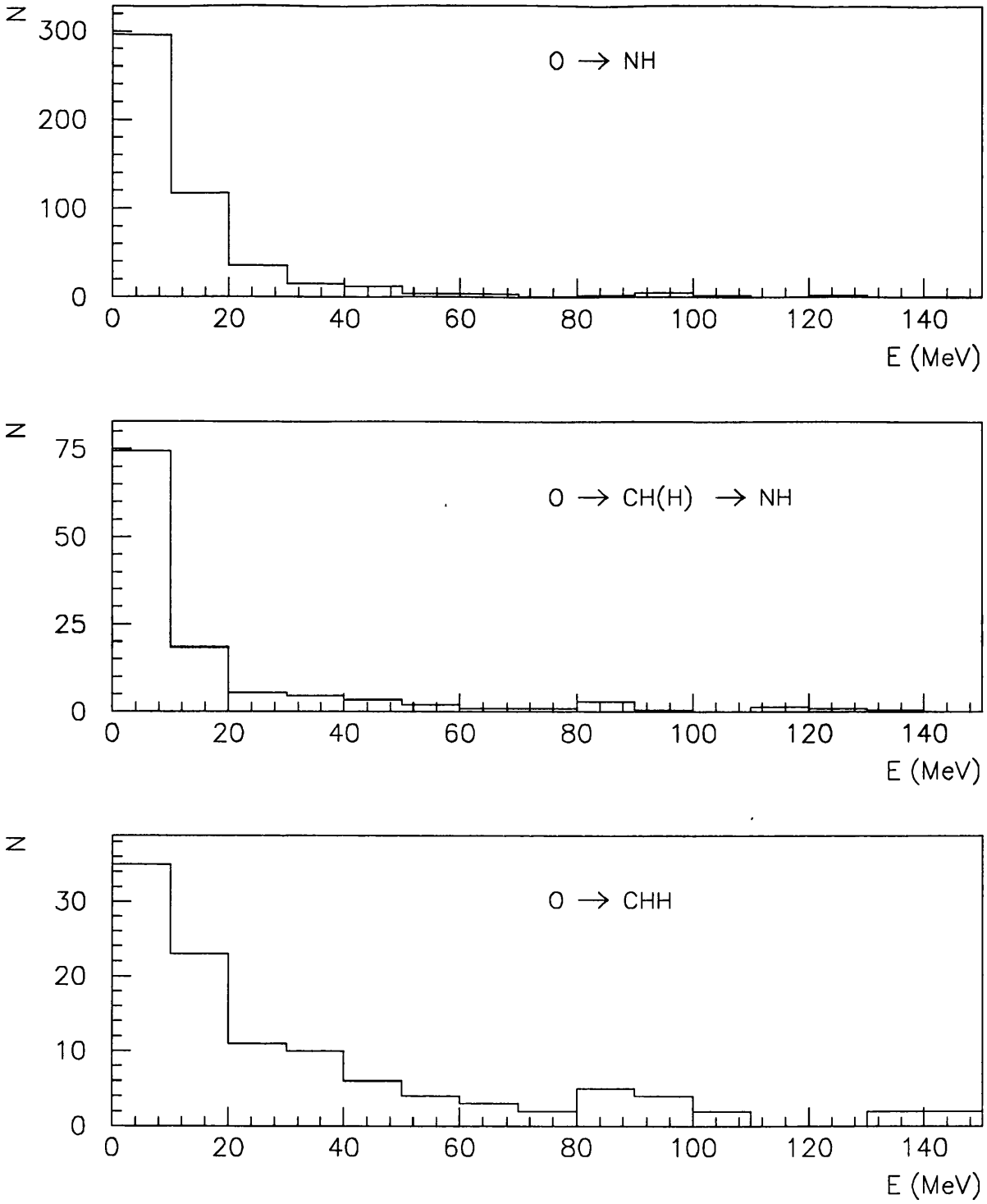

Figure 5.10: *Energy spectra from events in the channel $^{16}O \rightarrow$ CHH EMD computed by neglecting one proton, compared with the the original CHH and with the true NH-spectra.*

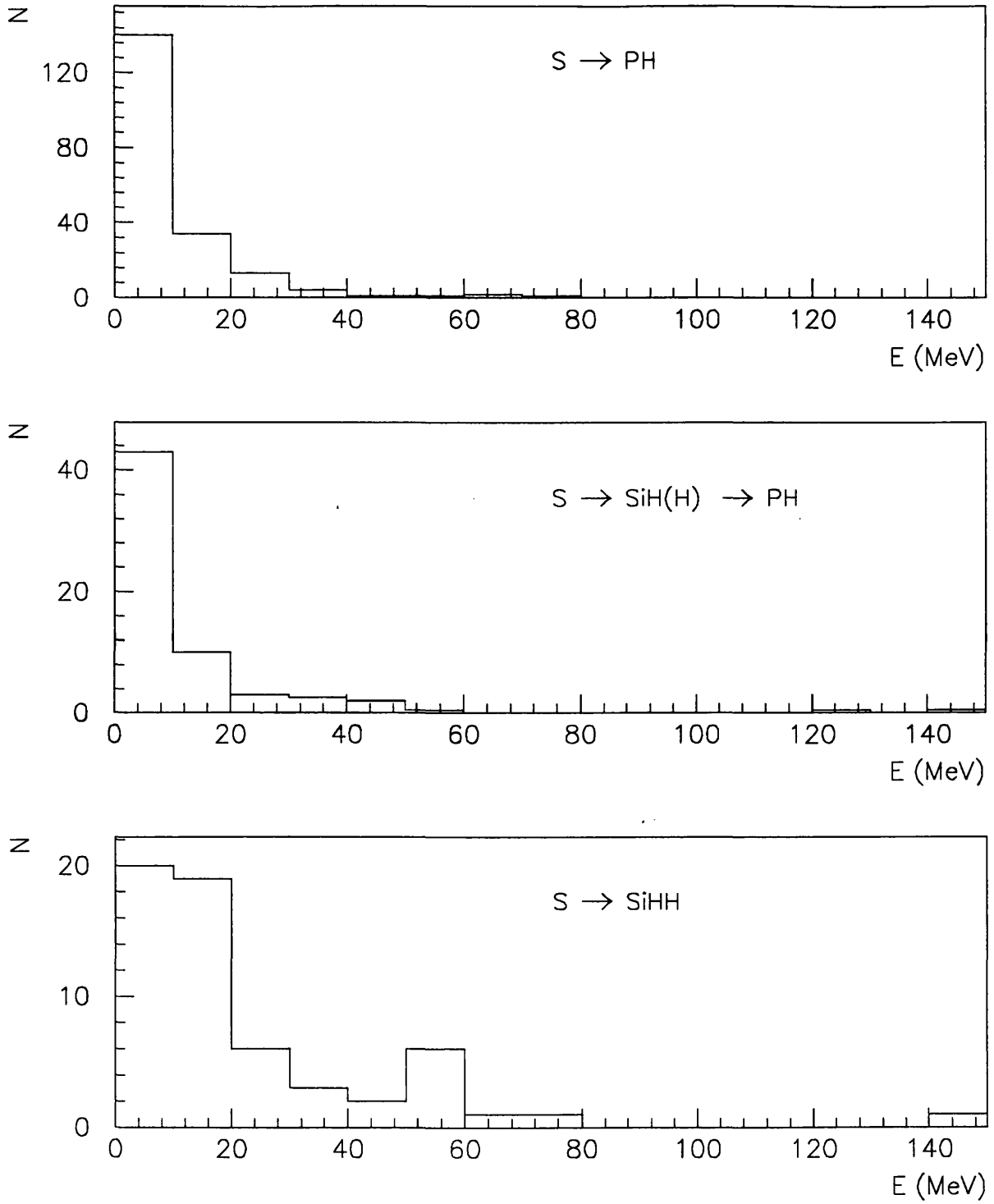

Figure 5.11: *Energy spectra from events in the channel $^{32}S \rightarrow$ SiHH EMD computed by neglecting one proton, compared with the the original SiHH and with the true PH-spectra.*

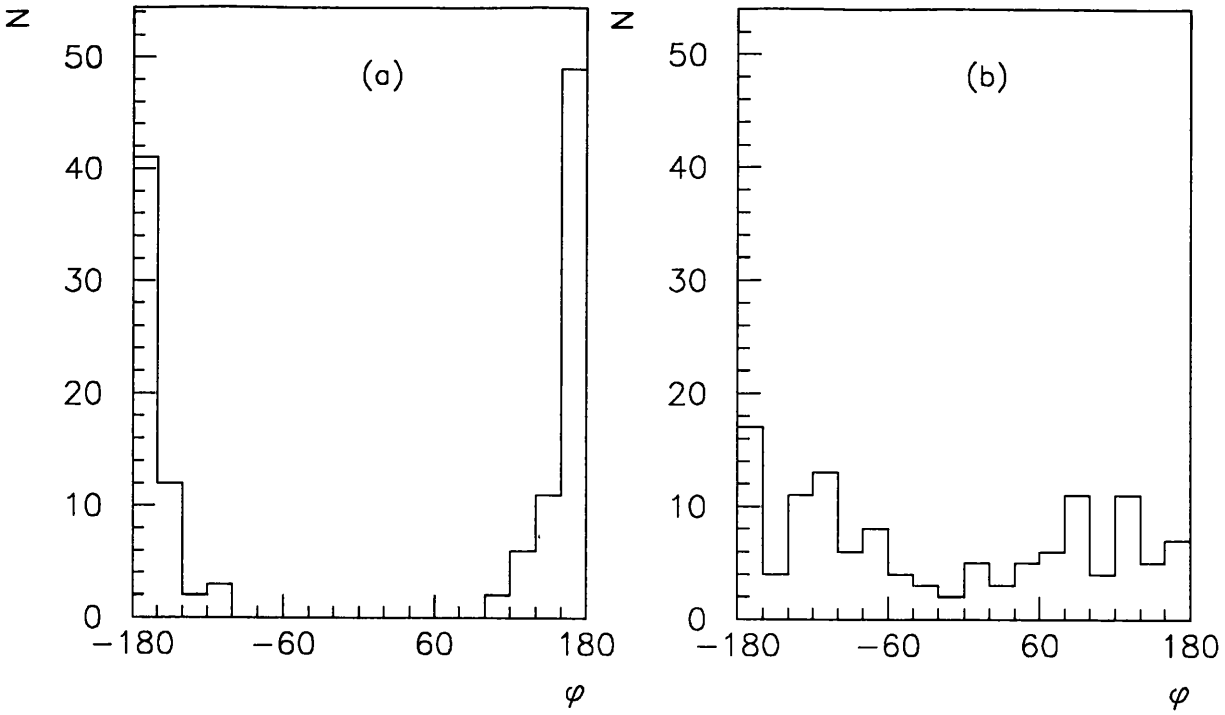

Figure 5.12: *Azimuthal angle ϕ between the carbon fragment and the (a) 'harder' proton or (b) 'softer' proton in the EMD channel $^{16}O\rightarrow$ CHH*

of the excited nucleus with respect to the c.m. system is small, the direction of emission of the second nucleon is almost unchanged when observed in the c.m. system. Isotropic emission of the second nucleon is observed. The azimuthal angle between the carbon fragment and the more energetic proton is almost 180°, and therefore the azimuthal angle between the two protons should also be uniformly distributed. This explains the uncorrelated emission of the protons in Fig. 5.1. In Fig. 5.13 a similar behaviour is observed in the distribution of the azimuthal angles between the silicon fragment and the protons, and it suggests that most of the events in the HH channel, in both oxygen and sulphur sample, originate from a two stage production process in which one nucleon is emitted at each stage.

The presence of events in the channels $^{16}O\rightarrow$ NH and $^{32}S\rightarrow$ PH, within the energy range where the quasi-deuteron mechanism is dominant, suggests that $^{16}O\rightarrow$ Npn and $^{32}S\rightarrow$ Ppn may be present. The energy thresholds(Table 5.7) for the reactions $^{16}O(\gamma,pn)^{14}N$ and $^{16}O(\gamma,pp)^{14}C$ are nearly equal(23.0 and 22.3 MeV, respectively), and one might expect a similar energy spectrum of the emitted nucleons. However, to subtract the normalized spectra of the HH channels from that

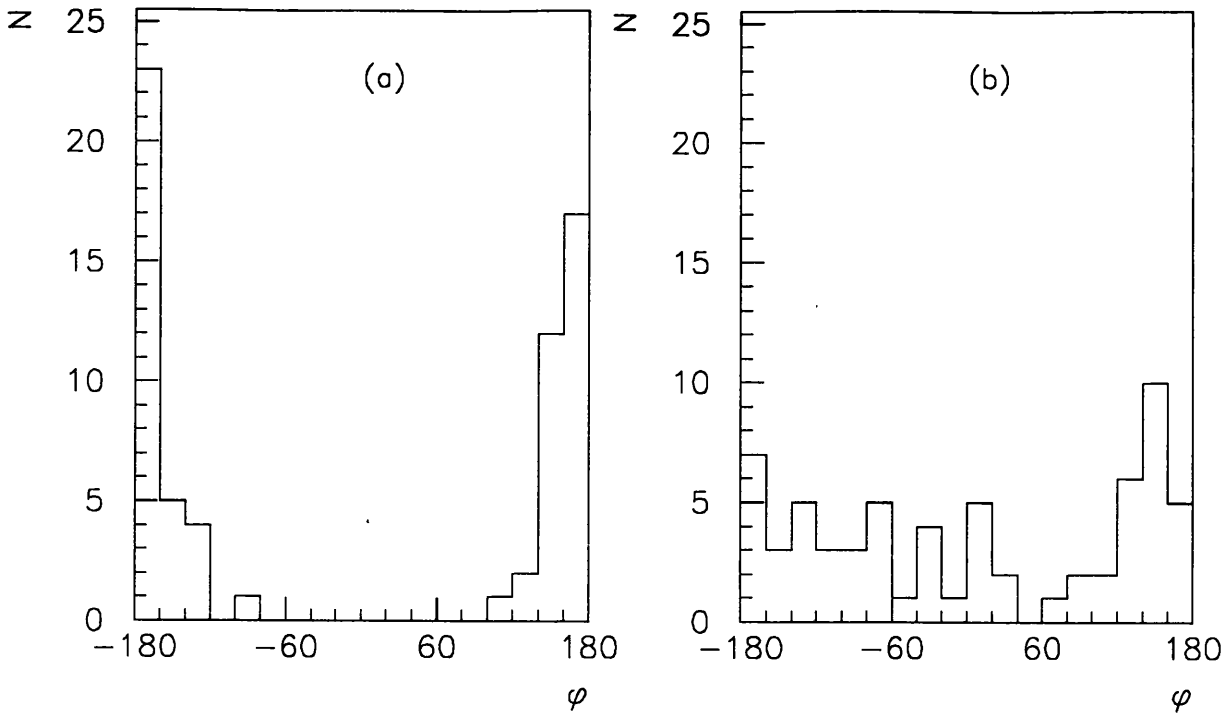

Figure 5.13: *Azimuthal angle ϕ between the silicon fragment and the (a) 'harder' proton or (b) 'softer' proton in the EMD channel $^{32}S\rightarrow$ SiHH*

of single-proton channels, based on the size of our sample, would be unreliable. In addition, if the above hypothesis is correct, most of the events in the HH channel are produced by a different mechanism from the quasi-deuteron process. We will for the moment ignore the pn contamination which will be shown to be small.

5.2.4 Integrated energy spectra and angular distributions

The integrated energy spectra for the most abundant channels are plotted in Fig. 5.14 in the low-energy region(<70 MeV) for the oxygen and sulphur samples. Since most of the BHeH events are in the low-energy region(Fig. 5.1), we have treated these events as ^{11}Bαp rather than as ^{10}Bαpn (sec. 5.1.3). All distributions exhibit exponential decrease with energy with anomalous tails at energies beyond 40 MeV. They resemble evaporation spectra, and the corresponding temperatures(T=8-12 MeV) for the H or He channel are very similar in both the oxygen and sulphur samples. Channels involving more than two fragments show higher values of the temperature.

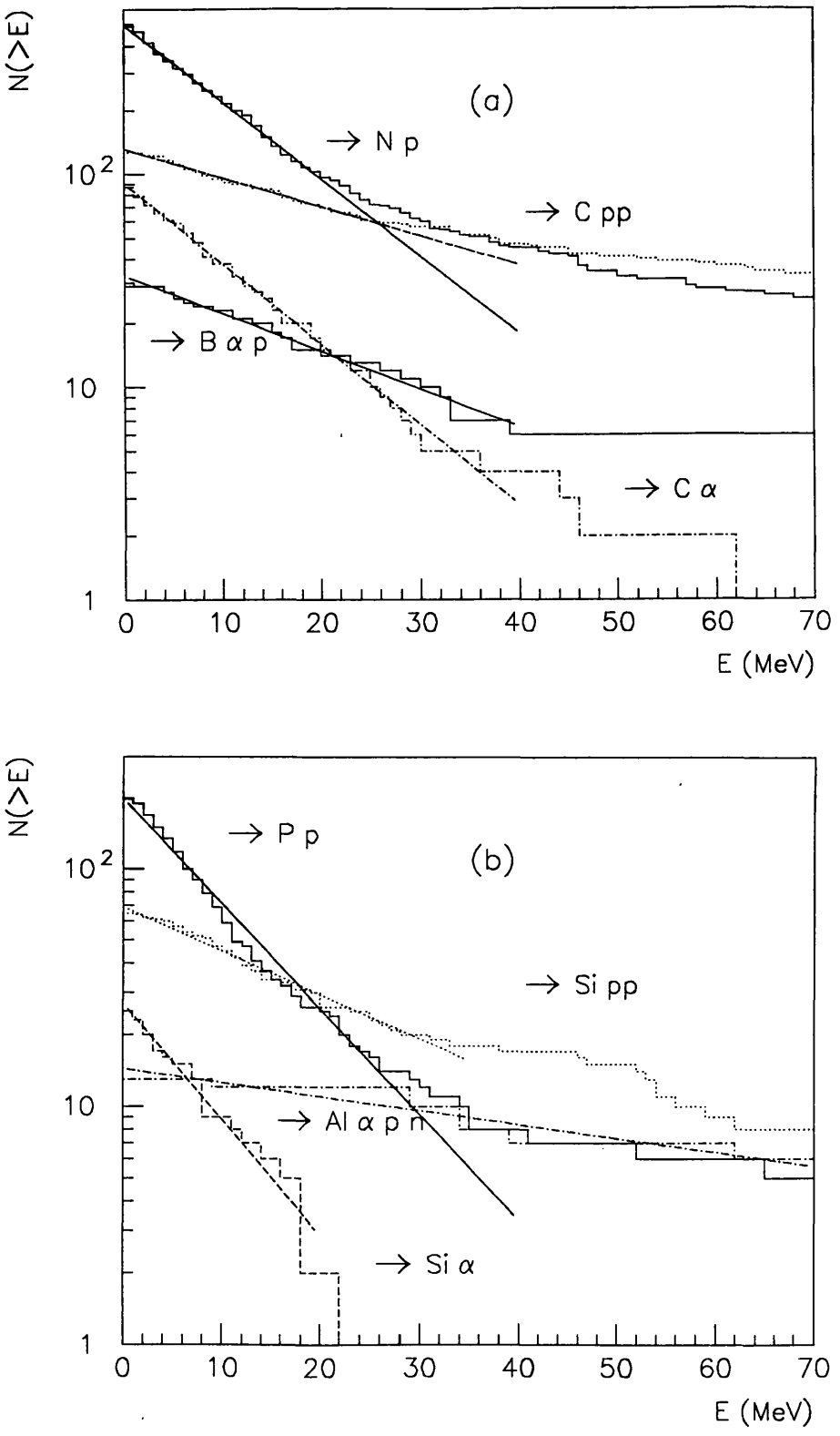

Figure 5.14: *Integrated Energy spectra of the most abundant channels in the EMD of 200 A GeV (a) ^{16}O and (b) ^{32}S.*

By fitting an exponential function up to a maximum energy cut E_1 to avoid any contribution of the anomalous tail, we obtained the inverse slopes(T) of the energy distributions for the different channels. The values of T are shown in Table 5.8. Both T and its error are determined by the least squares fit method. It is observed

Table 5.8: *Observed inverse slopes(T) of the energy distributions for the most abundant channels compared with separation energies(B) of the fragments. Fits to distributions of the form exp(-E/T) were performed up to E_1. T_0 is the value of T corrected for the c.m. angular distribution.*

		E_1(MeV)	T(MeV)	T_0(MeV)	T_0/B(MeV)
$^{16}O \rightarrow$	Np	20	12.0±0.4	10.7±0.4	0.88±0.03
	Cα	40	11.5±0.5	10.3±0.4	1.43±0.06
	Cpp	25	32.0±3.6	21.3±2.4	0.95±0.11
	Bαp	40	24.5±2.4	16.3±1.6	0.71±0.07
$^{32}S \rightarrow$	Pp	40	9.8±0.3	8.8±0.3	1.00±0.03
	Siα	20	8.9±1.1	7.9±0.9	1.15±0.14
	Sipp	30	22.6±1.9	15.0±1.3	0.93±0.08
	Alαpn	50	68.8±14.5	45.9±9.6	1.45±0.31

that the values of T when corrected for c.m. angular distribution(see below) are of the same order of magnitude as that of the separation energies for the respective channels. In addition, the values of T for channels of the sulphur sample are generally lower than the corresponding ones in the oxygen sample. This trend is also exhibited in the separation energies listed in Table 5.7.

Energy spectra reconstructed from the transverse momenta are distorted with respect to the original spectra, and the average value of the transverse energy thus obtained depends on the angular distribution. Fig. 5.15 shows the shape of the transverse energy spectra(dN/dE' versus E') for two-body events, reconstructed from a monochromatic spectrum(E^*) in the c.m. system, but with different angular distributions ranging from those peaked in the forward direction to those peaked at 90° to the beam. The lower energy region is seen to be particularly sensitive to the angular distribution. Therefore if the distribution is not isotropic, our estimate of the average energy will be biased.

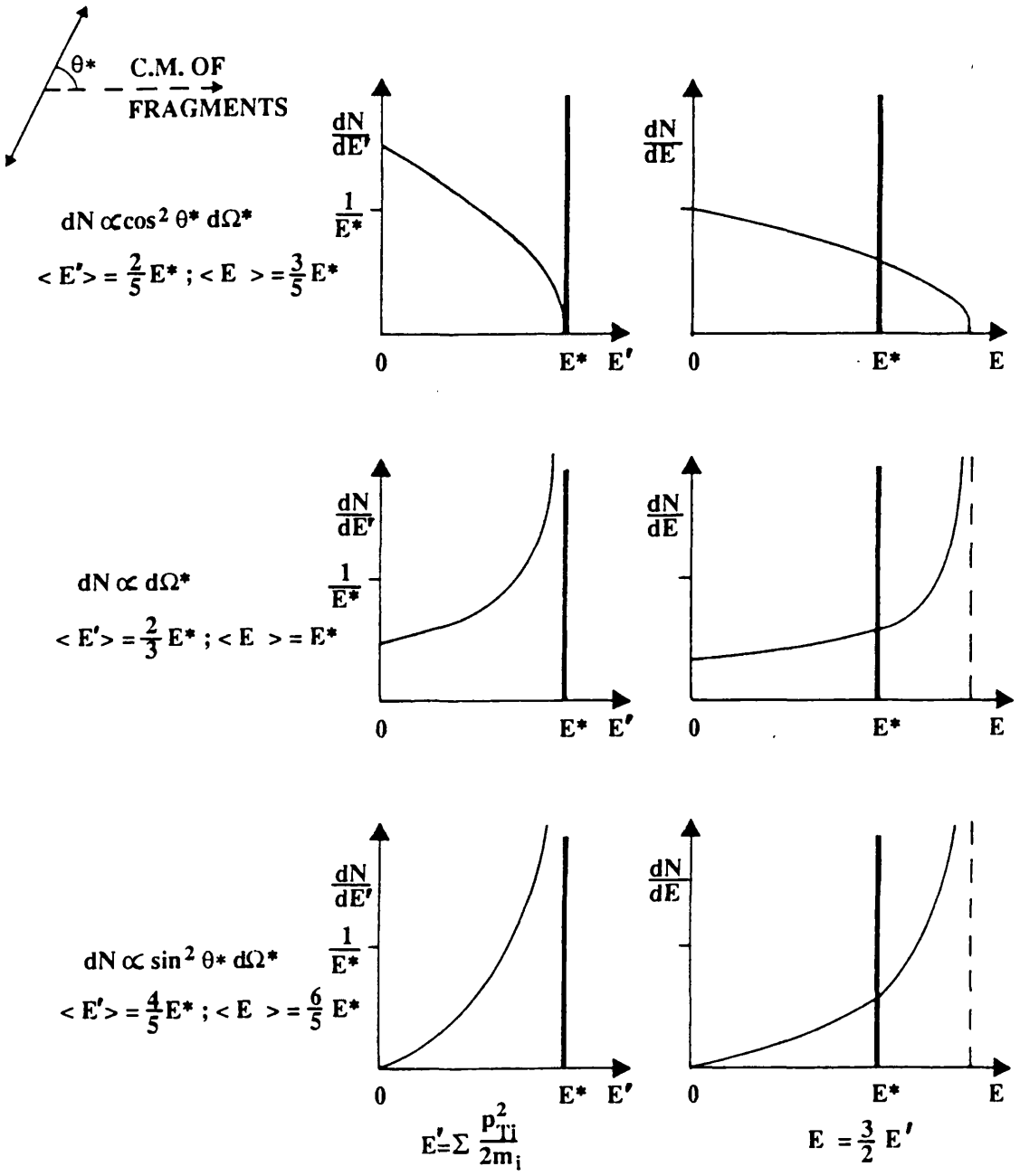

Figure 5.15: *Shape of two-body energy spectra reconstructed from transverse momenta with a monochromatic(E^*) spectrum in the c.m. system but different angular distributions of the outgoing fragments: E' is the 'transverse' energy; E is the total energy having assumed isotropy.*

Fig. 5.14 has shown that the energy distributions decrease exponentially, whereas Fig. 5.15 illustrates the effect of the angular distribution on the reconstructed energy spectra. Now, we calculate how an energy spectrum of the form

$$\frac{dN}{dE} = \begin{cases} T_0^{-1} exp[-(E - E_s)/T_0] & for E \geq E_s \\ 0 & for E < E_s, \end{cases} \tag{5.2.2}$$

in the c.m. system transforms in the laboratory frame when angular distributions shown in Fig. 5.15 are considered and the energy scale is adjusted assuming isotropy. Eq. 5.2.2 is a rough approximation to an evaporation spectrum with a sharp energy threshold E_s. Assuming the values T_0=7 MeV and E_s=3.5 MeV, we calculated the various distributions which are plotted in Fig. 5.16. For en-

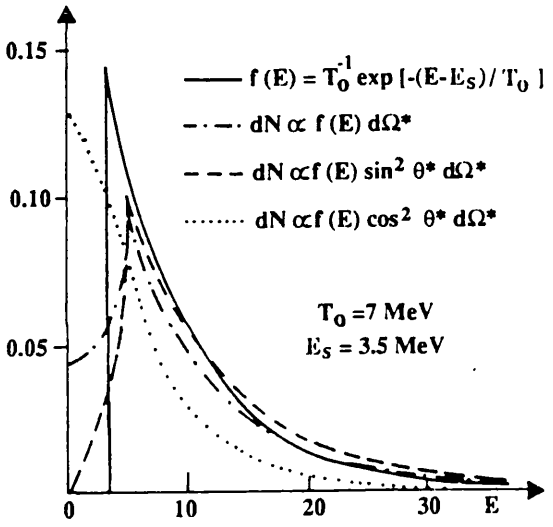

Figure 5.16: *Transformation of an exponentially decreasing energy spectrum in the c.m. system(full line) for different angular distributions and having assumed isotropy.*

ergies very much larger than T_0, all the distributions in the laboratory frame decrease exponentially with an inverse slope T=1.5T_0, while in the energy range $2E_s < E < 3T_0$, the slope is smaller with T=(1.05-1.2)T_0 and much closer to that of the c.m. distribution. For $E < E_s$, the distributions of Fig. 5.15 are reproduced.

In Fig. 5.17 we transformed, assuming isotropy, the c.m. energy spectrum of eq. 5.2.2 with T_0=9 MeV and fitted it to the experimental data of the channel O $\rightarrow$ Np for different values of E_s. It is found that E_s=1.5 MeV fits the experimental data best. Other two-body channels also exhibit similar trends.

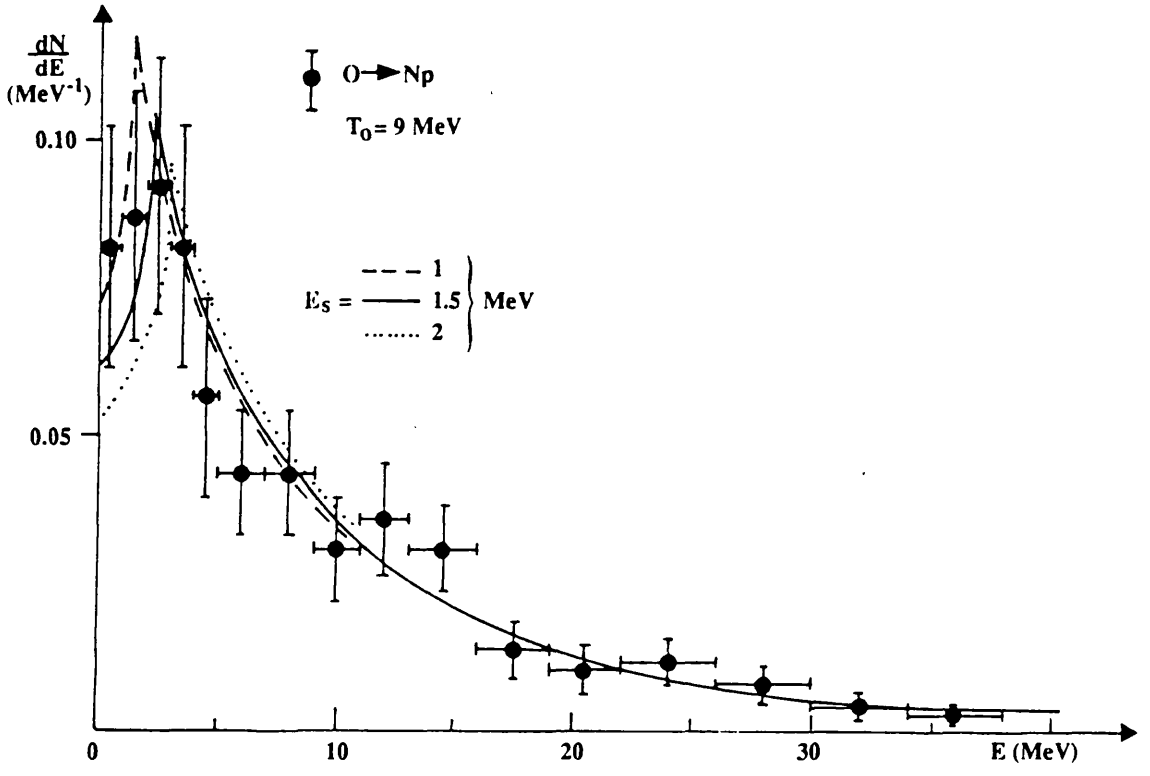

Figure 5.17: *Measured energy distribution of the $O \rightarrow Np$ sample compared with that transformed from equation 5.3.2 and isotropic emission.*

It is difficult to extract c.m. angular and energy distributions from the experimental data with the present statistics. Nonetheless, it has been shown that the hypothesis of isotropic emission in the c.m. system is a reasonable assumption. Moreover, we have reproduced the c.m. energy spectrum of the O $\rightarrow$ Np channel within statistical errors except in the distorted low-energy bins.

The corresponding values of T_0 for the more complex break-up channels in Table 5.8 are given by multiplying T by a factor of $\frac{2}{3}$.

5.3 EMD and Photoproduction cross-sections

5.3.1 Hadronic and EMD cross-sections on a silver target

Since emulsion is a medium composed of many kinds of atoms, a differential cross-section exists for every kind of interaction with each nuclear type. These cross-sections are not separately measurable due to the difficulty in identifying the target nucleus of a particular event. Instead the mean free path of the incident projectile is measured.

However, in order to compare our results with other high-energy heavy-ion data, we can estimate the absolute cross-sections on silver, the heaviest abundant constituent of the emulsions, from the observed mean free paths. Throughout this work we have ignored the presence of elements such as iodine or sulphur whose abundance is less than 1 % in emulsion.

The density of our emulsion is 3.60 ± 0.01 g/cm^3 which is about 6 % less than that of the standard emulsion[108]. Assuming the difference is entirely due to an increased water content, we estimated the density of silver to be $N = 93 \times 10^{20}$ Ag atoms/cm^3. The total hadronic cross-sections are calculated from the mean free paths in emulsion and from the number f of interactions on silver as a fraction of the total number of emulsion interactions[116]:

$$\sigma = \frac{f}{\lambda N} \ . \tag{5.3.1}$$

On the other hand, the projectile EMD cross-sections are computed in a similar manner, with f equal to the contribution of silver nuclei as a fraction of the total intensity of virtual photons. We have used the corrected values of the number of events, hence of the mean free paths, rather than those quoted in Table 5.1.

Table 5.9 lists the hadronic and projectile EMD cross-sections of the present experiment and data from experiments at the same energy[47,48,143]. In these

Table 5.9: *Pure nuclear and projectile EMD cross sections of ^{16}O and ^{32}S beam nuclei at 200 A GeV in Ag target, obtained in the present experiment and other experiments. $\sigma(\Delta Z > 0)$ is the total charge-changing cross section.*

	λ(mm)	f	σ(mb)	$\sigma(\Delta Z > 0)$(mb)	Refs.
Pure nuclear interactions					
O-Em.	120 ± 1	0.29	2588 ± 31		this exp.
O-Ag			2506 ± 47	2411 ± 63	[47]
S-Em.	92 ± 2	0.26	3023 ± 63		this exp.
S-Ag				2935 ± 100	[48]
S-Ag				3040 ± 120	[143]
Projectile EMDs					
O-Em.($E < 150$)	1046 ± 36	0.61		627 ± 22	this exp.
O-Em.(no cut)	949 ± 31	0.61		691 ± 23	this exp.
O-Ag				652 ± 60	[47]
S-Em.($E < 150$)	422 ± 19	0.61		1555 ± 69	this exp.
S-Em.(no cut)	391 ± 17	0.61		1678 ± 72	this exp.
S-Ag				1790 ± 120	[48]
S-Ag				1380 ± 190	[143]

experiments, usually only the charge-changing cross-sections are measured. Both hadronic and projectile EMD cross-sections are in good agreement amongst the different experiments even though the EMD cross-sections are derived differently. In the emulsion experiment, the hadronic and EMD components are measured separately, and a scaling factor f is used to obtain the contribution of a particular nuclear type. In other experiments using CR39 plastic detectors($C_{12}H_{18}O_7$), the EMD cross-sections are determined as the difference between total charge-changing cross-sections and the pure hadronic cross-sections which are expected

to be independent of energy beyond 2 GeV per nucleon. In addition, in ref.[47,48] factorization rules were used to give an overall fit. In our data on the total EMD cross-sections σ_{EMD}(labelled 'no cut' in Table 5.9), the contribution due to pion photoproduction has been excluded by the scanning and analysis criteria.

Beside total cross-sections, we can also compare the partial cross-sections for the production of fragments of charge Z_F as the heaviest outgoing fragment. Table 5.10 shows our data and those from ref.[47,48]. The partial cross-sections

Table 5.10: *Partial projectile EMD cross sections for the production of fragments of charge Z_F=2 to 7 and Z_F=8 to 15 in collisions of 200 A GeV ^{16}O and ^{32}S respectively, with a silver target.*

Z_F =	7	6	5	4	3	2	$\leq$ 5	Ref.
O-Em. (E < 150)	386 ± 17	150 ± 11	26 ± 5	38 ± 6	8 ± 2	19 ± 4	91 ± 9	this exp.
O-Em. (no cut)	392 ± 17	158 ± 11	31 ± 5	57 ± 7	17 ± 4	37 ± 5	142 ± 10	this exp.
O-Ag	342 ± 22	127 ± 21					183 ± 50	[47]
Z_F =	15	14	13	12	11+10	9+8	$\leq$ 7	Ref.
O-Em. (E < 150)	933 ± 57	468 ± 40	84 ± 17	30 ± 10	10 ± 6	20 ± 8	10 ± 6	this exp.
O-Em. (no cut)	942 ± 58	485 ± 42	102 ± 20	60 ± 15	30 ± 10	33 ± 11	26 ± 9	this exp.
O-Ag	832 ± 16	413 ± 15	94 ± 10	86 ± 8	83 ± 8	51 ± 6		[48]

of sulphur were computed using the formula suggested in the text of ref.[48], $\sigma_{EMD}(P,T,F) = \varepsilon_{PT}\varepsilon_P^F$, and the values of ε_{PT} and of ε_P^F were those quoted in their tables. However, they normalize arbitrarily ε_{PT} to 1 for a carbon target and hence the absolute scale of these cross-sections is uncertain. Therefore no value for $Z \leq 7$ is quoted.

The agreement between data of the two samples in Table 5.10 is reasonable. In both samples, channels involving the emission of fragments with Z_F differing by one or two units from that of the projectile exhaust more than 80% of the total EMD cross-section. Thus the inclusion of the high-energy tail of the photon

spectrum will increase the partial cross-sections for production of fragments with charges very much less than that of the projectile but will have little effect on the total EMD cross-section.

5.3.2 Photoproduction cross-sections of ^{16}O

By assuming the energy spectrum of the virtual photons presented in chapter 2(sec. 2.2.2) and the energy distributions of various dissociation channels (Fig. 5.1 and 5.2), the photoproduction cross sections on ^{16}O and ^{32}S nuclei, up to the energy threshold for pion production, may be determined for most of the possible photoreactions. It follows that:

$$\sigma_\gamma(E) = \frac{1}{N(E)} \frac{d\sigma_{EMD}}{dE} \tag{5.3.2}$$

where $N(E)$ is the number of virtual photons per energy interval and σ_{EMD} is projectile EMD cross-section for a given channel as in eq. 5.3.1, with all quantities referred to the whole emulsion. Then σ_γ and its integral up to a given energy E, $\sigma_{int}(E)$:

$$\sigma_{int}(E) = \int_0^E \sigma(E_\gamma) dE_\gamma \tag{5.3.3}$$

can be compared with results obtained for the same reactions with low-energy real photons.

By taking the energy E of the virtual photons for a given reaction as the sum of the c.m. kinetic energy(eq. 5.1.1) and of the binding energy of the emitted fragments(Table 5.7), we have neglected the possible excitation energy of the residual nucleus. In the following analysis, we have assumed that the residual nuclei remain in their ground state for all reactions, and the energy spectra obtained through eq. 5.1.1 are the true spectra in spite of the fact that in sec. 5.2.4 we have shown this assumption is valid only on the average. Furthermore the neglect of the excitation energy of the residual nuclei implies an average underestimation of the photon energies and because of the $1/E$ dependence of the virtual photon spectrum, an underestimation of the corresponding $\sigma_\gamma(E)$. On the other hand, the energy spread introduced by the estimate of the c.m. kinetic energy from the transverse momentum p_T(eq. 5.1.1) leads to an effect in the opposite direction. As a result, the two effects at least partially compensate each other.

The photoproduction cross-sections, calculated by using eq. 5.3.2, for the most abundant reactions and the total charge changing reactions(σ_γ^{ch}) for photon energies up to 150 MeV are shown in Fig. 5.18 and 5.19. Comparing with the photoproduction cross-sections in ref.[141,144], the giant resonance peaks in both figures lie in the expected positions, at a lower energy in sulphur than in oxygen. However, the widths of the resonance peaks are both considerably broadened by the energy estimate method.

From Fig. 5.18 it is clear that the channels (γ,p), (γ,α), and (γ,4α) contribute mainly to the giant resonance region, whereas (γ,pp) and (γ,αp) are significant in both the giant resonance region as well as the intermediate energy regions. Other high multiplicity channels contribute only to the region with $E > 50$ MeV.

Unlike the oxygen sample, the number of channels in sulphur contributing up to 150 MeV is much fewer. The channels (γ,p) and (γ,α) contribute mainly in the giant resonance region, while (γ,pp)'s contribution extends beyond 50 MeV. Only five out of the remaining 25 channels(totally 81 events) contribute in the region below 150 MeV.

The (γ,p) and (γ,pp) channels

Table 5.11 shows the integrated cross-sections $\sigma_{int}(E)$ (eq. 5.3.3) for different ^{16}O photoreactions up to 140 MeV. Comparison is made with total photoabsorption cross-sections from Ahrens *et al.*[145] and data on the most abundant channels from other experiments[144,146,147,148]. The normalization of photoabsorption cross-sections is far from trivial[149], and the recent review by Fuller[144] suggests strongly that the Ahrens *et al.*[145] values of the total absorption cross-section up to 40 MeV should be reduced by a factor of about 1.4. The data of the present experiment generally agree with the original data of the Ahrens *et al.*[145] if we take into account the contribution of the (γ,n) process not detected in our experiment. However, if the total cross-sections obtained from the summation of the partial ones are considered more reliable[144], our analysis based on single-photon exchange would indicate that our total absorption cross-section is some 40 % larger than expected.

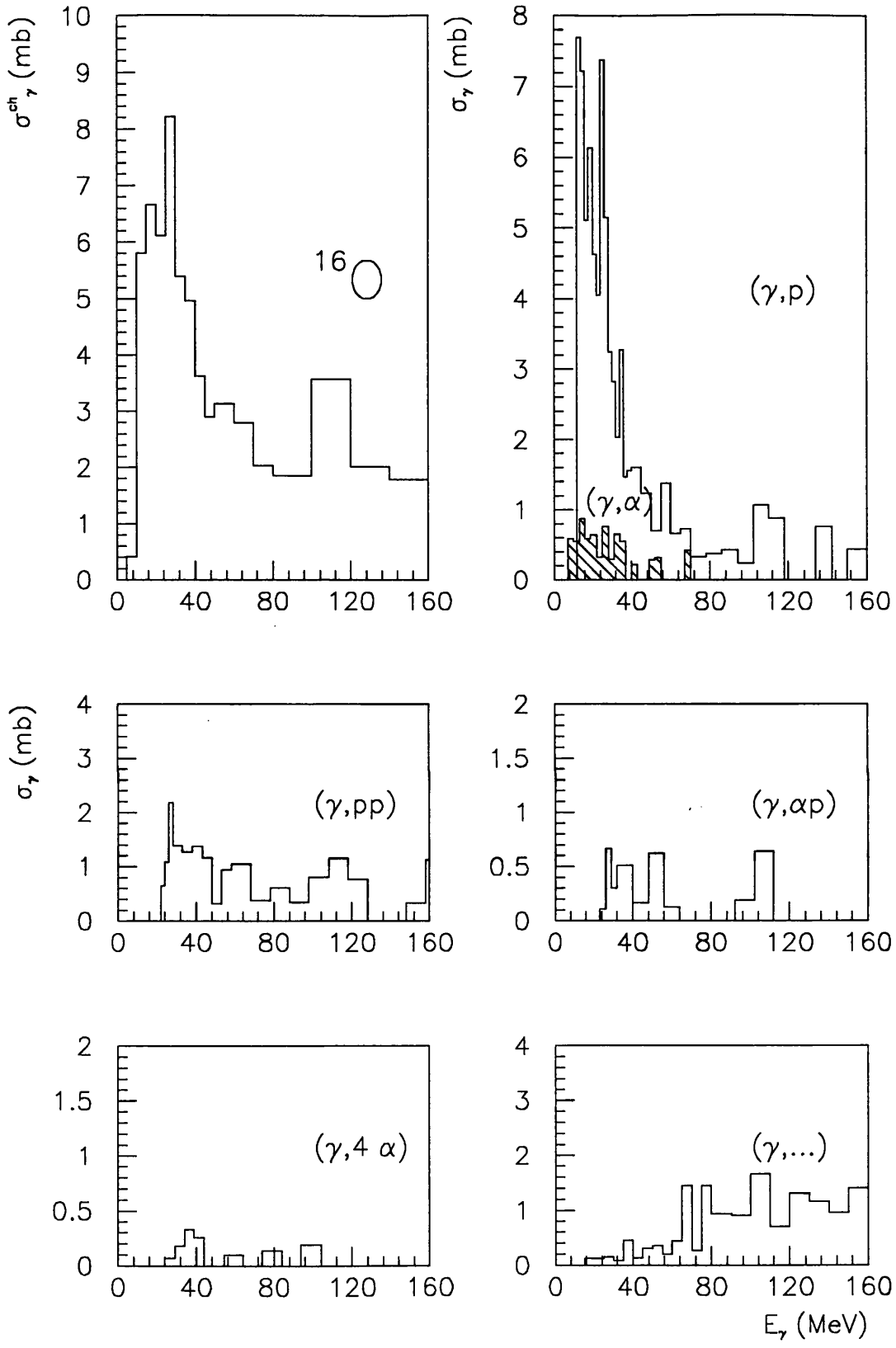

Figure 5.18: ***Single reactions(σ_{γ}) and total charge-changing (σ^{ch}_{γ}) photoproduction cross sections on oxygen determined from EMD cross sections and assuming a classical energy spectrum of virtual photons.***

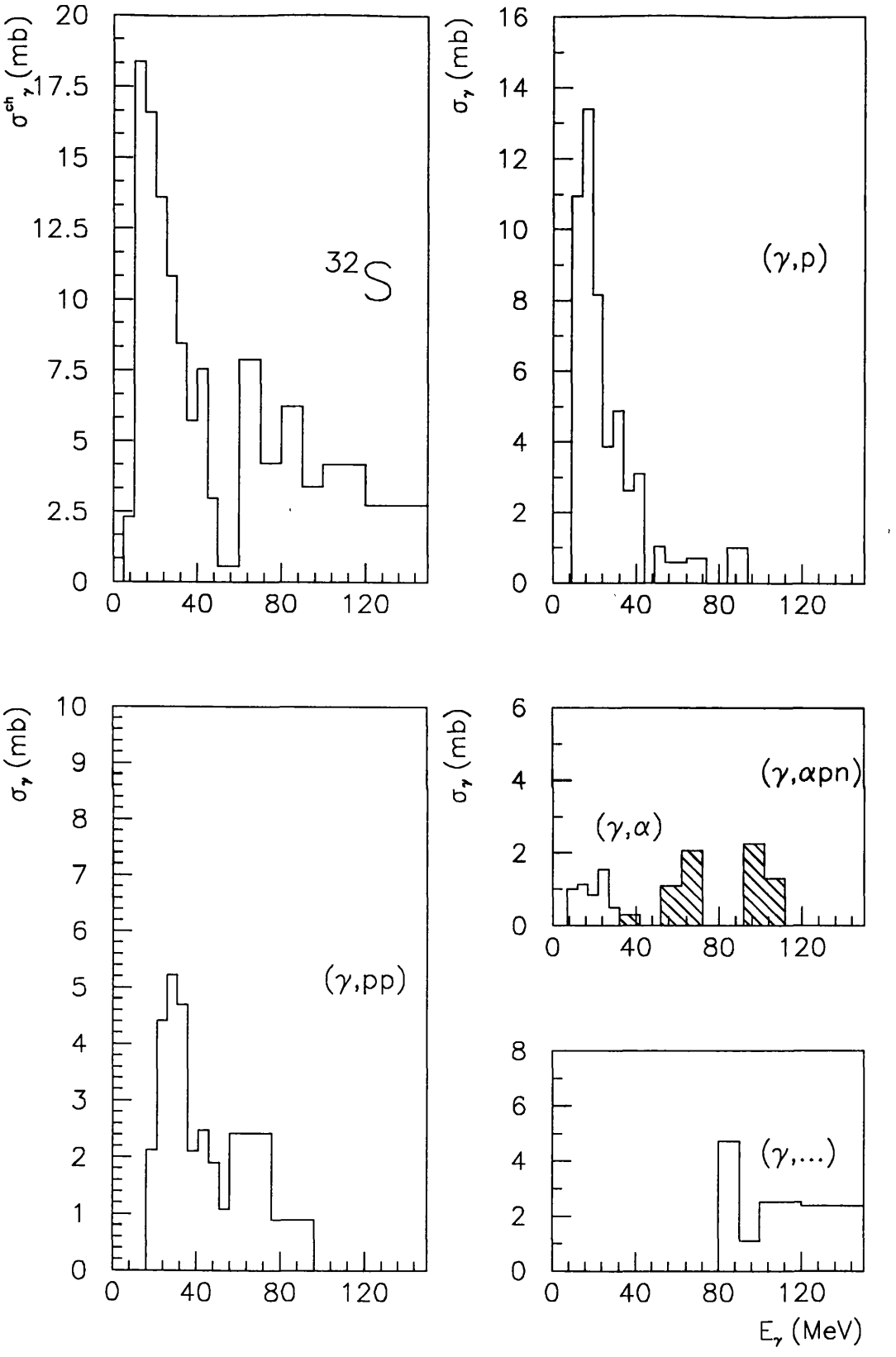

Figure 5.19: *Single reactions(σ_γ) and total charge-changing (σ^{ch}_γ) photoproduction cross sections on sulphur determined from EMD cross sections and assuming a classical energy spectrum of virtual photons.*

Table 5.11: *Integrated photonuclear cross sections(MeV mb) computed from oxygen EMD and compared with real photon cross sections. Errors are statistical.*

E (MeV)	(γ,p)	(γ,pp)	Others	Total charged	(γ,abs) ref.[145]	(γ,n) refs.[146] [148] [144]	(γ,p) refs.[146] [147] [144]	(γ,np) refs.[146] [148]
10			2	2				
15	25±2		6±1	31±2	10			
20	54		10	64	32			
25	80	2	13	95	135	27	85	
30	104±5	11±2	21±2	136±6	210	50	95	5
35	118	18	27	163	255	60		10
40	127	26	35	188	290	70	100	
50	142±7	37±4	41±4	220±8	330	75	105	
60	153	48	51	252	360	80	107	
80	165	60	75	300	410	80	107	
100	170±8	70±7	97±8	337±14	432			
140	194±9	97±9	158±13	449±18	508			

In the giant resonance region, the integrated cross-section for the reaction (γ,p) is in good agreement with the results from real photon experiments. In the higher energy region, our cross-section measurement is larger than previous results. This could be due to the inclusion of the reaction (γ,np) whose cross-section is small at low energies but increases rapidly with increasing energy: $\sigma_{int}(170)$= 60 MeV mb[146].

It is difficult to compare the photoabsorption cross-sections of single reactions since only a single or very few reactions are determined in a given experiment within a limited energy range. Furthermore, sometimes photoneutron cross-sections also include reactions with charged particles. Yet our experiment does not detect neutrons nor does it distinguish between various isotopes.

Table 5.12 shows the integrated cross-sections $\sigma_{int}(E)$ for different ^{32}S photoreactions up to 140 MeV. Comparison with previous results measured with real photons is not possible at all energies. Instead we have used the total absorption cross-section results from Wyckoff *et al.*[141] up to 35 MeV and due to the

Table 5.12: *Integrated photonuclear cross sections(MeV mb) computed from sulphur EMD and compared with real photon cross sections. Errors are statistical.*

E (MeV)	(γ,p)	(γ,pp)	Others	Total charged	(γ,abs) refs.[141] [145]	(γ,n) ref.[158]	(γ,p) ref.[160]	(γ,np) refs.[158] [159]
10	7		5	12				
15	100±9		10±3	110±10	12		75	
20	173	10	16	199	140	32		
25	206	44	26	276	310	84		
30	234±16	92±12	28±6	354±21	400	107	275	24
35	270	114	28	412	470	123		35
40	281	134	32	447	525*	131		46
50	293±20	178±20	36±8	507±30	600*	145		57
60	305	191	36	532	650*	155		64
80	327	253	92	672	730*			71
100	335±26	284±32	166±32	785±52	790*			
140	374±34	322±39	286±50	982±71	940*			

*Interpolated from data on Al and Ca in ref.[145].

lack of data interpolated results from Al and Ca[145] in the energies above. In addition, the results from ref.[158,159] on the reactions (γ,n) and (γ,np), up to E=60 and 80 respectively,have been included for comparison. Like in oxygen, the contribution from (γ,np) is much smaller than that observed for (γ,p) in the giant resonance region. Furthermore there is some disagreement in previous results. The total absorption cross-section measured by Wyckoff *et al.*[141] gave σ_{int}(15)=12 MeV mb, while Dolbilkin *et al.*[160] found σ_{int}(15)=75 MeV mb and estimated σ_{int}(30)=(275±70) MeV mb for the reaction (γ,p). Our measured values are consistent with that of ref.[160].

There is good agreement between previous results and our data if account is taken of the (γ,n) process not detected in this experiment, in the energy range E <50 MeV; above this energy our values are higher than those previously found. However, the interpolated data must be regarded with caution.

The (γ,α) channel

There are three reactions with characteristic final states but with relatively small integrated cross-sections $\sigma_{int}(E)$ with values as follows:

$^{16}O(\gamma,\alpha)^{12}C$	$\sigma_{int}(40)$=(18.7±2.1) MeV mb
$^{16}O(\gamma,\alpha p)^{11}B$	$\sigma_{int}(50)$=(10.4±2.4) MeV mb
$^{16}O(\gamma,4\alpha)$	$\sigma_{int}(50)$=(4.4±1.6) MeV mb

Previous results on the reaction $(\gamma,4\alpha)$ gave $\sigma_{int}(30)$= 5 MeV mb[146] and $\sigma_{int}(40)$=3.7 MeV mb[144]; taking the errors into account, our result compares well with that of the real photon experiments. On the other hand, the integrated cross-section of the reaction $(\gamma,\alpha p)$ is higher than the value obtained for real photons: $\sigma_{int}(55)$=(4.8±0.4)MeV mb[150]. Our value, although higher, is not inconsistent with that number if the errors is taken into account.

Ref.[144] gave the integrated cross-section for the reaction (γ,α) $\sigma_{int}(29)$=2.2 MeV mb. It contributes essentially through narrow peaks in the region 12 to 14 MeV. This result is based on measurements of inverse (α,γ_0) capture reactions, but direct measurements give similar results[146,151].

The small cross-section for the reaction $^{16}O(\gamma,\alpha)^{12}C$, despite the low-energy threshold, is due to the fact that in self-conjugate nuclei(i.e. Z=N) there is the isospin selection rule that ΔT=±1 for electric dipole transitions. Our integrated cross-section up to 40 MeV is an order of magnitude larger than the value for real photons, mainly at low energies. Since the present experiment does not observe neutron emission nor does it distinguish between various isotopes, one possible explanation is that there may be contaminations within our sample of (γ,α) data, for example the reactions $(\gamma,^3He)$ and $(\gamma,\alpha n)$. Based on the inverse $(^3He,\gamma)$ capture reaction, the integrated cross-section for the reaction $(\gamma,^3He)$ $\sigma_{int}(36)$=0.75 MeV mb[144]. Under the conditions of our experiment, this cross section would correspond to two to three events when the appropriate value of the energy threshold(B=22.8 MeV) is taken into account. However, if these two events were misidentified as (γ,α), they would yield $\sigma_{int}(20)$=0.3 MeV mb which cannot account for the excess of our cross section. Similarly previous results on

the reaction (γ,αn) gave σ_{int}(55)=(4.1±0.4) MeV mb[152] which would correspond to about seven events in our conditions. If all of them were interpreted as (γ,α), they would yield σ_{int}(40)=2 MeV mb. This value is still too small to explain the difference. Instead of using the integrated cross-section for (γ,αn) obtained for real photons, we may assume that the reaction (γ,αn) contributes as (γ,αp). This would mean a contamination of about 24 events and σ_{int}(40)=6 MeV mb. Another possible background is the reaction (γ,^{3}He n) whose contribution is not known.

As in oxygen, there is an excess in our integrated cross-section for the reaction (γ,α): σ_{int}(30)=(28±6)MeV mb when compared with results from measurements of the inverse (α,γ_0) capture process from 13 to 19 MeV which gave σ_{int}=1.4 MeV mb [161]. This reaction should have been suppressed for the same reason as in the case of oxygen.

So far in our analysis we have assumed the virtual photon energy spectrum to be derived classically by Fourier transformation of the time dependent electric and magnetic fields, or the Weizsäcker-Williams method[54,55,56]. However a quantum mechanical approach to the virtual photon method would yield virtual photon spectra distinguished by multipolarities(E1,M1,E2,...) [153,154,155,156,57]. The E1 spectrum is identical with the classically derived one, while for 200 A GeV $N_{E1} \approx N_{M1}$. However, in the low-energy regions the E2 intensity is considerably larger than that of E1 due to an additional term of the form[156]:

$$\frac{2K_1^2(x)}{\gamma^2} \tag{5.3.4}$$

which raises the intensity of the E2 spectrum with respect to E1 by a factor of 3.2, 1.6, and 1.3 for E_γ = 10, 20 and 30 MeV respectively. A small overall correction factor has been applied to the calculation of the total photonuclear cross-sections for comparison with EMD cross-sections in ref.[41,43,47,48]. For the reaction (γ,α) the correction factor is expected to be higher because the cross-section for E1 photon absorption is depressed and hence the contribution of the E2 photons is even larger[144]. This fact and the low value of the reaction threshold has made this reaction particularly sensitive to the different admixture of multipolarities. It is noted that in Martins *et al.*[157]'s analysis of electrodistintegration of nuclei using DWBA virtual photon spectra, a similar effect is found, the E2 virtual photon intensity being larger than that of E1 at low energies. However, it is estimated that

this effect could increase the integrated cross-section obtained with real photons at most by a factor of two and cannot wholly account for the high value found in the present experiment.

Ardito *et al.*[49] have suggested the possibility of multiphoton absorption which may be another possible explanation for the high rate of the reaction (γ,α) since $0^+ \xrightarrow{\alpha} 0^+$ transitions are easily accessible to two-photon processes. Within the model of Baur and Bertulani[162], in which the photons are considered incoherent, when a relativistic oxygen or sulphur ion impinges even on a silver nucleus, the chance for two-photon absorption is very small. However, the passage time for these ultra-relativistic ions through the Lorentz-contracted electromagnetic field of a heavy nucleus is very short $\sim 10^{-25}$ s so that the photons in the resulting pulse are temporally coherent. This coherence might enhance the multiphoton contribution to the cross-section. Furthermore, the harder photon spectrum observed for sulphur interactions and the excess in complex multiparticle breakup are also difficult to ascribe to single-photon absorption processes and suggest the possibility of multiphoton absorption. However, it should though be borne in mind that conventional estimates of multiphoton processes suggest that, in general, they should be small[162].

5.4 Diffractive dissociation

Therefore, neither the contamination from other EMD reactions nor the effect due to an enhanced E2 virtual photon spectrum can explain the high value of our (γ,α) cross-section. Even the multiphoton process seems unlikely to account for the large discrepancy between the real photon data and our measured cross-section. However, events have been observed, which seem to have all the features ascribed to EMD breakup, except that at the point of dissociation there is also a track of a very low-energy charged particle. In fact, on measurement, some of these events were found to be consistent with diffractive dissociation on free protons within the emulsion. It is unlikely that these events are electromagnetic in origin because of the proton's small charge. They must be caused by strong interaction.

Similar hadronic processes occurring on nuclei other than hydrogen would produce no recognizable recoil and hence such events are indistinguishable from those of electromagnetic origin.

Therefore a careful search was performed on the sample of 200 A GeV ^{16}O ion hadronic inelastic interactions to establish the extent of such processes, particularly those giving rise to (C He) and (N H) final states of the ^{16}O nucleus. Since isotopic identification is not possible in the present study ^{1}H and ^{2}H or ^{3}He and ^{4}He are not separated. However, it is expected that most of the H and He in the final states will be protons and ^{4}He(α) respectively.

5.4.1 Hydrogen Data

Eleven examples of the topology(C He + a low-energy 'proton') were located, by scanning 635.3 m of 200 A GeV ^{16}O track, i.e. 74 % of the total track length followed. The details of these events are listed in Table 5.13. From kinematic consideration it is expected that the magnitude of the 'proton' momentum q and its emission angle θ with respect to the beam direction should satisfy, to a good approximation, the relation

$$cos\theta = \frac{q}{2m} \tag{5.4.1}$$

where m is the mass of the struck proton. The estimated centre-of-mass kinetic energy spectrum is compared with those events classified as EMD(C He) candidates in Fig. 5.20(a). All nine events satisfying eq. 5.4.1 have similar spectrum to that of the EMD candidates. The other two events which do not satisfy the free hydrogen criterion may correspond to the knock-out of a proton from a heavier nucleus in the emulsion. In this case, the kinematic relation of eq. 5.4.1 would be modified by both the Fermi motion of the proton in the nucleus and its multiple scattering while emerging therefrom.

In the case of the (N H + a low-energy 'proton') events, the situation is much less clear since it is not possible to distinguish the tracks of a forward-going fast proton and a produced charged pion on the basis of ionization alone. However, nine evens with the correct scanning topology were found within 463.0 m of 200 A GeV ^{16}O track, amounting to 54 % of the total ^{16}O track length followed. The details

Table 5.13: *Events satisfying the C He p topology. The nine above the horizontal line satisfy the kinematics of* $^{16}Op \rightarrow {}^{12}C\alpha p$.

Proton range (μm)	Proton momentum (MeV/c)	Observed emission angle (deg.)	Predicted emission angle (deg.)	Energy E above $^{12}C\,\alpha$ threshold (MeV)
294	112	83.3 ± 2.8	86.6	8.7
1636	185	84.3 ± 2.2	84.3	18.6
> 7322[a)]	$\gtrsim$ 286	81.1 ± 0.9	$\lesssim$ 81.3	11.8
173	95	81.2 ± 3.3	87.1	8.4
> 10200[a)]	$\gtrsim$ 315	74.4 ± 2.2	$\lesssim$ 80.3	17.6
2401	207	85.1 ± 1.5	83.7	2.2
> 1154[a)]	$\gtrsim$ 167	82.4 ± 1.4	$\lesssim$ 84.9	28.0
> 4500[a)]	$\gtrsim$ 248	85.6 ± 2.6	$\lesssim$ 82.4	6.5
2125	200	82.9 ± 2.1	83.9	7.2
381	121	147.0 ± 2.2	86.3	16.3
208	101	107.4 ± 3.1	86.9	1.9

[a)] In these events the proton leaves the emulsion but it is already close to rest. The estimated residual range is less than 1 mm, which would imply only a small increase in the initial proton momentum.

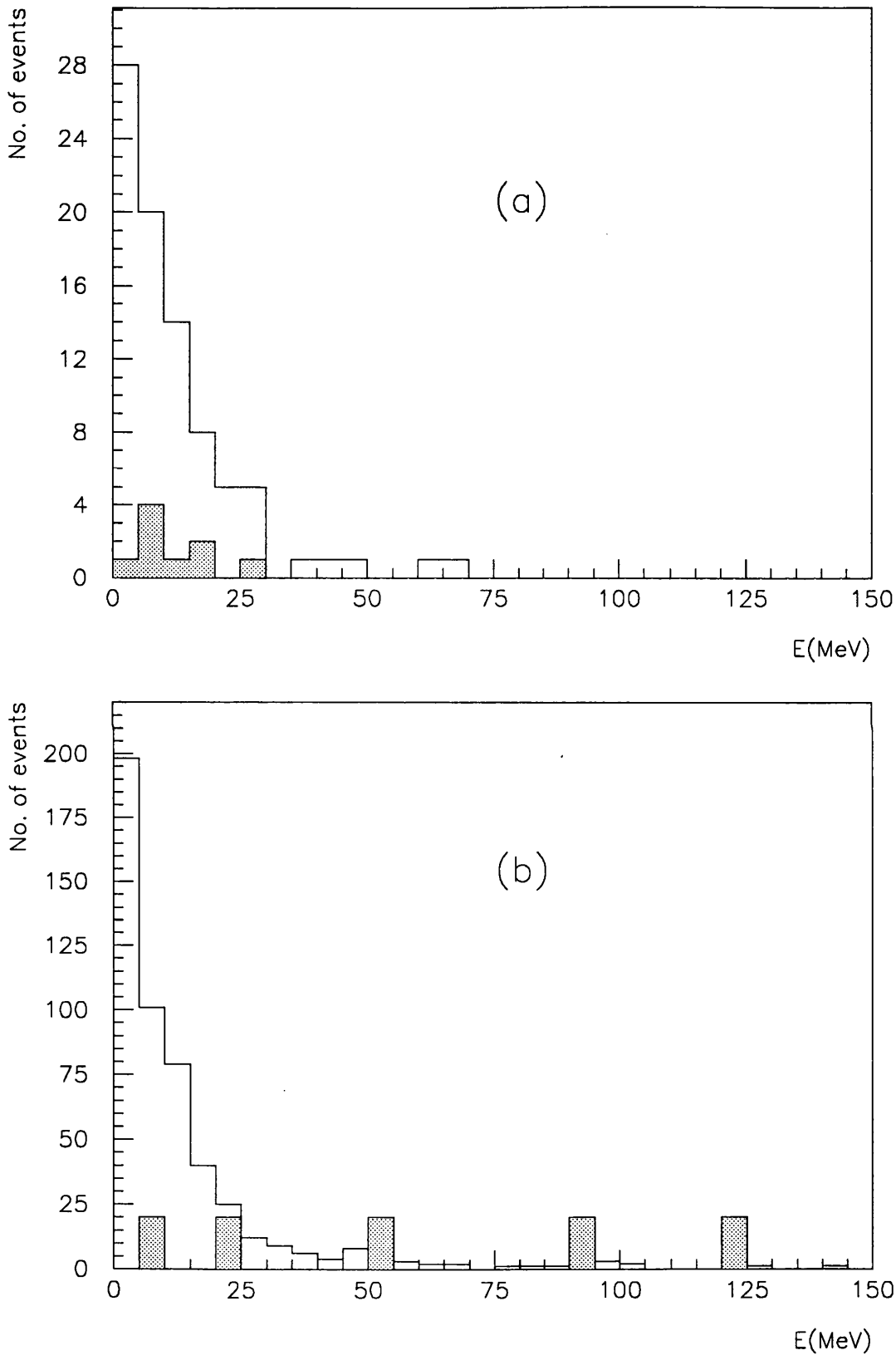

Figure 5.20: *Centre-of-mass energy spectra of candidates for EMD(open histogram) and hadronic diffraction on free protons(shaded histogram) of (a) (C He) and (b) (N H) final states. For clarity, the ordinate for the (N H p) events has been scaled by a factor of 20.*

Table 5.14: *Events satisfying the N H p topology. Only the two above the horizontal line satisfy the kinematics of* $^{16}Op \rightarrow {}^{15}N\ p\ p$ *with a value of the excitation energy compatible with electromagnetic dissociation.*

Proton range (μm)	Proton momentum (MeV/c)	Observed emission angle (deg.)	Predicted emission angle (deg.)	Energy E above ^{15}Np threshold (MeV)
425	125	92.6 ± 3.0	86.2	6.8
3170	224	84.0 ± 1.5	83.1	20.1
> 4693[a)]	$\gtrsim$ 251	79.9 ± 0.8	$\lesssim$ 82.3	51.0
> 9345[a)]	$\gtrsim$ 307	79.6 ± 1.2	$\lesssim$ 80.6	90.9
> 1820[a)]	$\gtrsim$ 191	70.1 ± 2.3	$\lesssim$ 84.2	106.9
12005	330	79.9 ± 1.0	79.9	122.7
442	126	91.3 ± 3.7	86.2	273.9
> 12650[b)]	$\gtrsim$ 335	87.4 ± 0.8	$\lesssim$ 79.7	493.1
126	86	147.0 ± 4.5	87.4	908.8

Note: In these events the proton leaves the emulsion but it is already close to rest. The estimated residual range is less than 1 mm[a)] or 2 mm[b)] respectively, which would imply only a small increase in the initial proton momentum.

of these events are listed in Table 5.14. Six of these nine events were kinematically consistent with eq. 5.4.1, but only two of them have opening angles, between the nitrogen and the supposed forward-going proton, that would give an excitation energy in the ^{16}O system of less than 50 MeV, the region in which 96 % of our EMD(N H) candidates lie. This is clearly displayed in Fig. 5.20(b). Therefore, the rest of the events do not look typical of EMD. It is likely that in most of these cases the minimum-ionizing singly charged particle is actually a pion rather than a stripped projectile proton, since at large outgoing angles a 200 GeV proton would have a larger than expected transverse momentum.

5.4.2 Theoretical predictions

The elastic form factor of ^{16}O is well described by harmonic oscillator wave functions with an r.m.s. charge radius of 2.72 fm[163]. In the inelastic case, electron scattering[164] data provide good measures on the transition form factors of the three low lying 2^+ states of ^{16}O. The form factors of the 2_1^+ and 2_3^+ levels at 6.92 and 11.52 MeV respectively are almost identical in shape, corresponding to surface-peaked transition densities, although the amplitude of the 2_3^+ level is about $\frac{1}{\sqrt{2}}$ smaller. After removing the proton size the form factors can be parameterized as

$$S2_1^+(q) = 0.1844q^2(1-q^2/1.935^2)e^{-0.80q^2} \quad (5.4.2)$$

$$S2_3^+(q) = 0.1217q^2(1-q^2/1.970^2)e^{-0.72q^2} \quad (5.4.3)$$

On the other hand, the overlap for the 2_2^+ state at 9.85 MeV is peaked in the interior so that its B2 moment is quite small and it shall not be considered further. Furthermore the threshold for α decay is at 7.16 MeV and thus the 2_1^+ state decaying into (C He) cannot not observed. The 2_3^+ state decays essentially 100 % into the (C He) mode and might therefore be observed in our experiment.

The factor of 2 between 6.92 and 11.52 MeV levels is also seen in proton scattering at 200 and 500 MeV[165,166], and the shapes of the two cross-sections are found to be very similar.

In addition experimental data are available on the 2_1^+ level by proton scattering at 800 MeV[167]. Using the eikonal distorted-wave impulse approximation(DWIA) described in Appendix A and taking the total nucleon-nucleon cross-section σ_{NN}=4.0 fm^2 and β^2=0.2 fm^2, it has been possible to evaluate the cross-sections for $p^{16}O \rightarrow p'^{16}O^*(6.92\ MeV)$ at 800 MeV as a function of momentum transfer and compare them with experimental data. The distribution is shown in Fig. 5.21. The predictions compare well with the data in both the shape and absolute normalization of the cross-section and confirms that both the reaction

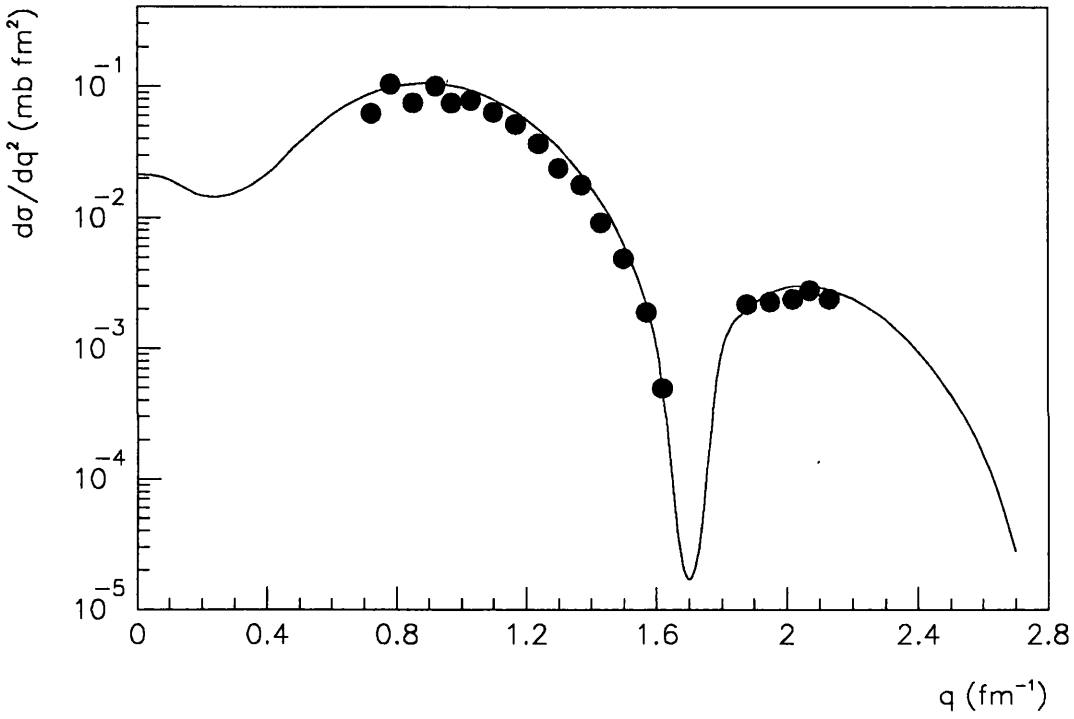

Figure 5.21: *Experimental cross-sections for p $^{16}O \rightarrow p'\ ^{16}O^*$ at 800 GeV[167] are compared with the predictions of the eikonal DWIA calculation described in Appendix A.*

mechanism and nuclear structure information are sufficiently well understood to make reliable estimates for both 2^+ levels.

The next step is to apply the eikonal DWIA model at our energy of 200 A GeV using σ_{NN}=3.9 fm^2 and β^2=0.44 fm^2[117]. The model predicts an integrated cross-section for the 11.52 MeV level of

$$\sigma[^{16}Op \rightarrow ^{16}O^*(11.52MeV)p] = 0.52mb\ , \qquad (5.4.4)$$

which would be seen finally in the $^{12}C + \alpha$ channel. The shape of the distribution in q^2 is broadly similar to the lower energy results of Fig. 5.21 with an r.m.s. value of $\langle q^2 \rangle^2$=200 MeV/c. This is in good agreement with the corresponding figure for the nine hydrogen events shown in Table 5.13(213±76 MeV/c).

The cross-section prediction in eq. 5.4.4 suggests that about 1.2 events, in which the final ^{16}O nucleus is excited to the 11.52 MeV level, should be observed. The total cross-section deduced from the nine events listed in Table 5.13 is 4.0±1.4 mb. Hence the 2_3^+ level accounts for about 13 % of the (C He p) events that were discussed in the previous section. The rest of the events are then due to other higher energy ^{16}O levels which have significant branching ratios to (^{12}C α)[142].

Beside hydrogen, similar coherent hadronic processes occurring on nuclei in emulsion would produce no recognizable recoil and therefore such events would be kinematically indistinguishable from those originally classified as being electromagnetic. The calculations for these events are identical with that of hydrogen events except that the elastic form factor for the target nucleus $S_A(q)$ has to be included. The predicted integrated cross-sections for $\sigma(^{16}O\ A \rightarrow {}^{16}O^*\ A)$, where the target nucleus A is left in its ground state, are evaluated with harmonic oscillator densities for the light (C,N,O) nuclei and Wood-Saxon densities for the heavy(Ag,Br) nuclei. Fig. 5.22 shows the predicted integrated cross-sections as a function of mass number of the target nuclei. In view of the strong damping and the large nuclear sizes, only the rim of the nucleus should contribute to such excitations so that a behaviour of roughly $A^{1/3}$ would be expected. Indeed a log-log fit to the results of the calculations in Fig. 5.22 is quite close to this with

$$\sigma(^{16}OA \rightarrow {}^{16}O^*A) = 0.865A^{0.29} = 1.65\sigma_p A^{0.29} mb \ . \qquad (5.4.5)$$

This form is not valid for hydrogen because the rim there encompasses the majority of the target.

From the abundance of different nuclear species in our emulsion stack given in Table 3.1, the relative number of events expected on medium/heavy nuclei as compared to those on hydrogen can be deduced:

$$\frac{N(A>1)}{N(A=1)} = 6.1 \ . \qquad (5.4.6)$$

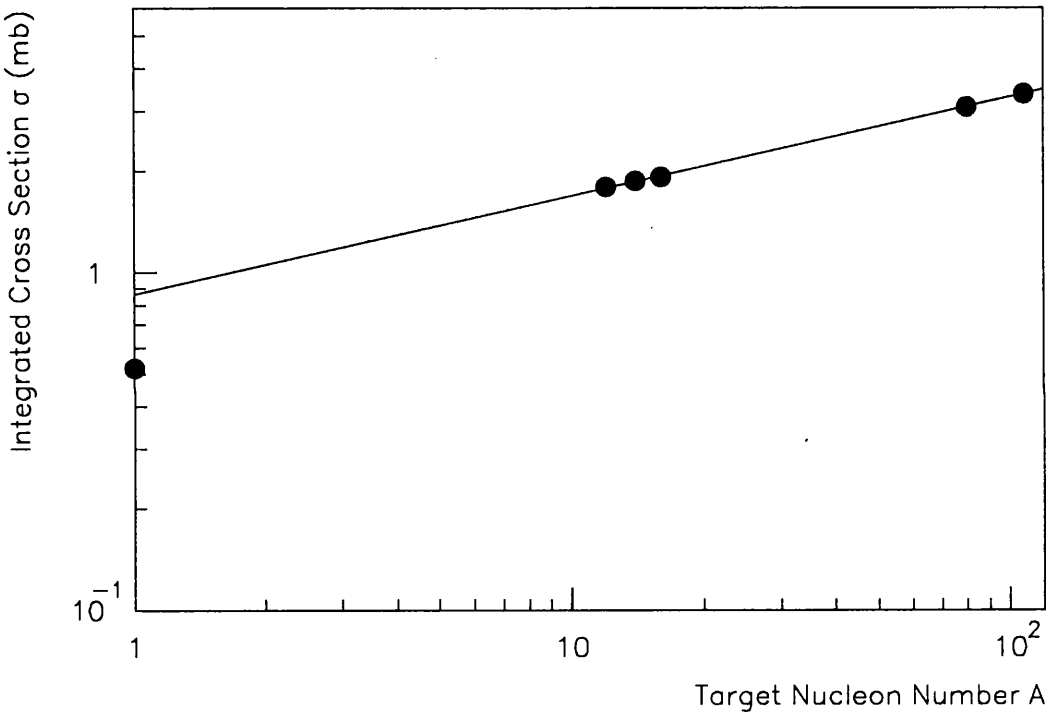

Figure 5.22: ***Predicted integrated cross-section for ^{16}O A $\rightarrow$ $^{16}O^*(11.52)$ A on various emulsion nuclei at 200 A GeV. The parameters of the straight line log-log fit are given in eq. 5.4.5.***

Therefore we would expect to have about 10 events corresponding to the excitation of the 2_3^+ nuclear level via the strong interactions where the elastically recoiling target nucleus would not have been detected. In Fig. 5.20(a), there are EMD candidates where the kinetic energy in the α-^{12}C system is of the order of 4 MeV and may therefore correspond to this level.

However, the majority are at higher excitation energies where the corresponding electromagnetic form factors have not been studied in detail for ^{16}O excitation energies above 12.1 MeV[164]. A similar estimation of the excitation of higher nuclear levels is precluded. To resolve this problem, it has been assumed that these higher energy levels behave broadly similarly to the 2^+ ones and in particular that the A dependence is given by eq. 5.4.5. Thus, the number of events observed on free hydrogen is scaled to the other target nuclei using the 6.1 factor of eq. 5.4.6. This scaling might still be reasonable if some of the events observed correspond, for example, to the production of ^{3}He rather than ^{4}He.

Therefore, the predicted number of hadronic events in which there is no observable low-energy recoil should be

$$N(CHe) = (9 \pm 3) \times 6.1/0.74 \doteq 74 \pm 25 \ , \qquad (5.4.7)$$

where the 0.74 denominator arises from the fraction of the track length scanned for these events. The quoted error is purely statistical, arising from the number of hydrogen events. This prediction suggests that the majority of the 85 events classified in previous sections as EMD candidates should in fact be hadronic. After these subtractions have been made our results would not be in disagreement with an estimate based on data from real photons which predicts about 9 events(sec. 5.3.2). In addition, there should be interference terms between the electromagnetic and hadronic excitations, but these are probably very small owing to the latter being dominantly imaginary with the former being dominantly real.

In the (N H) channel, only two events were found to be consistent with both the diffraction dissociation of an ^{16}O ion on free proton and with the EMD criteria. Scaling this number to other target nuclei using the 6.1 factor, it is expected that about $2\times\ 6.1/0.54 = 23\pm16$ events would be on the complex nuclei in the emulsion. This number is small compared to the total number of EMD candidates in the (N

H) channel and thus changes little the plausible agreement with real (γ,p) data shown in sec. 5.3.2.)

So far we have not considered a detailed examination of events of the type ^{32}S p $\rightarrow$^{28}Si He p worth while since no additional scanning has been performed to increase the size of our sample of (Si He)EMD candidate. Furthermore lack of nuclear-structure information precludes a similar estimation of the low-energy excitation levels of ^{32}S.

Chapter 6

Anomalons in 200 A GeV ^{16}O-Em Collisions

6.1 Introduction

The existence of projectile fragments(pfs) with anomalously short mean free path(MFP) values in relativistic heavy ion collisions has been reported since 1954. Because of limited statistics and systematic uncertainties over the energy and type of projectile nuclei, these cosmic rays findings have never been widely recognized.

However, the availability of relativistic heavy ion beams from facilities such as the Bevalac at the Lawrence Berkeley Laboratory(LBL) and the Synchrophasorton at the JINR Dubna opened up the possibility of controlled high-statistics experiments. Friedländer *et al.*[70,71] performed two experiments using beams of ^{16}O and ^{56}Fe at 2 A GeV and concluded that the reaction MFPs of relativistic pfs, $3 \leq Z \leq 26$, are shorter for a few centimetres after emission than at large distances, where they are compatible with values predicted from experiments on beam nuclei. Since then the results of a number of experiments supported the existence of anomalons[72,69,73,77,85,86,168,87], while others do not[81,82,83,84,91]. No definite conclusions can be reached at the present moment. Most of the experiments performed so far employ projectiles ranging from ^{12}C to ^{84}Kr at relativistic energies ($\sim$ 2 to 4 A GeV). Therefore, it is interesting to study the anomalous behaviour of pfs with the availability of ^{16}O and ^{32}S beams at 200 A GeV from the CERN SPS.

6.2 Mean Free Paths

The sample of projectile fragments under study are taken from an unbiased subsample of the 2048 peripheral interactions found in the first 349 metres of 200 A GeV ^{16}O track.

Since the hadronic events and the electromagnetic events involve entirely different production mechanisms, the pfs are divided into two categories: (1)those fragments originating from hadronic events and (2)those emitted from electromagnetic process. Moreover, with the view of testing the influence of different generations, each of the above category is divided into (a)those pfs originating from primary interactions(first generation *secondaries*) and (b)those originating from secondary or tertiary + ... interactions(second + third + ... generations *tertiaries* + ...). The results are shown in Table 6.1. Because of limited statistics, those pfs emitted from secondary electromagnetic dissociation is excluded from our study. The λ^*_{had}'s of the fragments agree within errors irrespective of their production mechanisms and generations.

The hadronic MFP λ^*_{had} observed for primary ^{16}O and ^{32}S beam nuclei is plotted as a function of the distance from the scan line in Fig. 6.1. The data are well accounted for by the constant values of λ^*_{had}, 12.0 cm for ^{16}O and 9.2 cm for ^{32}S. The observation that λ^* does not depend on D is typical of the behaviour of all MFP measurements of beam nuclei.

Throughout this study, the errors we assign to the MFP data points represent one standard deviation assuming the λ value from simplified Glauber model. It is assumed that all pfs should have the MFP λ as computed from simplified Glauber model and that λ^* values are just fluctuations around this value.

6.3 Z=2 projectile fragments

The λ^*_{had} of the He isotopes, 21.98 $\pm$ 1.20 cm, is comparable to those found for pfs from 200 A GeV ^{32}S ions[92], 60 A GeV ^{16}O ions[91], 2 A GeV ^{40}Ar and ^{56}Fe

Table 6.1: *Results of following secondary (+ tertiary....) projectile fragments.*

Z		2	3	4	5	6	7
first generation fragments from ^{16}O-Em inelastic collisions	No. followed	1533	103	107	130	312	300
	Length followed(m)	73.2	5.0	4.7	5.6	13.6	13.1
	No. of inelastic Interactions	333	31	36	46	99	101
	$\lambda^*_{had}(cm)$	22.0 ± 1.2	16.0 ± 2.9	13.0 ± 2.5	12.2 ± 2.1	13.6 ± 1.4	13.0 ± 1.2
first generation fragments from the EMD of ^{16}O	No. followed	151	6	6	18	67	158
	Length followed(m)	7.3	0.3	0.2	0.8	3.1	7.0
	No. of inelastic Interactions	28	0	2	6	16	58
	λ^*_{had} (cm)	26.2 ± 4.1	- -	11.8 ± 10.5	13.7 ± 5.8	19.5 ± 3.5	12.1 ± 1.7
second generation fragments from pf-Em inelastic collisions	No. followed	198	20	24	34	24	3
	Length followed(m)	9.1	0.9	1.1	1.4	1.0	0.1
	No. of inelastic Interactions	35	6	3	11	8	2
	λ^*_{had} (cm)	25.9 ± 3.7	14.4 ± 6.1	37.4 ± 8.6	12.6 ± 4.3	12.4 ± 4.9	5.2 ± 9.3

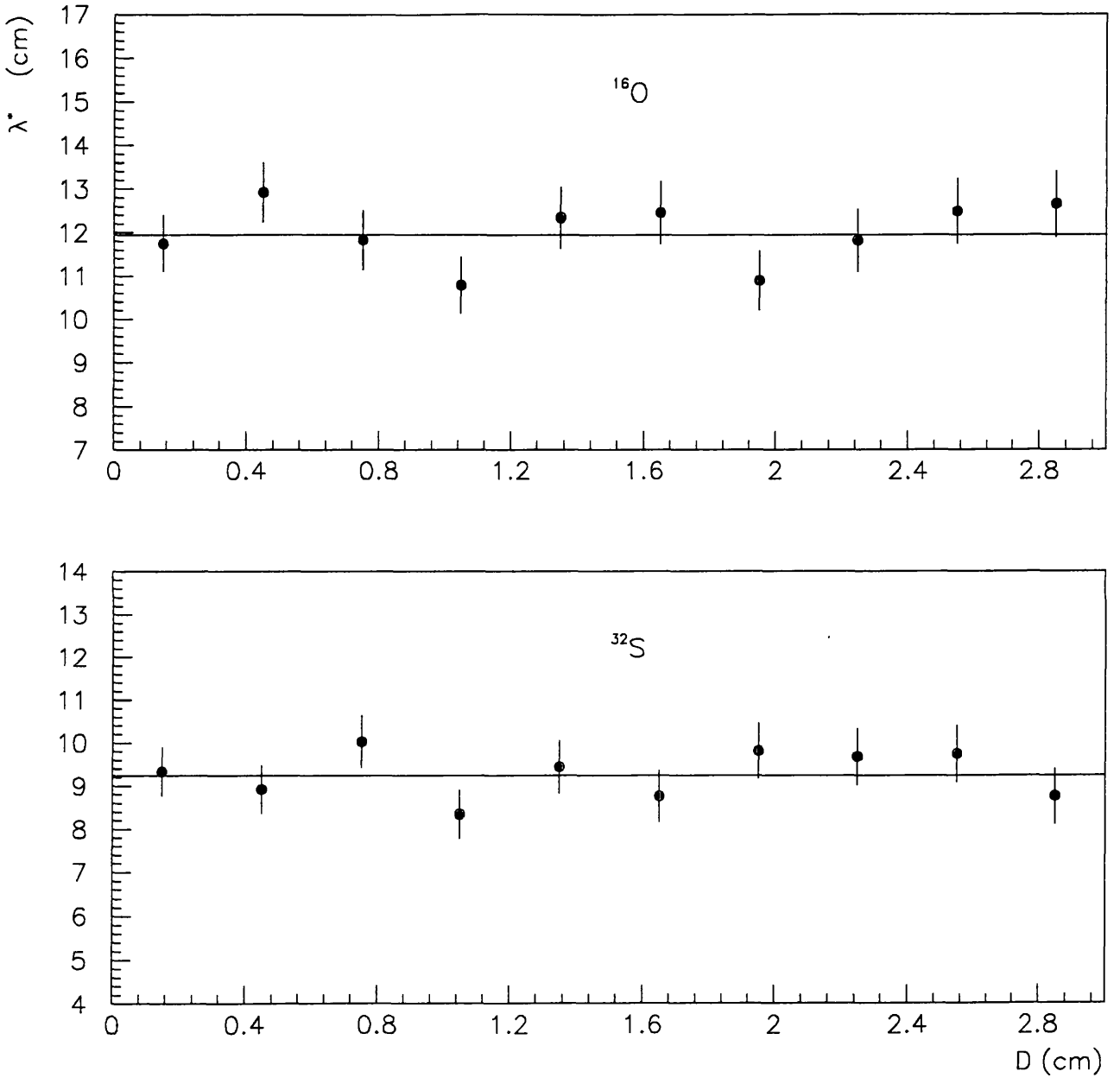

Figure 6.1: *Measurements of the primary 200 A GeV ^{16}O and ^{32}S MFP as a function of the distance from the scan line.*

ions[81,83], 4.5 GeV ^{12}C ions[85], and $1 \leq E \leq 2$ A GeV ^{40}Ar, ^{56}Fe and ^{84}Kr ions[82] and the primary He beam data[83,85,81], if consideration is taken of the higher water content in our emulsion which increases λ^*_{had} by 4 %.

However, several workers' data are in disagreement with ours. The results are shown in Table 6.2. El-Nadi *et al.*[85] and Ghosh *et al.*[86] reported the presence of anomalons in the first few centimetres from the production points, and their λ^*_{had} are considerably shorter than the MFP of beam nuclei; Friedländer[171] also reported the existence of a short MFP component up to about 3 cm path lengths from the point of primary interactions, but their overall λ^*_{had} is consistent with that found for primary He nuclei. The particularly small λ^*_{had} values in ref.[85,86] are probably due to the fact that observations were confined to the first few centimetres where the anomalous effects were reported. As a result, the average MFPs are shorter than that of beam nuclei. Furthermore, our λ^*_{had} value is higher than the result for 12 A GeV primary α particles of 18.1 ± 0.7 cm[130] and the difference cannot be explained wholly by the presence of ^{3}He fragments in our sample, the energy variation of the cross-sections and the different emulsion conditions.

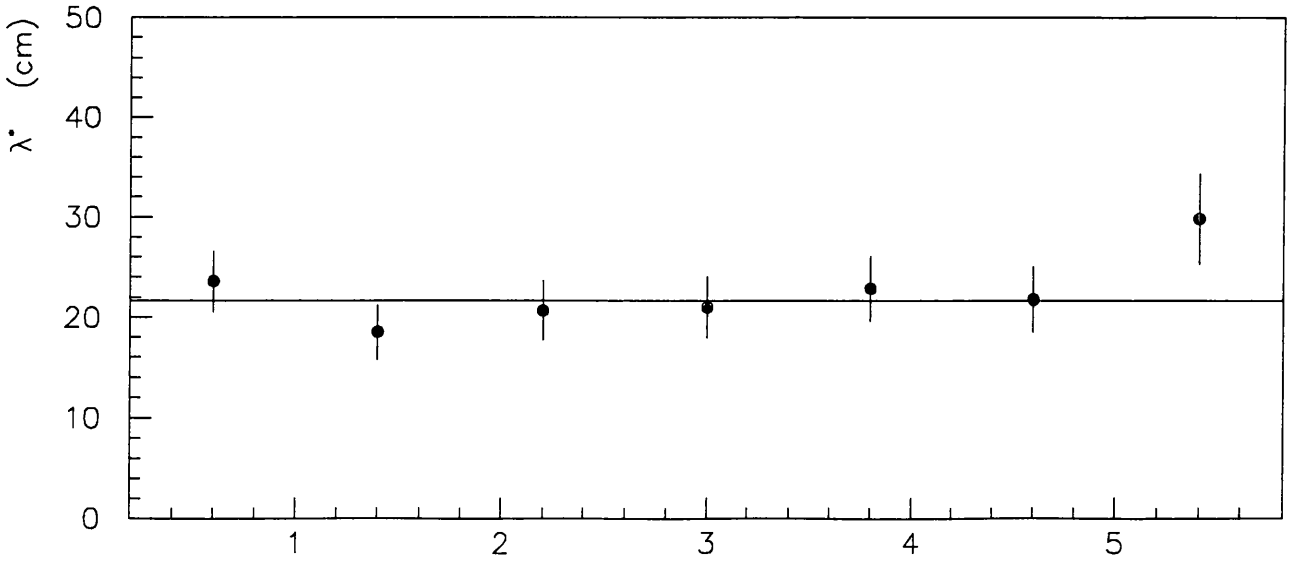

Figure 6.2: λ^*_{had} *versus distance from the production point for Z=2 pfs emitted from* ^{16}*O-Em collisions.*

In Fig. 6.2 λ^*_{had} of Z=2 pfs are plotted as a function of the distance D from the interaction vertex. The solid line shows the He MFP, assuming Glauber model, of

Table 6.2: *The experimental values of hadronic mean free path of He in nuclear emulsion.*

Energy(A GeV)	λ_{had} (cm)	Data Type	Reference
1.88	21.8 ± 0.5	pfs from ^{56}Fe	[171]*
2	19.8 ± 0.75	pfs from ^{40}Ar and ^{56}Fe	[81]
2	20.19 ± 0.7	pfs from ^{40}Ar and ^{56}Fe	[83]
4.5	16.51 ± 1.11	pfs from ^{12}C	[85]*
4.5	12.05 ± 1.15	pfs from ^{12}C	[86]*
1.8	19.52 ± 0.65	pfs from ^{40}Ar	[84]
1-2	21.5 ± 1.0	pfs from ^{40}Ar,^{56}Fe and ^{84}Kr	[82]
60	21.95 ± 1.15	pfs from ^{16}O	[91]
200	21.04 ± 0.94	pfs from ^{32}S	[92]
200	21.98 ± 1.20	pfs from ^{16}O	this exp.
2	20.19 ± 0.7	Primary He beam	[83]
4.5	19.9 ± 0.6	Primary He beam	[85]
-	19.3 ± 1.0	Primary He beam	[81]
-	20.2 ± 1.7	Primary He beam	[81]
-	19.2 ± 0.7	Primary He beam	[81]
12	18.1 ± 0.7	Primary He beam	[130]

* Anomalously shorter mean free path of He nuclei are reported.

21.7 cm. As can be seen from the figure, there is no indication of a shorter MFP in the first few centimetres of the interaction vertex.

6.3.1 Multiplicity of Z=2 fragments

It has been suggested by Bayman and Tang[172] that the presence of the isotope ^{6}He may cause the appearance of an anomalous behaviour in the fragment MFP. The isotope ^{6}He is a particle-stable system with a half life of 0.8 s, and is the isobaric analogue of the 3.56 MeV, T=1 excited state of ^{6}Li. It has a quasi-molecular α+2n cluster structure, with the dineutron cluster lightly bound by only 0.98 MeV. Calculation yields a value for $\lambda(^6\text{He})$ equal to 12.6 cm. A small admixture of ^{6}He can significantly decrease λ below the ^{3,4}He value of 20-22 cm. They further suggested that during peripheral collisions ^{12}C projectiles could be excited to ^{6}He + ^{6}Be binary cluster system which decays into one ^{6}He, one ^{4}He and two protons. Similarly, in the case of ^{16}O, we will need to investigate the MFPs of multiple He fragments produced in ^{16}O-induced interactions at 200 A GeV on the basis of the He multiplicity. In order to test this hypothesis, we divide our ^{16}O-Em collisions into the following channels:

1. 1 He channel - the projectile disintegrates into one Z=2 pfs and singly charged particles;
2. 2 He channel - the projectile disintegrates into two Z=2 pfs and singly charged particles;
3. 3,4 He channel - the projectile disintegrates into three or four Z=2 pfs and singly charged particles;
4. He's + 1 $\text{PF}_{Z\geq 3}$ channel - the projectile disintegrates into one $Z > 2$ pfs and other Z=2 particles.

The parameter λ^*_{had}, as a function of the distance from the production point, is plotted in Fig. 6.3(a)-(d) for 1 He, 2 He, 3,4 He and He's + 1 $\text{PF}_{Z\geq 3}$ multiplicity events respectively. Within their statistical errors, the observed MFPs of all channels, except for 1 He, do not seem to depend upon the He multiplicity in all the

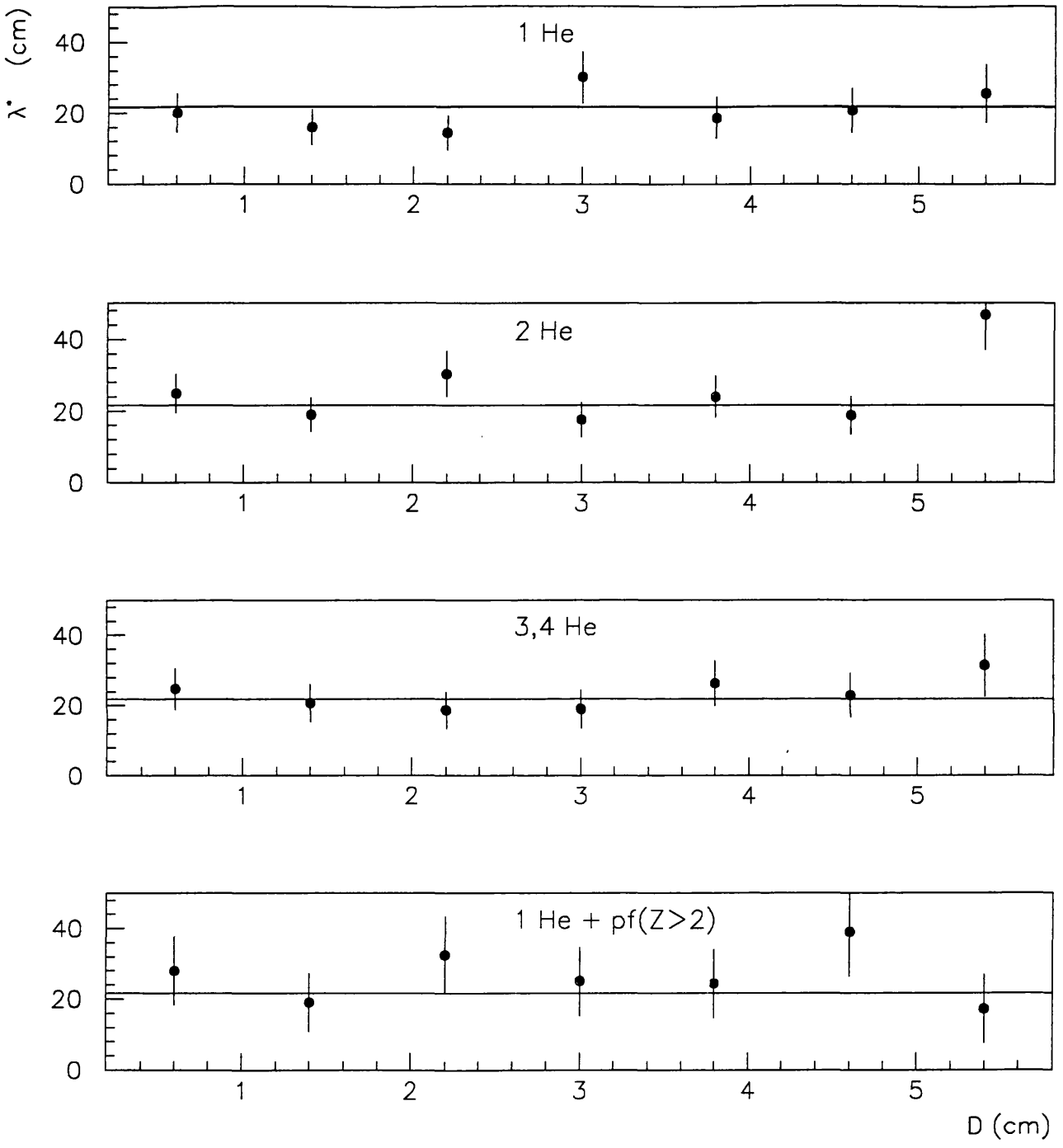

Figure 6.3: λ^*_{had} *as function of the distance from their points of production for (a)1 He, (b)2 He, (c)3,4 He and (d)He's + 1* $PF_{Z\geq 3}$ *multiplicity events. The solid lines represent the He MFP = 21.7 cm assuming the simplified Glauber model.*

path lengths. However, there appears to be a shorter MFP for Z=2 fragments, in the few cm from their production point, originating in events with the emission of one He. In order to see whether this dependence arises from statistical fluctuation, we need to assess the level at which the data are statistically significant.

In Table 6.3, we present the characteristics of the primary hadronic events along with the MFPs of the secondary He tracks on the basis of different He multiplicity. In Table 6.3 we have calculated the MFPs of He fragments in different He multiplicity events for the distances 0.2 cm $\leq D \leq$ 2.5 cm, yielding λ_1^*, and $D >$ 2.5 cm, yielding λ_2^*. The distance 2.5 cm is taken because this value was reported by Friedländer *et al.* [70,71] as the MFP of anomalous projectile fragment component. For each pair of λ^* values , the ratio $F = \lambda_1^*/\lambda_2^*$ is taken. Given the number of events N_1 and N_2, we compute the cumulative probabilities $P(< F)$ under the assumption that λ_1^* and λ_2^* are from the same population. The cumulative probability function $P(< \chi^2)$, which test the compatability of the observed MFPs with those predicted by the simplified Glauber model, are also given.

The values of the cumulative probability function $P(< \chi^2)$ in Table 6.3 show that the MFP of Z=2 fragments from various production channels are consistent with the simplified Glauber model $\lambda(Z$=2)= 21.7 cm. The only exception is the MFP of Z=2 fragments originating in 1 He events at distances $D \leq$ 2.5 cm from the production point. In this case, the MFP is -1.85 standard deviation away from the value of 21.7 cm, a deviation expected to be exceeded by fluctuations about once in thirty one trials($P(< \chi^2)$=0.032). In other words, this deviation will occur 3.2% of the time if the null hypothesis is true. This probability is not statistically significant enough to reject the null hypothesis.

Furthermore, the value of the F parameter for 1 He channel is 0.703 with 106 and 88 degrees of freedom for the two subsets, at distances 0.2 cm $\leq D \leq$ 2.5 cm and $D >$ 2.5 cm respectively. This shows a discrepancy at the level of -1.74 standard deviations with a probability $P(< F)$=0.041. This would imply a deviation expected to be exceeded by fluctuations about once in twenty four trials. However this discrepancy is again not significant enough to confirm the existence of a strong local-MFP effect. El-Nadi *et al.*[85] reported discrepancy of the F parameter which were statistical significant at level of -3.14 standard

Table 6.3: *The topological features observed for primary hadronic interactions of ^{16}O having different He multiplicity and the MFPs of the He fragments at 0.2 cm $\leq D \leq$ 2.5 cm, $D >$ 2.5 cm and all distance from the production point. The table also lists the cumulative probability for the measured MFP to occur as a fluctuation assuming the null hypothesis as well as the simplified Glauber model. The table also gives the value of the ratio F of the two estimates as well as the cumulative probability for F to lie below the observed value(without any assumption about the parameterization of λ). Numbers quoted in parentheses are the number of standard deviations.*

Information of the primary events				Information of the secondary events									
						0.2cm $\leq D \leq$ 2.5 cm		$D >$ 2.5 cm		F-test		average	
He multiplicity	No. of events	$\langle N_s \rangle$	$\langle N_h \rangle$	No. of events	Total track length followed(m)	λ_1^*(cm)	P($< \chi^2$)	λ_2^*(cm)	P($< \chi^2$)	F	P($< F$)	λ_{had}^*(cm)	P($< \chi^2$)
1	404	40.78	7.98	97	19.11	16.53 ± 2.98	0.032 (-1.850)	23.52 ± 3.27	0.723 (+0.593)	0.703	0.041 (-1.738)	19.70 ± 2.20	0.183 (-0.903)
2	257	23.96	4.87	106	24.44	22.90 ± 3.13	0.663 (+0.423)	23.19 ± 2.85	0.711 (+0.557)	0.987	0.476 (-0.060)	23.06 ± 2.11	0.747 (+0.664)
3,4	144	12.90	3.46	95	20.92	21.68 ± 3.27	0.518 (+0.045)	22.32 ± 3.04	0.598 (+0.248)	0.972	0.446 (-0.135)	22.02 ± 2.23	0.571 (+0.178)
1 pf($Z >$2) + He's	158	11.46	2.73	35	8.74	25.78 ± 5.60	0.780 (+0.774)	24.34 ± 4.85	0.725 (+0.598)	1.059	0.573 (+0.184)	24.96 ± 3.67	0.817 (+0.904)
All He	963	27.31	5.61	333	73.21	20.72 ± 1.72	0.290 (-0.552)	23.15 ± 1.65	0.812 (+0.887)	0.895	0.157 (-1.008)	21.98 ± 1.19	0.601 (+0.257)

deviations with a probability $P(< F)$=8.5 x 10^{-4}, while Friedländer *et al.*[70,71] observed a -3.4 deviation of F with a probability $P(< F)$=3.4 x 10^{-4}. It is clear that our discrepancy is two orders of magnitude more likely to occur as a random fluctuation than the other reported anomalous behaviour of projectile fragments.

The average MFP for the Z=2 pf emitted from 1 He channel is 19.70 ± 2.20 cm, whereas the average MFP for all other production channels with the emission of more than one He is 22.92 ± 1.41 cm. The corresponding value of the F parameter is 0.859 with 194 and 472 degrees of freedom for the two subsets, respectively. This shows a small discrepancy at the level of -1.23 standard deviations with a probability $P(< F)$=0.11 which again is not a small probability for random fluctuations.

To see whether there is a difference between the interaction characteristics of Z=2 pf originating in 1 He channel and those produced in the rest of the events, we present in Table 6.4 the topologies of hadronic interactions of Z=2 pf originating in primary hadronic interactions of ^{16}O having different He multiplicities. It is clear that the interaction characteristics of the two groups are consistent, and

Table 6.4: *Topologies of hadronic interactions of Z=2 pfs originating in primary hadronic interactions of ^{16}O having different He multiplicities.*

He Multiplicity of primary events	N_h of secondary events						$\langle N_h \rangle$	$\langle N_s \rangle$	Projectile fragment	
	0	1	2-4	5-8	9-15	≥ 16			none	1 He
1 He	17.5%	10.3%	25.8%	19.6%	14.4%	12.4%	6.19 ± 0.63	16.96 ± 1.72	89.7%	10.3%
>1 He	17.8%	6.8%	24.6%	17.4%	17.8%	15.7%	7.26 ± 0.47	18.28 ± 1.19	92.0%	8.0%
all He	17.7%	7.8%	24.9%	18.0%	16.8%	14.7%	6.95 ± 0.38	17.89 ± 0.98	91.3%	8.7%

hence no correlation between He multiplicity at primary production and secondary interaction characteristics is observed.

Ref.[85,86,172] pointed out that the MFPs of the secondary fragments may be shorter than the normal ones in the few cm from their production for more peripheral events. Generally, events with a lesser number of produced shower particles(N_s) are considered to be more peripheral. This is evident in Table 6.3 where the primary events with higher multiplicity of He have smaller $\langle N_s \rangle$. However even these events do not show any anomalous behaviour of the MFPs of He fragments produced at 200 A GeV ^{16}O-Em collisions. From the data given in Table 6.3, we conclude that the null hypothesis cannot be rejected for any kind of He interaction.

6.3.2 Size of targets

To see whether the target has any influence on the MFP, we divide the Z=2 pfs into three categories

1. pfs originating in collisions with $N_h = 0$;
2. pfs originating in collisions with N_h = 1-6 and
3. pfs originating in collisions with $N_h > 6$.

In Fig. 6.4 values of λ^*_{had} of Z=2 pfs belonging to the three categories are plotted. Within the experimental uncertainties indicated, λ^*_{had} for alpha emitted from N_h = 0 and $1 \leq N_h \leq 6$ events show no systematic variation with D. The systematically shorter MFP for Z=2 pfs emitted from peripheral(N_h=0) interactions reported by El-Nadi *et al.*[85] is not observed. However, in the case of Z=2 pfs emitted from ^{16}O-Em collisions with $N_h > 6$, the MFP are slightly shorter than the average value of 21.98 cm in the first 1 cm from the production vertex. In Fig. 6.5 the distributions of interaction distances D for the Z=2 secondary pfs emitted in interactions with $N_h \leq 0$, N_h=0, $1 \leq N_h \leq 6$ and $N_h > 6$ of the 200 A GeV ^{16}O in nuclear emulsions are shown. The number of interactions observed and expected are compared at different distances from the origin. The expected number of events, indicated by the dotted line in the figure is calculated from the expression $N_{exp} = S_N/\lambda$ where λ for Z=2 pfs is given by simplified Glauber calculation in

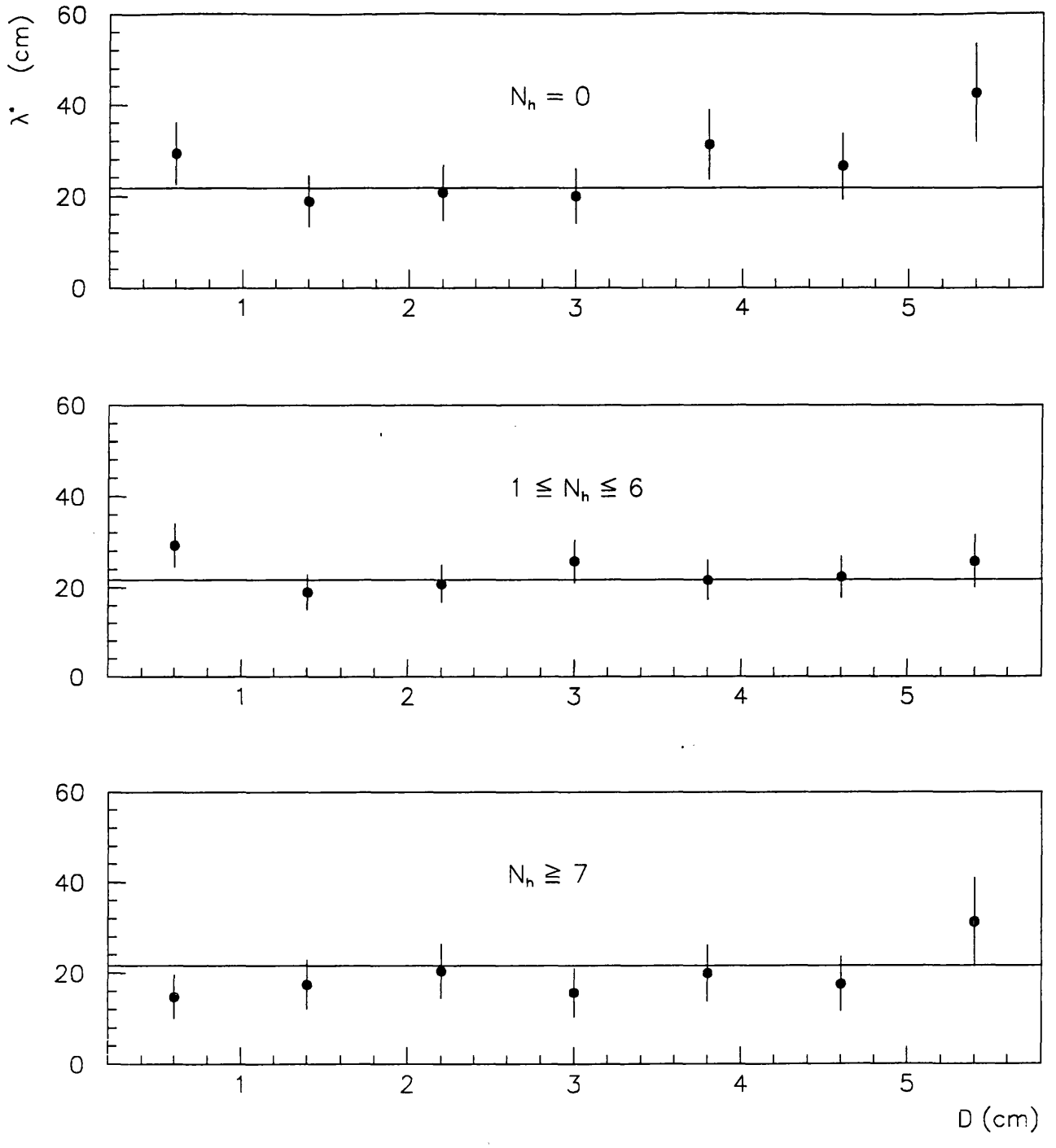

Figure 6.4: *λ^*_{had} versus distance from the production point for Z=2 pfs from collisions with (a)$N_h = 0$, (b)$1 \leq N_h \leq 6$ and (c)$N_h > 6$. The solid lines correspond to $\lambda_{had} = 21.7$ cm.*

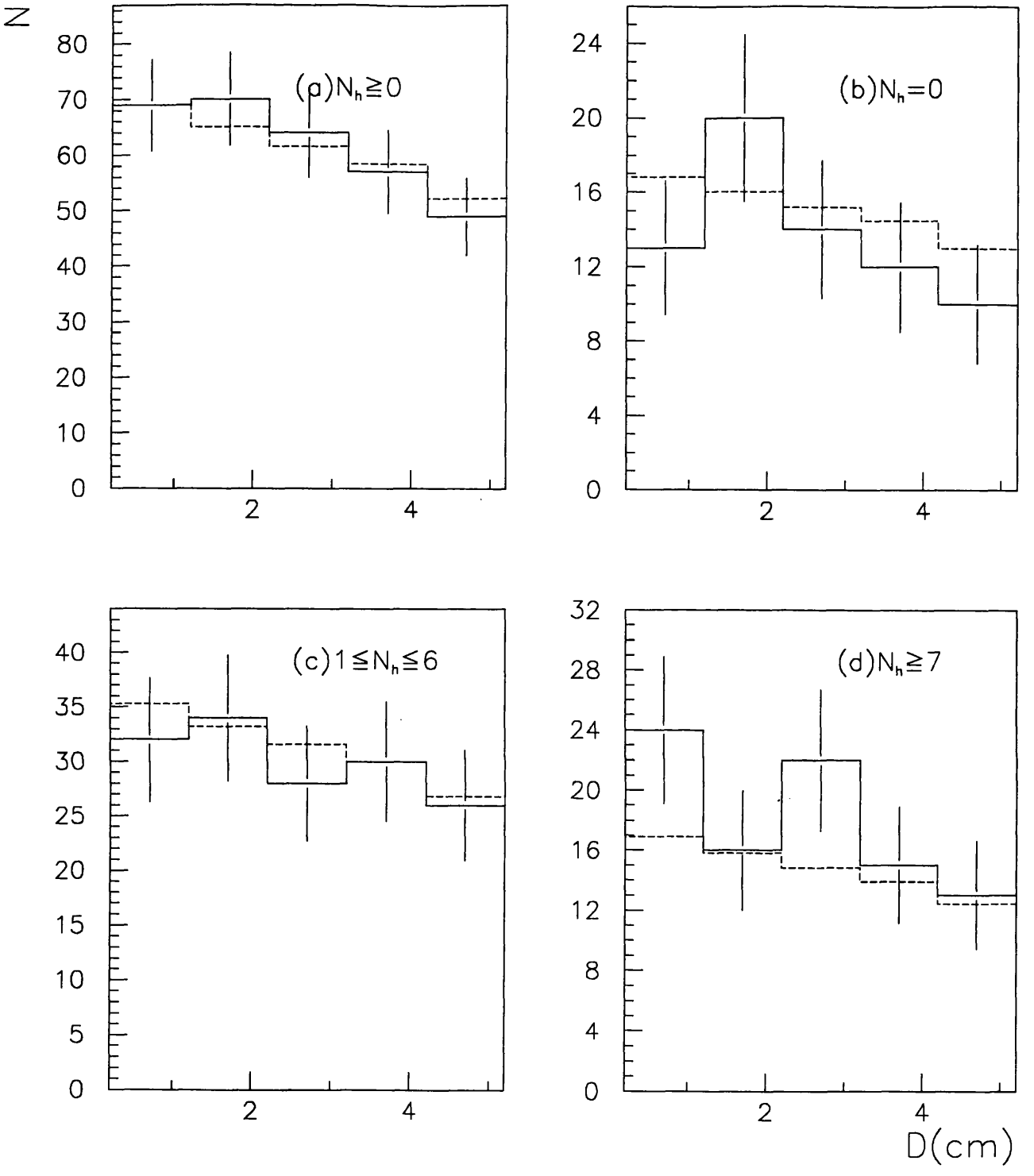

Figure 6.5: *Distributions of interaction distances D for Z=2 pfs (produced in $N_h \leq 0$, $N_h = 0$, $1 \leq N_h \leq 6$, and $N_h > 6$ primary events). Solid line is the experimental observation. The dashed line is the expected value obtained from simplified Glauber calculations.*

Table 4.2 and S_N is the total track length in a given segment. In Fig. 6.5(a)-(c) the experimental values(solid line) shown with statistical errors are within the value predicted (dotted line), and this shows no real anomalous effect. However the observed distribution for $N_h \geq 7$ in Fig. 6.5(d) shows an excess of events over the number predicted, indicating a shorter component in the first centimetre from the production points.

In order to confirm these observations, we have carried out the standard statistical tests again. Table 6.5 lists the cumulative probabilities, $P(< \chi^2)$ and $P(< F)$, for all different multiplicities of N_h. The MFPs are evaluated at two distance intervals, 0.2 cm$\leq D \leq$1.2 cm and $D >$1.2 cm, because in Fig. 6.4(d) the anomalous effect appear to occur in the first cm from the production points. It is seen that MFPs for the N_h=0 interactions do not exhibit any shorter component in the first few cm from the production points. In fact, the MFPs are over 1 standard deviation longer than that of beam nuclei, and this may be attributed to either random fluctuations or scanning inefficiency. On the other hand, the primary events with N_h>6, deemed to be collisions with heavy (AgBr) target nuclei, show a shorter MFP of He in the first interval. This deviation, however, is not statistically significant(λ^*=15.26 $\pm$ 4.43 cm with -1.56 S.D.) and may occur randomly once in seventeen trials. Consequently, this signal cannot confirm the existence of anomalous behaviour for Z=2 projectile fragments. Neither does the MFPs for all N_h events display any sign of anomalon.

From the data in Table 6.5 one observes that the MFP for Z=2 pf produced in collisions of ^{16}O with N_h>6 is 18.28 $\pm$ 2.21 cm whereas in the rest of oxygen interactions its value is 23.48 $\pm$ 1.41 cm. The corresponding value of the F parameter is 0.779 with 192 and 474 degrees of freedom for the two subsets, respectively. This shows a discrepancy at the level of -2.01 standard deviations with a probability $P(< F)$=0.022. The standard statistical tests for the data given in Table 6.5 indicate that there is only a small difference between the MFP values for the two segments(0.2 cm$\leq D \leq$1.2 cm and $D >$1.2 cm) or the interactions with $N_h \leq 6$ and N_h>6 in most cases(the difference never exceeds two standard deviations in all cases). The difference between the two segments and the values of primary He beam predicted by the simplified Glauber model gives also standard deviation less than 1.6. From the same table, we can also see that the average MFP values for each category are comparable with those of primary beam nuclei MFP values.

Table 6.5: *The topological features observed for primary hadronic interactions of ^{16}O having different N_h multiplicity and the MFPs of the He fragments at 0.2 cm $\leq D \leq$ 1.2cm, $D >$ 1.2cm and all distance from the production point. $\langle N_{Z\geq 2}\rangle$ is the average number of spectator fragments with $Z \geq 2$ undeviated from the original beam direction. Numbers quoted in parentheses are the number of standard deviations.*

Information of the primary events				Information of the secondary events									
						0.2cm $\leq D \leq$ 1.2 cm		$D >$ 1.2 cm		F-test		average	
N_h multiplicity	No. of events	$\langle N_s\rangle$	$\langle N_{Z\geq 2}\rangle$	No. of events	Total track length followed(m)	λ_1^*(cm)	P($<\chi^2$)	λ_2^*(cm)	P($<\chi^2$)	F	P($<F$)	λ_{had}^*(cm)	P($<\chi^2$)
N_h=0	217	13.06	1.98	74	18.07	28.08 ± 6.02	0.856 (+1.063)	23.64 ± 2.78	0.764 (+0.720)	1.19	0.739 (+0.639)	24.42 ± 2.52	0.859 (+1.074)
1≤N_h≤6	462	23.15	1.84	163	37.59	23.92 ± 3.84	0.732 (+0.619)	22.85 ± 1.90	0.734 (+0.626)	1.05	0.607 (+0.272)	23.06 ± 1.70	0.791 (+0.811)
N_h≤6	679	19.93	1.89	237	55.66	25.12 ± 3.23	0.855 (+1.056)	23.10 ± 1.57	0.816 (+0.900)	1.09	0.707 (+0.545)	23.48 ± 1.41	0.895 (+1.255)
N_h≥7	284	44.98	1.44	96	17.55	15.26 ± 4.43	0.059 (-1.558)	19.29 ± 2.56	0.173 (-0.941)	0.79	0.176 (-0.931)	18.28 ± 2.21	0.055 (-1.598)
N_h≥0	963	27.31	1.76	333	73.21	21.69 ± 2.61	0.515 (+0.038)	22.06 ± 1.34	0.812 (+0.289)	0.98	0.461 (-0.098)	21.98 ± 1.19	0.601 (+0.257)

El-Nadi *et al.*[85] reported that a significant correlation between N_h at production and at interaction of Z=2 carbon fragments was rigorously established. The probabilities for the production of N_h=0 secondary stars for Z=2 fragments produced in N_h=0 collisions of 4.5 A GeV carbon was about three times higher than for those produced in the rest ($N_h \neq 0$) of the collisions. In order to examine whether such correlation exists in our data sample, we present Table 6.6 which

Table 6.6: *Topologies of hadronic interactions of Z=2 pfs originating in primary hadronic interactions of ^{16}O having different N_h multiplicities.*

N_h Multiplicity of primary events	N_h of secondary events						$\langle N_h \rangle$	$\langle N_s \rangle$	Projectile fragment	
	0	1	2-4	5-8	9-15	≥ 16			none	1 He
N_h=0	15.1%	5.5%	27.4%	19.2%	17.8%	15.1%	7.19 ± 0.84	16.03 ± 1.88	89.0%	11.0%
$1 \leq N_h \leq 6$	19.6%	8.6%	23.3%	18.4%	16.6%	13.5%	6.61 ± 0.52	17.47 ± 1.37	91.4%	8.6%
$N_h > 6$	16.7%	8.3%	26.0%	16.7%	16.7%	15.6%	7.19 ± 0.73	19.71 ± 2.01	92.7%	7.3%
all N_h	17.7%	7.8%	24.9%	18.0%	16.8%	14.7%	6.95 ± 0.38	17.89 ± 0.98	91.3%	8.7%

gives the interaction characteristics of He fragments originating in ^{16}O interactions of various N_h. Although small differences exist between various intervals of N_h at production and at interaction, no significant correlation is observed.

It has been claimed that anomalons are likely to be produced in collisions of peripheral nature: the experiment of El-Nadi *et al.*[85] using 3.7 A GeV ^{12}C projectiles in nuclear emulsion, indicated that Z=2 projectile fragments exhibit anomalous behaviour only in N_h=0 events. Similarly, Ghosh *et al.*[86] reported the MFP of He emitted from the interaction stars of 4.5 A GeV ^{12}C of $N_h \leq 7$ is significantly shorter than for those emitted from stars of $N_h > 8$ in the path-length interval 0-4 cm. Furthermore, the propane bubble-chamber experiment of Gasparian and Grigalashvili[88], with 3.3 A GeV ^{12}C projectiles, showed that anomalons

are observed only when the incident particle suffers no loss either in mass or in charge from the interaction. Yet the data in the present study show that neither interactions with 3 or 4 Z=2 projectile fragments nor the ones with N_h=0, both of which are considered to be most peripheral, exhibit any detectable anomalous behaviour. On the contrary, many more central primary interactions(with only one Z=2 pf or N_h>6) show signals, though statistical insignificant for the rejection of the null hypothesis, for shorter MFP of He at the first few cm from their production points. At relativistic energies, reaction cross-sections seem to depend mainly on the geometrical sizes of the nuclei involved. Therefore, anomalons are suggested[172] to be significantly larger in geometrical size than the corresponding normal nuclei. Some reported MFP of anomalous Z=2 fragment would require the deformed He nuclei to be as large as the uranium nuclei. It seems puzzling that a peripheral interaction can produce such an effect.

6.3.3 Z=2 Fragments of different generations

So far, our analysis has only been applied to secondary Z=2 fragments. Besides comparing MFP at different distances after emission, one can also compare the MFPs of pfs from different generations. Friedländer [71] argued that shorter overall MFPs of pfs in the later generations are to be expected because the relative population of anomalous pfs among interacting particles increases as the potential path(the distance available for observation) decreases.

In order to see whether the MFPs change from generation to generation, we shall compute the F ratio between the MFP of secondary He pfs and that of tertiary and later generations, i.e., $F_{gen} = \lambda^*_{III}/\lambda^*_{II}$. From Table 6.1, one observes that the overall hadronic MFP for secondary He is 21.98 $\pm$ 1.13 cm and for later generation is 25.88 $\pm$ 3.49 cm. Thus, F_{gen}=1.18 and P($< F_{gen}$)=0.841(1.0 standard deviation), with 666 and 70 degrees of freedom for the two subsets, respectively. We therefore conclude that no anomalous behaviour is observed in the MFP of tertiary and later generation He pfs.

In Fig. 6.6(a) we present the values of the MFP for Z=2 tertiary (and later generation) pfs as a function of the distance D from their production points. Within

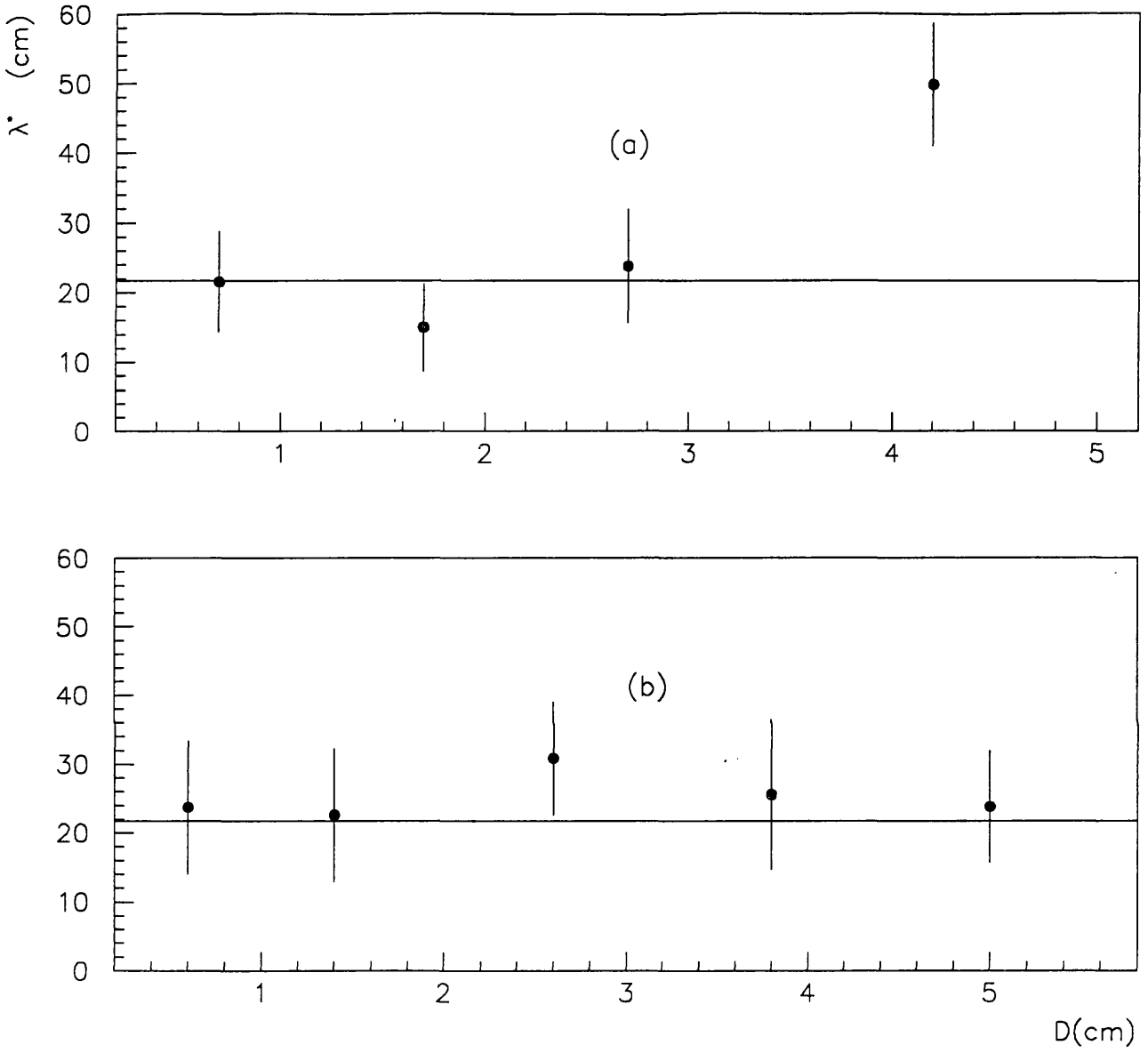

Figure 6.6: λ^*_{had} *versus distance from the production point for Z=2 pfs from (a)secondary(+tertiary...) hadronic interactions and (b)primary electromagnetic dissociation. The solid lines correspond to* λ_{had} *= 21.7 cm.*

their statistical errors, the observed MFPs do not show a shorter component in the first few cm from the production point.

6.3.4 He fragments from projectile EMDs

Most of the studies on anomalons have been concentrated on pfs produced in hadronic interactions of primary nuclei at the energies of several GeV's per nucleon. At these energies, the cross-section for the electromagnetic dissociation of the projectile is insignificant, and thus the availability of 200 A GeV heavy ion beams open up the possibility of studying the MFP of pfs produced in electromagnetic processes.

In this experiment, we observed 365 events(in the first scan) of ^{16}O EMD out of a sample of 3290 primary interactions. From these EMDs, 150 Z=2 pfs were followed. In Fig. 6.6(b) we show the distribution of the MFPs of the He fragments as a function of the distance. Once again, our experimental data do not show any anomalous effects, although the electromagnetic events involve entirely different production mechanism. In Table 6.7, we present the MFP of the He fragments in the distance intervals, 0.2 cm$\leq D \leq$2.5 cm and D >2.5 cm, and their corresponding F parameter. It is observed that no anomalous effect is present in our data sample. The overall MFP of the He fragments, 26.17 $\pm$ 3.90 cm, emerging from EMDs is comparable to that of the hadronic events(λ^{*}_{had}=21.98 $\pm$ 1.13 cm). Our results are in agreement with that of Singh *et al.*[92] who observed that the MFPs of the He fragments produced in collisions of ^{32}S at 200 A GeV are independent of their production mechanism(EMDs).

6.4 Mean Free Paths of $Z \geq 3$ Fragments

To study the dependence of the MFP on distance for $Z \geq$3 fragments, we pool the data on the MFP from different charges by parameterizing $\lambda(Z) = \Lambda Z^{-b}$ eq. 2.3.8, where the charge independent parameters Λ and b are calculated by fitting eq. 2.3.8 to only our own data in Table 6.1 to avoid different scanning bias

Table 6.7: *The MFPs of He fragments emerging from electromagnetic dissociation of primary ^{16}O nucleus at two track length intervals, 0.2≤ D ≤ 2.5cm and D >2.5cm, and their corresponding F-ratio as well as their cumulative probability P. Numbers quoted in parentheses are the number of standard deviations.*

No. of primary EMD	No. of secondary events	Total track length followed(m)	λ^*(cm)	P($<\chi^2$)	F-test F	P($<F$)	average λ^*_{had}(cm)	P($<\chi^2$)
		0.2cm ≤ D ≤ 1.2 cm						
	11	3.28	29.78 ± 6.23	0.918 (+1.39)				
85					1.25	0.727 (+0.60)	26.17 ± 3.90	0.914 (+1.37)
		D > 1.2 cm						
	17	4.05	23.83 ± 5.01	0.753 (+0.69)				

in different experiments. For N_Z secondary events of charge Z and MFP $\lambda(Z)$, we get, using eq. 2.3.8 at fixed b, the maximum likelihood estimate of the charge independent MFP parameter Λ^* for each interval of path length. This is expressed in eq. B.2.1(see Appendix B).

In Fig. 6.7 Λ^* is plotted as a function of D, the distance from the interaction vertex, for $Z \geq 3$ fragments emitted from $N_h \geq 0$, $N_h = 0$ and $N_h \geq 1$ primary interactions of ^{16}O. The solid line is the average value of Λ obtained by fitting eq. 2.3.8 to our own data. The error bars we have assigned to the data points represent one standard deviation assuming the primary beam value for Λ=27.27 cm. In neither case is evidence found for anomalous $Z \geq 3$ fragments. The estimate Λ^* is compatible with the average value except that there appears to be a small fluctuation in the interval 0.2-0.5 cm in the case pf $N_h > 0$. This result can be visualized also by considering the frequency distribution of interaction distances $N(D)$, displayed as Fig. 6.8. The number of interactions observed and expected are compared at different distances from the production points. The expected number of events, indicated by the dotted line in the figure is calculated from the expression $N_{exp} = \sum_{Z=3}^{7}(S_N(Z)/\lambda(Z))$ where $\lambda(Z)$ is given by simplified Glauber

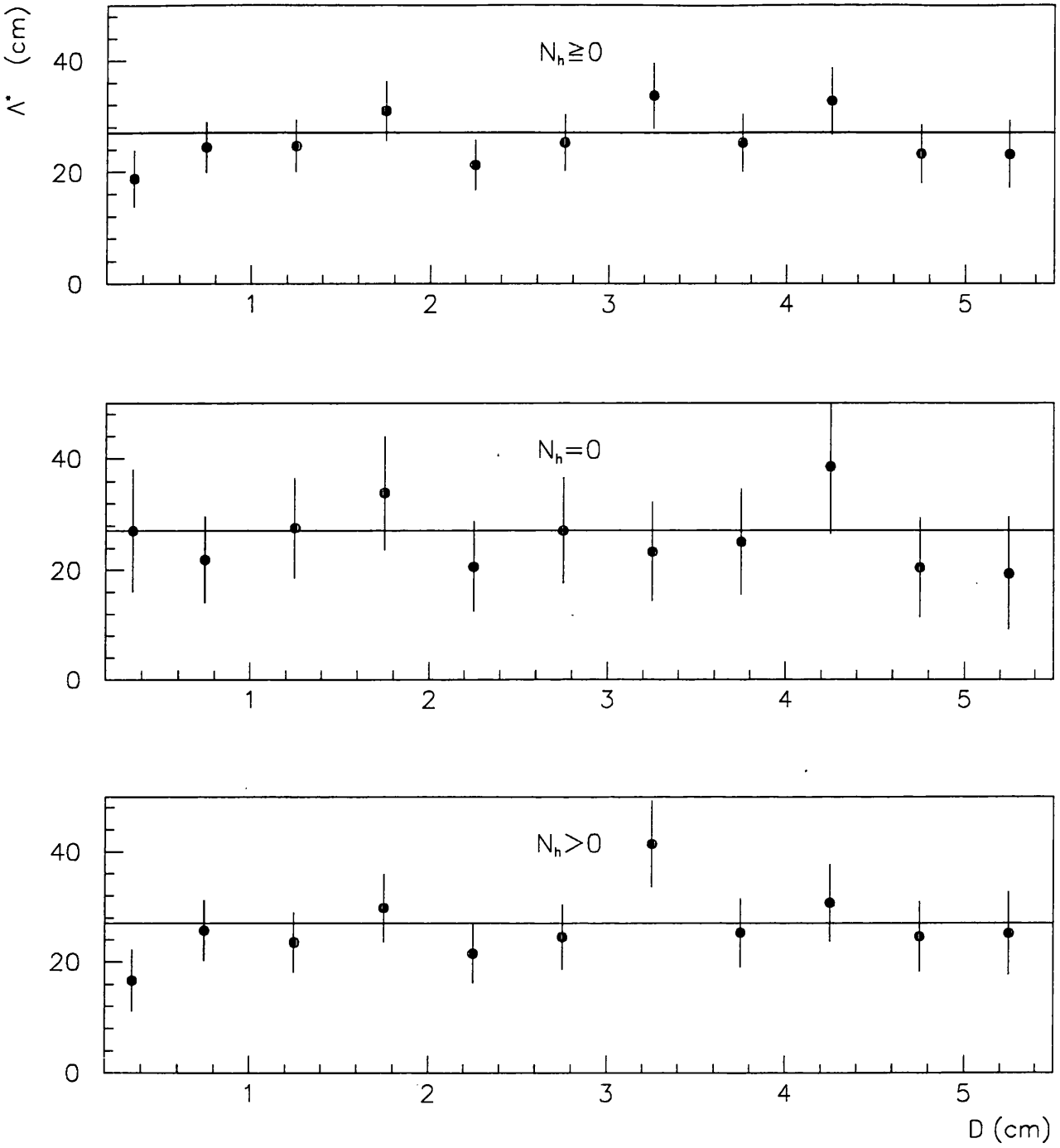

Figure 6.7: *Estimates Λ^* for the MFP parameter Λ at different distances D from the origins of $Z \geq 3$ pfs from interactions with different target groups. The solid line is average value by fitting $\lambda(Z) = \Lambda Z^{-b}$ to the data of the present work.*

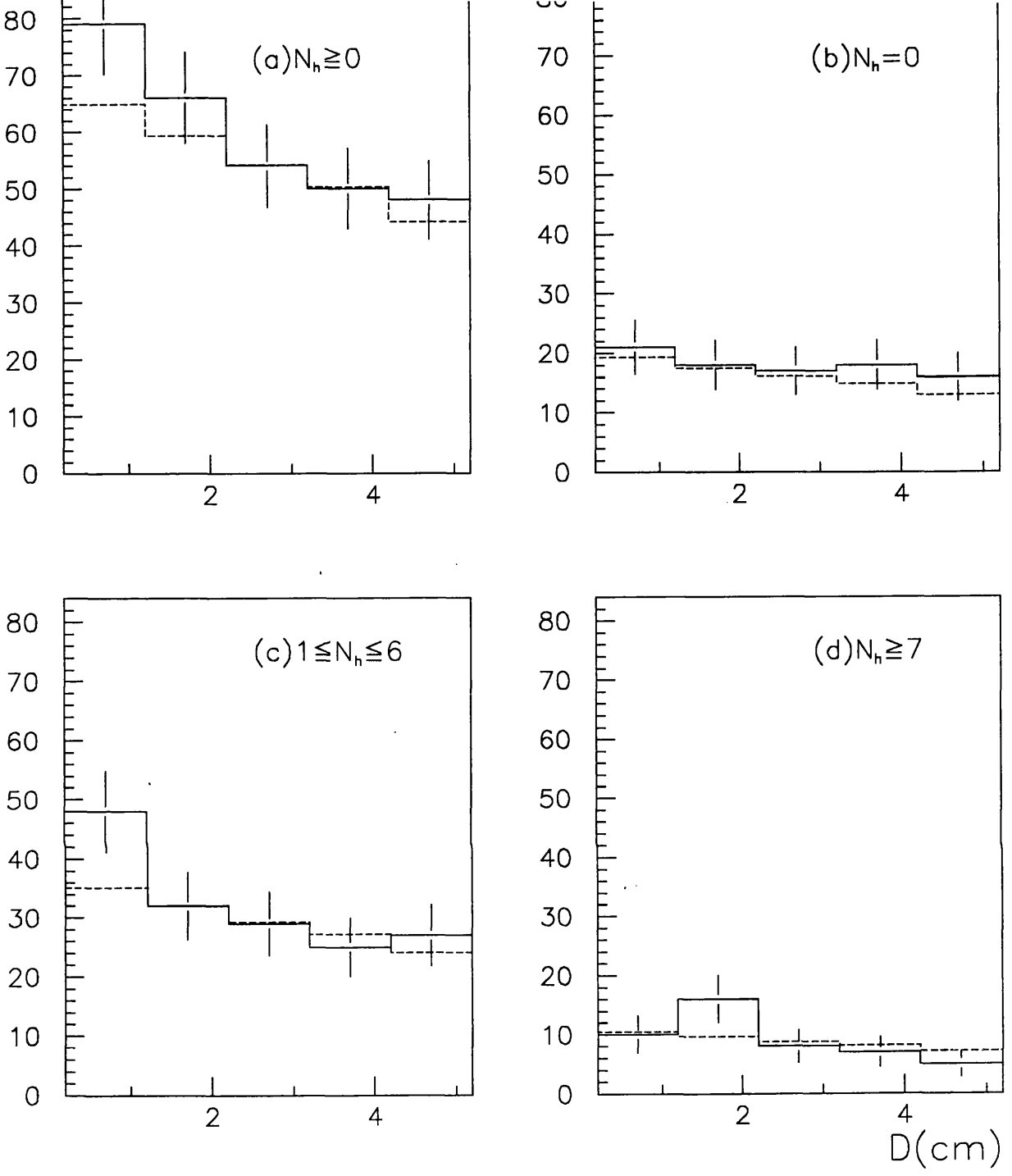

Figure 6.8: *Distributions of interaction distances D for $Z \geq 3$ pfs (produced in $N_h \leq 0$, $N_h = 0$, $1 \leq N_h \leq 6$, and $N_h > 6$ primary events). Solid line is the experimental observation. The dashed line is the expected value obtained from simplified Glauber calculations.*

calculation in Table 4.2, and $S_N(Z)$ is the total track length of a particular charge in a given segment. Again it is observed that there is an excess in the number of secondary interactions in the interval 0.2-1.2 cm for the fragments emitted from interactions with $1 \leq N_h \leq 6$. With a total of 952 $Z \geq 3$ fragments followed over a distance of 42 metres, we expect 299 stars assuming for the MFPs the results of simplified Glauber calculation. In the data, there are actually 313 stars, a fluctuation expected to occur with a probability of 2.1×10^{-1} at the level of 0.81 standard deviations.

In order to check the abnormality of the MFP as a function of distance independent of the validity of eq. 2.3.8, we perform the F-test. The data are divided into two groups: (i) 0.2 cm $\leq D \leq$ 2.5 cm, yielding λ_1^*, with N_1 stars and (ii) $D >$2.5 cm, yielding λ_2^*, with N_2 stars. The results are summarized in Table 6.8. The standard statistical tests for the data indicate that there is only a small difference between the MFP values for the two segments(0.2 cm $\leq D \leq$ 2.5 cm and $D >$ 2.5 cm) in most cases(the difference never exceeds two standard deviation in all cases). Note that no statistically significant deviations for the MFP of $Z \geq 3$ fragments in the two segments from that of the simplified Glauber model is observed. From the same table also see that the average MFP values for each fragment charge are comparable with those predicted by the simplified Glauber model.

Besides considering the MFP of each fragment charge individually, we can also use the test mentioned in sec. B.2(Appendix B) for comparison of many estimated MFPs[71]. Using eq. B.2.2 and B.2.3, we get g^2 for the MFPs of $Z \geq 3$ fragments in the first segment, 0.2 cm $\leq D \leq$ 2.5 cm, to be 15.07 with 10 degrees of freedom. This gives the cumulative probability for g^2 to lie above the observed value(the larger the departure from the expected λ^*'s, the higher the value for g^2) $Q(> g^2)$ = 0.132 as the chance for random fluctuation, assuming no anomaly. Similarly, we can apply the same test to the $P(< F)$ values and get g^2 = 15.43 with 10 degrees of freedom. Assuming that both λ_i^*'s in the two segments belong to the same population, the probability for the differences to occur as random fluctuation is 0.114.

Our results indicate no statistically significant deviations for the MFP of $Z \geq$ 3 projectile fragments from that of the expected values assuming the simplified

Table 6.8: *Detailed experimental information used in the F-test for the comparison of estimated MFPs at 0.2 cm $\leq D \leq$ 2.5 cm and at $D >$ 2.5cm from the origin of the projectile fragments(Z=3-7). For each fragment charge the table lists the track length followed within the segment under consideration, the number of interactions occurring in the segment, the estimated MFP, and the cumulative probability for this value to occur as a fluctuation assuming the null hypothesis as well as the simplified Glauber model. The table also gives the value of the ratio F of the two estimates as well as the cumulative probability for F to lie below the observed value(without any assumption about the parameterization of λ). Numbers quoted in parentheses are the number of standard deviations.*

PF charge	0.2 cm $\leq D \leq$ 2.5 cm				$D >$ 2.5 cm				Average		F-test	
Z	Length(m)	Stars	λ_1^*(cm)	$P(<\chi^2)$	Length	Stars	λ_2^*(cm)	$P(<\chi^2)$	λ^*(cm)	$P(<\chi^2)$	F	$P(<F)$
3	2.23	13	17.16 ± 4.47	0.627 (+0.325)	2.72	18	15.13 ± 3.79	0.428 (-0.182)	15.98 ± 2.89	0.508 (+0.019)	1.13	0.642 (+0.363)
4	2.22	20	11.11 ± 3.33	0.120 (-1.176)	2.45	16	15.30 ± 3.72	0.576 (+0.191)	12.97 ± 2.48	0.225 (-0.757)	0.73	0.167 (-0.965)
5	2.72	23	11.82 ± 2.96	0.216 (-0.785)	2.92	23	12.68 ± 2.96	0.322 (-0.464)	12.25 ± 2.09	0.176 (-0.929)	0.93	0.406 (-0.238)
6	6.33	56	11.30 ± 1.84	0.081 (-1.400)	7.22	43	16.80 ± 2.10	0.917 (+1.382)	13.69 ± 1.39	0.481 (-0.047)	0.67	0.025 (-1.967)
7	6.21	49	12.67 ± 1.89	0.406 (-0.238)	6.90	52	13.27 ± 1.83	0.533 (+0.084)	12.98 ± 1.31	0.554 (-0.137)	0.95	0.409 (-0.229)

Glauber model. As far as we know, the MFPs of the secondary projectile fragments with $Z \geq 3$ produced in hadronic interactions at ultra-relativistic energies(200 GeV per nucleon) have not been investigated as a function of the distance from their production points prior to the present work. However, our results agree with those of Ismail *et al.*[83] and Beri *et al.*[84] who did not observe any dependence of the MFPs of $Z \geq 2$ fragments at $\approx$ 2 A GeV on the distance from the production point.

Contradictory results for fragments(Z=2-26) emitted from $\approx$ 2 A GeV ^{16}O and ^{56}Fe projectiles were observed by Friedländer *et al.*[70,71]. Similarly Aggarwal *et al.*[73,77] reported anomalous MFP for interactions of projectile fragments produced by primary collisions of ^{40}Ar and of ^{56}Fe at 1.52 A GeV(Z=3-26) and of ^{84}Kr at 1.52 A GeV(Z=15-36). Khan *et al*[89] also observed anomalously shorter MFP for fragments(Z=3-6) produced in 4.5 A GeV ^{12}C-Em collisions.

Our results imply the non-existence of anomalons for fragments(Z=2-7) produced in 200 A GeV ^{16}O-Em collisions and seem to disagree with data reported by other authors mentioned above. The obvious suspicion is that the interpretation of this experiment may be influenced by systemic errors. One objection may be the rejection of data at $<$ 2 mm from the production point. However, all anomalously shorter MFP were reported at a distance of at least 1.5 cm from their production point and thus imposing a cutoff distance at 2 mm should not prevent us from observing the phenomenon. Indeed Friedländer *et al.*[71] repeated their analysis by selecting cutoff distances up to 5 mm and found no changes in their conclusions. Other possibilities include systematic errors in distance and charge measurements as well as differential scanning efficiency. Since our results are collected by scanners and checked by physicists independently in laboratories at London, Dublin, Rome, Torino and Salerno, it seems unlikely that the systematic errors can produce such an effect. For track lengths on the order of 2 mm or more, accuracy is good enough to detect unambiguously a difference of one unit of charge. By making systematic shifts of 1 charge unit into the data, the relative values of the observed MFPs are not significantly affected. Furthermore, since all anomalous MFP are reported for fragments produced at relativistic energies(1 to 4.5 GeV), it may be the case that there is an upper energy limit for the production of anomalons. In order to verify this point, further investigations at different energies will be necessary. Finally, some of our analysis base on very poor statistics and clearly more experimental data are needed.

Nevertheless, the above analysis has its limitations. If anomalous projectile fragments are produced at small abundance or with mean free paths merely slightly shorter than that of beam nuclei or both, the preceding analysis would not resolve them from normal statistical fluctuations. Therefore, it is important to conclude this study with an estimate of its sensitivity in detecting anomalons.

El-Nadi *et al.*[85] reported the existence of an anomalous mean free path at the level of about 4 standard deviations shorter than that expected of normal Z=2 beam nuclei. They concluded that their results were consistent with an anomalous component with $\lambda_{anom} \approx 25$ mm, the fraction of this component α being estimated to be 20% and 5-6% for the N_h=0 and all N_h samples, respectively.

The effect on the observed mean free path of He ions in the first 25 mm from the primary vertex has been computed for a variety of λ_{anom} for anomalons present at various concentration, α. The curves in Fig. 6.9 show respectively the area in the (α, λ_{anom}) plane where an anomalous signal may be detected at a level of 3 or 4 standard deviations in our sample. For example, if the value λ_{anom}=25 mm reported by El-Nadi *et al.* is used, anomalons must be produced at a rate of at least 4.4%(3 standard deviations) or 6.0%(4 standard deviations) in order to be detected.

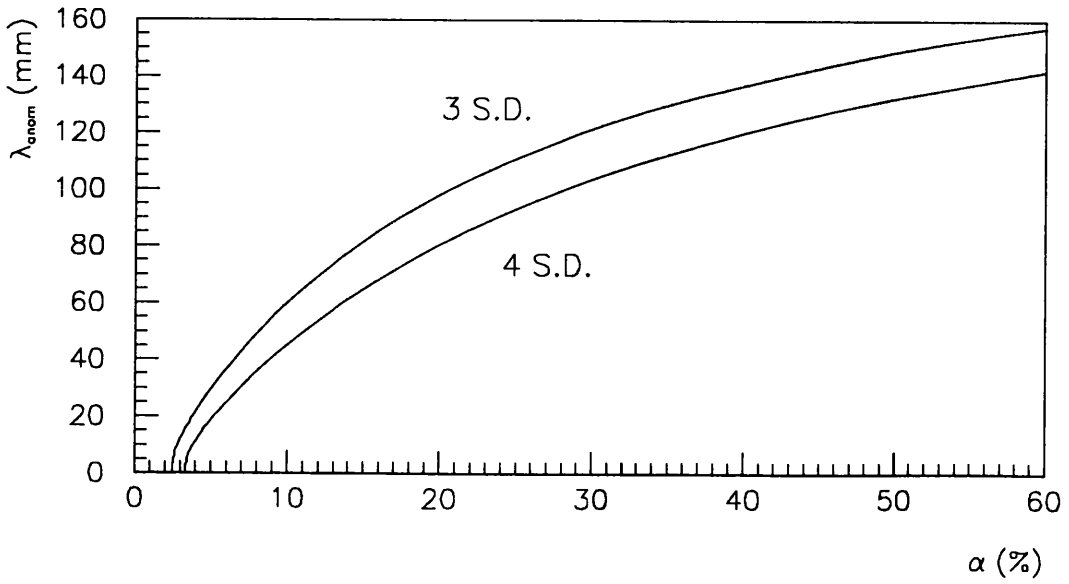

Figure 6.9: *Variation of the abundance of anomalons and their mean free paths for the observed mean free paths of Z=2 fragments to be 3 and 4 standard deviations shorter than normal nuclei in the first 25 mm from the primary vertex.*

Chapter 7

Conclusions

This thesis has described a study of the hadronic and electromagnetic interactions of 200 A GeV ^{16}O and ^{32}S ions in nuclear research emulsion. The main aim of this study was to understand the 'normal' features of these interactions at ultra-relativistic energy.

The hadronic mean free paths for primary ^{16}O and ^{32}S ions as well as projectile fragments of $2 \leq Z \leq 7$ produced by an initial oxygen beam have been measured. Although the statistics are in many cases poor and the isotopic constitutions are not known, there is reasonable agreement with expected values calculated from a simplified Glauber model.

Both the oxygen and sulphur hadronic interactions exhibit very similar general features, the greater the disruption of the projectile nucleus, the greater that of the target and the higher the number of shower particles produced. The measurement of the charges of the projectile fragments from oxygen interactions has enabled these correlations to be clearly demonstrated.

The low-energy fragments(black tracks) are shown to arise predominantly from isotropic evaporation from the target nuclei, while the grey tracks are strongly peaked forwards, as to be expected if arising from knock-on processes. The angular distributions of grey tracks, obtained in the present experiment and previous studies, display independence from the energy or nature of the projectile and the

centrality of the collision. Several models of nucleus-nucleus interactions currently used fail to reproduce the observed distribution.

Although the average numbers of heavy prongs, $\langle N_h \rangle$, are similar for hadronic interactions in emulsion produced by projectiles ranging from proton to ^{32}S ions, the shapes of their N_h distributions are different. The apparent anomaly is explained in part by the more peripheral nature of ion interactions and also by the growing importance of the contribution of light target nuclei in the emulsion, especially hydrogen, to the cross-section with increasing projectile mass. Moreover, as the projectile mass increases, the N_h distributions show an increasing trend of separation between contributions from collisions with light and heavy emulsion nuclei. For a given ion projectile, the shapes of the N_h distributions of subsamples, selected according to the type and/or the number of forward-going projectile fragments, are very different.

Similarly the distributions of grey tracks show that with increasing projectile size it becomes easier to distinguish the contributions from light and heavy nuclei. On the other hand, the distributions of black tracks are relatively insensitive to the variation of the ion projectiles, but the forward velocity of the residual target nuclei tends to increase with the size of the projectile. These trends are consistent with the geometrical picture in which at a given impact parameter the increase in projectile size increases the number of participant nucleons.

The correlation between $\langle N_b \rangle$ and N_g is independent of projectile mass and is linear at small N_g indicating the low degree of cascading in the target nucleus. However $\langle N_b \rangle$ becomes saturated at high N_g values due to the 'finiteness' of the target nucleus as well as the high excitation energies of the residue nuclei resulting in the emission of fragments having energies beyond the energy limit of black tracks.

The mean number of shower particles, $\langle N_s \rangle$, rises with increasing projectile mass as expected. The multiplicity correlations between the shower and grey particles are given by the linear relation $\langle N_s \rangle = a + bN_g$. The coefficients grow with projectile mass as well as the centrality of collisions. In addition, the distribution $\langle N_s \rangle / D$, where D is the dispersion, increases linearly with the increase in

N_g, regardless of projectile size. Such behaviour indicates that the fluctuations in the number of intranuclear collisions decline with increasing centrality. This interpretation is supported by the fact that in central or near-central interactions both pion production and evaporation energy depend primarily upon $\sum Z_i$, the sum of the charges of the projectile fragments, and not on the detailed nature of the projectile fragmentation, while in peripheral collisions the values of $\langle N_h \rangle$ and $\langle N_s \rangle$ fluctuate with the projectile breakup mode for a given $\sum Z_i$.

For those hadronic interactions in which the primary oxygen and sulphur ions are completely disrupted, their N_h distributions indicate that the contribution from light nuclear targets is significant. A study of the multiplicities and rapidity distributions of a subset of these interactions in which there is no apparent low-energy target fragmentation(N_h=0) shows that for the oxygen sample these events arise dominantly from interactions on free protons, while for sulphur they are almost exclusively from (C,N,O) target nuclei. The probability for oxygen projectile nuclei to overlap completely light target nuclei and the collision of a sulphur projectile with a proton to result in its complete disruption must both be small, and this has been borne out by the observations. On the other hand the rapidity distributions of the shower particles rule out this subsample as arising from electromagnetic or diffractive dissociation processes.

Besides hadronic interaction, electromagnetic dissociation processes have been shown to contribute significantly to the total nuclear inelastic cross-section of ultra-relativistic heavy ions traversing through nuclear emulsion. In this study, the pure EMD cross-section due to the charge-changing channels is at the level of 13 % of the pure hadronic cross-section for ^{16}O and 22 % for ^{32}S. Our results are in excellent agreement with those other heavy-ion experiments, which employ completely different techniques and only infer indirectly the EMD cross-section from the observed increase in the total charge-changing cross-section with increasing energy of the projectile.

The set-up of our experiment does not allow a thorough detection of neutrons and separation of isotopes, and only the components of the momentum transverse to the beam direction may be estimated. Furthermore EMD events showing pion production are either eliminated from the sample by the scanning procedure or

are misclassified as hadronic in origin. However, the present experiment provides the opportunity for the simultaneous study of a large number of different photoreactions on a given nuclear species using high-energy ions as targets for a flux of comparatively low-energy photons, which would otherwise be difficult in direct photoproduction experiments.

Both the total and the various individual integrated photonuclear cross-sections have been determined by using the estimated energy release in each interaction and assuming a Weizsäcker-Williams spectrum of virtual photons. When compared with results from direct photodisintegration or photon emission experiments, there is good agreement between our data and the directly measured (γ, p) cross-sections, especially in the giant resonance region. However, the situation with respect to the total integrated cross-section measurement is far less clear. After due allowance has been made for those not observed channels involving only the emission of neutrons, our integrated cross-section is in reasonable agreement with the results of Ahrens *et al.*[145] for ^{16}O. However, our values are some 40% greater than the reassessed values up to photon energies of 40 MeV presented in the review of $\gamma-^{16}$O by Fuller[144].

In addition the integrated photonuclear cross-section for the reactions (γ, α) in both oxygen and sulphur are much larger than those observed in direct photon experiments. Contributions from misidentified interactions such as (γ, ^{3}He) or (γ, αn) or from an enhanced effect due to virtual photons with E2 multipolarity do not account for the large discrepancy found. However, in the oxygen sample of hadronic interactions, events have been found to satisfy the kinematics of p(^{16}O, C He p). An eikonal distorted-wave impulse approximation(DWIA) estimate of the target A dependence of strong interaction diffractive dissociation suggests that, on the basis of these hydrogen data, most of the EMD (C, α) final states may in fact be of hadronic interaction origin. A detailed examination of events of the type ^{32}S p $\rightarrow$ ^{28}Si He has not been carried out. In addition a theoretical estimate of the absolute cross-section for the low excitation (Si He) states of ^{32}S is not possible because of poor knowledge of the electromagnetic transition form factors for the ^{32}S nucleus.

Finally our data show no indication of anomalons in the He and $Z \geq 3$ fragmentation-charge groups. Although in some occasions the mean free path

of the He projectile fragments is found to be shorter than that of beam nuclei, these deviations are not unexpected within statistical limits. Hence we conclude that in our sample we do not observe anomalons produced at a rate exceeding 6% with an anomalous mean free path of 25 mm.

Appendix A

Estimate of Diffractive Dissociation Cross-section

In the distorted wave impulse approximation (DWIA) for the excitation of nucleus B in the reaction $A + B \rightarrow A + B^*$, the transition from the ground to excited state is assumed to take place in a single step but with purely elastic distortion coming before and after the transition. At high energies it is legitimate to evaluate such distortion in the eikonal approximation[173,174], the resulting amplitude then corresponding to the dominant subset of terms given by the Glauber theory[115].

If we neglect the spin and isospin dependence of the high energy nucleon-nucleon amplitudes $f_{NN}(q)$ then the amplitude for the excitation of a state of angular momentum ℓ and projection m in nucleus B is

$$F_{\ell m}(\vec{q}) = \sqrt{4\pi}\, f_{NN}(0) \int e^{i\vec{q}\cdot\vec{r}}\, D(b)\, Y_{\ell m}(\hat{r})\, \rho_\ell^{tr}(r)\, d^3r, \qquad \text{(A..1)}$$

where it is assumed that both A and B are of spin zero.

In the eikonal approximation the trajectory is a straight line at constant impact parameter vector $\vec{b}$ so that in the integration $\vec{r} = (\vec{b}, z)$. The distortion factor

$$D(b) = e^{i\chi(b)} \qquad \text{(A..2)}$$

is then given by an integral over the momentum transfer $\vec{q}$,

$$\chi(b) = \frac{A\,B}{2\pi^{3/2}} \int e^{-i\vec{q}\cdot\vec{b}}\, S_A(q)\, S_B(q)\, f_{NN}(q)\, d^2q. \qquad \text{(A..3)}$$

Here S_A and S_B are the ground state point matter form factors of the two nuclei with A and B nucleons respectively.

To avoid frame transformations the amplitudes are normalised to the momentum transfer such that

$$\left(\frac{d\sigma}{dq^2}\right)_{\ell m} = |F_{\ell m}(\vec{q})|^2 . \qquad \text{(A..4)}$$

In the absence of distortion, $D(b) = 1$, it is convenient to quantise along the direction of the momentum transfer vector $\vec{q}$ and in this limit one recovers the plane wave impulse approximation result

$$F^{pw}_{\ell m}(q) = A\,B\,\sqrt{2\ell+1}\,i^{-\ell}\,S_A(q)\,S^{tr}_B(q)\,f_{NN}(q)\,\delta_{m,0} \qquad \text{(A..5)}$$

where $S^{tr}_B(q)$ is the transition matter form factor to the excited state.

The comparison of equations (3.1) and (3.5) allows us to evaluate the effective nuclear transition density

$$\rho^{tr}_\ell(r) = \frac{\sqrt{4\pi}}{(2\pi)^3}\,A\,B\int S_A(q)\,S^{tr}_B(q)\,\frac{f_{NN}(q)}{f_{NN}(0)}\,j_\ell(qr)\,q^2 dq, \qquad \text{(A..6)}$$

which therefore depends upon the shape of the nucleon-nucleon amplitude as well as nuclear structure information.

At high energies the nucleon-nucleon amplitude is dominated by the imaginary part and the diffraction peak may be parameterised as

$$f_{NN}(q) = \frac{i\sigma_{NN}}{4\sqrt{\pi}}\,e^{-\beta^2 q^2/2}, \qquad \text{(A..7)}$$

where, with the normalisation of equation (3.4), σ_{NN} is the total nucleon-nucleon cross section.

Appendix B

Statistical Treatment of Mean Free Path

Since its first discovery, the problem of the anomalously short MFP of pfs has been plagued by the small statistical samples involved, which caused a general mistrust about the reality of the effect. The solution to this problem lies in an exact statistical treatment, which should enable one to extract the maximum amount of information from the data available. This means that one has to test the null hypothesis which in physical terms can be stated as that pfs are just ordinary nuclei, with no exceptional properties. Such a test is a test of significance designed to assess the strength of the evidence against the null hypothesis. The term *null hypothesis* is abbreviated as H_0 and stated in terms of some population parameters. In our case the null hypothesis is

$$H_0 : \lambda_1 = \lambda_2 = ... = \lambda_i \qquad \text{(B..1)}$$

where λ_i's are the mean free paths of fragments with the same charge originating in different samples.

B.1 Analysis of projectile fragments with the same charge

Suppose that the null hypothesis is rejected and anomalons do exist amongst the pfs. Consequently, the γ will not be independent of x but may be anomalously

large when x is smaller than a few centimetres. In order to test the existence of this effect, one needs to measure the fractions of tracks with interactions between $x + \frac{1}{2}dx$ and $x - \frac{1}{2}dx$ for very small values of dx. For an emulsion detector, this would require enormous efforts to identify and measure each track. Instead the average values of $\gamma(x)$ for finite intervals(d_1,d_2) are estimated. Such an estimate is labelled as a function of $D = \frac{1}{2}(d_1 + d_2)$ by γ^*, and the associated local MFP by $\lambda^*(\equiv 1/\gamma^*)$. Any significant deviation of these averages as the finite interval is moved along the track will provide evidence for the x-dependence of γ and hence the existence of anomalons in the pfs.

In an infinite detector, each pf interacts, and thus the number of interactions is identical to the number of pfs. However, our detector in reality is finite. It can be shown [71,169] that λ^* is a consistent estimate for the MFP λ which is independent of whether the detector is finite or not. Throughout this thesis, the MFP is defined as the ratio:

$$\lambda^* = S_N/N \tag{B.1.1}$$

where S_N is the sum of the total path length followed for both the interacting and the noninteracting particles, and N is the number of interactions. It can be shown[71,169] that the probability distribution for λ^* is

$$f_N(\lambda^*)d\lambda^* = \frac{(N/\lambda)^N}{(N-1)!}(\lambda^*)^{N-1}e^{-N\lambda^*/\lambda}d\lambda^*, \quad (N \geq 1) \tag{B.1.2}$$

and the mean value of λ^* and its standard deviation are

$$\langle\lambda^*\rangle = \int_0^\infty f_N(\lambda^*)\lambda^* d\lambda^* = \lambda \tag{B.1.3}$$

$$\sigma = [\langle(\lambda^*)^2\rangle - \langle\lambda^*\rangle^2]^{1/2} = \lambda/N^{1/2} \ . \tag{B.1.4}$$

The variation of λ^* with distance from the interaction vertex D is determined by dividing each track into finite intervals and calculating λ^* using eq. B.1.1 for each interval.

Furthermore, the distribution in eq. B.1.2 is a Γ distribution of order N and can be transformed to a χ^2 distribution[71,169],

$$W(h^2)dh^2 = \frac{1}{2^N(N-1)!}(h^2)^{N-1}e^{-h^2/2}dh^2 \tag{B.1.5}$$

and its cumulative probability function is

$$P(< h^2) = \int_0^{h^2} W(t)dt \tag{B.1.6}$$

where the quantity

$$h^2 \equiv \frac{2S_N}{\lambda} = \frac{2N\lambda^*}{\lambda} \tag{B.1.7}$$

is distributed like χ^2 with $2N$ degrees of freedom. This can be used to find the goodness of fit and test the null hypothesis, the confidence level of a given result. Yet this analysis has one disadvantage: λ is unknown. Using eq. 2.3.8 or the simplified Glauber model will immediately make assumptions about the functional dependence of λ.

Friedländer *et al.*[71] have introduced an analysis which does not involve eq. 2.3.8 and can be used for small samples in which each individual Z value is considered separately. Consider two non-overlapping intervals (d_1, d_1') and (d_2, d_2') along each track, and let (S_{N_1}, N_1) and (S_{N_2}, N_2) respectively denote the total track length and number of interactions in each interval. A ratio F is defined as

$$F \equiv \frac{\lambda_1^*}{\lambda_2^*} = \frac{S_{N_1}/N_1}{S_{N_2}/N_2} = \left[\left(\frac{2S_{N_1}}{\lambda}\right) / \left(\frac{2S_{N_2}}{\lambda}\right)\right] \frac{N_2}{N_1} = \left(\frac{h_1^2}{2N_1}\right) / \left(\frac{h_2^2}{2N_2}\right). \tag{B.1.8}$$

Suppose that (S_{N_1}, N_1) and (S_{N_2}, N_2) belong to a population of measurements, each of them having N_1 interactions in (d_1, d_1') and N_2 in (d_2, d_2'). Assuming the validity of the null hypothesis, i.e., both intervals being governed by the same MFP, the ratio obeys the so-called F or variance ratio distribution[170]

$$f_{N_1N_2}(F) = \frac{N_1^{N_1} N_2^{N_2}}{\Gamma(N_1)\Gamma(N_2)/\Gamma(N_1+N_2)} \frac{F^{N_1-1}}{(N_2+N_1F)^{N_1+N_2}} \ . \tag{B.1.9}$$

To see whether the measured ratios are consistent with the F distribution, and thus with the null hypothesis, the cumulative distribution function(CDF) $P_{N_1N_2}(F)$ is used and defined by

$$P_{N_1N_2}(F) = \int_0^F f_{N_1N_2}(F')dF' \ . \tag{B.1.10}$$

It has the general property of CDF's that it is uniformly distributed between 0 and 1. Therefore, the mean value of $P_{N_1N_2}(F)$ is $\frac{1}{2}$ and its standard deviation is $(12)^{-1/2}$. If anomalons exist, one would expect $P_{N_1N_2}(F) < \frac{1}{2}$.

B.2 Analysis of projectile fragments with different charges

Since the number of pfs of a particular Z value in each distance interval may be rather small, statistical fluctuations will reduce the usefulness of the above method. In order to increase the statistics it is necessary to analyze the data for different Z values together. This would require knowing the specific Z-dependence of the MFP and the approximation of eq. 2.3.8 is therefore assumed. For each distance interval, λ^* is determined for each Z value, and $\Lambda^*(Z) = Z^b\lambda^*$ is computed. These Λ^* are then averaged over Z, weighted according to the number of interactions $N(Z)$ in the distance interval under consideration; i.e.,

$$\Lambda^*(D) = \frac{\sum_z N(Z)\Lambda^*(Z)}{\sum_z N(Z)} = \frac{\sum_z N(Z)Z^b\lambda^*(Z)}{\sum_z N(Z)} = \frac{\sum_z Z^b S_N(Z)}{\sum_z N(Z)} \qquad \text{(B.2.1)}$$

Since $N(Z)$ may be very small or equal to zero in some cases, the last equality in eq. B.2.1 is used to calculate $\Lambda^*(D)$. This latter quantity is compared with the value of Λ in order to see if there is any significant anomalous behaviour.

Furthermore, we can also construct a test statistic for comparison of many estimated MFPs[71]. If there are n values of estimated MFPs λ_1^*,λ_2^*,.....,λ_n^* with N_1.....N_n stars ,and let λ_1 .....λ_n be the MFPs that we expect, we first calculate for each λ^* the cumulative distribution function $P(h^2|\lambda_i, N_i)$[eq. B.1.6]. Since each P is uniformly distributed between zero and one, its logarithm is exponentially distributed and thus the quantity

$$g_i^2 \equiv -2lnP \qquad \text{(B.2.2)}$$

obeys a χ^2 distribution with two degrees of freedom. Because of the additivity of χ^2 variables, the quantity

$$g^2 \equiv \sum_{i=1}^{n} g_i^2 \qquad \text{(B.2.3)}$$

is itself χ^2 distributed with 2n degrees of freedom and can be used to test the consistency of the λ^* values with their expectations. Similarly, the same test can be used to pool the information from many pairs of (λ_1^*,λ_2^*) values, using eq. B.1.8 and B.1.10. $P(h^2|\lambda_i, N_i)$ in eq. B.1.6 is replaced by $P(< F)$ in eq. B.1.10. Then the g^2 tests the hypothesis that all (λ_1^*,λ_2^*) pairs have the same expected λ_i.

Bibliography

[1] M. Gyulassy, Nucl. Phys. A**354**, 395(1981).

[2] P. Freier *et al.*, Phys. Rev. **74**, 213(1948).

[3] P. Freier *et al.*, Phys. Rev. **74**, 1818(1948).

[4] H. L. Bradt and B. Peters, Phys. Rev. **74**, 1828(1948).

[5] H. L. Bradt and B. Peters, Phys. Rev. **75**, 1779(1949).

[6] H. L. Bradt and B. Peters, Phys. Rev. **77**, 54(1950).

[7] H. L. Bradt and B. Peters, Phys. Rev. **80**, 943(1950).

[8] M. F. Kaplon *et al.*, Phys. Rev. **85**, 295(1952).

[9] Y. Eisenberg, Phys. Rev. **96**, 1378(1954).

[10] D. E. Greiner *et al.*, Phys. Rev. Lett **35**, 152(1975).

[11] J. Papp *et al.*, Phys. Rev. Lett **10**, 601(1975).

[12] J. C. Cumming *et al.*, Phys. Rev. C**10**, 739(1974).

[13] J. C. Cumming *et al.*, Phys. Rev. C**14**, 1554(1976).

[14] J. C. Cumming *et al.*, Phys. Rev. C**17**, 1632(1978).

[15] J. C. Cumming *et al.*, Phys. Rev. C**18**, 1372(1978).

[16] C. R. Rudy and N. T. Porile, Phys. Rev. B**59**, 240(1975).

[17] N. T. Porile *et al.*, Phys. Rev. Lett. **43**, 918(1979).

[18] S. B. Kaufman *et al.*, Phys. Rev. C**22**, 1897(1980).

[19] J. Benecke *et al.*, Phys. Rev. **188**, 2159(1969).

[20] W. R. Frazer *et al.*, Rev. Mod. Phys. **44**, 284(1972).

[21] D. L. Olson *et al.*, Phys. Rev. C**24**, 1529(1981).

[22] G. D. Westfall *et al.*, Phys. Rev. Lett. **37**, 1202(1976).

[23] J. Gosset *et al.*, Phys. Rev. C**16**, 629(1977).

[24] R. Hagedorn *et al.*, Nuovo Cimento Suppl. **3**, 147(1965).

[25] W. D. Myers *et al.*, Nucl. Phys. A**296**, 177(1978).

[26] J. Gosset *et al.*, Phys. Rev. C**18**, 844(1978).

[27] R. L. Hatch and S. E. Koonin, Phys. Lett. B**81**, 1(1979).

[28] T. J. M. Symons *et al.*, Phys. Rev. Lett. **42**, 40(1979).

[29] G. D. Westfall *et al.*, Phys. Rev. Lett. **43**, 1859(1979).

[30] M. Jacob and H. Satz, eds., *Quark Matter Formation and Heavy Ion Collisions*, Proc. Bielefeld Workshop, 1982(World Scientific, Singapore, 1982); T.W. Ludlam and H. E. Wegner, eds., *Quark Matter* 1983, Brookhhaven, Nucl. Phys. A**418**, 1984; K. Kajantie, ed., *Quark Matter* 1984, Helsinki, Lecture Notes in Physics **221**(Springer, Heidelberg, 1984); M. Gyulassy, ed., *Quark Matter* 1986, Nucl. Phys. A**461**(1987); H. Satz, H. J. Specht and R. Stock, eds., *Quark Matter* 1987, Nordkirchen, Germany, Z. Phys. C**38**(1988); G. A. Baym, P. Braun-Munzinger and S. Nagamiya, eds., *Quark Matter* 1988, Lenox, USA, Nucl. Phys. A**498**(1989).

[31] L. McLerran, Rev. Mod. Phys. **58**, 1021(1986).

[32] T. Biro *et al.*, Nucl. Phys. A**386**, 617(1982).

[33] B. Muller and J. Rafelski, Phys. Rev. Lett. **48**, 1066(1985).

[34] R. C. Hwa and K. Kajantie, Phys. Rev. D**32**, 1109(1985).

[35] T. Matsui and H. Satz, Phys. Lett. B**178**, 416(1986).

[36] S. T. Butler and C. A. Pearson, Nuovo Cimento **19**, 1266(1961)

[37] C. P. Powell, P. H. Fowler and D. H. Perkins, *The Study of Elementary Particles by the Photographic Method*(Pergamon, London, 1959).

[38] K. Rybicki, Nuovo Cimento Ser. **49B**, 203(1967).

[39] H. H. Heckman and P. J. Lindstrom, Phys. Rev. Lett. **37**, 56(1976).

[40] G. D. Westfall *et al.*, Phys. Rev. C**19**, 1309(1979).

[41] M. T. Mercier *et al.*, Phys. Rev. Lett. **52**, 898(1984).

[42] M. T. Mercier *et al.*, Phys. Rev. C**33**, 1655(1986).

[43] J. C. Hill *et al.*, Phys. Rev. Lett. **60**, 999(1988).

[44] J. C. Hill *et al.*, Phys. Rev. C**38**, 1722(1988).

[45] J. C. Hill *et al.*, Phys. Rev. C**39**, 524(1989).

[46] C. Brechtmann, W. Heinrich and E. Benton, Phys. Rev. C**39**, 2222(1989).

[47] C. Brechtmann and W. Heinrich, Z. Phys. A**330**, 407(1988).

[48] C. Brechtmann and W. Heinrich, Z. Phys. A**331**, 463(1988).

[49] N. Ardito *et al.*, Europhys. Lett. **6**, 131(1988).

[50] P. B. Price *et al.*, Phys. Rev. Lett. **61**, 2193(1988).

[51] G. Singh, K. Sengupta and P. L. Jain, Phys. Rev. C**41**, 999(1990).

[52] G. Baroni *et al.*, Nucl. Phys. A**516**, 673(1990).

[53] E. Fermi, Z. Phys. **29**, 315(1924).

[54] C. F. von Weizsäcker, Z. Phys. **88**, 612(1934).

[55] E. J. Williams, Phys. Rev. **45**, 729(1934).

[56] J. D. Jackson, in *Classical Electrodynamics*, 2nd ed.(Wiley, New York, 1975).

[57] C. A. Bertulani and G. Baur, Nucl. Phys. A**442**, 739(1985).

[58] C. A. Bertulani and G. Baur, Phys. Reports **163**, 299(1988).

[59] G. Baur and C. A. Bertulani , Phys. Rev. C**34**, 1654(1986).

[60] J. S. Levinger, Phys. Rev. **84**, 43(1951).

[61] A. Milone, Nuovo Cimento Suppl. **12**, 353(1954).

[62] S. Tokunaga, T. Ishii and K. Nishikawa, Nuovo Cimento **5**, 517(1957).

[63] H. Yagoda, Nuovo Cimento **6**, 559(1957).

[64] E. M. Friedländer and M. Spîrchex, Nucl. Sci. Abstr. **15**, 3457(1961).

[65] B. Judek, Can. J. Phys. **46**, 343(1968).

[66] T. F. Cleghorn *et al.*, Can. J. Phys. Suppl. **46**, 572(1968).

[67] B. Judek, Can. J. Phys. **50**, 2082(1972).

[68] P. S. Freier and C. J. Waddington, Astrophy. Space Sci. **38**, 419(1975).

[69] H. B. Barber *et al.*, Phys. Rev. Lett. **48**, 856(1982).

[70] E. M. Friedländer, Phys. Rev. Lett. **45**, 1084(1980).

[71] E. M. Friedländer *et al.*, Phys. Rev. C**27**, 1489(1983).

[72] P. L. Jain and G. Das, Phys. Rev. Lett. **48**, 305(1982).

[73] M. M. Aggarwal *et al.*, Phys. Lett. B**112**, 31(1982).

[74] M. L. Tincknell *et al.*, Phys. Rev. Lett. **51**, 1948(1983).

[75] W. Heinrich *et al.*, Phys. Rev. Lett. **52**, 1401(1984).

[76] R. Bhanja *et al.*, Phys. Rev. Lett. **54**, 771(1985).

[77] M. M. Aggarwal *et al.*, Phys. Rev. C**32**, 6661985.

[78] J. D. Stevenson *et al.*, Phys. Rev. Lett. **52**, 515(1984).

[79] T. J. M. Symons *et al.*, Phys. Rev. Lett. **52**, 982(1984).

[80] P. L. Jain *et al.*, Phys. Rev. Lett. **52**, 2213(1984).

[81] P.L. Jain *et al.*, Phys. Rev. C**25**,3216(1982).

[82] P. L. Jain *et al.*, Phys. Lett. B**154**, 252(1985).

[83] A. Z. M. Ismail *et al.*, Phys. Rev. Lett. **52**, 1280(1984).

[84] S. B. Beri *et al.*(BCJJL Collaboration), Phys. Rev. Lett. **54**, 771(1985).

[85] M. El-Nadi *et al.*, Phys. Rev. Lett. **52**, 1971(1984).

[86] D. Ghosh *et al.*, Phys. Rev. Lett. **54**, 396(1985).

[87] M. Bano *et al.*, Phys. Lett. **B166**, 453(1986).

[88] A. P. Gasparian and N. S. Grigalashvili, Z. Phys. **A320**, 459(1985).

[89] M. Q. R. Khan *et al.*, Nuovo Cimento **A101**, 93(1989).

[90] G. Singh *et al.*, Phys. Lett. **B214**, 480(1988).

[91] K. Sengupta *et al.*, Europhys. Lett. **8**, 15(1989).

[92] G. Singh, K. Sengupta and P. L. Jain, Phys. Rev. **C42**, 1757(1990).

[93] E. S. Pshenin and V. G. Voinev, Phys. Lett. **B128**, 133(1983).

[94] B. F. Bayman *et al.*, Phys. Rev. Lett. **49**, 532(1982).

[95] M. H. MacGregor, *Proceedings of the Sixth Pan-American Workshop on Condensed Matter Theories*(1982) p.63.

[96] Y. E. Kim and M. Orlowski, Phys. Rev. **C29**, 2299(1984).

[97] W. J. Romo and P. J. S. Watson, Phys. Lett. **B88**, 354(1979).

[98] S. Fredriksson and M. Jänel, Phys. Rev. Lett. **48**, 14(1982).

[99] R. Slansky *et al.*, Phys. Rev. Lett. **47**, 887(1981).

[100] R. Saly *et al.*, Phys. Lett. **B115**, 239(1982).

[101] P. J. S. Watson *et al.*, Phys. Rev. **D27**, 1468(1983).

[102] A. De Rujula *et al.*, Phys. Rev. **D17**, 285(1978).

[103] J. Boguta, Phys. Rev. Lett. **50**, 148(1983).

[104] G. F. Chapline, Phys. Rev. **D25**, 911(1982).

[105] H. Stöcker *et al.*, Phys. Lett. **B95**, 192(1980).

[106] W. C. McHarris and J. O. Rasmussen, Phys. Lett. **B120**, 49(1983).

[107] G. N. Fowler *et al.*, Phys. Rev. Lett. **52**, 891(1984).

[108] W. H. Barkas, *Nuclear Research Emulsions*, Vol.1(Academic Press, New York, 1963).

[109] A. J. Apostolakis and J. V. Major, Brit. J. Appl. Phys. **8**, 9(1957).

[110] B. Rossi, *High Energy Particles*(Prentice Hall, Englewood Cliffs, 1952).

[111] H. H. Heckman *et al.*, Phys. Rev. C**17**, 1735(1978).

[112] M. I. Adamovich *et al.*, Phys. Lett. B**223**, 262(1989).

[113] K. Sengupta, G. Singh and P. L. Jain, Phys. Lett. B**222**, 301(1989).

[114] L. M. Barbier *et al.*, Phys. Rev. Lett. **60**, 405(1988).

[115] R.J. Glauber, in *Lectures in Theoretical Physics*, Ed. W. E. Brittin, Interscience, New York(1959) Vol.1, p.315.

[116] G. Baroni *et al.*, Nucl. Phys. A**531**, 691(1991).

[117] M. K. Carter *et al.*, Rutherford Appleton Laboratory compilation RAL-86-002(1986).

[118] I. Stenlund and I. Otterlund, Nucl. Phys. B**198**, 407(1982).

[119] H. Sato and Y. Okuhara, Phys. Lett. B**168**, 305(1986).

[120] M. I. Adamovich *et al.*, Phys. Rev. C**40**, 66(1989).

[121] V. S. Barashenkov *et al.*, Nucl. Phys. **14**, 522(1959); B. Jakobsson and R. Kullberg, Phys. Scri. **13**, 327(1976).

[122] B. Andersson, I. Otterlund and E. Stenlund, Phys. Lett. B**73**, 343(1978).

[123] I. Otterlund *et al.*, Nucl. Phys. B**142**, 445(1978).

[124] P. L. Jain, K. Sengupta, and G. Singh, Nuovo Cimento A**99**, 9(1988).

[125] M. I. Adamovich *et al.*, Phys. Lett. B**262**, 369(1991).

[126] P. L. Jain, K. Sengupta, and G. Singh, Phys. Rev. C**44**, 844(1991).

[127] M. I. Adamovich *et al.*, Phys. Lett. B**230**, 175(1989).

[128] M. I. Adamovich *et al.*, Phys. Rev. Lett.**67**, 1201(1991).

[129] M. I. Adamovich *et al.*, Phys. Lett. B**234**, 180(1990).

[130] V. S. Shukla *et al.*, Mod. Phys. Lett. A**18**, 1753(1988).

[131] A. Abduzhamilov *et al.*, Phys. Rev. D**39**, 86(1989).

[132] V. E. Dudkin *et al.*, Nucl. Phys. A**509**,783(1990).

[133] A. Abduzhamilov *et al.*, Phys. Rev. D**35**, 3537(1987).

[134] Z. Koba *et al.*, Nucl. Phys. B**40**, 317(1972).

[135] G. J. Alner *et al.*, Phys. Lett. B**106**, 193(1985).

[136] A. Bamberger *et al.*, Phys. Lett. B**205**, 583(1988).

[137] P. L. Jain *et al.*, Phys. Lett B**235**, 351(1990).

[138] M. I. Adamovich *et al.*, Phys. Lett. B**242**, 512(1990).

[139] T. Akesson *et al.*, Nucl. Phys. B**342**, 279(1990).

[140] P. M. Endt and C. van der Leun, Nucl. Phys. A**310**, 1(1978).

[141] J. M. Wyckoff *et al.*, Phys. Rev. B**137**, 576(1965).

[142] F. Ajzenberg-Selove, Nucl. Phys. A**449**, 1(1986).

[143] E. Andersen *et al.*, Phys. Lett. B**220**, 328(1989).

[144] E. G. Fuller, Phys. Reports **127**, 185(1985).

[145] J. Ahrens *et al.*, Nucl. Phys. A**251**, 479(1975).

[146] A. N. Gorbunov *et al.*, Sov. Phys.-JETP **15**,520(1962); A. N. Gorbunov and V. A. Osipova, Sov. Phys.-JETP **16**,27(1963).

[147] J. T. Caldwell *et al.*, Phys. Rev. Lett. **19**, 447(1967).

[148] A. Veyssière *et al.*, Nucl. Phys. A**227**, 513(1974).

[149] P.J. Carlos, Lecture Notes in Physics **137**, 168(1981).

[150] V. M. Maikov, Sov. Phys.-JETP **7**, 973(1958).

[151] M. E. Toms, Nucl. Phys. **54**, 625(1964).

[152] K. Kramer *et al.*, Z. Phys. **207**, 1(1967).

[153] R. Jäckle and H. Pilkuhn, Nucl. Phys. A**247**, 521(1975).

[154] A. Winther and K. Alder, Nucl. Phys. A**319**, 518(1979).

[155] A. Goldberg, Nucl. Phys. A**420**, 636(1984).

[156] B. Hoffmann and G. Baur, Phys. Rev. C**30**, 247(1984).

[157] M. N. Martins *et al.*, Phys. Rev. C**26**, 1936(1982).

[158] D. W. Anderson *et al.*, Nucl. Phys. A**156**, 74(1970).

[159] G. Bonazzola *et al.*, Nucl. Phys. **34**, 637(1962).

[160] B. S. Dolbilkin *et al.*, Sov. J. Nucl. Phys. **8**, 626(1969).

[161] L. Meyer-Schützmeister *et al.*, Nucl. Phys. A **108**, 180(1968).

[162] G. Baur and C. A. Bertulani, Phys. lett. B**174**, 23(1986).

[163] C. Hyde-Wright *et al.*, Phys. Rev. C**35**, 880(1987).

[164] T. N. Buti *et al.*, Phys. Rev. C**33**, 755(1987).

[165] J. J. Kelly *et al.*, Phys. Rev. C**41**, 2504(1990).

[166] B. S. Flanders *et al.*, Phys. Rev. C**43**, 2103(1991).

[167] G. S. Adams *et al.*, Phys. Rev. Lett. **43**, 42(1979).

[168] G. Dersch *et al.*, Phys. Rev. Lett. **55**, 1176(1985).

[169] E. Ganssauge, in *Nuclear Structure and Heavy-Ion Dynamics*, Ed. L. Moretto and R. A. Ricci, North-Holland, New York(1984), p.551.

[170] M. Abramovitz and J. A. Stegun, *Handbook of Mathematical Functions*, Dover, New York(1970), p.925.

[171] E. M. Friedländer *et al.*, Lawrence Berkeley Laboratory, Report No. LBL-12652, 1981(unpublished), p.416.

[172] B. F. Bayman and Y. C. Tang, Phys. Report **147**, 155(1987).

[173] H. K. Lee and H. McManus, Phys. Rev. Lett. **20**, 337(1968).

[174] C. Rogers and C. Wilkin, Nuovo Cimento Lett. **1**, 575(1971).